LA-UR-13-24014
Approved for public release; distribution is unlimited.

Title:	Groundwater Pathway Model for the Los Alamos National Laboratory Technical Area 54, Area G, Revision 1
Author(s):	Stauffer, Philip H.; Chu, Shaoping; Miller, Terry A.; Strobridge, Daniel M.; Cole, Gregory L.; Birdsell, Kay H.; Robinson, Bruce Alan; Gable, Carl Walter; Broxton, David E.; Springer, Everett P.; Shofield, Tracy
Intended for:	DOE Report Report
Issued:	2017-02-10 (rev.1)

LA-UR-13-24014
Approved for public release; distribution is unlimited.

Title: Groundwater Pathway Model for the Los Alamos National Laboratory Technical Area 54, Area G, Revision 1

Author(s): Stauffer, Philip H.
Chu, Shaoping
Miller, Terry A.
Strobridge, Daniel M.
Cole, Gregory L.
Birdsell, Kay H.
Robinson, Bruce A.
Gable, Carl W.
Broxton, David E.
Springer, Everett P.
Shofield, Tracy G.

Intended for: DOE Report

Issued: 2013-06-03

NOTE: Use these buttons to print or save the form. DO NOT use the browser tool bar. SAVE PRINT

LA-UR-13-21014

Approved for public release;
distribution is unlimited.

Title: Groundwater Pathway Model for the Los Alamos National Laboratory Technical Area 54, Area G, Revision 1

Groundwater Pathway Model for the Los Alamos National Laboratory Technical Area 54, Area G, Revision 1

Author(s):

Stauffer, Philip H.
Chu, Shaoping
Miller, Terry A.
Strobridge, Daniel M.
Cole, Gregory L.
Birdsell, Kay H.
Robinson, Bruce A.
Gable, Carl W.
Broxton, David E.
Springer, Everett P.
Shofield, Tracy G.

Philip H. Stauffer
Shaoping Chu
Terry A. Miller
Dan Strobridge (Weston Solutions, Inc.)
Greg Cole
Kay H. Birdsell

Submitted to: NNSA, DOE-EM

U.S. Department of Energy

SAVE PRINT CLEAR FORM

Los Alamos
NATIONAL LABORATORY

Table of Contents

Table of Contents i
List of Figures i
List of Tables iii
List of Attachments iii
Acronyms and Abbreviations iv

1.0 Introduction 1
2.0 Background 2
2.1 Site Description 2
2.2 Previous Investigations 10
3.0 Methods 13
3.1 Geologic Framework Model 13
3.2 Three-Dimensional Model Development 14
3.2.1 Development of Computational Mesh 14
3.2.2 Model Configuration and Boundary Conditions 19
3.2.2.1 Infiltration 21
3.2.2.2 Initial and Boundary Conditions 24
3.2.3 Hydrogeologic Input Data 25
3.2.4 Model Simulations 27
3.2.4.1 Conservative Breakthrough Curves 27
3.2.4.2 Longitudinal Dispersivity 29
3.2.4.3 Well Capture 29
3.3 Model Abstraction 33
3.4 Hydrologic Property Uncertainty Analysis 34
4.0 Results and Discussion 37
4.1 Breakthrough at the Compliance Boundary 37
4.1.1 Effects of Changes in Permeability and Infiltration 42
4.1.2 Model Sensitivity to Dispersivity 47
4.2 Well Capture 52
4.3 Comparison of 3-D and 1-D Breakthrough Curves 52
4.4 Comparison of 2005 and 2011 Model Projections 56
4.5 Impact of Hydrologic Property Uncertainty on Breakthrough 57
5.0 References 59

List of Figures

Figure 1 Locations of Area G and Groundwater Model Domain 3
Figure 2 Aerial Photograph of Area G Looking West toward Jemez Mountains 4
Figure 3 Waste Disposal Pits at Material Disposal Area G 5
Figure 4 Digital Elevation Model with the Boreholes and Regional Wells Used to Create the Geologic Framework Model for the 2011 Area G Groundwater Pathway Modeling Effort 7

Figure 5 Geologic Cross Section from Northwest to Southeast in the Vicinity of Area G (A-A' line of section shown on Figure 4) 8
Figure 6 Stratigraphic Nomenclature for the Bandelier Tuff 9
Figure 7 Elevations of Geologic Units in the WC09b GFM and Differences in Layer Thickness Relative to the FY03 GFM 15
Figure 8 Numerical Mesh for 3-D Groundwater Transport Model Showing Mesh Resolution and Digital Elevation Model 17
Figure 9 Cutaway of the Refined Portion of the Area G Mesh with Reduction in Vertical and Horizontal Spacing 18
Figure 10 Waste Disposal Pits and Waste Disposal Regions Superimposed on the Numerical Mesh 20
Figure 11 Normalized Histogram of Mesa-Top Infiltration Rates 23
Figure 12 Sensitivity Analysis of Particle Breakthrough to Size of Release Area at Waste Disposal Region 5 28
Figure 13 Distribution of Particle Release Points for Waste Disposal Region 5 (well capture simulation) 31
Figure 14 Cross Section of Numerical Mesh Showing Vertical Steps in Water Table 32
Figure 15 Two-Dimensional Views of Pathways for Particles Released from Waste Disposal Region 5 (high- and low-infiltration rates) 38
Figure 16 Breakthrough Curves for Particles Released from All Waste Disposal Regions (background infiltration of 0.5 mm/yr) 40
Figure 17 Breakthrough Curves for Particles Released from All Waste Disposal Regions (background infiltration of 10 mm/yr) 41
Figure 18 Effects of Permeability Reductions on Subsurface Saturation at Waste Disposal Region 5 43
Figure 19 Effects of Permeability Reductions on Breakthrough for Releases from Waste Disposal Regions 1 and 5 44
Figure 20 Subsurface Saturations at Waste Disposal Region 5 for Range of Steady-State Infiltration Rates (without increased Pajarito Canyon infiltration) 45
Figure 21 Effect of Pajarito Canyon Infiltration on Subsurface Saturation at Waste Disposal Region 5 46
Figure 22 Effect of Pajarito Canyon Infiltration on Breakthrough for Releases from Waste Disposal Regions 1 and 5 48
Figure 23 Breakthrough Curves for Particles Released from Waste Disposal Region 1 (range of steady-state infiltration rates) 49
Figure 24 Breakthrough Curves for Particles Released from Waste Disposal Region 5 (range of steady-state infiltration rates) 50
Figure 25 Model Sensitivity to Vadose-zone Longitudinal Dispersivity at Waste Disposal Region 5 (high- and low-infiltration rates) 51
Figure 26 Capture Zone for Hypothetical Well with High Pumping Rate 53
Figure 27 Comparison of Three-Dimensional Particle and One-Dimensional Plume Breakthrough Curves 55

List of Tables

Table 1 Depths and Elevations of Area G Disposal Pits 6
Table 2 Particle Release Locations Representing the Eight Waste Disposal Regions 21
Table 3 Hydrogeologic Properties Used for the Three-Dimensional Model 25
Table 4 Transformed Values for Shift of Tracer Particle Release Points for the Well Capture Analysis[a] 33
Table 5 Parameter Statistics and Assigned Distributions for Bandelier Tuff Stratigraphic Units 35
Table 6 Capture Efficiencies for Waste Disposal Regions 1 through 5 and 8 54
Table 7 Approximate Peak Breakthrough Times by Waste Disposal Region, 2005 vs. 2011 56

List of Attachments

Attachment I Update of the Vadose-Zone Geologic Framework Model for the Los Alamos National Laboratory TA-54, Area G Groundwater Pathway Model
Attachment II Generation of the Three-Dimensional Computational Mesh for the Los Alamos National Laboratory TA-54, Area G Groundwater Pathway Model
Attachment III Statistical Description of Vadose-Zone Hydrologic Properties for the Los Alamos National Laboratory TA-54, Area G Groundwater Pathway Model
Attachment IV Incorporation of Sorption in the Micromixing Model for the Los Alamos National Laboratory TA-54, Area G Groundwater Pathway Model
Attachment V Details on the Coupling of GoldSim and the Finite Element Heat and Mass (FEHM) Transfer Code for the Los Alamos National Laboratory TA-54, Area G Groundwater Pathway Model
Attachment VI Summary of Pre- and Post- Processing Codes for the Los Alamos National Laboratory TA-54, Area G Groundwater Pathway Model
Attachment VII Comparison of 2005 and 2011 Results for the Los Alamos National Laboratory TA-54, Area G Groundwater Pathway Model
Attachment VIII Quantifying Transport Uncertainty in Unsaturated Soil using Monte Carlo Sampling of Retention Curves for the Los Alamos National Laboratory TA-54, Area G Groundwater Pathway Model

Acronyms and Abbreviations

1-D	One-dimensional
3-D	Three-dimensional
DEM	Digital elevation model
FEHM	Finite Element Heat and Mass (transfer code)
GFM	Geologic Framework Model
LANL or Laboratory	Los Alamos National Laboratory
MDA	Material Disposal Area
msl	Mean sea level
OMR	Octree mesh refinement
PA/CA	Performance Assessment/Composite Analysis
RTD	Residence time distribution functions
TA	Technical Area

1.0 Introduction

This report describes the groundwater flow and transport modeling conducted in support of the Los Alamos National Laboratory (LANL or the Laboratory) Area G performance assessment and composite analysis. The Area G performance assessment and composite analysis use models created with GoldSim™ (GoldSim, 2010a and 2010b), a system-level modeling tool that allows the integration of numerous process-level models and provides the tools needed to conduct probabilistic assessments of long-term facility performance. The groundwater transport model detailed in this report is one of several process models incorporated into the performance assessment and composite analysis model.

The groundwater transport modeling effort builds on the knowledge gained through previous studies at Area G and is augmented by the use of new data, modeling tools, and computer simulations. The approach combines geologic, hydrologic, and topographic data into a three-dimensional (3-D) site-scale model. Mathematical models are used to simulate the transport of radionuclides from the surface through a deep vadose (unsaturated) zone, into the saturated zone, and finally, to the compliance boundary located 100 m (330 ft) east of Area G. Although the compliance period for the performance assessment and composite analysis is 1,000 years, the simulations are designed to be robust and can be used to estimate groundwater impacts well past the regulatory timeframe to provide insight into possible long-term issues.

This report consists of four major sections, including this introductory section. Section 2 provides an overview of previous investigations related to the development of the current site-scale model. The methods and data used to develop the 3-D groundwater model and the techniques used to distill that model into a form suitable for use in the GoldSim models are discussed in Section 3. Section 4 presents the results of the model development effort and discusses some of the uncertainties involved. Eight attachments that provide details about the components and data used in this groundwater pathway model are also included with this report.

The groundwater modeling effort reported here is a revision of the work that was conducted in 2005 (Stauffer et al., 2005a) in support of the 2008 Area G performance assessment and composite analysis (LANL, 2008). The revision effort was undertaken primarily to incorporate new geologic information that has been collected since 2003 at, and in the vicinity of, Area G. The new data were used to create a more accurate geologic framework model (GFM) that forms the basis of the numerical modeling of the site's long-term performance. The groundwater modeling uses mean hydrologic properties of the geologic strata underlying Area G; this revision includes an evaluation of the impacts that natural variability in these properties may have on the model projections.

2.0 Background

Area G, the only active low-level waste repository at the Laboratory, has been in operation since 1957. The location, topography, and general stratigraphy of Area G are described briefly in Section 2.1. Section 2.2 summarizes some of the details of previous geologic and groundwater transport studies relevant to the groundwater modeling effort.

2.1 Site Description

As shown in Figure 1, Area G is located on the eastern edge of the Laboratory in Technical Area (TA) 54, approximately 2 km (1.2 mi) west of the town of White Rock and about 5 km (3.1 mi) west of the Rio Grande. The site lies on Mesita del Buey, which is bounded to the north by Cañada del Buey and to the south by Pajarito Canyon (Figure 2). The surface of Area G slopes to the east from an elevation of 2,070 m (6,790 ft) above mean sea level (msl) in the expansion area near Material Disposal Area (MDA) L, to an elevation of approximately 2,033 m (6,670 ft) above msl at the eastern end of Area G.

The Area G disposal facility consists of an active material disposal area (MDA G) and the Zone 4 expansion area (Figure 2). Disposal operations have been confined to MDA G since the facility began receiving waste in 1957; current plans call for the expansion of disposal operations into Zone 4 when the disposal capacity of MDA G has been exhausted. Radioactive waste generated at the Laboratory has been disposed of in pits (Figure 3) and shafts. Table 1 lists the depth and average surface and bottom elevations of each of the waste disposal pits. The shafts range in depth from approximately 8 to 20 m (26 to 66 ft) and are typically 0.5 to 1.0 m (1.6 to 3.3 ft) in diameter.

Subsurface information about the basic stratigraphy beneath Area G has been obtained from regional characterization wells and numerous boreholes drilled at the site (Figure 4). Surface and near-surface geology in the vicinity of Area G is dominated by the Bandelier Tuff Formation, which overlies Tertiary-age Cerros del Rio basalt flows and volcanics that range from approximately 200 to 235 m (660 to 770 ft) thick and include the upper portion of the regional water table (Figure 5). The Bandelier Tuff increases in thickness from east to west beneath Mesita del Buey. The formation is divided into the upper Tshirege Member and the lower Otowi Member. These members are sometimes separated by a thin (3 to 9 m [9.8 to 29 ft]) deposit of epiclastic sediments known as the Cerro Toledo interval, which is technically not a part of the Bandelier Tuff, but has material properties more similar to the tuff than to the underlying Cerros del Rio basalts. The Tshirege and Otowi Members are further subdivided into the lithostratigraphic units shown in Figure 6 (Broxton and Reneau, 1995). Both the Tshirege and Otowi Members contain basal pumice beds, although these are not always present at a given location. Recent borehole data indicate that the thickness of individual lithologic units varies greatly across Area G, with the Guaje Pumice, Otowi Member ash flow tuffs (referred to in this report as the Otowi Member), and Cerro Toledo interval being entirely absent at some locations.

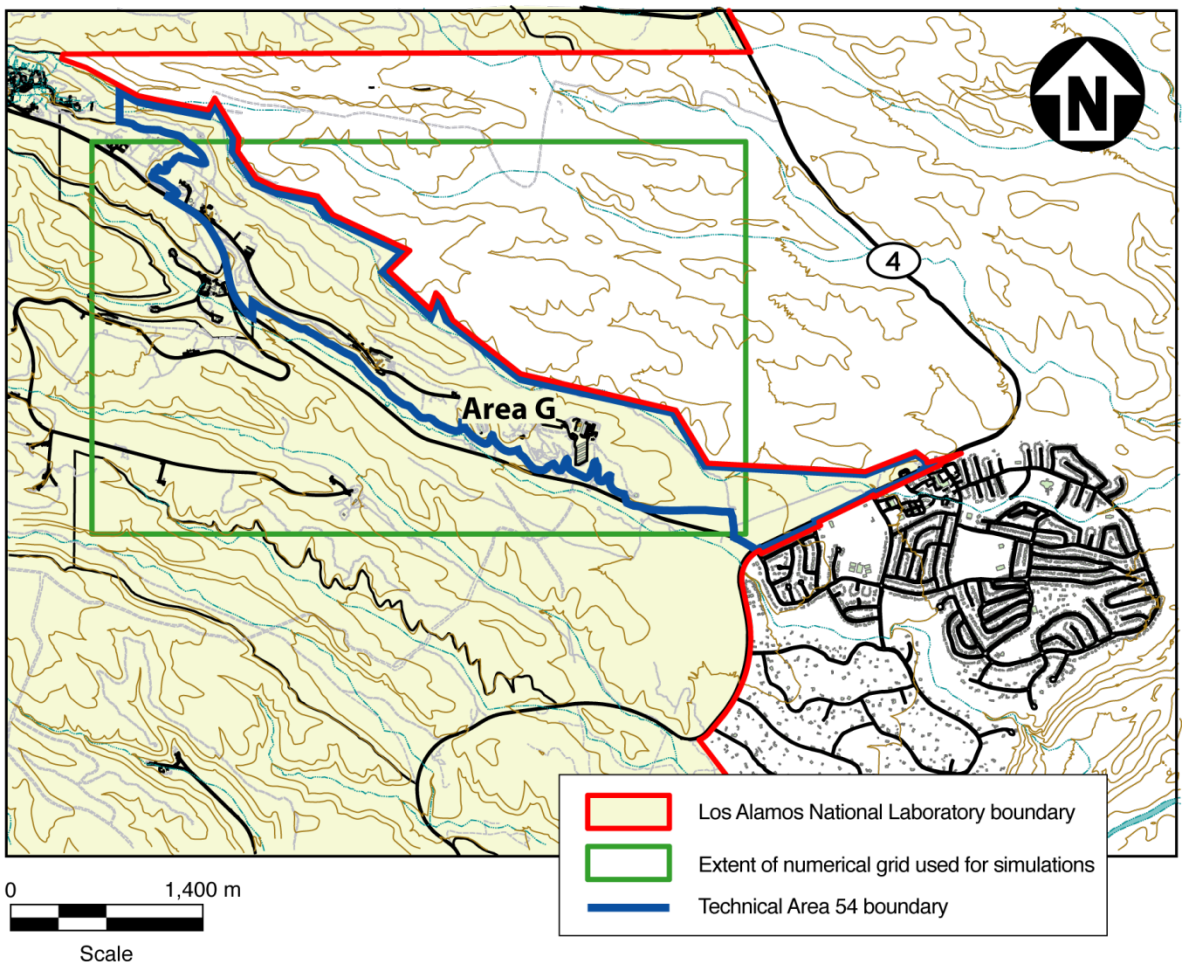

Figure 1
Locations of Area G and Groundwater Model Domain

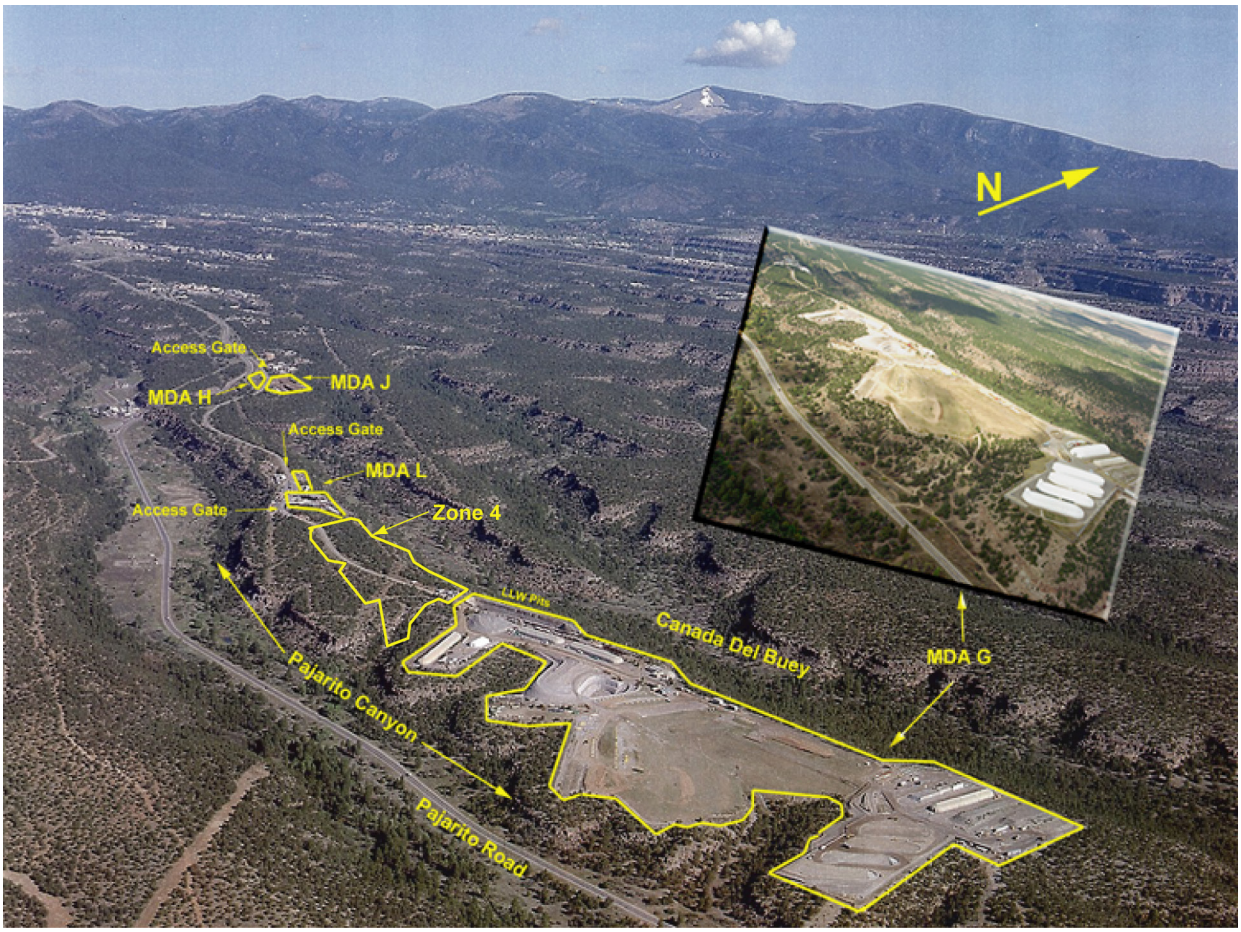

Figure 2
Aerial Photograph of Area G
Looking West toward Jemez Mountains

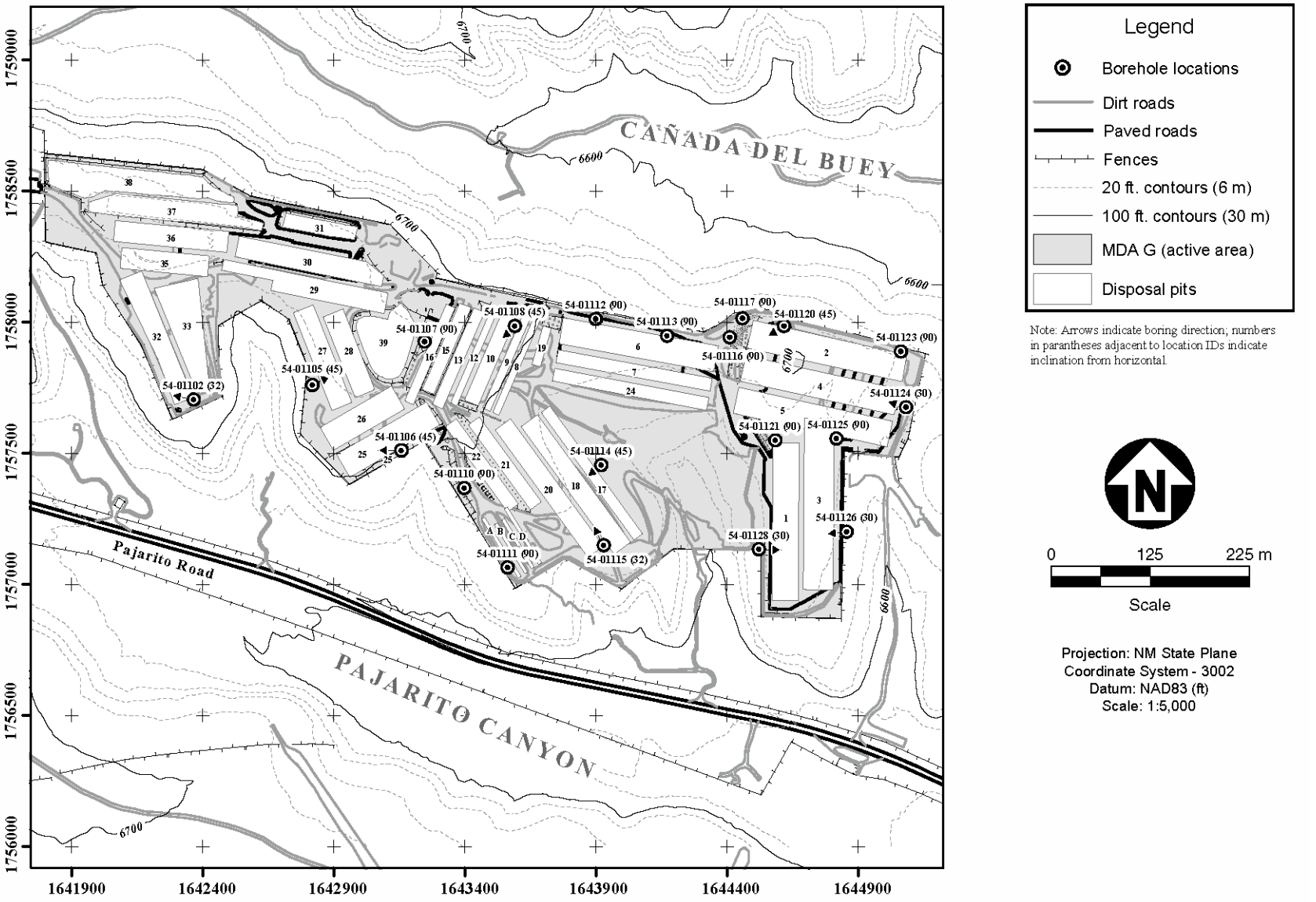

Figure 3
Waste Disposal Pits at Material Disposal Area G

Table 1
Depths and Elevations of Area G Disposal Pits

Pit Number	Depth (m)	Elevation above Mean Sea Level (m)	
		Surface	Bottom of Pit
1	6	2,034	2,028
2	8	2,037	2,029
3	10	2,034	2,024
4	10	2,036	2,026
5	9	2,034	2,025
6	8	2,039	2,031
7	9	2,039	2,030
8	8	2,042	2,034
9	6	2,043	2,037
10	8	2,044	2,036
12	8	2,047	2,039
13	9	2,047	2,038
15	9	2,047	2,038
16	8	2,047	2,039
17	7	2,034	2,027
18	12	2,035	2,023
19	5	2,042	2,037
20	11	2,038	2,027
21	8	2,041	2,033
22	10	2,042	2,032
24	9	2,033	2,024
25	12	2,044	2,032
26	11	2,050	2,039
27	14	2,055	2,041
28	12	2,047	2,035
29	15	2,050	2,035
30	11	2,050	2,039
31	8	2,043	2,035
32	16	2,051	2,035
33	12	2,052	2,040
35	12	2,052	2,040
36	13	2,052	2,039
37	19	2,052	2,033
38	18	2,055	2,037
39	14	2,047	2,033

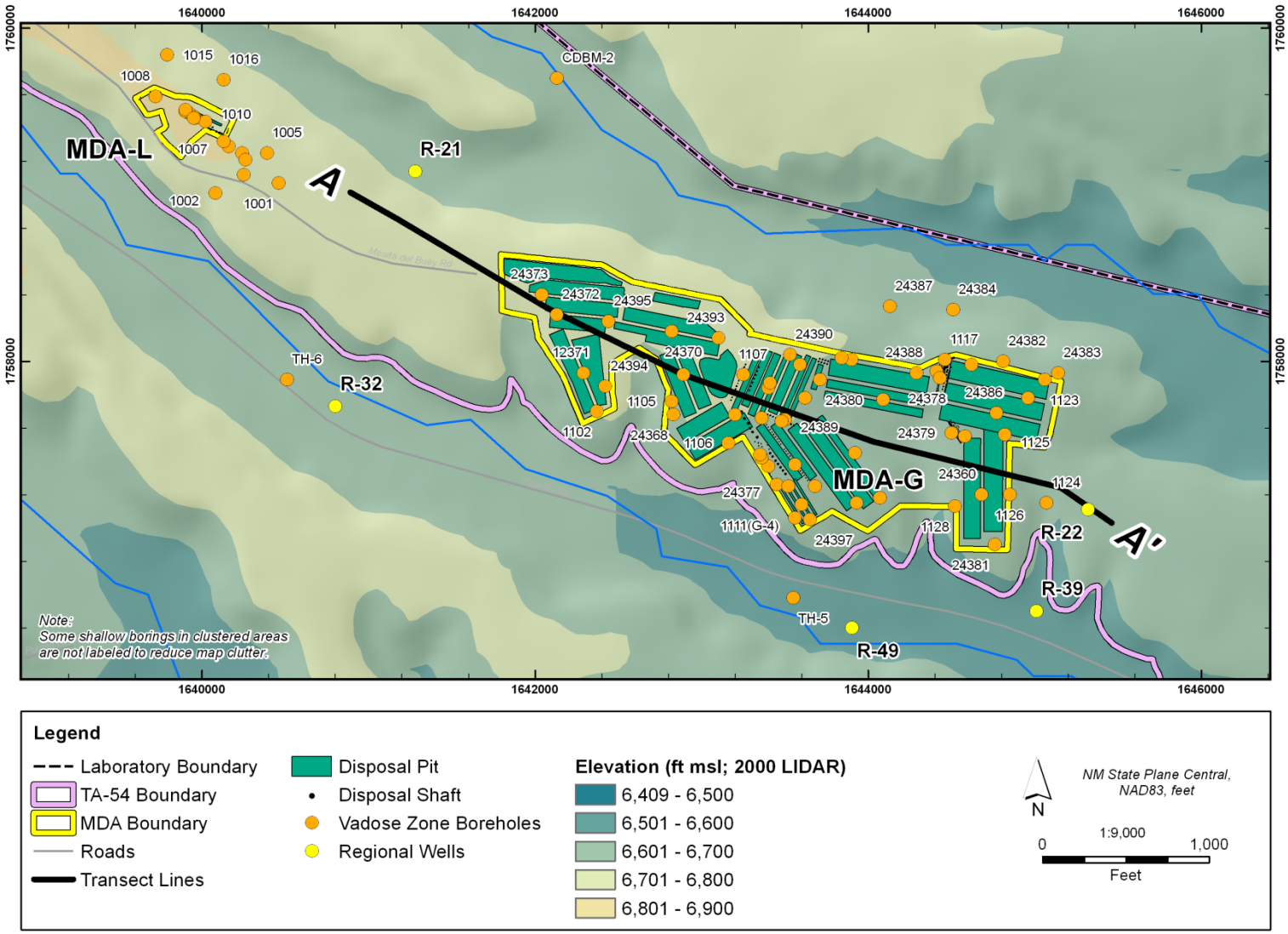

Figure 4
Digital Elevation Model with the Boreholes and Regional Wells Used to Create the Geologic Framework Model for the 2011 Area G Groundwater Pathway Modeling Effort

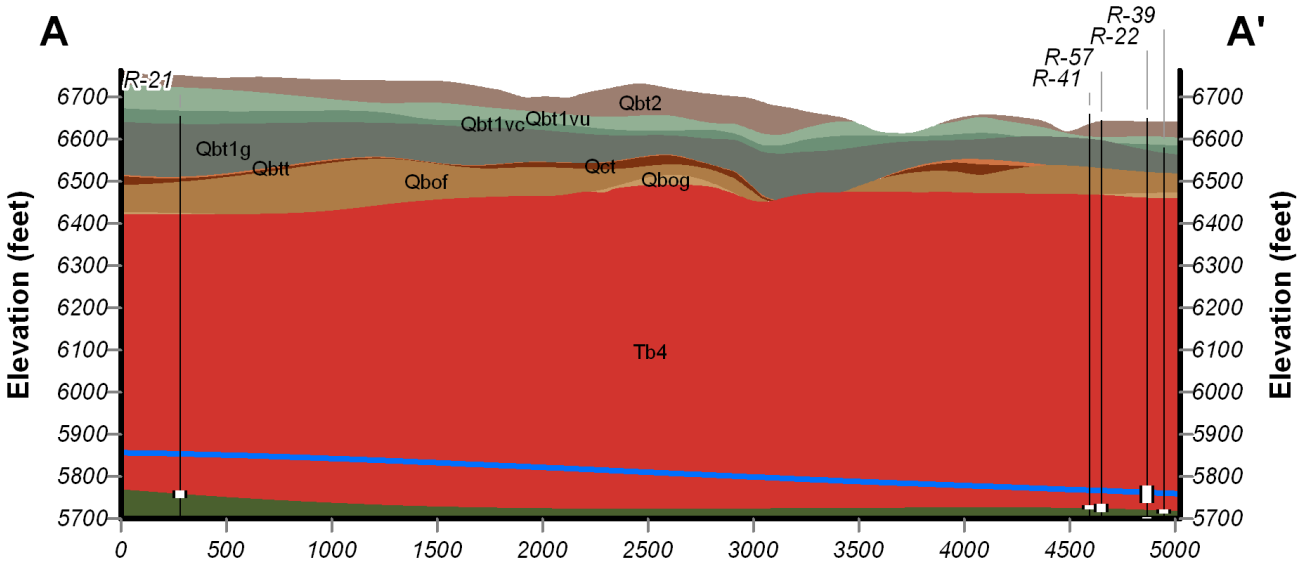

Legend

- Well Casing
- Well Screen
- Top of Regional Water Table

Geologic Unit

- Qbt2 - Bandelier Tuff - unit 2
- Qbt1vu - Bandelier Tuff - unit 1vu
- Qbt1vc - Bandelier Tuff - unit 1vc
- Qbt1g - Bandelier Tuff - unit 1g
- Qbtt - Tsankawi Pumice
- Qct - Cerro Toledo interval
- Qbof - Bandelier Tuff - Otowi unit
- Qbog - Bandelier Tuff - Guaje Pumice
- Tb4 - Cerros del Rio Basalts
- Tvt2b - Younger Tschicoma dacite flow
- Tpf - Puye Formation
- Tpt - Totavi Lentil

Note:
These point to point cross-sections were extracted from EarthVisions model grids representing layer top elevations. A 1000-ft buffer around the transect line was used to filter the borehole data set to those locations pertinent to the section. As a result of this buffer, some boreholes may not appear to plot correctly relative to ground due to the high topographic relief on the Pajarito plateau. Likewise, some screen intervals may not appear to plot in the correct geologic unit due to changes in layer top elevations off-transect.

Figure 5
Geologic Cross Section from Northwest to Southeast in the Vicinity of Area G (A-A′ line of section shown on Figure 4)

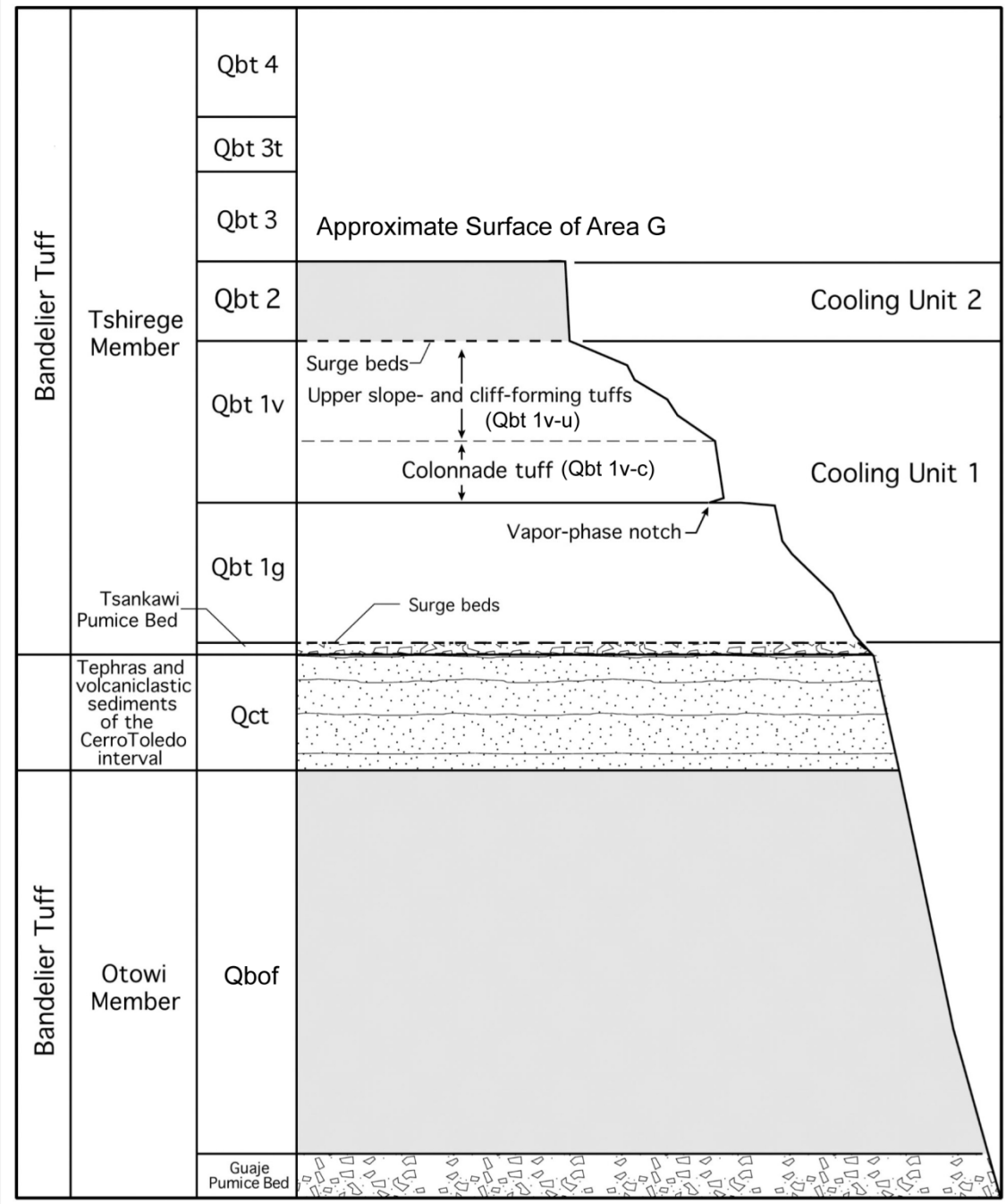

Figure 6
Stratigraphic Nomenclature for the Bandelier Tuff

Source: Adapted from Broxton and Reneau (1995)

The Tshirege Member extends 60 to 109 m (197 to 348 ft) below the ground surface (bgs) in the vicinity of Area G and consists of a series of cooling units whose physical properties vary both vertically and laterally. The disposal pits and shafts at Area G have been excavated into units 2, 1v-u, and 1v-c of the Tshirege Member. Surge beds are typically present at the base of units 2 and 1g. A notable feature at the base of cooling unit 1v is a thin, horizontal zone of preferential weathering known as the vapor-phase notch. This notch represents a break between an upper devitrifried zone and a lower vitrified unit that is a mappable marker horizon throughout the Pajarito Plateau (Broxton and Reneau, 1995).

2.2 Previous Investigations

The groundwater pathway modeling presented in this report builds upon the findings and information provided by a number of earlier investigations. A solid foundation was provided by data compiled in support of the 1997 performance assessment and composite analysis (Hollis et al., 1997); this includes geologic information (Vaniman et al., 1996) and hydrologic parameters for Area G (Krier et al., 1996; Rogers and Gallaher, 1995). Information developed since the completion of the 1997 analyses increased understanding of groundwater flow and transport in the vicinity of Area G, and the comprehensive modeling effort undertaken in 2005 provides the basis for the new work described in Section 3. A brief summary of many of these investigations is provided below.

Groundwater modeling conducted in support of the 2008 performance assessment and composite analysis took advantage of a high-resolution digital elevation model (DEM) of the surface topography (Carey and Cole, 2002) and used a GFM that incorporated stratigraphic data from recent regional characterization wells. The updated DEM and geologic model were used to develop a 3-D representation of the site that was more accurate than the model used to conduct the 1997 performance assessment and composite analysis. The LANL Fiscal Year 2009 (FY09) GFM (Cole et al., 2010) builds on earlier geologic models by incorporating information that was collected from regional characterization wells and boreholes that were drilled in the vicinity of Area G from 2003 through 2009 (e.g., Ball et al., 2002; Kleinfelder, 2003; LANL 2003; LANL 2009a; LANL 2009b); the locations of the wells and boreholes, and the DEM upon which the LANL FY09 GFM is based are shown in Figure 4. As discussed in Section 3.1, the LANL FY09 GFM was the starting point for defining the geology that was used to conduct the groundwater modeling update.

New hydrogeologic datasets include an updated compilation and statistical analysis of subsurface material properties of the Bandelier Tuff at TA-54 (Springer, 2005), a statistical analysis of mesa-top infiltration (Springer and Schofield, 2004), and constraints on the properties of vadose-zone, fractured basalt (Stauffer et al., 2005b). These new data, discussed below, are important inputs to the groundwater pathway model.

Springer (2005) examined geographical differences among vadose-zone hydrologic properties across the Laboratory as a means of estimating vadose-zone model parameters for the Bandelier Tuff. Hydrologic properties include measured properties such as bulk density, saturated water content, and saturated hydraulic conductivity, and fitted parameters such as the van Genuchten equation parameters (α and n) and residual water content. Nonparametric analyses were used to identify differences among the measured hydrologic properties for (1) lithologic units within a LANL TA, (2) at different TAs, (3) in mesa-top versus canyon settings, and (4) across lithologic units. For any given TA, most hydrologic properties were similar within lithologic units. No consistent relationships were found among TAs, except for the residual water content, which was essentially zero at all locations. Hydrologic properties of Tshirege unit 1g were somewhat similar for both mesa-top and canyon settings, but this was not true for the properties of the Otowi Member. Hydrologic properties for Tshirege units 1v and 1g were essentially the same.

Stauffer et al. (2005b) used data from a bromide tracer test at the Los Alamos Canyon low-head weir to constrain material properties in the unsaturated zone of the Cerros del Rio basalts. This study showed that, under ponded conditions, the Cerros del Rio basalts behave like a very low-porosity, high-permeability system.

Previous groundwater transport investigations at Area G (Birdsell et al., 1995, 1999, and 2000; Hollis et al., 1997; Soll, 1995) provide insight into the local transport of radionuclides; these studies relied on the process-level, multidimensional, finite-element porous flow and transport simulator known as FEHM (Finite Element Heat and Mass) (Zyvoloski et al., 1995a and 1995b) to model the movement of water-soluble radionuclides from the disposal pits and shafts at Area G to a drinking water compliance point. Summaries of pertinent aspects of these studies, which guided the current effort, are provided below.

Birdsell et al. (1999) conducted investigations into specific flow processes that are relevant to the modeling approach adopted for this study. To determine the effect of transient pulses of moisture on radionuclide transport in the vicinity of Area G, Birdsell et al. ran 1-D and 2-D models of liquid-phase C-14 transport through the Bandelier Tuff. Four scenarios were evaluated. These scenarios had nearly identical long-term infiltration rates of 5.5 mm/yr (0.22 in./yr); however, infiltration rates for individual years varied greatly (from zero to over 100 mm/yr [3.9 in./yr]), and the four selected scenarios had different temporal distributions. Simulations were run for 5,000 years, and the results of the C-14 transport modeling were compared to a simulation that used the long-term average infiltration rate. This study showed that a steady-state flow assumption is valid within the range of likely infiltration rates for Area G and its environs because the transient pulses were damped out as they propagated downward through the system.

Other modeling examined the effect that fractures in the tuff may have on water flow by evaluating possible scenarios where significant fracture flow may occur (Birdsell et al., 1999; Soll and Birdsell, 1998). The effects of fracture coatings and fills, locations of fractures with respect to the waste, and interactions between fractures and the surrounding matrix were considered. High-infiltration rates were assigned to the top of the simulated fracture systems to ensure that "worst case" conditions were achieved. The results showed that limited fracture flow was activated only during extreme events such as surface ponding of water. The authors concluded that, in most cases, fractures in tuff at Area G are not a major conduit for the movement of water from the surface to the water table.

Birdsell et al. (1999) also examined how evaporation from the surge bed at the base of Tshirege unit 2 (see Figure 6) might affect vadose-zone flow. Their results showed that evaporation could cause extremely high capillary forces and result in the flow of water toward the surge bed.

Modeling by Robinson et al. (1999) showed that changes in hydrologic properties at the subgrid scale can lead to reduced permeability across unit interfaces. Robinson et al. (1999) reported that the permeability decreased by a factor of about 1,000 at the top of the Cerros del Rio, leading to the accumulation of perched water beneath Los Alamos Canyon. This study is applicable to the Area G groundwater transport modeling because saturation data from regional characterization well R-32, located southwest of Area G (Figure 4)**,** indicate that reductions in permeability occur at two interfaces, one at the base of Tshirege unit 1g and the other at the top of the Cerros del Rio basalts.

Another consideration for the groundwater pathway modeling is the effect that increased infiltration in nearby canyons may have on the transport of contaminants from Area G. As described in Pratt (1998), the lower Pajarito Canyon, just south of Area G, has more subsurface water than Cañada del Buey and thus is more likely to have an impact on radionuclide transport. Pajarito Canyon is relatively wide and has a fairly flat bottom in the area near Area G, as seen in Figure 2. Shallow wells located along the canyon bottom between TA-18 to the west of Area G and White Rock to the east indicate the presence of alluvial groundwater, which is attributed to the fact that this section of Pajarito Canyon is a major drainage between the Jemez Mountains and the Rio Grande (Pratt, 1998). The section of Pajarito Canyon just south of Area G is hydrologically similar to other major drainages at the Laboratory**,** such as lower Los Alamos Canyon (Nylander et al., 2003). Runoff from higher elevations is focused into Pajarito Canyon and creates a transient stream that flows intermittently, sometimes resulting in pooled water in the canyon bottom to the south of Area G (Pratt, 1998). The most recent estimate of average annual infiltration in lower Pajarito Canyon is 18.5 m^3/m (200 ft^3/ft) (Kwicklis et al., 2005, Table 2). This value represents the average volume of water infiltrating per length of canyon across the average canyon width between two stream gauges; the upstream gauge is located several kilometers west of Area G and the downstream gauge lies just west of White Rock. The infiltration value does not account for stream losses due to evapotranspiration.

3.0 Methods

The Area G groundwater pathway modeling effort documented in this report included (1) the development of a 3-D model capable of simulating the transport of water-soluble radionuclides released from the pits and shafts at Area G and (2) the abstraction of this complex model to a 1-D form suitable for implementation within GoldSim. As was the case for the previous round of groundwater modeling (Stauffer et al., 2005a), the 3-D modeling was conducted using FEHM (Zyvoloski et al., 1995a, and1995b, and Zyvoloski, 2007). Stochastic modeling of groundwater transport can require thousands of simulations. Given the computer-resource-intensive nature of the full 3-D FEHM model, 1-D abstractions of the 3-D model were developed for use in the probabilistic analyses. The GoldSim model controls these 1-D model abstractions, allowing the bulk transport properties of the radionuclides to be modified as desired.

The groundwater modeling effort described here represents a revision of the work that was conducted in 2005 (Stauffer et al., 2005a) in support of the 2008 Area G performance assessment and composite analysis (LANL, 2008). The revision effort was undertaken primarily to include changes to the GFM upon which the 3-D modeling is based. The updated model relies on mean hydrologic properties for the geologic strata underlying the disposal facility. These parameters are naturally variable, and that variability introduces uncertainty into the projections of groundwater travel times. The impacts of uncertain hydrologic properties were evaluated as part of the revision.

The 3-D modeling requires a numerical mesh that represents the topography and geology of Area G and the surrounding area. Section 3.1 discusses the GFM adopted for this modeling effort and compares it to prior geologic models. Section 3.2 describes how the mesh was developed from the GFM and how the 3-D model was configured to enable more realistic simulations of flow and transport. Section 3.3 describes how the resultant 3-D breakthrough curves were abstracted to a series of 1-D models that recreate particle breakthrough at the compliance boundary. Finally, Section 3.4 discusses the methods used to conduct an uncertainty analysis of hydrologic properties.

3.1 Geologic Framework Model

A GFM, known as WC09b, was developed to provide a more accurate 3-D representation of the site specifically for this revision of the groundwater transport model and was mapped to the numerical mesh used to calculate transport from the waste disposal units to the regional aquifer. The WC09b GFM represents an update of the LANL FY09 GFM that is discussed in Section 2.1. It improves upon the geologic model that was used in the 2005 groundwater modeling effort by incorporating well and borehole data collected in the vicinity of Area G from 2003 to 2009, and updates the LANL FY09 GFM by including borehole data collected in 2010. The inclusion of

data from the additional wells and boreholes provides a more accurate representation of geologic conditions at the site, relative to previous GFMs. A complete description of the GFM is provided in *Attachment I*.

The contours of the geologic units that are estimated using the WC09b GFM are shown in Figure 7; this figure also shows differences in unit thicknesses relative to the FY03 GFM that was used to conduct the 2005 groundwater modeling. The two thickest units in the model, the Cerros del Rio (Tb4) and the Otowi Member (Qbof), exhibit the most change between the two GFMs, up to 76 m (250 ft) and 46 m (150 ft), respectively, and exert significant control on the shapes of the remaining layers. Thicknesses of all other layers have changed by less than 15 m (50 ft).

3.2 Three-Dimensional Model Development

The 3-D model developed using FEHM draws on the modeling conducted in 2005 and information and techniques that have become available since that time. Section 3.2.1 discusses the development of the 3-D computational mesh used to conduct the updated groundwater modeling, Section 3.2.2 explains how the model was configured to simulate actual conditions, and Section 3.2.3 presents the hydrogeologic input data used to populate the model. Descriptions of the simulations that were conducted in conjunction with the model development effort are presented in Section 3.2.4.

3.2.1 Development of Computational Mesh

The 3-D computational mesh used to conduct the 2011 groundwater modeling retains the same mesh coordinates as the mesh used in Stauffer et al. (2005a), but the rock type associated with each node has been reassigned to reflect the updated GFM. The mesh was designed to meet several conditions:

- Continuity and correlation with the Española basin site-scale regional aquifer computational model (Keating et al., 2003)
- Resolution adequate to accurately locate features such as waste pits, truncated material layers along the mesa, fence boundaries, and the compliance boundary
- Incorporation of the 3-D WC09b GFM to define the hydrogeologic layers
- Adequate hydrogeologic layer resolution to provide accurate streamline-particle-tracking solutions

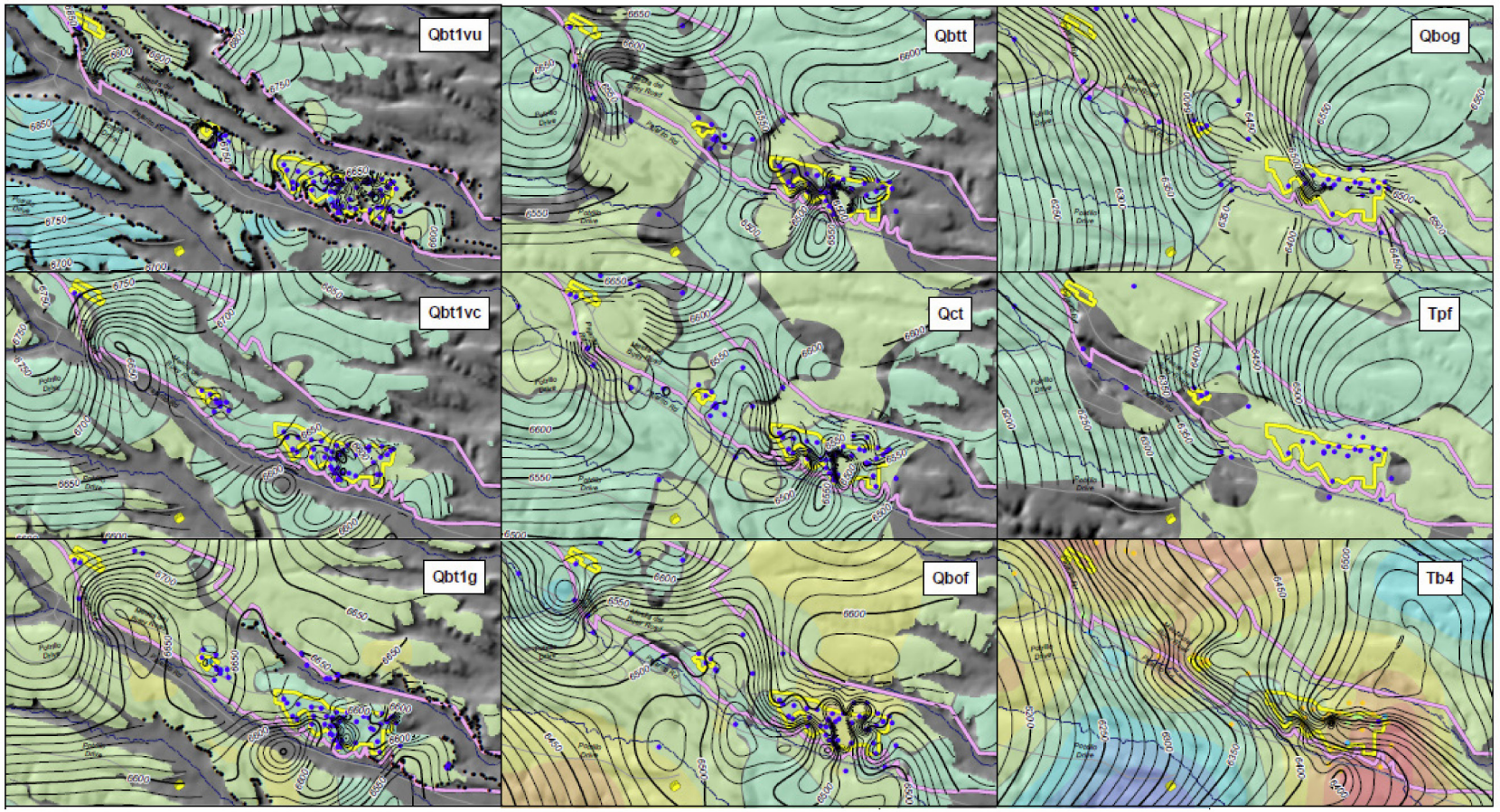

Figure 7
Elevations of Geologic Units in the WC09b GFM and Differences in Layer Thickness Relative to the FY03 GFM

The new mesh incorporates a refinement technique that provides high resolution near the Area G waste disposal units and lower resolution away from the Area G fence line (Figure 8). The mesh spans an area of nearly 15 km^2 (5.8 mi^2), which is large enough to avoid edge effects that may lead to nonphysical transport simulations. The mesh extends well below the water table and is used to follow contaminant pathways from the surface of the disposal facility through the vadose zone, into the saturated zone, and finally to the point of compliance 100 m (330 ft) downgradient of the Area G fence line. Stauffer et al. (2005a) used the metric-based polar stereographic coordinate system used in the Española basin site-scale regional aquifer computational model (Keating et al., 2003). For the revised modeling, the coordinate system was converted to a state map projection system based on the North American Datum of 1983 (State Plane NAD83). A complete description of the mesh generation process is presented in *Attachment II*.

The numerical mesh measures 4,750 m (3 mi) from east to west and 2,875 km (1.8 mi) from north to south (Figure 1). The footprint of the mesh was designed to encompass several important wells, including regional characterization wells R-20, R-21, R-22, R-23, R-32, R-37, R-38, R-39, R-49, and water supply well PM-2, to the northwest of well R-20. Several of these wells are included in Figure 4; the locations of all wells are shown in *Attachment I*, Figure I-1.

The surface elevation of the mesh was interpolated from a high-resolution DEM (Carey and Cole, 2002) that ranges from 2,150 m (7,055 ft) above msl in the northwest to approximately 2,000 m (6,560 ft) above msl in the southeast; this model is shown in Figure 8. As discussed earlier, the mesh resolution decreases with distance from Area G, yielding the most accurate representation of the surface topography near the disposal pits. This can be seen in Figure 9, in which the well-defined topography on Mesita del Buey (where Area G is located) contrasts with the blocky appearance of the mesa to the south. The mesh spacing between nodes in the horizontal direction reaches a minimum of 7.8 m (26 ft) in the vicinity of the pits and shafts and is coarsest (125 m [410 ft]) in the regions farthest from the disposal facility. The high-resolution section extends more than 100 m (328 ft) beyond the boundary of Area G to ensure that lateral transport can be modeled adequately.

The vertical resolution of the mesh varies; the resolution is greatest in the vadose zone and the upper part of the saturated zone where most contaminant transport is expected to occur, and decreases with depth below ground surface. In the vicinity of Area G, a vertical resolution of 6.25 m (20.5 ft) is used to represent the Bandelier Tuff and the uppermost 50 to 70 m (160 to 230 ft) of the basalt. Below this, a two-step transition is applied, resulting in a vertical mesh spacing of 37.5 m (123 ft) from the bottom of the high resolution region to approximately 1,000 m (3,300 ft) below ground surface, and a 150 m (490 ft) mesh spacing at greater depths. To minimize boundary effects, the mesh extends to an elevation of 100 m (330 ft) above msl. This is far below the surface of the water table, which lies at an elevation of 1,740 to 1,800 m (5,700 to 5,900 ft) above msl.

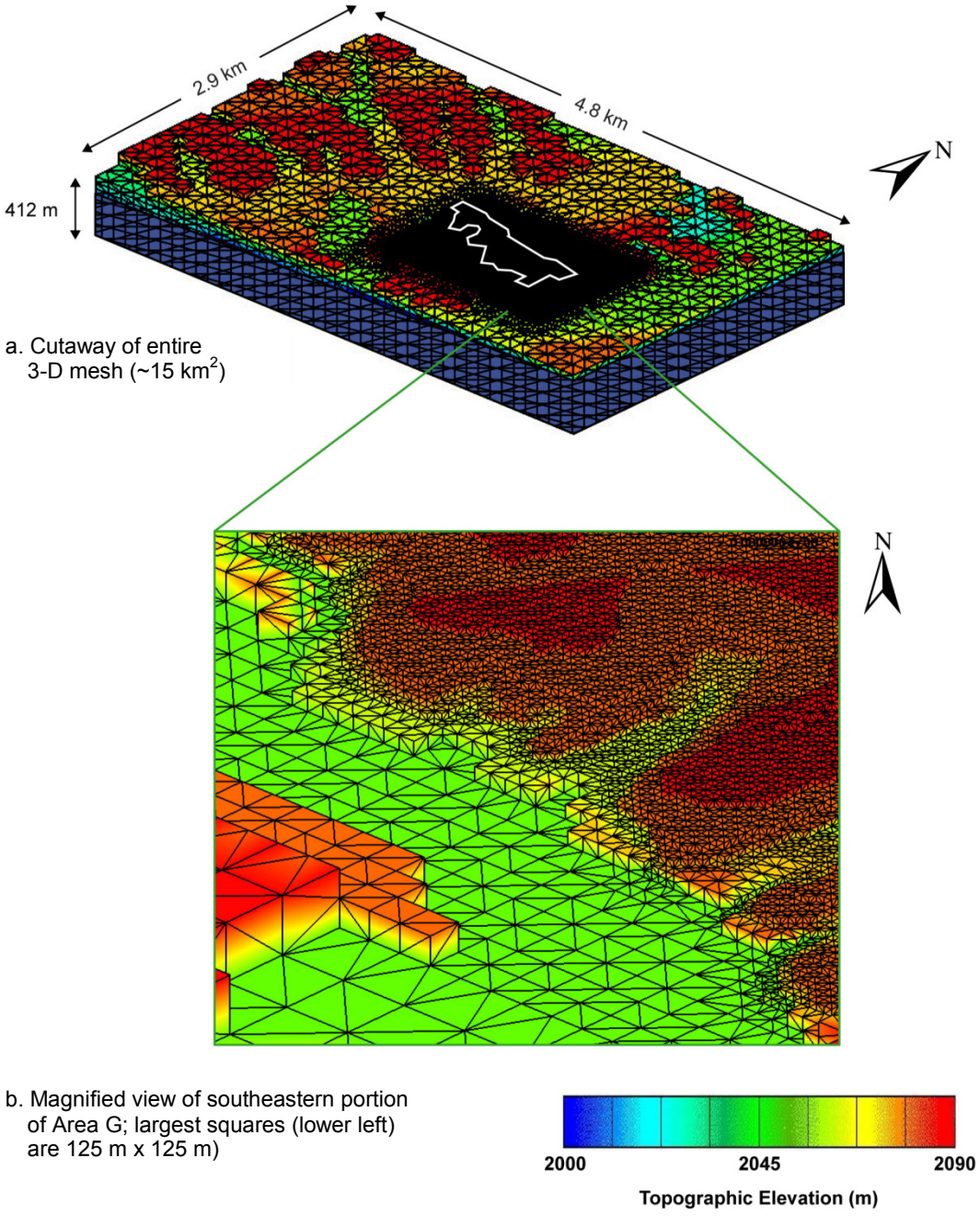

Figure 8
Numerical Mesh for 3-D Groundwater Transport Model Showing Mesh Resolution and Digital Elevation Model

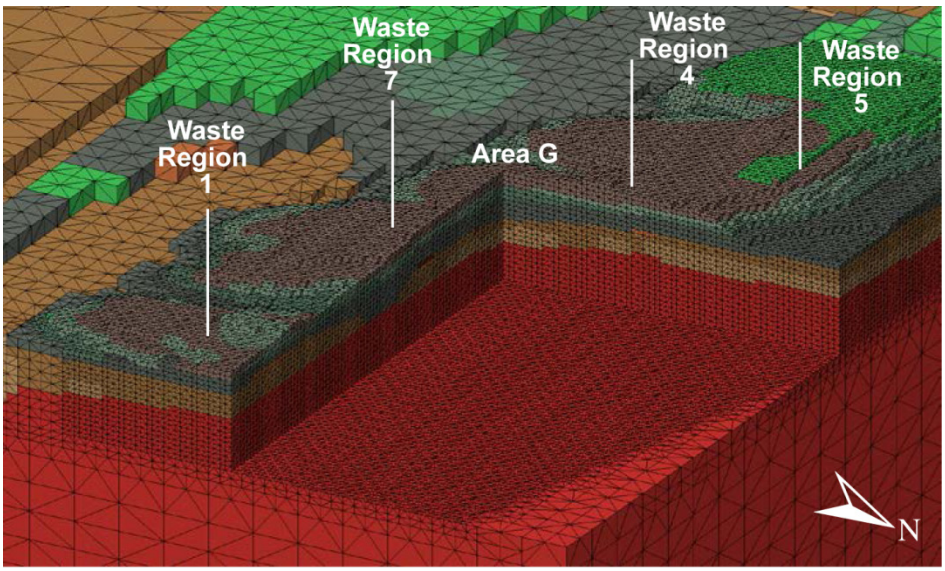

Geologic Unit	
Qbt2	Bandelier Tuff (Tshirege Member), Unit 2
Qbt1vu	Bandelier Tuff (Tshirege Member), Unit 1, vitric portion
Qbt1vc	Bandelier Tuff (Tshirege Member), Unit 1, colonnade portion
Qbt1g	Bandelier Tuff (Tshirege Member), Unit 1, glassy
Qbtt	Bandelier Tuff (Tshirege), Unit 1, Tsankawi Pumice
Qct	Cerro Toledo Interval
Qbof	Bandelier Tuff (Otowi Member), Ash Flow
Qbog	Bandelier Tuff (Otowi Member), Guaje Pumice Bed
Tpf	Puye Formation, fanglomerate
Tb4	Cerros del Rio Basalts and other lower units

Figure 9
Cutaway of the Refined Portion of the Area G
Mesh with Reduction in Vertical and Horizontal Spacing

3.2.2 Model Configuration and Boundary Conditions

The 3-D site-scale model is used to trace the travel times of particles released from Area G and to generate conservative breakthrough curves, otherwise known as residence time distribution functions (RTDs). Because the RTDs vary with release location and infiltration rate, the complexity of the model is reduced by adopting a number of assumptions and boundary conditions that constrain the groundwater transport model and simplify the modeling task.

To account for variations in particle travel times across Area G, the facility was divided into eight discrete waste disposal regions, each representing an area where flow and contaminant transport behavior will be different. These variations occur because (1) the thickness of the Bandelier Tuff, which largely determines particle breakthrough behavior, increases from east to west, and (2) the differences in the depths of the disposal units influence particle travel time to the compliance boundary. Figure 10 shows the locations of the waste disposal regions. Disposal regions 1 and 8 contain aggregates of pits and shafts with similar depths, while the remaining disposal regions contain either all pits or all shafts. Although the shafts in disposal region 6 are immediately adjacent to the shafts included in disposal region 1, region 6 is modeled separately because its shafts are significantly deeper than those in region 1. Similarly, the shafts in waste disposal region 7 are interspersed among the pits in region 3, but are modeled separately because of differences in depth. Figure 10 shows the approximate areas where large numbers of the region 6 and 7 shafts are located. Disposal region 8, west of the active portion of the disposal facility, is within the expansion area of Area G referred to as Zone 4. The location shown in the figure for the disposal units in this region represents a reasonably conservative release point for the poorly constrained future contaminant releases from expansion area.

All of the waste disposal regions fall within the high-resolution portions of the 3-D model mesh (Figure 10). Each square in the figure corresponds to one node on the surface of the mesh. Disposal units occur in regions characterized by small nodes; larger nodes are used to represent the nearby canyons.

Table 2 provides the model coordinates for, and a brief description of, the pits and shafts included in each waste disposal region. The average bottom elevation of the disposal units in each region was calculated and used as the entry point into the groundwater model for radionuclides leached from the waste. The controlling GoldSim model estimated contaminant mass fluxes exiting from the bottom of each waste disposal region.

Particle breakthrough was specified relative to a vertical plane approximately 100 m (330 ft) east of the Area G fence line. Figure 10 shows the compliance boundary plane in map view with respect to the numerical mesh and the locations of the disposal pits.

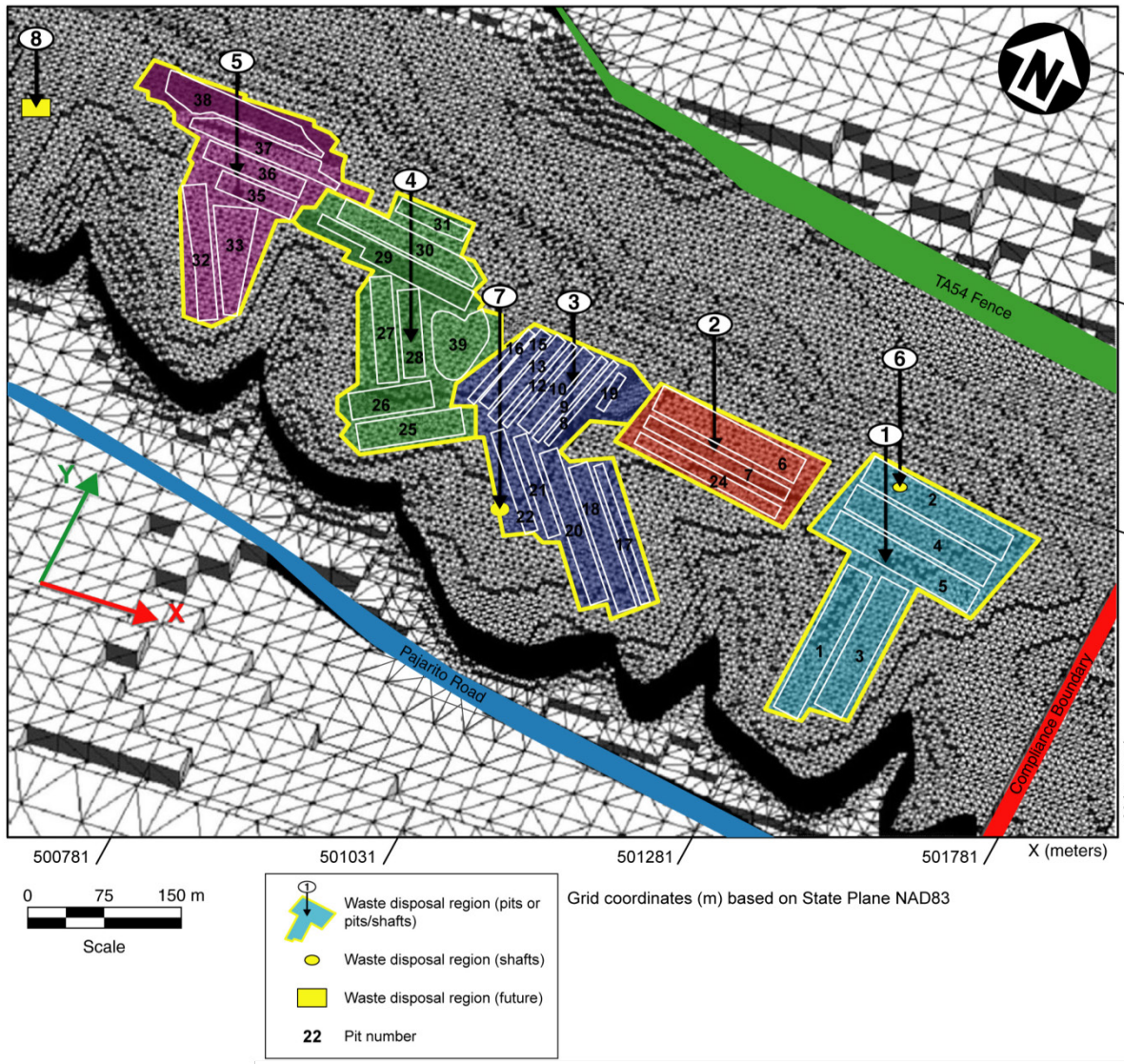

Figure 10
Waste Disposal Pits and Waste Disposal Regions Superimposed on the Numerical Mesh

Table 2
Particle Release Locations Representing the Eight Waste Disposal Regions

Waste Disposal Region	Mesh Location Coordinates (m) [a]			Description
	East-West Axis (x-coordinate)	North-South Axis (y-coordinate)	Elevation above msl (z-coordinate)	
1	501,304	535,715	2,024	Pits 1–5, shallow shafts near pit 2
2	501,102	535,778	2,028	Pits 6,7,24
3	500,969	535,738	2,032	Pits 8 through 22
4	500,781	535,801	2,036	Pits 25 through 31, 39
5	500,563	535,903	2,037	Pits 32 through 38
6	501,281	535,817	2,015	Deep shafts near pit 2
7	500,938	535,645	2,020	Deep shafts among pits 8 – 22
8	500,344	535,926	2,038	Zone 4 pits and shafts

msl = Mean sea level

[a] *State Plan NAD83 Coordinates in m*

3.2.2.1 Infiltration

Long-term infiltration on the mesa is one of the primary uncertainties in simulations of contaminant transport from Area G to the compliance boundary. For this study, it was assumed that Area G will remain hydrologically similar to an undisturbed mesa-top site, especially after final closure. To capture the uncertainty in transport travel times through the unsaturated zone, a probability distribution that spans a reasonable range of infiltration rates was used. This distribution was based on data compiled in Springer and Schofield (2004), as described below. Another uncertainty identified at the outset of this study was the effect of elevated infiltration in nearby canyons on the transport of contaminants from Area G. The modeling performed to evaluate the potential impacts of canyon infiltration on the Area G groundwater modeling is discussed at the end of this section.

Springer and Schofield (2004) compiled almost 200 mesa-top infiltration estimates from modeling, field, and chloride mass balance studies to estimate rates of infiltration. Their statistical analysis shows that the data are trimodal, with modal values around 0, 15, and 60 mm/yr (0, 0.59, and 2.4 in./yr) (Springer and Schofield, 2004, Fig. 4). In their analysis, Springer and Schofield indicated that infiltration rates greater than 10 mm/yr (0.39 in./yr) were typically associated with disturbed sites.

It is anticipated that the landfill cover designed for Area G will behave at least as well as the undisturbed mesa top. Consequently, the probability distribution of infiltration rates adopted for the groundwater transport modeling considers infiltration rates of 10 mm/yr (0.39 in./yr) or less.

Figure 11 shows a normalized histogram of infiltration rates for undisturbed mesa tops near Area G. This histogram was generated with the Springer and Schofield (2004) data by dividing the total number of samples in a given infiltration increment by the size of the increment. For example, there are 37 estimates in the 0 to 0.1 mm/yr (0 to 0.0039 in./yr) increment (yielding a normalized probability of about 0.37) and only eight estimates in the 8 to 10 mm/yr (0.32 to 0.39 in./yr) interval (yielding a normalized probability of approximately 0.004).

This preliminary estimate of the probability distribution function for infiltration rate was used to determine the range of likely Area G infiltration rate values. Ten infiltration rates spanning this range were identified and used to create a series of 3-D breakthrough curves for releases from the eight waste disposal regions. This resulted in the creation of 80 unique breakthrough curves that can be sampled from within GoldSim and used to generate the 1-D pipe pathways needed for calculating contaminant migration to the compliance boundary. With this approach, GoldSim samples the actual, continuous infiltration rate distribution during model simulations and selects the breakthrough curve that most closely corresponds to this rate within the waste disposal region under consideration. The discretization of the infiltration distribution in the manner described above provides a mechanism for considering the effects of variable infiltration rates on facility performance while maintaining model complexity at a reasonable level.

Potential groundwater pathway risks are expected to be small during the 1,000-year compliance period at low rates of infiltration. However, at infiltration rates of 2 to 10 mm/yr (0.079 to 0.39 in./yr), the possibility for exposure within the compliance period increases substantially. Thus, although the infiltration probability distribution is heavily weighted toward values below 2 mm/yr (0.079 in./yr), an effort was made to include several discrete infiltration rates at the upper end of the distribution because of the associated potential higher dose.

Each infiltration, or mass flow, value (kg/yr) was assigned to every surface node within the numerical model. This value represents the product of the desired infiltration rate (mm/yr), the surface area over which infiltration occurs (m^2), and the density of water (1,000 kg/m^3 [62 lb/ft^3]). For example, if a node has a surface area of 1.0 m^2 (11 ft^2) and the desired infiltration rate is 1.0 mm/yr (0.039 in./yr), the infiltration value would be 1.0 kg/yr (2.2 lb/yr) or 3.2×10^{-8} kg/s (7.0×10^{-8} lb/yr). If a node was located along the edge of Mesita del Buey, only the area on top of the mesa was used to calculate infiltration; the mesa sides were assumed to have zero net infiltration.

High rates of infiltration in the canyons adjacent to Area G may influence contaminant breakthrough times. Consequently, modeling was performed to determine how infiltration from nearby Pajarito Canyon—the wettest canyon in the vicinity of the disposal facility—should be considered in the groundwater pathway model. Simulations were conducted assuming three

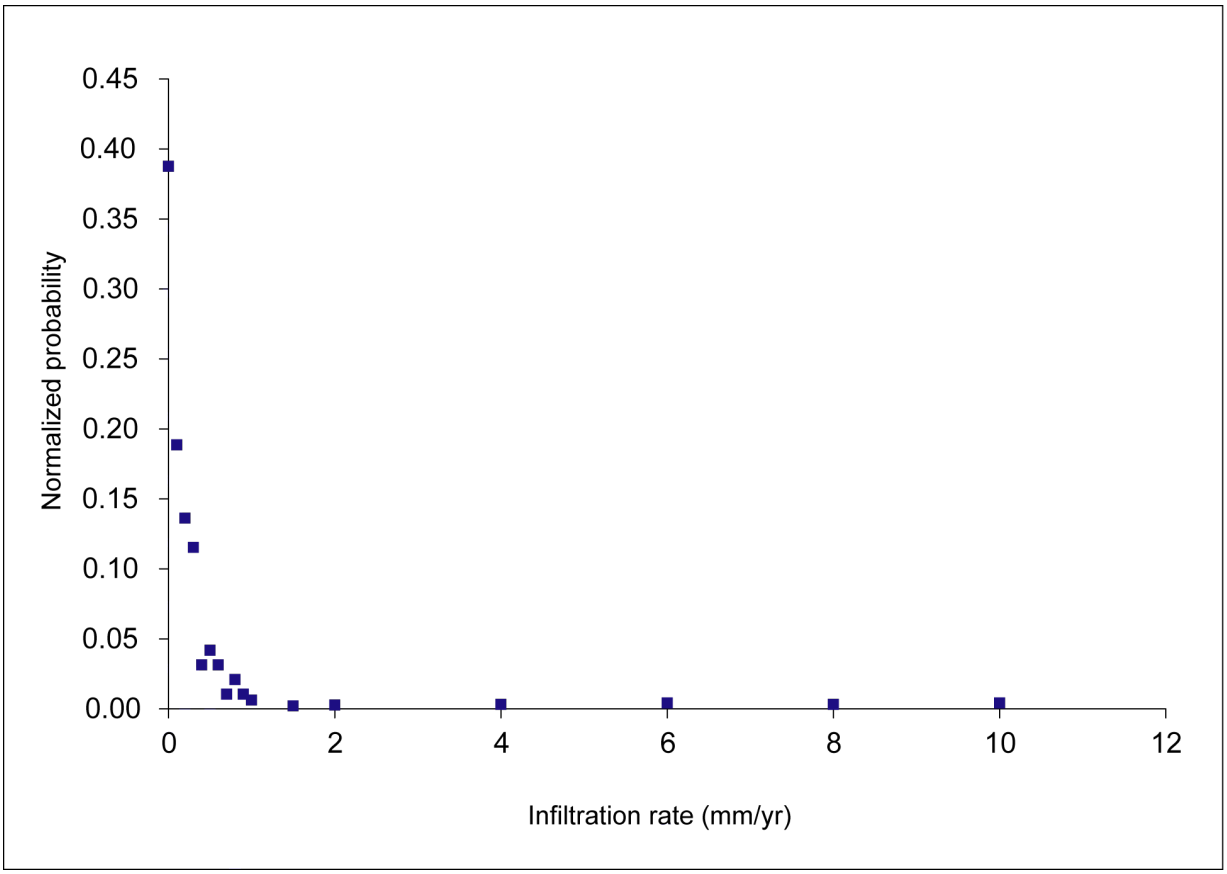

Figure 11
Normalized Histogram of Mesa-Top Infiltration Rates

infiltration rates for the canyon. Two of these assumed infiltration rates in Pajarito Canyon were the same as the background rate observed in areas surrounding the canyon; infiltration rates of 0.1 and 0.5 mm/yr (0.0039 and 0.02 in./yr) were used to conduct the modeling. The third simulation used an annual volumetric infiltration value of 6 m^3/m (65 ft^3/ft), which is based on an infiltration rate of 100 mm/yr (3.9 in./yr) over a 60-m (200-ft) wide, 3-km (1.9-mi) long stream channel. This is about one-third of the value estimated by Kwicklis et al. (2005) for lower Pajarito Canyon. The lower value was used to represent infiltration under conditions of high evapotranspiration, conditions that are expected to prevail in the canyon and that were not taken into account by the infiltration estimate provided by Kwicklis et al.

3.2.2.2 Initial and Boundary Conditions

High capillary forces within the Bandelier Tuff lead to very low flow rates at the low-to-moderate saturations typical of the subsurface beneath mesas on the Pajarito Plateau. As discussed in Section 2.2, Birdsell et al. (1999) showed that evaporation could cause extremely high capillary forces resulting in the flow of water toward the surge bed. Although this hypothesis is supported by some data (Rogers et al., 1996), the result of implementing an internal evaporative boundary at the base of Tshirege unit 2 would be to stop transport below this horizon. This "dry barrier" hypothesis was not considered in the current study because the extent of this phenomenon has not been adequately confirmed.

All lateral boundaries in the vadose zone were assumed to be no-flow boundaries, that is, no mass could enter or leave the system via these boundaries. Lateral gradients on these boundaries were not considered for two reasons. First, the simulation domain boundaries are located more than a kilometer away from the Area G fence line. Second, previous modeling studies of the Pajarito Plateau found the magnitude of lateral gradients in the unsaturated zone to be generally quite small (Birdsell et al., 1999; Stauffer et al., 2000).

Groundwater flow in all simulations was assumed to be from west to east following the water table gradient in the area. The gradient was fixed for all simulations and was based on a water table elevation of 1,798 m (5,900 ft) along the western boundary and 1,737 m (5,700 ft) to the east. These elevations yield an average gradient across the domain of approximately 0.013 m/m (0.042 ft/ft) toward the Rio Grande. This gradient, based on data from Stone et al. (1999) and Keating et al. (2003), is expected to capture the general trend of flow near the water table.

Saturated zone pressure was fixed along the east and west boundaries of the model such that a constant head is maintained on each of these faces. The northern and southern boundaries in the saturated zone are no-flow boundaries. This method ignores data reported by Keating et al. (2003) that indicates there may be downward vertical gradients as high as 0.10 m/m (0.33 ft/ft). Some uncertainty surrounds these data; one interpretation is that the gradients are caused by groundwater pumping while another postulates that deeper flow in the aquifer is confined with respect to flow

near the water table. After discussions with Keating and other co-authors of the 2003 study, the second interpretation was adopted for this study, and no downward gradients were prescribed in the simulations. This is a conservative assumption because downward gradients would lead to increased mixing and lower contaminant concentrations in the saturated zone near any pumping well.

All groundwater flow simulations were performed using an assumed temperature of 15°C. The variation in average temperatures observed at the site (which range from 10°C at the surface to 20°C at the water table) is assumed to have a negligible impact of water density and viscosity.

3.2.3 Hydrogeologic Input Data

The hydrogeologic properties used in the modeling are presented in Table 3. These values are based on data from Springer (2005), Stauffer et al. (2005b), and Birdsell et al. (1999 and 2000). The results of Springer's analysis (2005), described in Section 2.2, were used to identify the hydrologic properties for the Bandelier Tuff. Springer found that most hydrologic properties were not different for a given TA and hydrogeologic unit, which indicates that the values can be pooled within a TA. No consistent relationships were found among TAs except for the residual water content, the value of which was essentially zero. Properties compared for mesa-top and canyon settings revealed limited consistencies in the Tshirege unit 1g and no consistency in the Otowi Member. A comparison of properties among hydrogeologic units showed that the hydrologic properties of Tshirege unit 1v and Tshirege unit 1g were essentially the same. On the basis of Springer's analysis, the hydrologic properties for the Bandelier Tuff used in this study are based only on measured data from TA-54.

Table 3
Hydrogeologic Properties Used for the Three-Dimensional Model

Geologic Unit	Bulk Density (kg/m^3)	Permeability (m^2)	Porosity	van Genuchten Parameters		
				s_r	α (m^{-1})	n
Tshirege Unit 2	1.4E+03	2.0E–13	4.1E–01	2.4E–02	4.7E–01	2.1E+00
Tshirege Unit 1v	1.2E+03	1.2E–13	4.9E–01	6.0E–03	3.6E–01	1.7E+00
Tshirege Unit 1g	1.2E+03	1.5E–13	4.6E–01	2.2E–02	5.E–01	1.8E+00
Cerro Toledo Interval	1.2E+03	1.8E–13	4.5E–01	7.0E–03	1.3E+00	1.5E+00
Otowi Member	1.2E+03	2.3E–13	4.4E–01	4.3E–02	5.9E–01	1.8E+00
Guaje Pumice	8.1E+02[c]	1.5E–13[a]	6.7E–01[a]	0.0E+00[a]	8.1E–02[a]	4.0E+00[a]
Cerros del Rio Basalts, Vadose Zone	2.6E+03	1.0E–12[b]	1.0E–03[b]	1.0E–03[a]	3.8E+00[a]	1.5E+00[a]
Cerros del Rio Basalts, Saturated Zone	2.6E+03	1.0E–12[b]	5.0E–02	NA	NA	NA

SOURCE: All data represents mean values from Springer (2005) unless otherwise noted

Numbers are rounded to two significant digits

NA = Not applicable

[a] *Birdsell, et al., 1999 and 2000* [b] *Stauffer et al., 2005b* [c] *Estimated in Stauffer et al., 2005a*

The Springer data represent mean values determined through the statistical analysis described in *Attachment III*, in which Springer calculated descriptive statistics and correlation properties for geologic units and all data. Retention data by geologic unit and across the Bandelier Tuff were pooled and fitted to Equation 1 in *Attachment IV* to provide additional estimates of the hydrologic parameters.

The hydrogeologic properties adopted for the groundwater modeling differ somewhat from the properties used in earlier modeling efforts (Birdsell et al., 1995, 1999, and 2000). However, the overall characteristics of the geologic units remain the same. For example, the vadose-zone basalt permeability and porosity values used for the model were adopted from Stauffer et al. (2005b), and are conservative estimates that yield the fastest travel times. These properties are more defensible than those used by Birdsell et al., but the general transport behavior through this rock unit is unchanged. Because of the presence of numerous fractures, calculated travel times through the basalt remain quite low, and this unit has little impact on the total calculated travel times of contaminants from the source region to the compliance boundary for the groundwater pathway.

Two zones of reduced permeability are supported by data collected from regional well R-32. The uppermost zone occurs at the base of Tshirege unit 1g, and was represented in the model simulations using a permeability reduction factor of 0.1. This reduction factor allows increased saturations to occur near the base of the unit when infiltration is high, for example, in wetter canyon bottoms. The second reduction in permeability occurs at the top of the Cerros del Rio basalts, and was modeled using a permeability reduction factor of 0.01. The reduction factor for this zone, which is higher than that noted by Robinson et al. (1999) for simulations of Los Alamos Canyon, was selected because it yields increased saturations in the overlying few meters of Bandelier Tuff, but does not result in ponding on top of the basalt during the simulations. This is consistent with the fact that perched water has not been found beneath Area G.

Values for some of the hydrogeologic properties used in the modeling were estimated because of an absence of reported values in the literature. The Guaje Pumice is a high-silica basal pumice located at the base of the Otowi Member of the Bandelier Tuff (Figure 6) (Broxton and Reneau, 1995). The bulk density of this unit was assigned a value of 810 kg/m3 (51 lb/ft3), which leads to a grain density for the minerals of approximately 2,400 kg/m3 (151 lb/ft3) and a reported mean porosity of 0.667 (Birdsell et al., 1999 and 2000). The effective porosity of the basalt below the water table is expected to be greater than that in the vadose zone (i.e., the water in the saturated zone encounters more flow paths). The basalt within this region was assigned a porosity of 0.05 based on massive basalt porosity values found in the literature (Doughty, 2000) and discussions with Dr. V. Vesselinov at LANL (2004), whose unpublished work, conducted in conjunction with the work by Keating et al. (2003), supports this value.

The groundwater pathway modeling adopted an approximate mean value of the longitudinal dispersivity for modeling flow and transport within the vadose zone. A dispersivity of 2 m (7 ft) was used throughout the model domain except for a section of the basalt in which the vertical resolution of the mesh changes (see *Attachment II*). Dispersivity in the octree mesh refinement (OMR) mesh area was set to zero because, at the time the initial 2005 modeling was performed, coding limitations precluded the application of dispersion across OMR sections. This code limitation has since been corrected; however, for consistency with the original modeling, we have retained the same zero dispersivity region in the current modeling.

3.2.4 Model Simulations

The 3-D site-scale model was used to trace the travel times of particles released from Area G and to generate conservative breakthrough curves. Particle tracer simulations were also run to determine appropriate dispersivity values and to predict how contaminants might be captured by a nearby groundwater well. All simulations of contaminant transport assumed steady-state flow throughout the domain. To generate a steady-state flow field, simulations were run with constant boundary conditions for 2.5 million years.

3.2.4.1 Conservative Breakthrough Curves

Conservative RTDs of particle breakthrough at the compliance boundary were generated for each waste disposal region by releasing over 3,000 particles instantaneously from eight 1-m^3 (35-ft^3) volumes. The volumes were centered on each of the release locations listed in Table 2. Because each particle has a random component that influences its pathway through the complex 3-D mesh, thousands of particles must be released at the same time and at the same surface location to create an RTD. The RTD shows the probability that a given particle will arrive at the compliance boundary in a given amount of time. A sensitivity analysis was performed to ensure that the area of the release location did not affect the RTD. The results of this analysis, shown in Figure 12, indicate that there was little difference in the RTD curves even when the area of the release location was increased by a factor of 4.

Prior to the 2005 modeling effort, simulations of transport beneath Area G used the advection-dispersion equation to solve for tracer concentrations and were strongly affected by numerical dispersion (Birdsell et al., 1999). For the 3-D simulations conducted in 2005 and 2011, particles were chosen to simulate transport because they are not affected by numerical dispersion (Lichtner et al., 2002). Another benefit associated with using particles is that their exact position in the numerical mesh is known at all times, allowing very accurate tracer pathways to be analyzed. Particle tracking is also much faster than the traditional finite-element implementation of the advection-dispersion solution. Particle-tracking simulations were implemented using the *sptr* macro in FEHM (Dash, 2003).

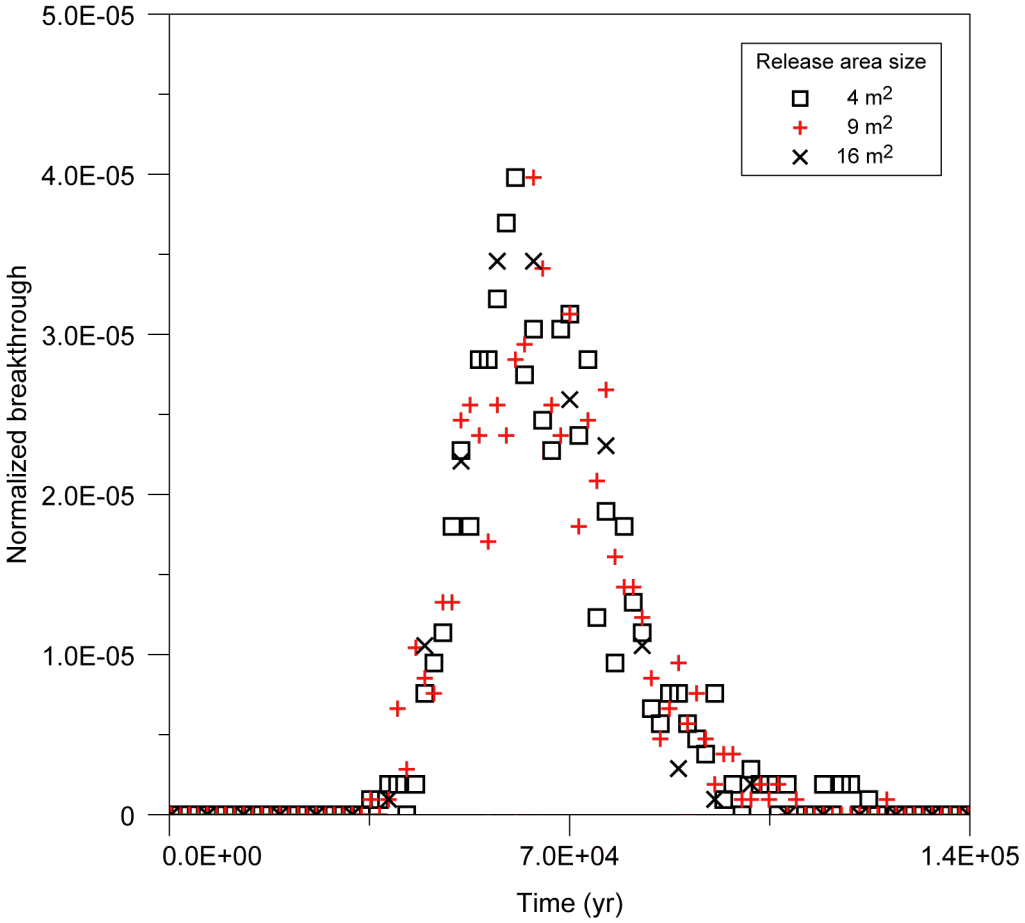

Figure 12
Sensitivity Analysis of Particle Breakthrough to Size of Release Area at Waste Disposal Region 5

.

3.2.4.2 Longitudinal Dispersivity

Several simulations were conducted to estimate suitable values of longitudinal dispersivity within the vadose zone. Disposal region 5, the westernmost waste disposal region in MDA G, was chosen as the release point because particles released there must travel a greater distance to the compliance boundary than those from most other regions. As a result, particles from region 5 should be more prone to dispersion.

The range of longitudinal dispersivities considered in the evaluation was selected on the basis of work conducted by Neuman (1990) and Gelhar et al. (1992) that shows longitudinal dispersivity increasing with the length of the flow path. Gelhar et al. found that the maximum expected longitudinal dispersivity is approximately one-tenth the total flow path length. Although the Gelhar et al. results pertained to saturated systems, they were applied to this study because there are no similar vadose-zone dispersion studies. Particle breakthrough at Area G is predominantly controlled by the travel time through the Bandelier Tuff because flow in the basalt is very rapid relative to flow in the tuff. This means that the expected vadose-zone flow path length is effectively 60 m (200 ft), the approximate thickness of the tuff across the site. Since dispersivity is generally expected to be lower in the vadose zone than in the saturated zone, 6 m (20 ft), or one-tenth of the 60 m (200 ft) flow path length, was used as an upper limit for vadose-zone longitudinal dispersivity. On this basis, the sensitivity analysis explored how changes in dispersivity ranging from 1 m to 6 m (3.3 to 20 ft) affected model behavior.

3.2.4.3 Well Capture

The groundwater pathway modeling estimates the contaminant-specific mass that crosses the compliance boundary 100 m (330 ft) downgradient of the Area G fence line. Only a portion of the mass that crosses this boundary would, in fact, be captured by a domestic well and contribute to the exposure projected for the individual using the well. Simulations were performed to estimate the size of the capture zone and, in so doing, the capture efficiencies for a hypothetical downgradient well.

The hypothetical well, which was assumed to supply a single household, was assumed to be located at the compliance boundary, 100 m (330 ft) directly downgradient (east) of Area G. The radius was set at 0.125 m (0.41 ft) and the screened interval was assumed to extend downward 37.5 m (123 ft) from the top of the water table. A range of pumping rates was used to estimate the size of the well's capture zone; these rates were 50, 600, 1,200, and 2,500 m3/yr (1.3 ×104, 1.6 ×105, 3.2 ×105, and 6.6 × 105 gal/yr). An infiltration rate of 10 mm/yr (0.39 in./yr) across the top surface of the domain was assumed, and a steady-state flow field was established with the pumping well in place.

To determine the radius of influence, simulations introduced particles along a line source that was situated 100 m (330 ft) upgradient of the well and at an elevation corresponding to the

midpoint of the well screen interval, or nearly 19 m (62 ft) below the top of the water table. The particles were released at a closer spacing than the pit node distribution so that the radius of influence of the well could be determined to within hundredths of a meter.

Capture efficiency, or the fraction of contaminant released from the disposal facility that is intercepted by the well, was estimated for each waste disposal region. The pumping well was fixed for all simulations at approximate mesh coordinates of x = 501,281 m, y = 535,863 m, and z = 1,750 m. Ten particles were introduced at every x-y mesh location corresponding to a disposal unit node. Because the capture efficiency relies mainly on the number of particles coming from directly upgradient of the well, the disposal units were shifted along the y-direction so that the maximum east-west point density was aligned with the pumping well. To do this, the release points from each disposal region were first binned into groups with the same north-south (y) coordinate, then the east-west (x) section with the most points was shifted to align with the pumping well. The locations were mapped vertically to the midpoint of the pumping well (i.e., 19 m [62 ft] below the water table), and the effect of transverse dispersivity (the amount of spread perpendicular to the direction of travel) on particle capture was evaluated using dispersivities ranging from 0 to 10 m (0 to 33 ft). Figure 13 shows the adjusted alignment for the release from waste disposal region 5. Capture efficiencies were calculated separately for all waste disposal regions except regions 6 and 7, to account for the regions' unique geometries. Regions 6 and 7 were assumed to have capture efficiencies equal to those of disposal regions 2 and 3, respectively.

The finite vertical resolution of the 3-D numerical mesh causes two vertical steps in the cells that represent the water table (Figure 14). The easternmost step occurs just past the compliance boundary and causes the particles to dive deeper into the saturated zone in an unrealistic fashion near the hypothetical well. Because the well's screened interval extends only 37.5 m (123 ft) downward from the top of the water table, this discontinuity in the water level can lead to low calculated capture efficiencies. For these well capture simulations, the source regions were shifted westward in the x-direction to ensure that the step in the simulated water table did not reduce the well capture efficiency. This shift improves the calculation of the capture efficiency and does not negatively affect the analysis because all nodes below the water table are in homogeneous basalt, and the gradient used for the analysis is fixed and linear from west to east. In this case, the capture efficiency is strictly a function of the distance traveled to the hypothetical well.

Table 4 presents the shift distances applied for the well capture analysis to every particle from a given disposal region in both the x-direction (east-west) and y-direction (north-south). As explained, the north-south shift was made to ensure that the well was aligned with the greatest density of particles along the line source. The shift from east to west was made to ensure that the step in the mesh due to the change in vertical resolution did not reduce the well capture efficiency because of the proximity of the compliance boundary to the step.

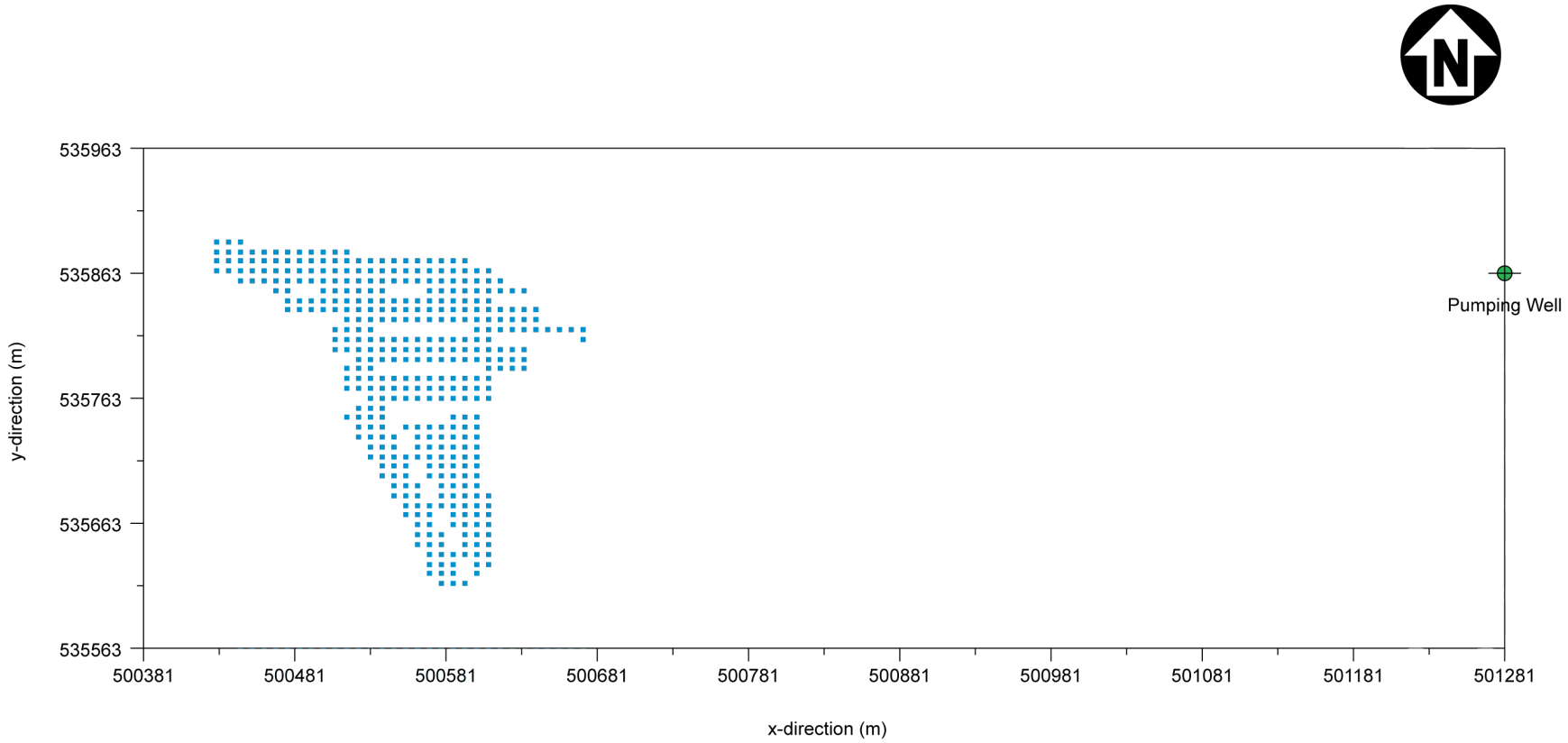

Figure 13
Distribution of Particle Release Points for Waste Disposal Region 5 (well capture simulation)

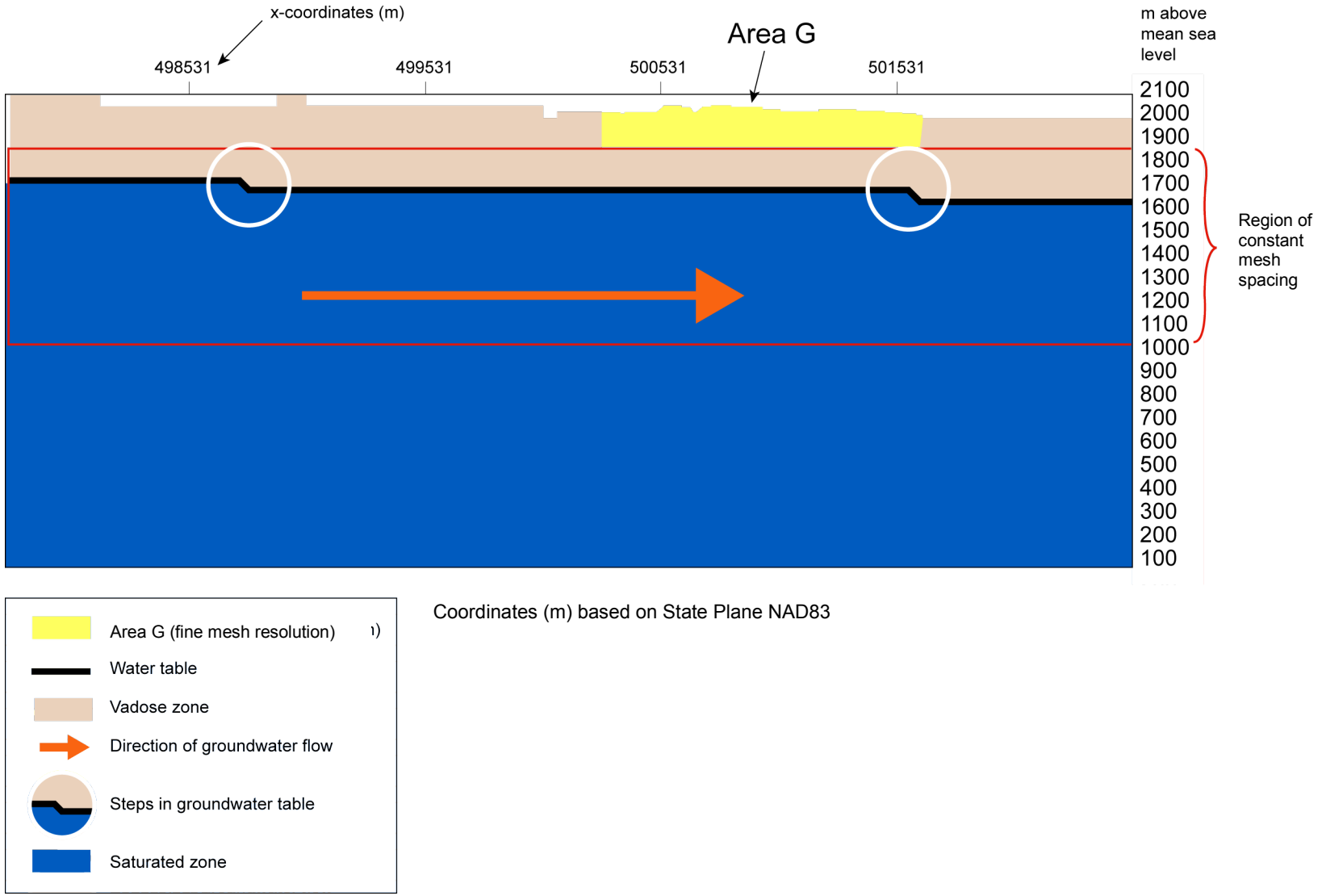

Figure 14
Cross Section of Numerical Mesh Showing Vertical Steps in Water Table

Table 4
Transformed Values for Shift of Tracer Particle Release Points for the Well Capture Analysis[a]

Waste Disposal Region	Horizontal Shift (m)[b]		Path Length to Well (m) from Region	
	X-Direction	Y-Direction	Shortest (from eastern boundary)	Longest (from western boundary)
1	–250	94	109	304
2	–250	62.5	328	515
3	–250	203	421	680
4	–250	–23.5	656	900
5	–250	–125	855	1101
8	–250	–57	1120	1468

[a] *All particles were released at an elevation of 1,750 m above mean sea level*

[b] *Represents change from original x or y coordinate; a negative change in the x-direction represents a shift to the west and a negative change in the y-direction represents a shift to the south.*

3.3 Model Abstraction

The 3-D site-scale model takes significant computer time and memory to run. Consequently, an approach was developed to reduce the FEHM model complexity while retaining the overall characteristics of the transport simulations. The theory of micromixing (Robinson and Viswanathan, 2003) was used to reduce complex 3-D simulations to 1-D abstractions that recreate particle breakthrough at the compliance boundary and retain the ability to modify the bulk transport properties of the subsurface for all radionuclides undergoing groundwater transport. The development of these 1-D abstractions provided the means for incorporating the groundwater pathway model directly into the GoldSim model that was used to project long-term performance of the disposal facility.

To support the development of the 1-D abstractions, the FEHM model was modified so that GoldSim controls the contaminant mass flux, the specified surface infiltration, and the bulk transport properties (i.e., sorption parameters) used in the groundwater pathway modeling. As implemented for the performance assessment and composite analysis, the FEHM model recreates an approximation of the complex 3-D RTD on a simple 1,000-node, 1-D mesh using the algorithm described in *Attachment IV*. GoldSim calls eight separate FEHM simulations, each of which corresponds to a waste disposal region, and passes the appropriate data to FEHM. Using these data, FEHM calculates the mass of each radionuclide crossing the compliance boundary as a function of time, and passes the results back to GoldSim. Details of the coupling between GoldSim and FEHM, with information about the directory structure and examples of input structure and code, are included in *Attachment V*. Specialized codes used to create the 1-D abstraction are described in more detail in *Attachment VI*.

The 1-D abstraction mesh uses the advection-dispersion formulation of the transport equations (Zyvoloski et al., 1995a) to simulate tracer movement. As explained in *Attachment IV*, this allows simulation of sorption and radioactive decay, processes that are important for estimating the breakthrough of the multiple species that may be released into the vadose-zone from the pits and shafts at Area G.

To mimic the instantaneous release of particles used in the 3-D simulations, many small time steps, each with a single pulse input of tracer mass, must be used by GoldSim for the 1-D simulations. It was found that a time step equal to one one-thousandth of the simulation period results in convergence between the 3-D and 1-D breakthrough curves. Thus, for a 5,000-year simulation, a GoldSim time step of 5 years is used to recreate an instantaneous release of particles moving from the mesa top to the compliance boundary.

3.4 Hydrologic Property Uncertainty Analysis

A series of hydrologic properties were defined for the geologic strata underlying Area G; mean values of these properties were used to conduct the 3-D FEHM modeling. It is reasonable to expect that the natural variability in these parameters will affect the groundwater and contaminant travel times projected using the model. An uncertainty analysis was conducted to investigate the potential impacts of parameter variability on the long-term performance projections for the disposal facility. The methods used to conduct the analysis are summarized below; a complete description of the evaluation may be found in *Attachment VIII*.

Unsaturated flow is described using the constitutive relationships of unsaturated hydraulic conductivity versus pressure head, and effective water content versus pressure head. The FEHM modeling adopts the van Genuchten–Mualem model (van Genuchten, 1980):

$$K(\boldsymbol{x},t) = K_s(\boldsymbol{x})\sqrt{S(\boldsymbol{x},t)}\{1-[1-S^{1/m}(\boldsymbol{x},t)]^m\}^2 \quad (1)$$

$$S(\boldsymbol{x},t) = \{1+[-\alpha(\boldsymbol{x})\psi(\boldsymbol{x},t)]^n\}^{-m} \quad (2)$$

Where

ψ is pressure head
$K_S(\boldsymbol{x})$ is the saturated hydraulic conductivity (m/s)
$S(x,t)$ = effective saturation, $\theta_e/(\theta_s-\theta_r)$, where
θ_e = effective water content, $\theta_r \le \theta_e \le \theta_s$
θ_r = residual (irreducible) water content
θ_s = saturated water content
α is a pore-size distribution parameter (m^{-1})
n is fitting parameters
$m = 1 - 1/n$

The uncertainty analysis treats the hydrologic properties of four strata of the Bandelier Tuff (Tshirege units 2, 1v, and 1g and the Otowi Member) as random variables. The saturated hydraulic conductivity K_s, the pore size distribution parameter α, the fitting parameter n, the saturated water content θ_s, and residual water content θ_r are treated as piece-wise random functions, which vary from unit to unit but are constants within each unit. Information provided in Springer (2005) was used to estimate distributions for these input parameters; the parameter statistics provided in Springer and the distributions assigned to the hydrologic properties of the four units are summarized in Table 5. The parameters K_S and α are described using log-normal distributions; n is assumed to follow a truncated normal distribution (with a lower bound of 1.0) and θ_s and θ_r are assumed to be normally distributed

Table 5
Parameter Statistics and Assigned Distributions for Bandelier Tuff Stratigraphic Units

Parameter	Unit	No. of Samples	Mean	Standard Deviation	Lower Bound	Upper Bound
ln K_s (m/s)	Tshirege Member unit 2 (Qbt2)	17	–13.12	1.13		
	Tshirege Member unit 1v (Qbt1v)	44	–13.63	1.06		
	Tshirege Member unit 1g (Qbt1g)	17	–13.59	0.69		
	Otowi Member (Qbof)	12	–12.89	0.46		
ln α (1/m)	Qbt2	8	–0.76	0.69	–6.91	4.61
	Qbt1v	34	–0.87	0.94	–6.91	4.61
	Qbt1g	9	–0.90	0.32	–6.91	4.61
	Qbof	12	–0.53	0.21	–6.91	4.61
n	Qbt2	8	2.06	0.51	1	5
	Qbt1v	34	1.73	0.28	1	5
	Qbt1g	9	1.81	0.17	1	5
	Qbof	12	1.76	0.25	1	5
θ_s	Qbt2	10	0.41	0.03	0	0.6
	Qbt1v	35	0.5	0.04	0	0.6
	Qbt1g	14	0.46	0.05	0	0.6
	Qbof	12	0.43	0.01	0	0.6
θ_r	Qbt2	8	0.01	0.013	0	0.05
	Qbt1v	34	0.003	0.009	0	0.05
	Qbt1g	9	0.01	0.015	0	0.05
	Qbof	12	0.019	0.015	0	0.05

Monte Carlo simulations were conducted using the 3-D FEHM model to estimate the impacts of variability in hydrologic properties on particle breakthrough. Two approaches for conducting these simulations were used. First, parameters sampled from the distributions of hydrologic

properties shown in Table 5 were sampled and used in FEHM simulations of particle breakthrough; four simulations were conducted, using 25, 50, 100, and 1,000 realizations. Particles released from the disposal facility were tracked until they reached the groundwater pathway compliance boundary, 100 m (330 ft) downgradient of the Area G fence line and the particle data were used to construct normalized cumulative breakthrough curves. The second series of simulations sampled directly from distributions of retention curves (Equation 1); these retention curves were generated using the hydrologic property distributions presented in Table 5. Simulations using 25, 50, 100, and 200 realizations were conducted using FEHM 3-D to estimate particle breakthrough; normalized cumulative breakthrough curves were developed using the model output. The breakthrough curves from all simulations were compared to the breakthrough curves estimated using mean hydrologic properties.

4.0 Results and Discussion

This section presents the results of the groundwater pathway modeling. Section 4.1 summarizes breakthrough at the compliance boundary, and Section 4.2 describes the results of well capture simulations. The results obtained from the 1-D and 3-D models are compared in Section 4.3. As discussed earlier, this updated modeling incorporates a major revision to the GFM used to represent the geology at, and in the vicinity of, Area G. Section 4.4 compares the results from the 2005 modeling to those obtained using the updated GFM. Finally, Section 4.5 presents the results of the hydrologic property uncertainty analysis.

4.1 Breakthrough at the Compliance Boundary

The breakthrough plots presented in this report show normalized breakthrough. For the normalization, the number of particles crossing the compliance boundary during a given time interval is divided by the time increment and the total number of particles that reach the boundary, such that the integral of the area under the curve is 1 for all plots. Figure 15 shows typical particle pathways through the complex 3-D model domain for contaminants released from waste disposal region 5; pathways are shown in the z (vertical), x (east-west), and y (north-south) directions. Results for high- (10 mm/yr [0.39 in./yr]) and low- (0.1 mm/yr [0.039 in./yr]) infiltration cases are included.

Particles migrate from the bottom of the disposal units to the regional aquifer; as seen in Figures 15a and 15b, the particles do not move far in the x-direction (eastward) during transit through the vadose zone. However, upon reaching the aquifer (at a value of z of approximately 1,770 m [5,807 ft]), the particles migrate readily toward the compliance boundary (shown with a dashed line on Figures 15a, 15b, 15e, and 15f). Because lateral transport in the vadose zone is relatively minor, any particles that cross the compliance boundary do so in the saturated zone. The particles appear to drop suddenly just east of the compliance boundary because the mesh spacing at this elevation creates a step in the surface of the water table (Figure 14). However, all transport to the compliance boundary occurs before this step. Also, once the particles reach the saturated zone, they travel more quickly and the extra drop in elevation does not add significant travel time.

For both high- and low-infiltration cases, particles are diverted to the south within the Guaje Pumice (Figures 15c and 15d); this pumice layer lies directly over the Cerros del Rio basalts at an elevation of about 1,960 m (6,414 ft) above msl. The southward spreading in the vadose zone occurs when the particles enter the zone of increased saturation (reduced permeability) just above the basalts. From this point, the particles take various paths, but follow the flow of water to the south. Once the particles drop through this zone of reduced permeability, the particles travel downward to the water table then eastward to the compliance boundary.

Figure 15a: Movement in x and z directions with high infiltration (10mm/yr)

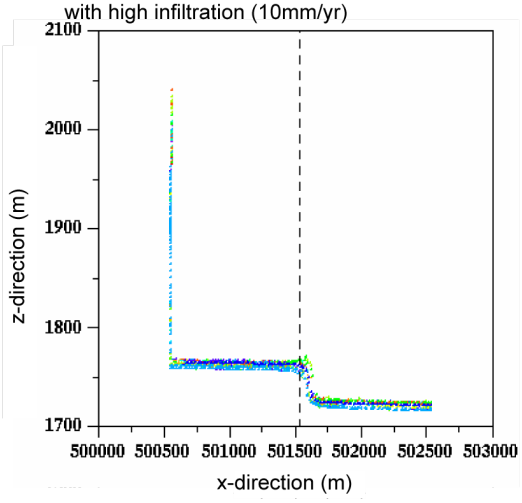

Figure 15b: Movement in x and z directions with low infiltration (0.1mm/yr)

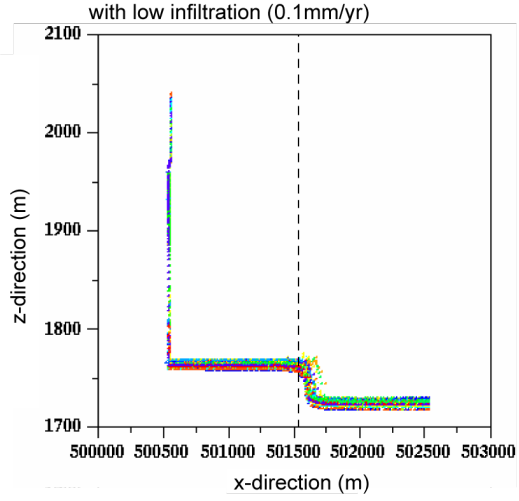

Figure 15c: Movement in y and z directions with high infiltration (10mm/yr)

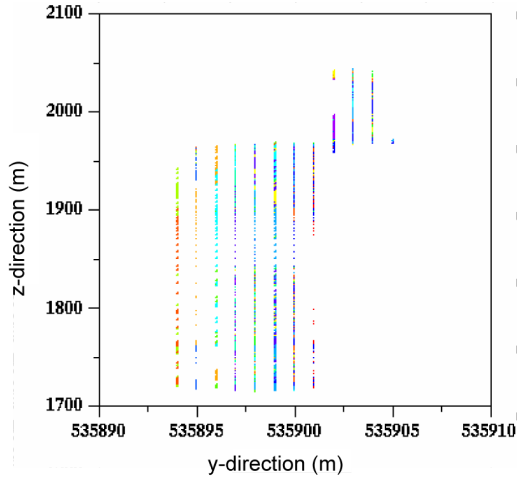

Figure 15d: Movement in y and z directions with low infiltration (0.1mm/yr)

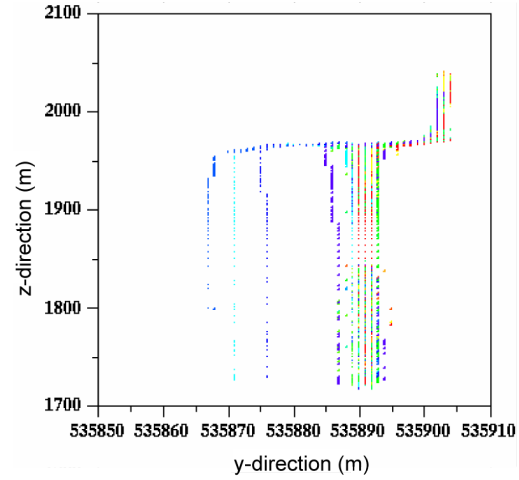

Figure 15e: Movement in x and y directions with high infiltration (10mm/yr)

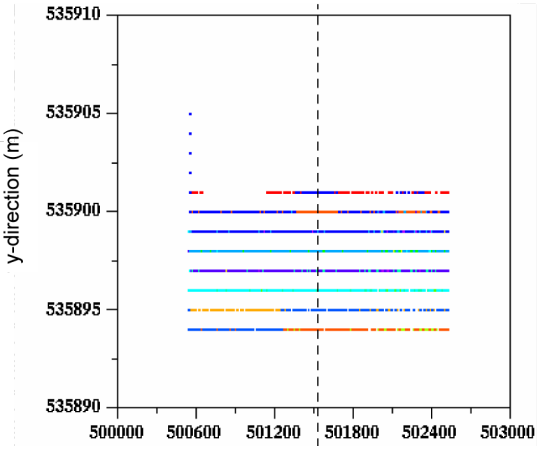

Figure 15f: Movement in x and y directions with low infiltration (0.1mm/yr)

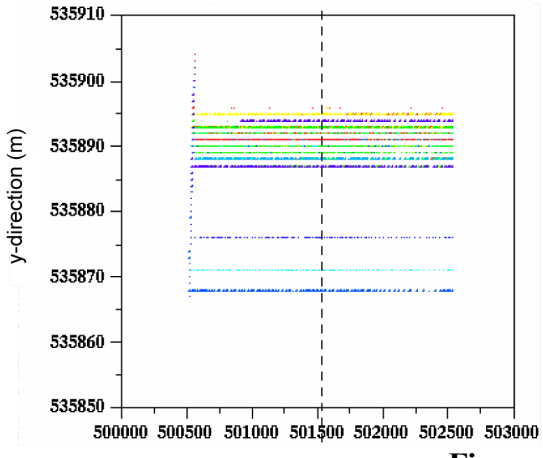

Figure 15
Two-Dimensional Views of Pathways for Particles Released from Waste Disposal Region 5 (high- and low-infiltration rates)

The amount of spreading that occurs is influenced by the infiltration rate. For the high-infiltration case (Figure 15c), the particles disperse about 7 m (23 ft) laterally by the time they reach the water table. Under low infiltration conditions (Figure 15d), the particles disperse about 30 m (98 ft), less than the 100 m (328 ft) observed in the 2005 modeling results.

Figures 15e and 15f provide a view of particle movement in both horizontal directions (x,y) for high- and low-infiltration cases for a plane located beneath the water table. These figures illustrate that the particles have spread toward the south within the vadose zone (primarily within the Guaje Pumice) and from their arrival locations at the regional aquifer, they move due east as dictated by the pressure gradient. These flow paths do not include the capture zone analysis discussed in section 3.2.4.3.

Figure 16 shows conservative breakthrough curves at the compliance boundary for particles released from each of the eight disposal regions. The background infiltration rate for this example is 0.5 mm/yr (0.2 in./yr). Waste disposal region 6, consisting of a cluster of deep shafts located near the eastern boundary of Area G, has the fastest breakthrough, beginning at about 2,500 years and peaking at around 7,100 years. The arrival of particles from disposal region 2 occurs later than than the region 6 breakthrough, which is to be expected because of the higher elevation of the release points within this region (Table 2). Disposal regions 5 and 8, located to the west, show much longer breakthrough times, beginning at around 7,000 years and peaking at about 14,000 years.

Although breakthrough times from the disposal regions tend to increase as the thickness of the tuff increases, other factors complicate the matter. For example, although the depth to basalt is similar in regions 3 and 4, the breakthrough times for region 3 are significantly longer. One major difference between these two regions is the absence of the Guaje Pumice beneath disposal region 3. It appears that the absence of Guaje Pumice may lead to longer travel times, perhaps due to differences in water retention behavior that leads to lateral spreading; water flows downward more easily when the Guaje Pumice is present. See *Attachment VII* for figures showing depth from the surface to the basalt for each region as well as the presence and absence of the Guaje pumice.

Figure 17 shows the conservative breakthrough curves for releases from the eight disposal regions at a background infiltration rate of 10 mm/yr (0.39 in./yr); this infiltration rate is the upper limit of the probability distribution used for infiltration rates (as shown in Figure 11). The relative breakthrough for the different regions is similar to the situation noted above for an infiltration rate of 0.5 mm/yr (0.2 in./yr). However, breakthrough times are much shorter at the higher infiltration rate. For example, the first breakthrough occurs for disposal region 6 in less than 300 years, with peak breakthrough at about 570 years.

Travel time within the saturated zone is brief compared to travel time in the vadose zone. Assuming an aquifer velocity of 70 m/yr (230 ft/yr), the travel time from the point at which particles discharge to the aquifer to the compliance boundary is approximately 2 years.

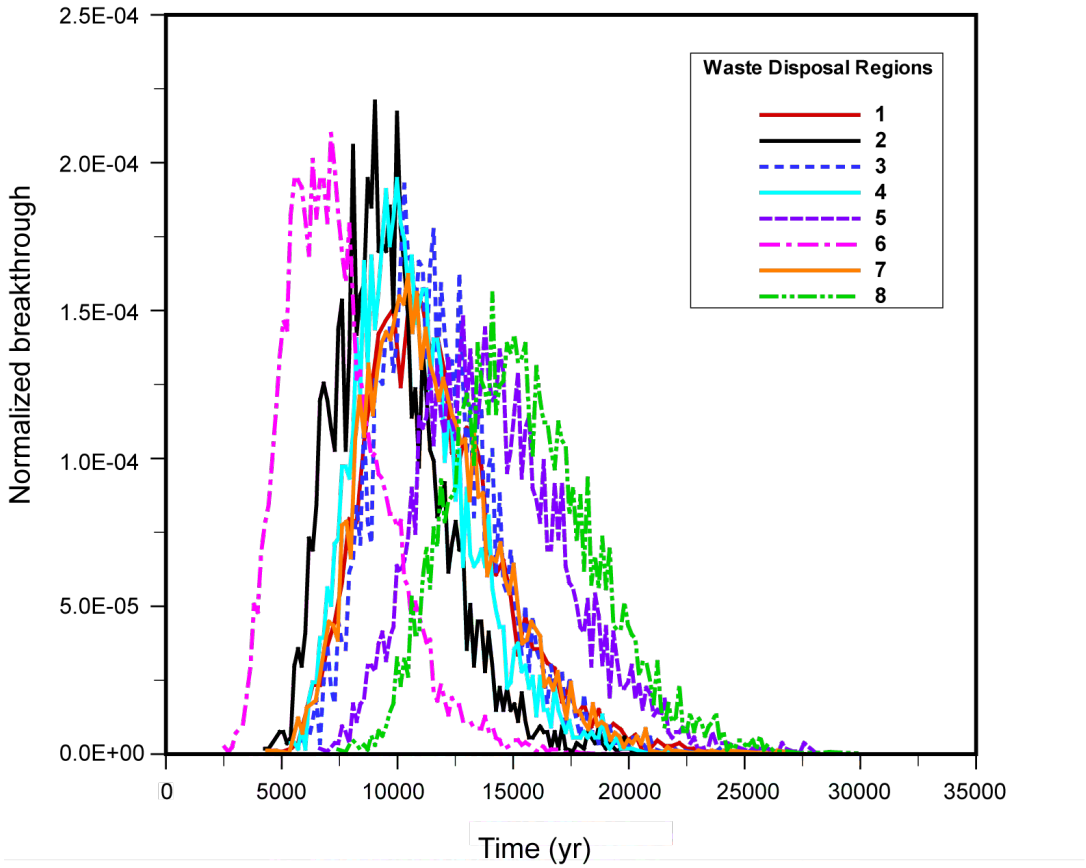

Figure 16
Breakthrough Curves for Particles Released from All Waste Disposal Regions (background infiltration of 0.5 mm/yr)

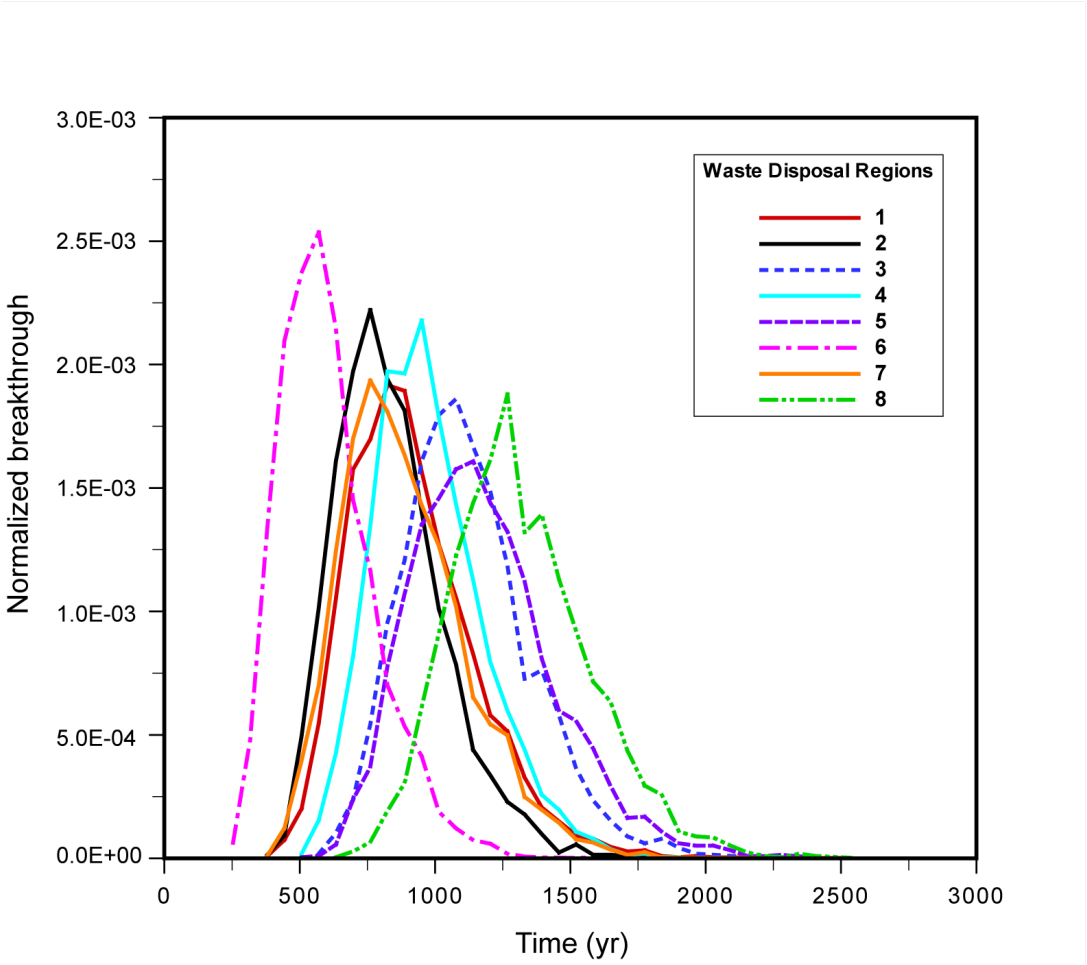

Figure 17
Breakthrough Curves for Particles Released from All Waste Disposal Regions (background infiltration of 10 mm/yr)

4.1.1 Effects of Changes in Permeability and Infiltration

Figure 18 shows how interface permeability reductions affect subsurface saturations; a high infiltration rate of 10 mm/yr (0.39 in./yr) was chosen to more clearly demonstrate the effect. The permeability reduction at the base of Tshirege unit 1g results in an increase in saturation from 30 to 40 percent in the lower part of this unit, while the permeability reduction at the top of the basalt yields an increase in saturation from 30 to about 60 percent in the lower few meters of the Otowi Member. Figure 19 shows how the reduced permeability interfaces impact conservative tracer breakthrough at the compliance boundary for particle releases from waste disposal regions 1 and 5 at an assumed background infiltration of 10 mm/yr (0.39 in./yr).

Interestingly, breakthrough from disposal region 1 was unaffected by reduced permeability. Particles released from disposal region 5 behaved as expected, with the reduced permeability scenario leading to slightly later breakthrough. As was the case in the 2005 groundwater modeling, interface permeability reductions were included in all subsequent simulations, but had fairly minor impacts on predicted travel times.

As seen in Figure 20, an increase in the infiltration rate yields higher in-situ saturation. At a net infiltration rate of zero, saturations beneath Area G are below 10 percent in all units. As infiltration rate increases to 10 mm/yr (0.39 in./yr), the effects of the permeability reductions at the base of Tshirege unit 1g and the top of the basalt are evident. The behavior seen in these simulations spans the range of in-situ saturations reported in Birdsell et al. (1999).

Birdsell et al. (1999) report that no single infiltration rate can reproduce moisture content data from individual boreholes; the suggestion is made that mesa-top infiltration has changed over time, perhaps in response to climate and rainfall changes. This complexity was not explored in the current modeling, which assumes steady-state infiltration throughout the simulation period. As a result, the modeling is expected to under-predict saturations in the deeper part of the Bandelier Tuff when infiltration is low, and over-predict saturations in the upper portions of the tuff when infiltration is higher.

The quantity of water infiltrating through Pajarito Canyon appears to have little impact on infiltration rates beneath Area G. Simulations were run using increased infiltration in Pajarito Canyon of 6 m^3/m (65 ft^3/ft) over a width of 60 m (200 ft) (see Section 3.2.2.1). As shown in Figure 21, the steady-state saturation profile beneath the mesa at waste disposal region 5 remains constant when the infiltration rate through the canyon is increased from 0.1 mm/yr (0.0039 in./yr) to 100 mm/yr (3.9 in./yr) over the 60-m (200-ft) wide, 1.9 km (1.2 mi.) long channel. Likewise, when the background infiltration rate within the canyon is increased from 0.5 mm/yr (0.02 in./yr) to 100 mm/yr (3.9 in./yr), the steady-state saturation profile at waste disposal region 5 remains unchanged.

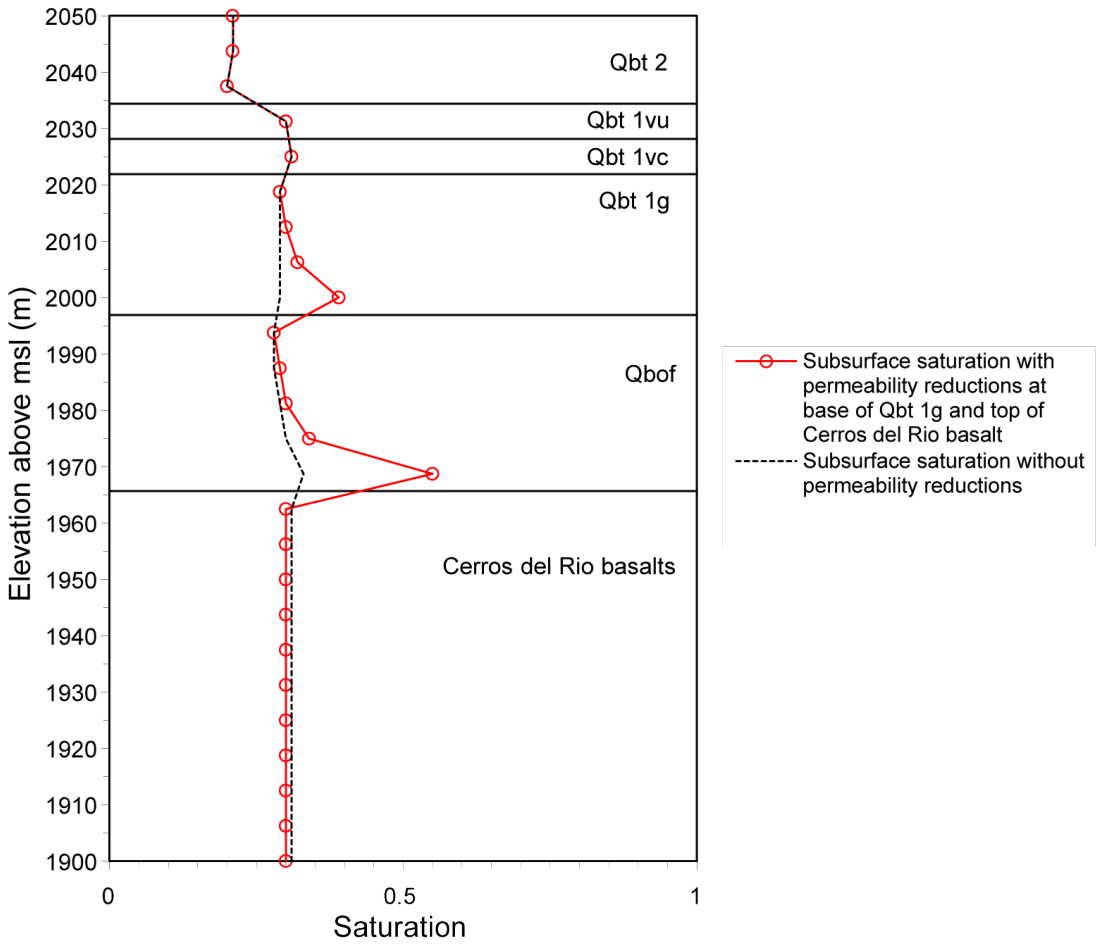

The assumed infiltration rate in Pajarito Canyon is 100 mm/yr (3.9 in./yr)

Figure 18
Effects of Permeability Reductions on Subsurface Saturation at Waste Disposal Region 5

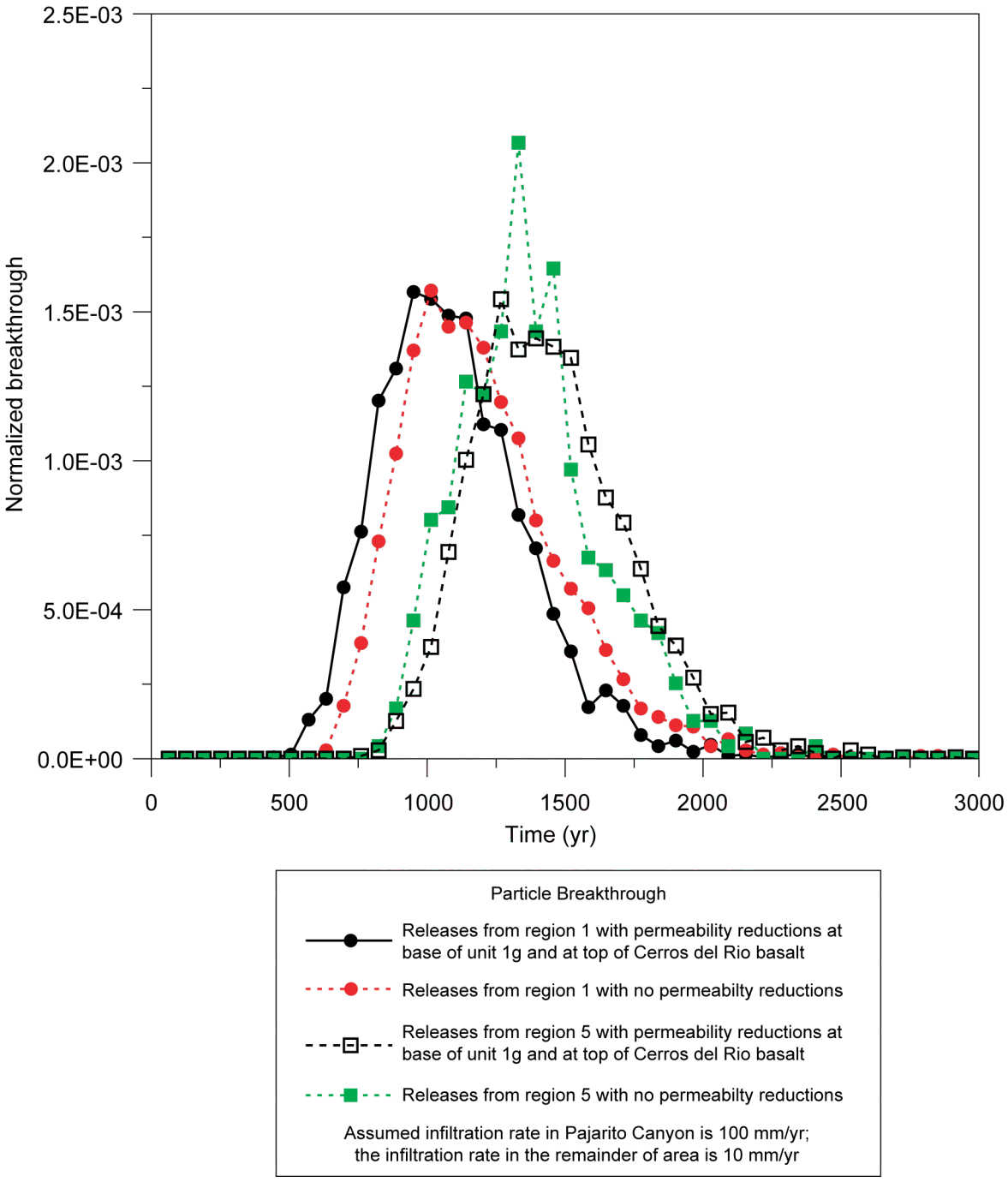

Figure 19
Effects of Permeability Reductions on Breakthrough for Releases from Waste Disposal Regions 1 and 5

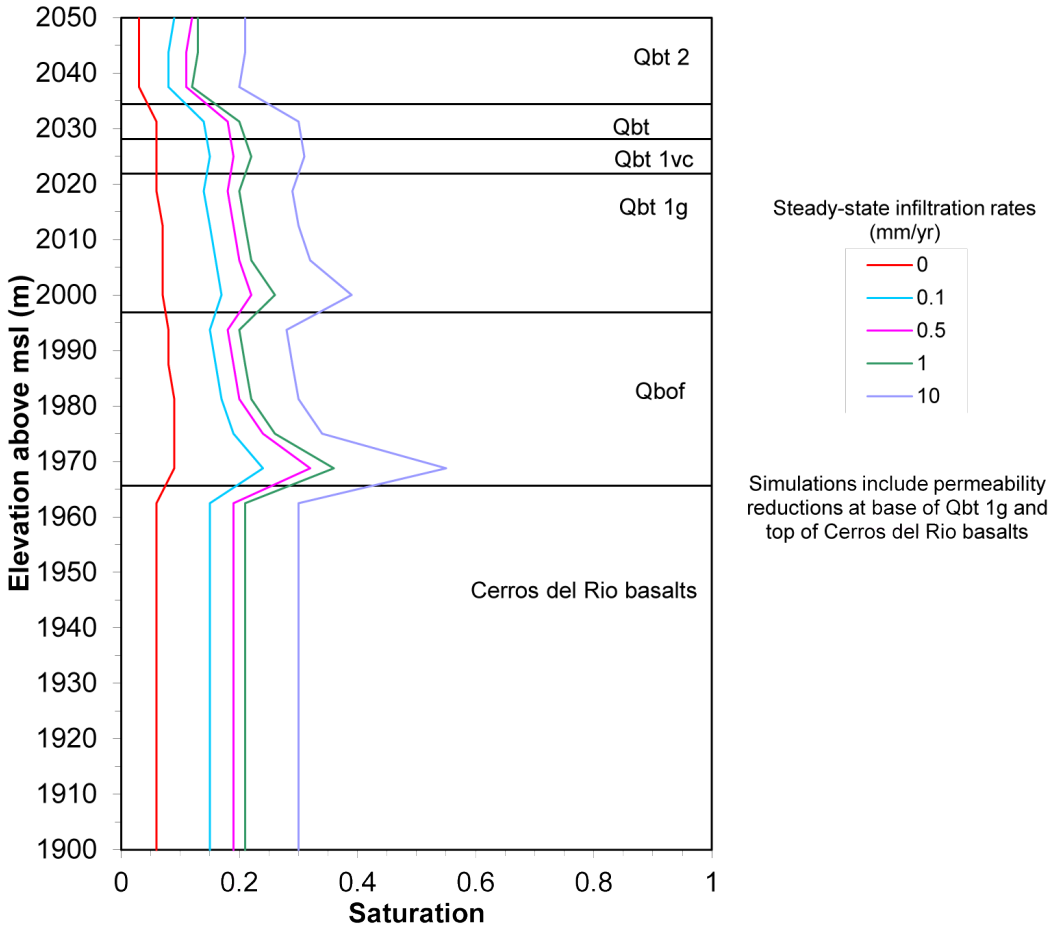

Figure 20
Subsurface Saturations at Waste Disposal Region 5 for Range of Steady-State Infiltration Rates (without increased Pajarito Canyon infiltration)

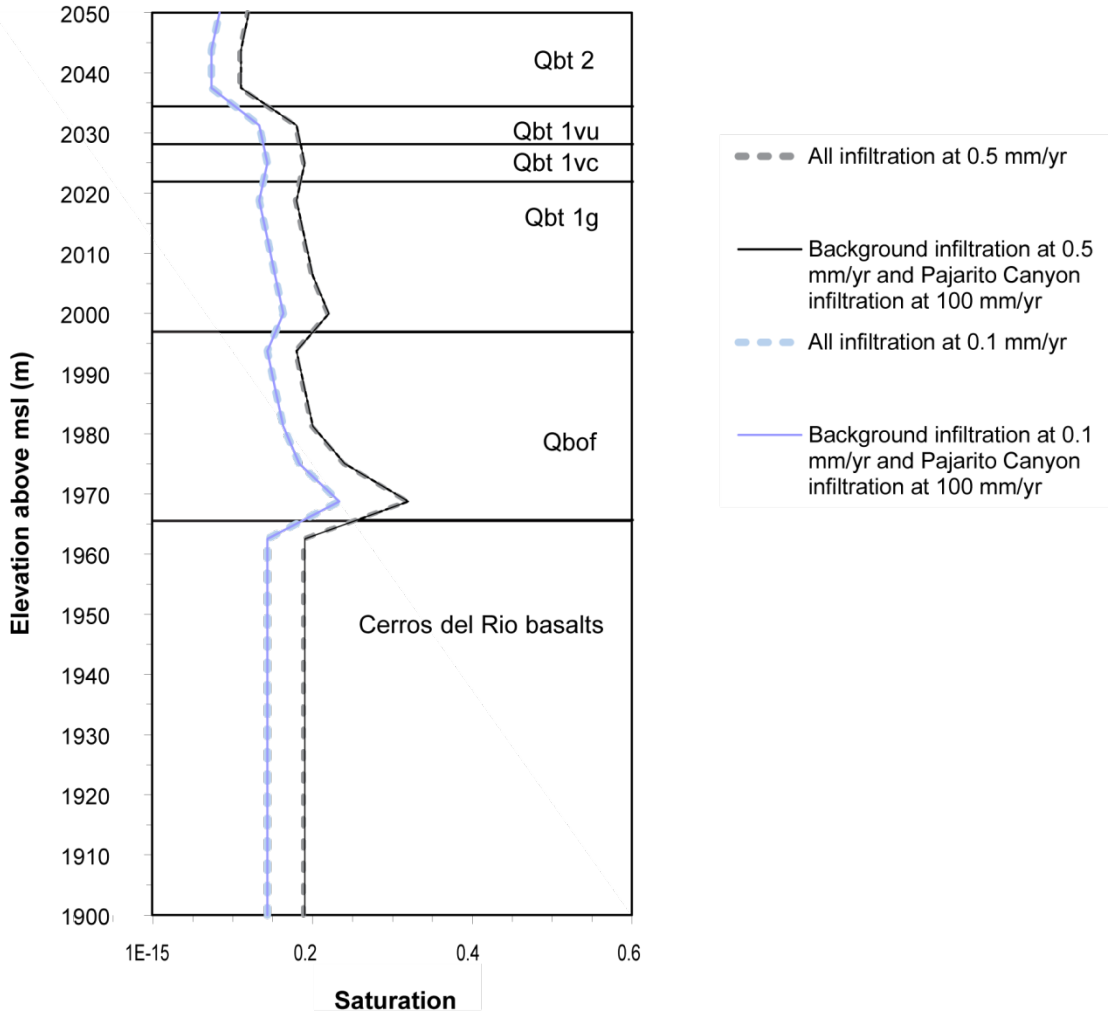

Figure 21
Effect of Pajarito Canyon Infiltration on Subsurface Saturation at Waste Disposal Region 5

A permeability reduction is observed between the Otowi Member and the underlying basalt in disposal region 5 despite the absence of the Guaje Pumice at this location. This abrupt change in permeability would be expected to cause water to spread laterally along the top of the basalt and, assuming sufficient supply in Pajarito Canyon, could cause water to spread northward beneath the disposal units at Area G. However, lateral spreading of this type was not projected to occur (Figure 21), probably because the southward dip of the paleosurface that forms the contact between the basalt and overlying tuff (see *Figure II-11 in Attachment II*) diverts flow to the south, preventing water in Pajarito Canyon from flowing under Mesita del Buey.

Consistent with the saturation profiles, increasing infiltration in Pajarito Canyon has a limited impact on breakthrough times. At an assumed background infiltration rate of 0.1 mm/yr (0.0039 in./yr), the particles released from disposal regions 1 and 5 behaved nearly identically with and without increased Pajarito Canyon infiltration (Figure 22), despite the fact that the Guaje Pumice occurs at the base of the Otowi Member in disposal region 1 but not in region 5. These results demonstrate that transport is insensitive to increased recharge from the canyon for realistic rates of Pajarito Canyon infiltration and channel width. Therefore, infiltration rates in Pajarito Canyon were assumed to be the same as for the mesa-top, or background, when calculating breakthrough from the waste disposal units.

Figures 23 and 24 show breakthrough curves for waste disposal regions 1 and 5 at the 10 infiltration rates chosen as representing the expected range of behavior. These figures show the curves for three time spans: 5,000 years, 20,000 years, and 80,000 years; breakthrough curves corresponding to some of the lower infiltration rates do not fall within the shorter time spans. As previously described, breakthrough at a given infiltration rate generally occurs more quickly for releases at locations where tuff deposits are thinner (disposal region 1) than where they are thicker (disposal region 5). Breakthrough for disposal region 5 typically takes about 1.3 times as long as for region 1. Thus, peak breakthrough with a 0.25 mm/yr (9.8×10^{-3} in./yr) background infiltration rate occurs for disposal region 1 at approximately 19,000 years, while the corresponding peak breakthrough for disposal region 5 occurs at approximately 25,000 years.

4.1.2 Model Sensitivity to Dispersivity

Figure 25 shows the model sensitivity of the breakthrough curves for particles released from waste disposal region 5 for a range of vadose-zone longitudinal dispersivities at both high (10 mm/yr [0.39 in./yr]) and low (0.1 mm/yr [0.0039 in./yr]) infiltration rates. Changes in longitudinal dispersivity in the vadose zone cause little change in the peak breakthrough times for either case. However, higher vadose-zone longitudinal dispersivities cause the width of the breakthrough curves to increase while the peak particle counts decrease. This is consistent with the theory of dispersion and confirms that the model is functioning as expected (Fetter, 1999). Because vadose-zone longitudinal dispersivity is expected to be smaller than one-tenth of the flow path length (see discussion in Section 3.2.4.2), longitudinal dispersivity in the vadose zone was fixed at 2 m (7 ft) for all simulations.

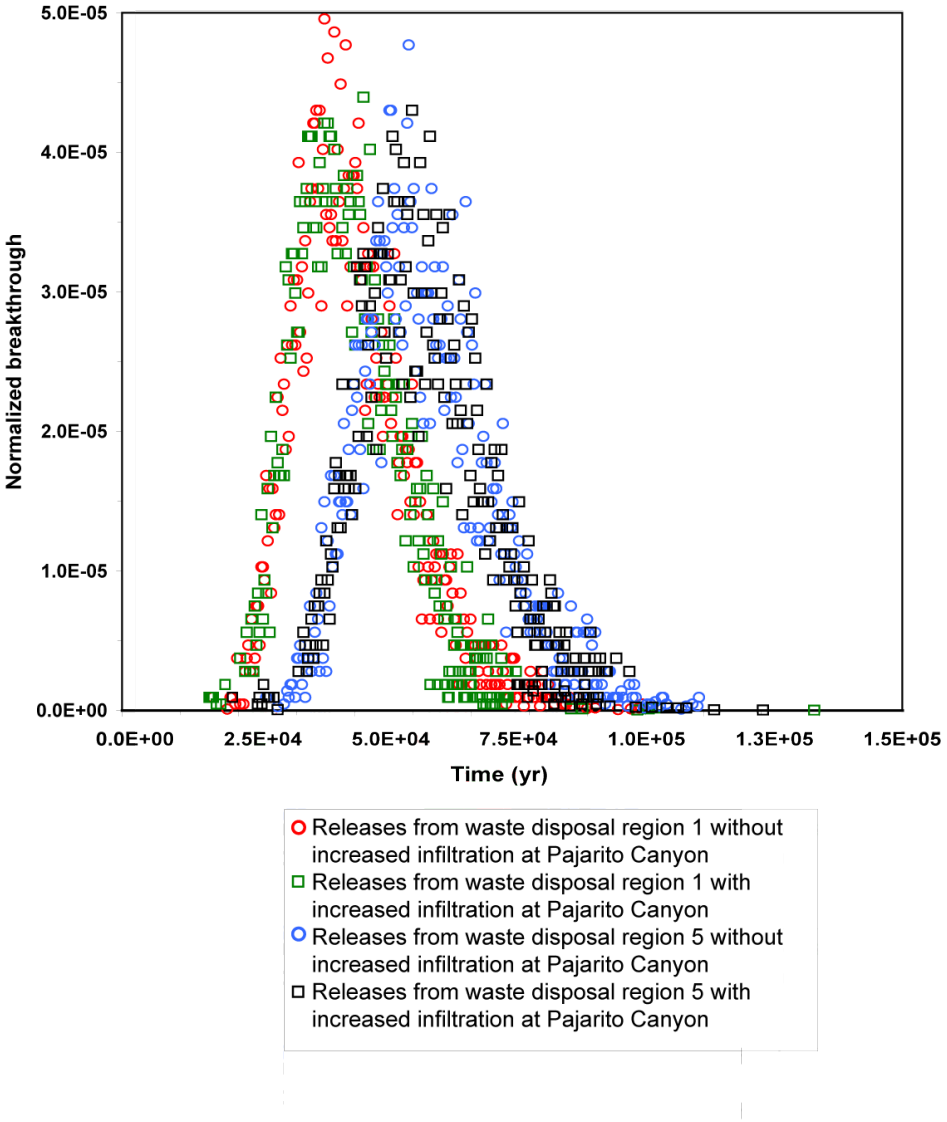

Figure 22
Effect of Pajarito Canyon Infiltration on Breakthrough for Releases from Waste Disposal Regions 1 and 5

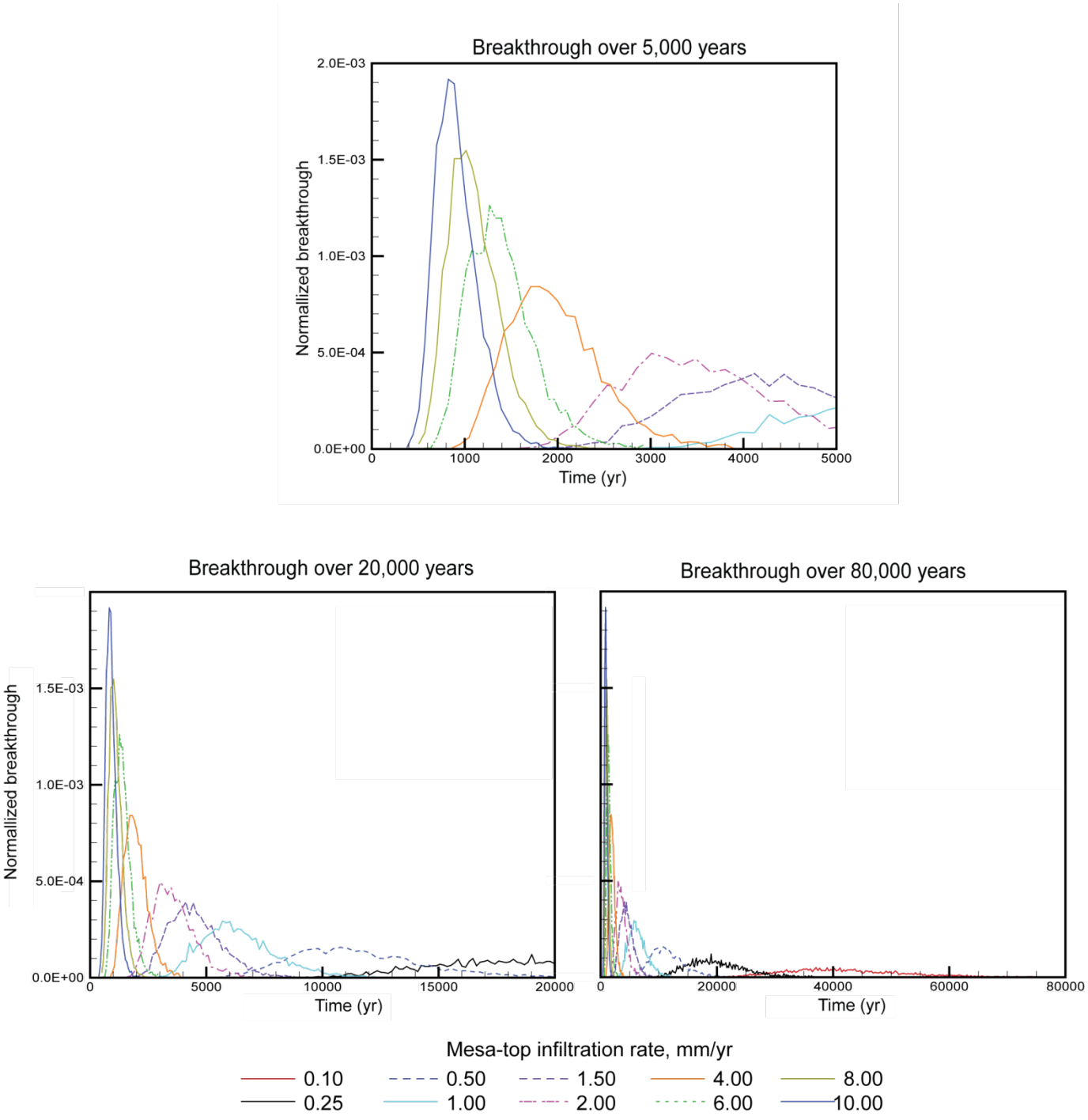

Figure 23
Breakthrough Curves for Particles Released from Waste Disposal Region 1 (range of steady-state infiltration rates)

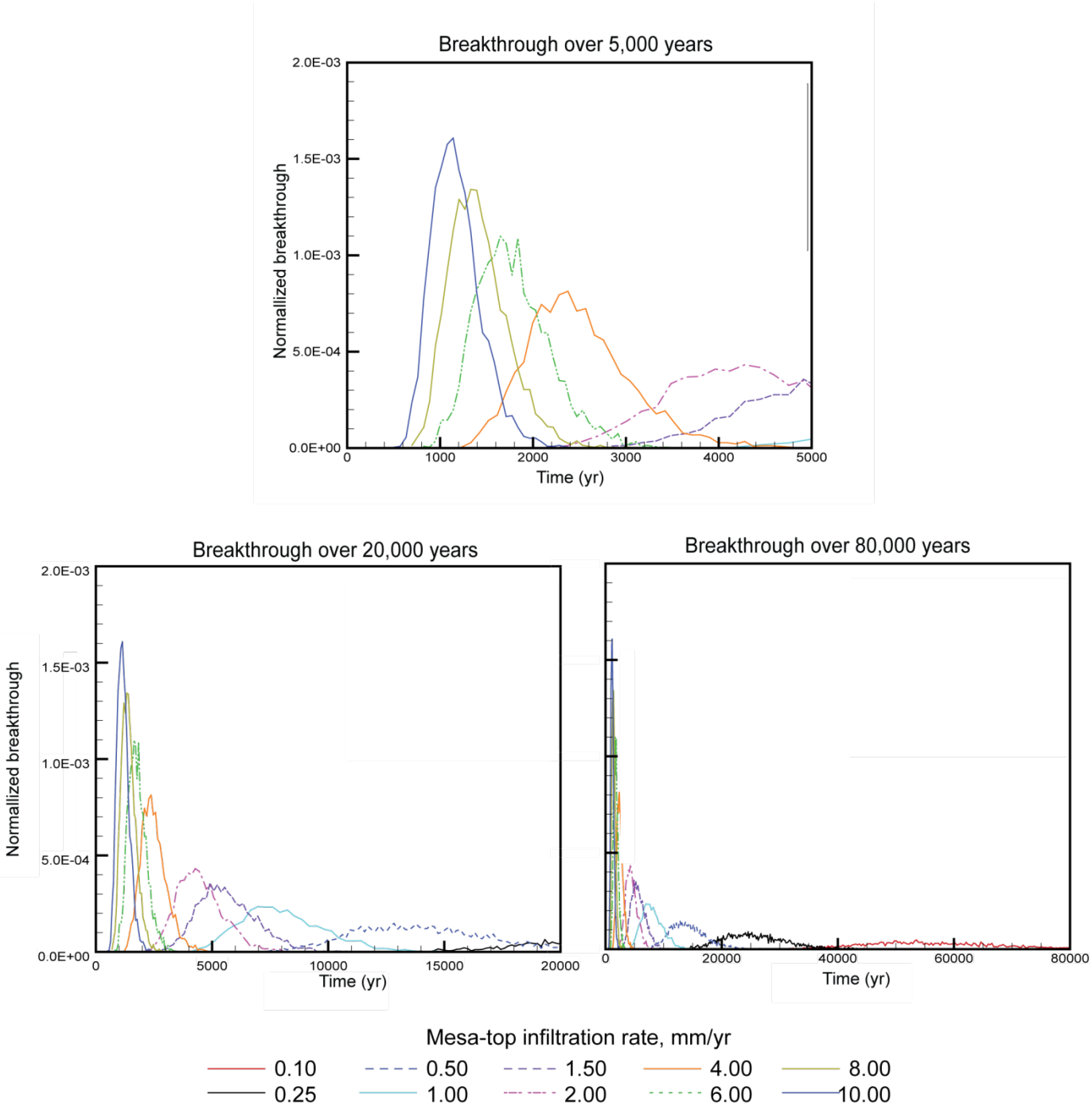

Figure 24
Breakthrough Curves for Particles Released from Waste Disposal Region 5 (range of steady-state infiltration rates)

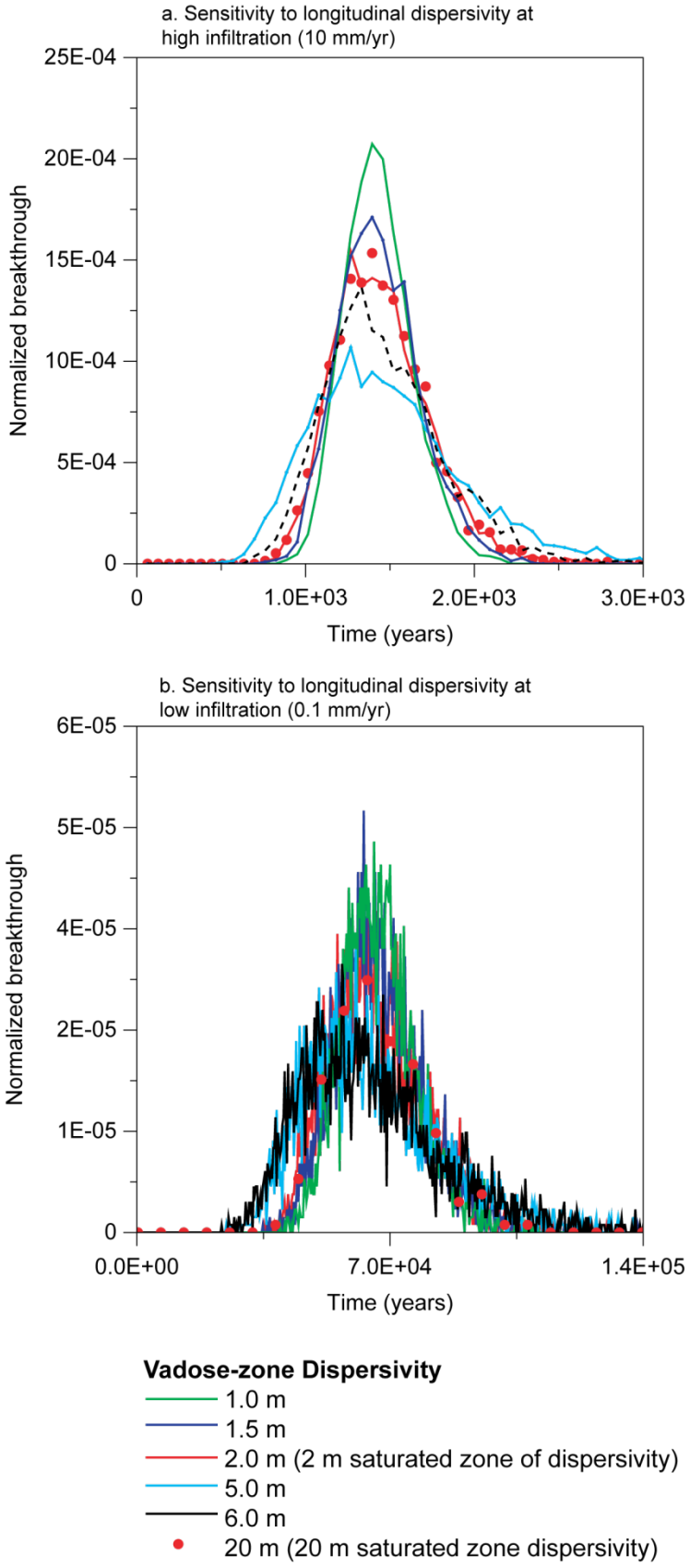

Figure 25
Model Sensitivity to Vadose-zone Longitudinal Dispersivity at Waste Disposal Region 5 (high- and low-infiltration rates)

This value was chosen because it is intermediate in what is considered to be a reasonable range of possible values. Changes in the longitudinal dispersivity of the saturated zone has little impact on breakthrough when the vadose-zone dispersivity is set at 2 m (7 ft). As seen in Figure 25, breakthrough curves are functionally the same when the saturated-zone dispersivity is changed from 2 to 20 m (7 and 70 ft).

4.2 Well Capture

The well capture simulations were used to determine the capture zone radius and capture efficiency of a hypothetical pumping well. Because the background gradient in the aquifer is fairly high, the well capture simulations project relatively narrow capture zones for the pumping rates considered. The capture radius ranged from 0.4 m (1.3 ft) for the 50 m^3/yr (1,300 gal/yr) pumping rate to 5.7 m (19 ft) for a pumping rate of 2,500 m^3 (6.6×10^5 gal/yr). Figure 26 shows the capture zone for a pumping rate of 1,200 m^3/yr (3.2×10^5 gal/yr). Table 6 summarizes the well capture efficiencies calculated using the 3-D particle tracer simulations. Capture efficiency is highly dependent on the transverse dispersivity, decreasing most rapidly between dispersivities of 0 and 2 m (0 and 6.6 ft).

The capture efficiencies estimated for the waste disposal regions are expected to be conservative. As discussed earlier, the efficiencies for each region were estimated by aligning the maximum particle densities with the well and then releasing the particles directly within the aquifer. This approach does not consider the north-south spatial distribution of the different disposal regions or the lateral spreading of contaminants at material contacts within the vadose zone. Taking these distributions into account, it is expected that a single well would be capable of intercepting maximum radionuclide releases from only one disposal region, capturing only fractions of the peak releases from the other disposal regions. However, the well capture efficiencies listed in Table 6 assume the well intercepts the maximum radionuclide release from all eight disposal regions.

4.3 Comparison of 3-D and 1-D Breakthrough Curves

The complex 3-D model produced the breakthrough curves described in Section 4.1. Comparisons of breakthrough from the 3-D simulations and the 1-D abstractions (*Attachment IV*) show that the 1-D abstractions recreate the breakthrough curves of the complex 3-D simulations. Although the input RTDs from the 3-D model are more detailed than the 1-D abstraction RTDs, the peak breakthrough times and standard deviations are similar. Thus, simulations performed on either mesh will lead to the same conclusions.

Similarities in peak breakthrough times for releases from waste disposal regions 1 and 3 can be seen in Figure 27. The breakthrough curves in Figure 27 are normalized so that the greatest number of particles arriving during a time step is scaled to equal one; this is different than the normalization scheme used in the previous figures, but makes it easier to compare the time-histories of the curves. The fits between the 1-D abstraction breakthrough curves and the 3-D particle breakthrough

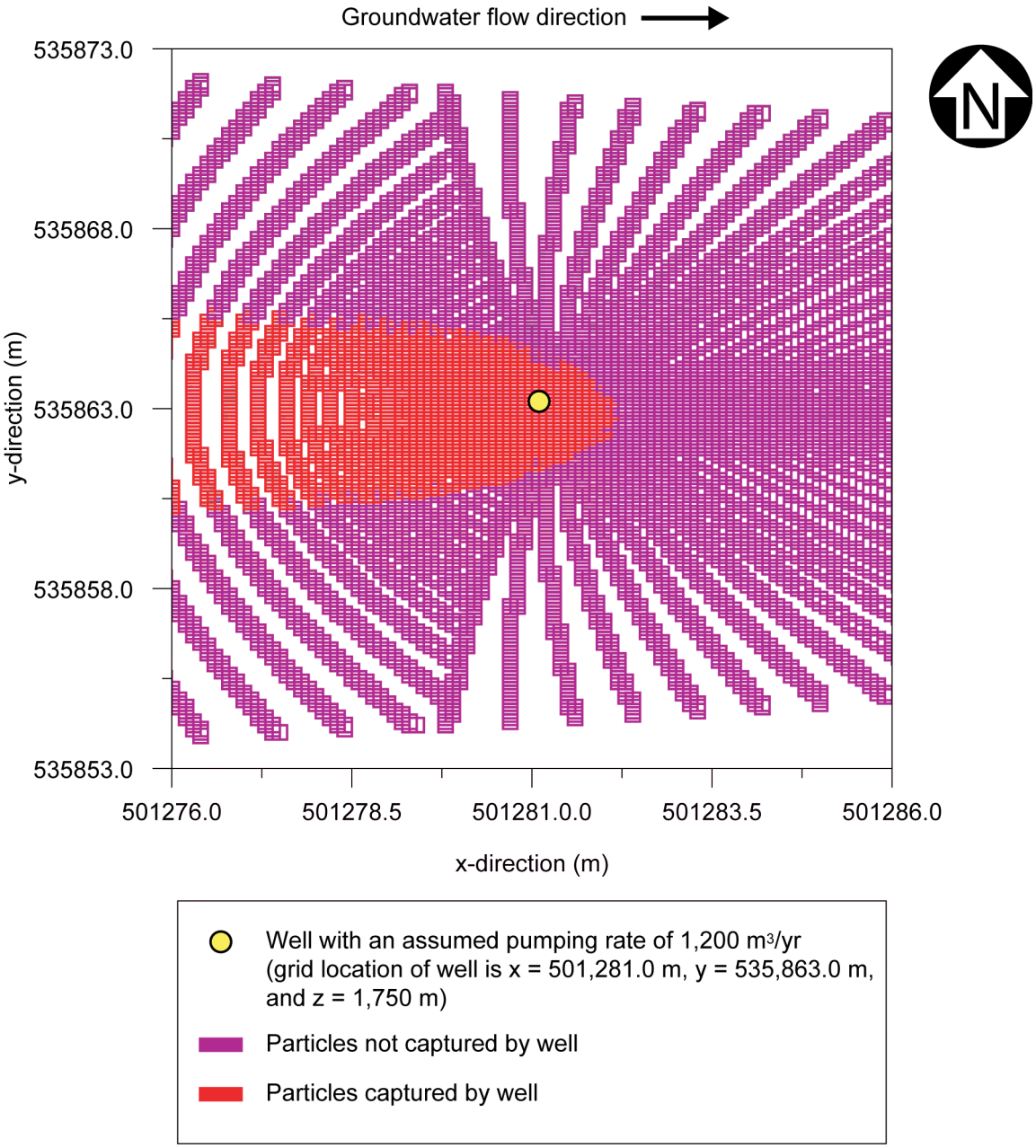

Figure 26
Capture Zone for Hypothetical Well with High Pumping Rate

Table 6
Capture Efficiencies for Waste Disposal Regions 1 through 5 and 8

Waste Disposal Region	Transverse Dispersivity (m)	Well Pumping Rates (m3/yr)			
		50	600	1,200	2,500
1	0	4.1E–02	4.1E–02	4.1E–02	4.1E–02
	1	1.7E–03	9.9E–03	1.9E–02	3.1E–02
	2	1.5E–03	9.2E–03	1.5E–02	2.6E–02
	5	2.0E–03	5.3E–03	1.3E–02	2.0E–02
2	0	1.1E–01	1.1E–01	1.1E–01	1.1E–01
	1	6.7E–03	2.3E–02	3.9E–02	7.1E–02
	2	5.3E–03	8.6E–03	2.2E–02	4.7E–02
	5	7.3E–04	6.7E–03	1.2E–02	2.7E–02
3	0	3.6E–02	3.6E–02	3.6E–02	3.6E–02
	1	1.2E–03	5.4E–03	9.7E–03	2.4E–03
	2	3.1E–03	2.8E–03	6.8E–03	1.4E–02
	5	3.0E–04	4.1E–03	4.2E–03	7.7E–03
4	0	3.6E–02	3.6E–02	3.6E–02	3.6E–02
	1	5.6E–04	5.0E–03	5.9E–03	1.7E–02
	2	0.0E+00[a]	1.6E–03	5.5E–03	1.1E–02
	5	2.6E–04	2.1E–03	2.7E–03	4.8E–03
5	0	5.8E–02	5.8E–02	5.8E–02	5.8E–02
	1	1.5E–03	9.2E–03	9.3E–03	1.9E–02
	2	5.8E–04	2.0E–03	5.5E–03	1.3E–02
	5	2.8E–04	2.2E–03	1.4E–03	3.9E–03
	10	0.0E+00[a]	2.8E–04	8.3E–04	2.7E–03
8	0	2.7E–02	2.7E–02	3.2E–02	8.1E–02
	1	1.7E–03	7.3E–03	8.0E–03	2.1E–02
	2	0.0E+00[a]	4.1E–03	4.9E–03	1.2E–02
	5	2.6E–04	1.3E–03	3.9E–03	5.1E–03
	10	2.5E–04	1.3E–03	1.8E–03	2.3E–03

[a] *No particles were captured under the indicated conditions.*

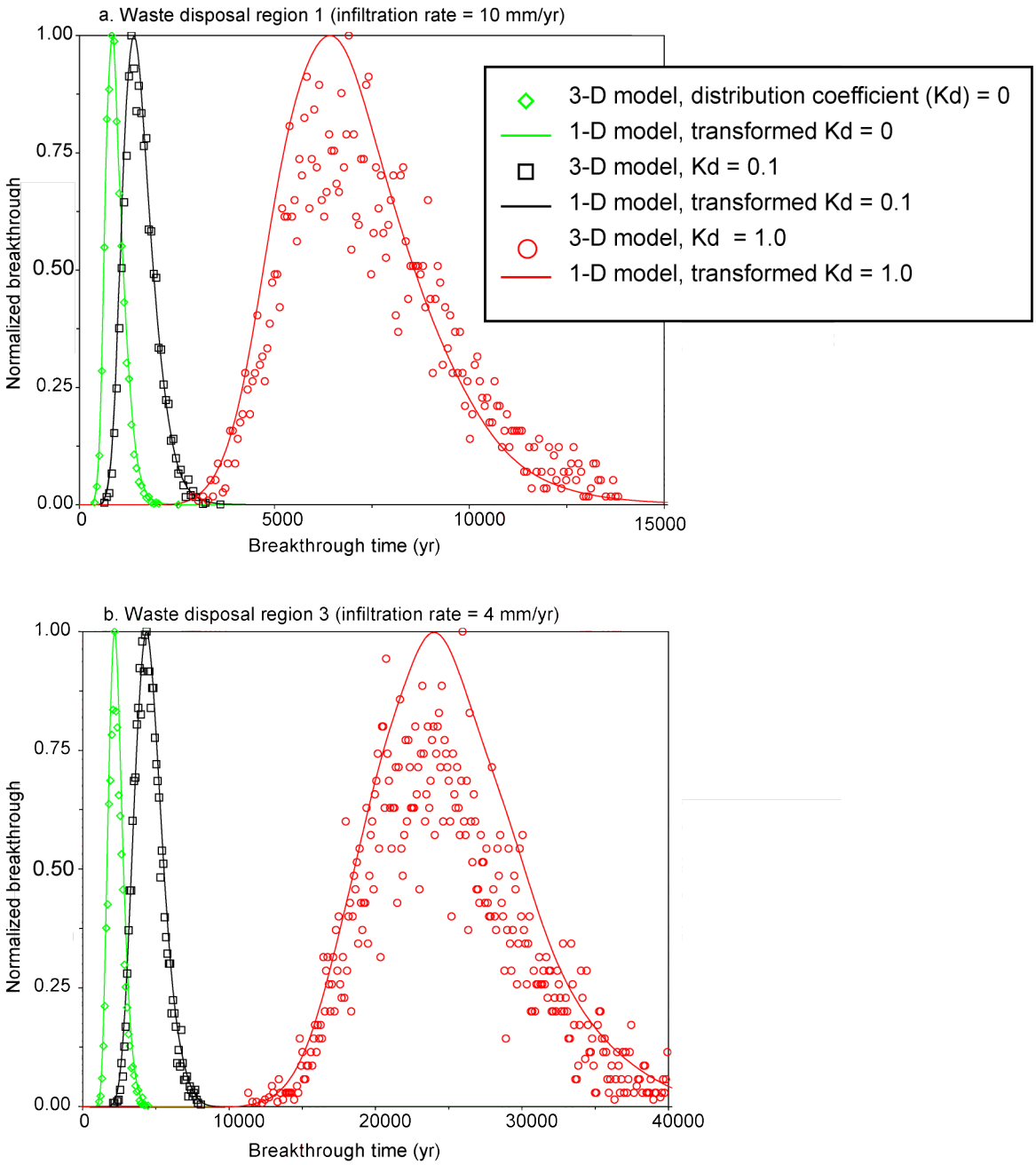

Figure 27
Comparison of Three-Dimensional Particle and One-Dimensional Plume Breakthrough Curves

distributions are quite good when the sorption distribution coefficient (K_d) is low. As the distribution coefficient increases, the scatter in the 3-D breakthrough curves becomes more pronounced and the fit is less accurate. The algorithm used to create the 1-D abstraction leads to some smoothing of the scattered data and approximations of the shape and peak value of the 3-D data. Although the fits appear poorer at longer times, these times fall well beyond the 1,000-year compliance period, and the approximate fit is acceptable for the analysis. More importantly, the 1-D and 3-D results for times less than 5,000 years match well and provide confidence that the 1-D abstraction retains the information embedded in the 3-D model. Results for the low end of the infiltration distribution or for higher distribution coefficients were not included because the breakthrough times are quite long for these cases and lie well beyond the compliance period.

4.4 Comparison of 2005 and 2011 Model Projections

The groundwater modeling revision was undertaken primarily to incorporate new geologic information collected at, and in the vicinity of, Area G since 2003. The new data were used to create the WC09b GFM, which forms the basis of the modeling conducted using FEHM. As discussed in Section 3.1, and detailed in *Attachment I*, the updated GFM reveals significant reductions in the thickness of the Bandelier Tuff and increases in the thickness of the Cerros del Rio basalts over some portions of the disposal site. The decreased thickness of the Bandelier Tuff included in the 2011 model may result in shorter travel times to groundwater than predicted by the 2005 groundwater modeling.

The breakthrough curves projected by the 2005 and 2011 groundwater modeling are compared across the eight waste disposal regions in *Attachment VII*; comparisons are shown for model simulations that used infiltration rates of 1 and 10 mm/yr (0.039 and 0.39 in./yr). The results of these comparisons are summarized in Table 7, which lists the approximate peak breakthrough times for each disposal region for the two models.

Table 7
Approximate Peak Breakthrough Times by Waste Disposal Region, 2005 vs. 2011

	Peak Breakthrough Time			
	Infiltration 1 mm/yr		Infiltration 10 mm/yr	
Waste Disposal Region	2005	2011	2005	2011
1	7050	6000	1000	840
2	8120	5120	1180	760
3	7840	6680	1210	1050
4	8680	5890	1320	950
5	9420	7320	1260	1100
6	6210	3500	950	570
7	7110	6000	1050	830
8	9170	8220	1440	1330

Overall, the 2011 modeling projects earlier particle breakthrough than the 2005 results; differences in breakthrough times are smaller for the higher rate of infiltration. Differences in the modeled breakthrough behavior are small for some waste disposal regions (e.g., disposal regions 1, 3, 7, and 8), where the thickness of the tuff is similar between the two GFMs. On the other hand, differences in breakthrough times are large, especially at an infiltration rate of 1 mm/yr (0.039 in./yr), for disposal regions 2, 4 and 6; the 2011 GFM predicts much thinner tuff for these regions.

The results shown in Table 7 support the notion that the thickness of the Bandelier Tuff is the primary determinant of breakthrough times beneath Area G. However, the permeability reduction present at the top of the Cerros del Rio basalts also plays a role in determining breakthrough behavior. This reduction in permeability causes water to spread laterally at the contact between the Otowi Member/Guaje Pumice Bed and the basalts before it flows downward to the water table; this spreading action causes delays in breakthrough. For waste disposal region 8, lateral spreading at the top of the basalts was estimated to be 30 m (98 ft) in the 2011 modeling, much less than the spread of 100 m (328 ft) seen in 2005. As a result, the updated modeling estimates earlier breakthrough, even though the Bandelier Tuff layer is slightly thicker at this location in the new GMF.

Differences in the peak breakthrough times projected by the 2005 and 2011 modeling will be larger than those shown in Table 7 at infiltration rates less than 1 mm/yr (0.039 in./yr). Although breakthrough times projected by the 2011 modeling will be shorter than those projected in 2005, all breakthrough times will occur well after the 1,000-year compliance period.

4.5 Impact of Hydrologic Property Uncertainty on Breakthrough

The groundwater modeling conducted using FEHM used mean hydrologic properties for the geologic strata underlying the disposal facility. The analysis described in Section 3.4 examined the uncertainty introduced into the breakthrough projections by the natural variability of hydrologic properties of the Bandelier Tuff (Tshirege units 2, 1v, and 1g and the Otowi Member ash flow tuffs). The methods used to conduct the uncertainty analysis and the results of the evaluation are provided in *Attachment VIII*.

The use of mean hydrologic properties for the tuff units yields breakthrough projections that are almost identical to the median breakthrough curves projected by the probabilistic simulations. At an infiltration rate of 1 mm/yr (0.039 in./yr), groundwater travel times were found to range over an order of magnitude, from thousands to tens of thousands of year. The projections indicate particles will first appear at the groundwater compliance boundary at a time that is about two-thirds of that projected when the geologic strata are characterized using mean hydrologic properties. To illustrate, at an infiltration rate of 1 mm/yr, the uncertainty analysis indicates that earliest time by which half of the particle mass has arrived at the compliance boundary is about 4,000 years into the simulation. The time projected for the arrival of half of the particle mass is

about 6,500 years when mean hydrologic properties are used in the modeling. A much greater difference in travel times is observed between the arrival time estimated using mean hydrologic properties and the maximum travel time estimated by the uncertainty analysis. The time required for half of the particle mass to reach the compliance boundary increases from 6,500 years to about 30,000 years.

5.0 References

Ball, T., M. Everett, P. Longmire, D. Vaniman, W. Stone, D. Larssen, K. Greene, N. Clayton, and S. McLin, 2002, *Characterization Well R-22 Completion Report*, Los Alamos National Laboratory report LA-13893-MS, Los Alamos, New Mexico, February.

Birdsell, K.H., W.E. Soll, N.D. Rosenberg, and B.A. Robinson, 1995, *Numerical Modeling of Unsaturated Groundwater Flow and Radionuclide Transport at MDA G*, Los Alamos National Laboratory Report LA-UR-95-2735.

Birdsell, K., K. Bower, A. Wolfsberg, W. Soll, T. Cherry, and T. Orr, 1999, *Simulations of Groundwater Flow and Radionuclide Transport in the Vadose and Saturated Zones beneath Area G, Los Alamos National Laboratory*, Los Alamos National Laboratory Report LA-13299-MS.

Birdsell, K.H., A.V. Wolfsberg, D.H. Hollis, T.A. Cherry, K.M. Bower, 2000, "Groundwater Flow And Radionuclide Transport Calculations for a Performance Assessment of a Low-Level Waste Site," *J. Contaminant Hydrology*, 46, pp. 99-129.

Broxton, D.E. and S.L. Reneau, 1995, *Stratigraphic Nomenclature of the Bandelier Tuff for the Environmental Restoration Project at Los Alamos National Laboratory*, Los Alamos National Laboratory Report, LA-13010-MS.

Carey, J.W. and Cole, G., 2002, *Description of the Cerro Grande Fire Laser-Altimetry (LIDAR) Data Set*, Los Alamos National Laboratory, Report LA-13892-MS, 57pp. plus appendices.

Cole, G., A.M. Simmons, D. Coblentz, E. Jacobs, D. Koning, D. Broxton, F. Goff, D. Vaniman, G. WoldeGabriel, and J. Heikoop, April 2010. "The 2009 Three-Dimensional Geologic Models of the Los Alamos National Laboratory Site, Southern Española Basin, and Española Basin," Los Alamos National Laboratory document LA-UR-09-3701, Los Alamos, New Mexico.

Dash, Z.V., 2003, *Software Users Manual (UM) for the FEHM Application Version 2.22*, Los Alamos National Laboratory Document 10086-UM-2.22-00.

Doughty, C., 2000, "Numerical Model of Water Flow in a Fractured Basalt Vadose Zone: Box Canyon site, Idaho," *Water Resources Research*, Vol.36, No.12, pp. 3,521-3534.

Fetter, C.W., 1999, *Contaminant Hydrogeology*, Prentice-Hall: NJ, USA.

Gelhar, LW; C. Welty, and K.R. Rehfeldt, 1992, "A Critical-Review of Data on Field-Scale Dispersion in Aquifers," *Water Resources Research*, Vol. 28, No. 7.

GoldSim, 2010a, *User's Guide – GoldSim – Probabilistic Simulation Environment,* Version 10.5, Volumes I and II, GoldSim Technology Group, December.

GoldSim, 2010b, *User's Guide – GoldSim Contaminant Transport Module,* Version 6.0, GoldSim Technology Group, December.

Hollis, D., E. Vold, R. Shuman, K. Birdsell, K. Bower, W. Hansen, D. Krier, P. Longmire, B. Newman, D. Rogers, E. Springer, 1997, *Performance Assessment and Composite Analysis for the Los Alamos National Laboratory Disposal Area G*, Los Alamos National Laboratory Report LA-UR-97-85, Report-54G-013, March.

Keating, E.H., V.V. Vesselinov, E. Kwicklis, and Z. Lu, 2003, "Coupling Basin- and Local-Scale Inverse Models of the Española Basin," *Ground Water*, Vol. 41, No. 2, pp. 200-211.

Kleinfelder, 2003, *Characterization Well R-21 Completion Report*, prepared for Los Alamos National Laboratory, Project No. 22461, Albuquerque, New Mexico, June 6.

Krier, D., R. Longmire, and H.J. Turin, 1996, *Geologic, Geohydrologic and Geochemical Data Summary of MDA G, TA-54, Los Alamos National Laboratory*, Los Alamos National Laboratory Report LA-UR-95-2696.

Kwicklis, E., M. Witkowski, K. Birdsell, B. Newman, and D. Walther, 2005, "Development of an Infiltration Map for the Los Alamos Area, New Mexico," *Vadose Zone Journal,* Vol. 4, No. 3, pp. 672-693.

LANL (Los Alamos National Laboratory), 2003, *Characterization Well R-32 Completion Report*, Los Alamos National Laboratory document LA-UR-03-3984, Los Alamos, New Mexico, June.

LANL, 2008, *Performance Assessment and Composite Analysis for Los Alamos National Laboratory Technical Area 54, Area G, Revision 4*, Los Alamos National Laboratory Report LA-UR-08—6764, October.

LANL, 2009a, *Completion Report for Regional Aquifer Well R-39*, Los Alamos National Laboratory document LA-UR-09-1343, Los Alamos, New Mexico, April

LANL, 2009b, *Completion Report for Regional Aquifer Well R-41*, Los Alamos National Laboratory document LA-UR-09-4334, Los Alamos, New Mexico, July.

Lichtner P.C., S. Kelkar, and B.A. Robinson, 2002, "New Form of Dispersion Tensor for Axisymmetric Porous Media with Implementation in Particle Tracking," *Water Resour. Res*., Vol. 38, No. 8.

Neuman, S.P., 1990, "Universal Scaling of Hydraulic Conductivities and Dispersivities in Geologic Media", *Water Resources Research*, Vol. 26, No. 8.

Nylander, C.L, K. A. Bitner, G. Cole, E. H. Keating, S. Kinkead, P. Longmire, B. Robinson, D. B. Rogers, and D. Vaniman, 2003, *Groundwater Annual Status Report for Fiscal Year 2002*, Los Alamos National Laboratory Report LA-UR-03-0244.

Pratt, A.R., 1998, Work *Plan for Pajarito Canyon: Environmental Restoration Project*, Los Alamos National Laboratory Report LA-UR-98-2550.

Robinson, B.A. and H. Viswanathan, 2003 "Application of the Theory of Micromixing to Groundwater Reactive Transport Models," *Water Resources Res*., Vol. 39, No. 11.

Robinson, B.A., M. Witkowski, C. J. Elliot, L. Dale, and R. Koch, 1999, *Numerical Model of Flow and Transport for Los Alamos Canyon*, Los Alamos National Laboratory (contact author at robinson@lanl.gov for an electronic copy).

Rogers, D.B. and B.M. Gallaher, 1995, *The Unsaturated Hydraulic Characteristics of the Bandelier Tuff*, Los Alamos National Laboratory Report LA-12968-MS, September.

Rogers, D.B., B.M. Gallaher, and E.L. Vold, 1996. "Vadose Zone Infiltration Beneath the Pajarito Plateau at Los Alamos National Laboratory," New Mexico Geological Society Guidebook: 47th Field Conference, Jemez Mountains Region, New Mexico, F. Goff, B.S. Kues, M.A. Rogers, L.D. McFadden, and J.N. Gardner (Eds.), pp. 413-420.

Soll, W.E., 1995, *Influence of Fracture Fills and Fracture Coatings on Flow in Bandelier Tuff*, Los Alamos National Laboratory Report LA-UR-95-2695.

Soll, W. and K. Birdsell, 1998, "The Influence of Coatings and Fills on Flow in Fractured, Unsaturated Tuff Porous Media System," *Water Resour. Res.*, Vol. 34, pp. 193 –202.

Springer, E.P., 2005, "Statistical Exploration of Matrix Hydrologic Properties for the Bandelier Tuff, Los Alamos, New Mexico", *Vadose Zone Journal,* Vol 4, No. 3, pp. 505-521.

Springer, E.P and T.G. Schofield, 2004, *Statistical Analyses of Mesa-Top Percolation Rates at Los Alamos National Laboratory, New Mexico*, Los Alamos National Laboratory Report LA-UR-04-7801.

Stauffer, P.H., B.A. Robinson, and K.H. Birdsell, 2000, *Modeling Transport in Los Alamos Canyon: Effects of Hypothetical Increased Infiltration after the Cerro Grande Fire*, Los Alamos National Laboratory Report LA-UR-00-5923.

Stauffer P.H., H.S. Viswnathan, B.A. Robinson, C.W. Gable, G.L. Cole, D.E. Broxton, E.P. Springer, and T.G. Schofield., 2005a, Groundwater Pathway Model for the Los Alamos National Laboratory Technical Area 54, Material Disposal Area G, LA-UR-05-7393

Stauffer, P.H., K Birdsell, M.S. Witkowski, and J.K. Hopkins, 2005b, "Vadose Zone Transport of 1,1,1-Trichloroethane: Conceptual Model Validation through Numerical Simulation," *Vadose Zone Journal,* Vol. 4, No. 3, pp. 760–773.

Stone, W.J., G.L. Cole, and M.A. Jones, 1999, *Documentation for the Preliminary Hydrogeologic Atlas for Los Alamos National Laboratory*, Los Alamos National Laboratory Report LA-UR-99-4619.

Vaniman, D., G. Cole, J. Gardner, J. Conaway, D. Broxton, S. Reneau, M. Rice, G. WoldeGabriel, J. Blossom, and F. Goff, 1996, *Development of a Site-Wide Geologic Model for Los Alamos National Laboratory*, Los Alamos National Laboratory Report LA-UR-96-2059.

Zyvoloski, G.A., 2007, FEHM: A control volume finite element code for simulating subsurface multi-phase multi-fluid heat and mass transfer. Los Alamos National Laboratory Report LA-UR-07-3359.

Zyvoloski, G. A., B. A. Robinson, Z. V. Dash, and L. L. Trease, 1995a, *Models and Methods Summary for the FEHMN Application*, Los Alamos National Laboratory Report LA-UR-94-3787, Rev. 1.

Zyvoloski, G. A., B. A. Robinson, Z. V. Dash, and L. L. Trease, 1995b, *User's Manual for the FEHMN Application*, Los Alamos National Laboratory Report LA-UR-94-3788, Rev. 1.

Attachment I
Update of the Vadose Zone Geologic Framework Model for Los Alamos National Laboratory Technical Area 54, Area G

Authors:
Greg Cole, LANL ENV-EDA
Dan Strobridge, Weston Solutions, Inc.

I.1 Introduction

Groundwater pathway modeling for the 2008 Area G performance assessment and composite analysis (LANL, 2008) relied on a partial geologic framework model (GFM) that included data collected through 2003. The updated groundwater modeling effort documented in this attachment uses version b of the Weston-Cole 2009 GFM, referred to as the WC09b GFM. This three-dimensional (3-D) representation of the geology underlying Area G and the surrounding canyons was developed using Dynamic Graphics' EarthVision® 7.5.3 software. The WC09b GFM is a subset of the Los Alamos National Laboratory (LANL or Laboratory) Fiscal Year 2009 (FY09) GFM (Cole et al., 2010), updated to incorporate data that were unavailable during the construction of the latter.

Section I.2 of this attachment provides a brief history of the development of the WC09b GFM. Specific details of the model are presented in Section I.3 along with a discussion of the major differences between this GFM and the FY03 GFM used for the 2008 Area G performance assessment and composite analysis. This is followed by a brief evaluation of model quality (Section I.4) and a comparison of the WC09b GFM and the WC09d GFM (Section I.5), which was issued to reflect new data obtained after the groundwater modeling effort was underway.

I.2 Model History

The Laboratory-wide GFM, first developed in 1996, was created in ArcInfo using rectangular grids that represent the top and bottom surfaces of each modeled geologic unit (Cole et al., 1997). Revisions to the LANL GFM occur periodically to incorporate new data (Cole et al., 1998; Cole et al., 2006); the latest revision at the time the groundwater modeling described in this report was undertaken was the FY09 GFM (Cole et al., 2010). Weston developed an EarthVision version of the FY09 GFM, designated as WC09, to improve 3-D model visualization and enable the GFM to be incorporated into Finite Element Heat and Mass (FEHM) meshes for vadose-zone and groundwater modeling. Figure I-1 shows the well and borehole data incorporated into the revisions of the GFMs discussed in this attachment.

The gridded surfaces of the model's shallow units (top of Puye and above to surface) are truncated by the surface topography. This effect is handled differently by ArcInfo and EarthVision. ArcInfo requires definition of top and bottom surfaces for each unit and allows these surfaces to be coincident (zero thickness isopach) where a unit does not exist. EarthVision units are represented by top surfaces only; these surfaces cannot be coincident with either underlying layers or the topography. Due to these inherent differences, the shallow units were re-gridded to remove areas that were coincident with the topography or the layers below.

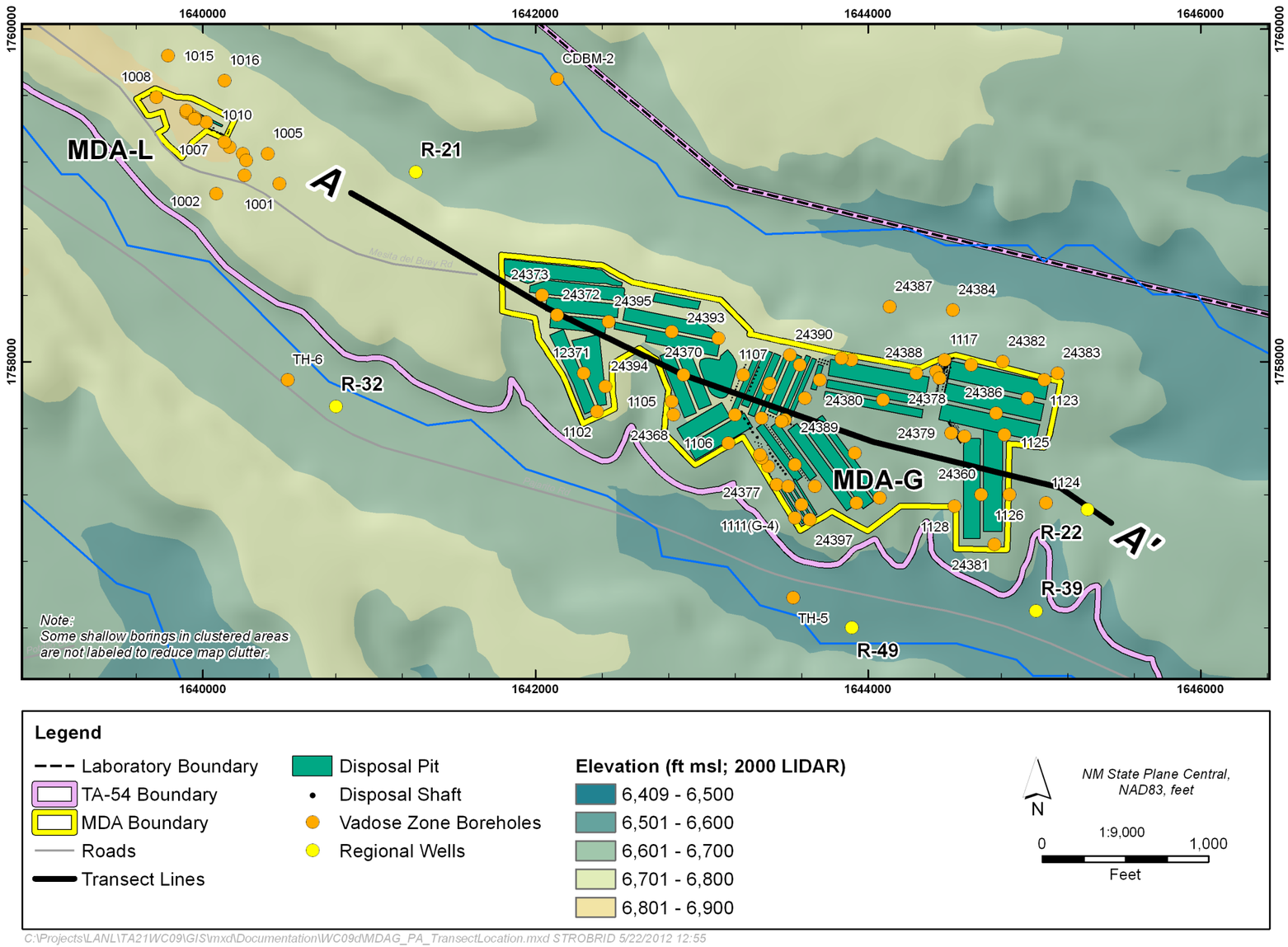

Figure I-1
Area G Model Domain and Wells and Boreholes Used to Construct and Update the GFM Versions

The WC09 model representations of the Bandelier units were based solely on the FY09 contacts database. Subsequent model iterations (WC09b, WC09c, and WC09d) incorporate the structural contours from LANL's FY09 GFM, information in the FY09 contacts database, and new 2010 borehole data to help honor the original intended shapes of the FY09 surfaces without duplicating the curious undulations. The modeling documented in this report relies on the WC09b GFM, which more closely honors the original shapes of the FY09 GFM (ArcInfo) surfaces and provides more coverage specific to Area G than the WC09 model. Model iterations WC09c and WC09d were constructed after this modeling had begun.

I.3 Model Details

The domain of the Area G GFM is a 4.8 km (3 mi) by 3.2 km (2 mi) rectangle (Figure I-1), with southwest and northeast New Mexico State Plane Central (NAD83, feet) corner points of 1634775E, 1755050N and 1647250E, 1764545N, respectively. It extends well beyond the fence line of the disposal facility to reduce the impact of boundary effects on Area G model solutions. The 1,067-m (3,500-ft) vertical range of the model extends from a maximum ground surface elevation of 2,195 m (7,200 ft) above mean sea level (msl) to just below the regional water table at 1,737 m (5,700 ft) above msl.

Similar to previous GFMs, the WC09b GFM is characterized by an unfaulted depositional sequence of nine Bandelier Tuff units underlain by the Puye Formation and the Cerros del Rio basalts. Detailed descriptions of the lithologic units are provided in well completion reports (e.g., Ball et al., 2002). The layers of the model were interpolated sequentially starting with the Cerros del Rio as the base of the model, and working upward through stratigraphic section. The interpolation process accounted for borehole, outcrop, and structural contour information as well as the surface of the underlying layer in a series of gridding passes for each layer. First, the outcrop data were examined to identify points that represent the native top surfaces for each layer and interpolated using EarthVision's conformal minimum tension algorithm, which allows the surface to inherit the general shape of the underlying layer. During a second conformal gridding pass, inferred structural contour information from the LANL FY09 GFM was incorporated to impose the intended shape of that model onto the surface. Lastly, the borehole data were filtered to exclude non-native surfaces and incorporated into a final polishing step to force the surface to honor existing borehole data as well as data added to the contacts database in 2010 (Figure I-1). Grid resolution was increased throughout the multistep process to yield final surfaces with 15-m (50-ft) cell resolution, which captures most of the detail offered by the clustered data.

The surface geology for the WC09b GFM is presented in Figure I-2. Because Quaternary alluvium was not incorporated into the WC09b GFM, the model predicts that Bandelier Tuff units outcrop in the canyons where alluvium actually occurs; the canyon-bottom alluvium was not included in the model because it is not an important geologic unit for the mesa-top groundwater transport model.

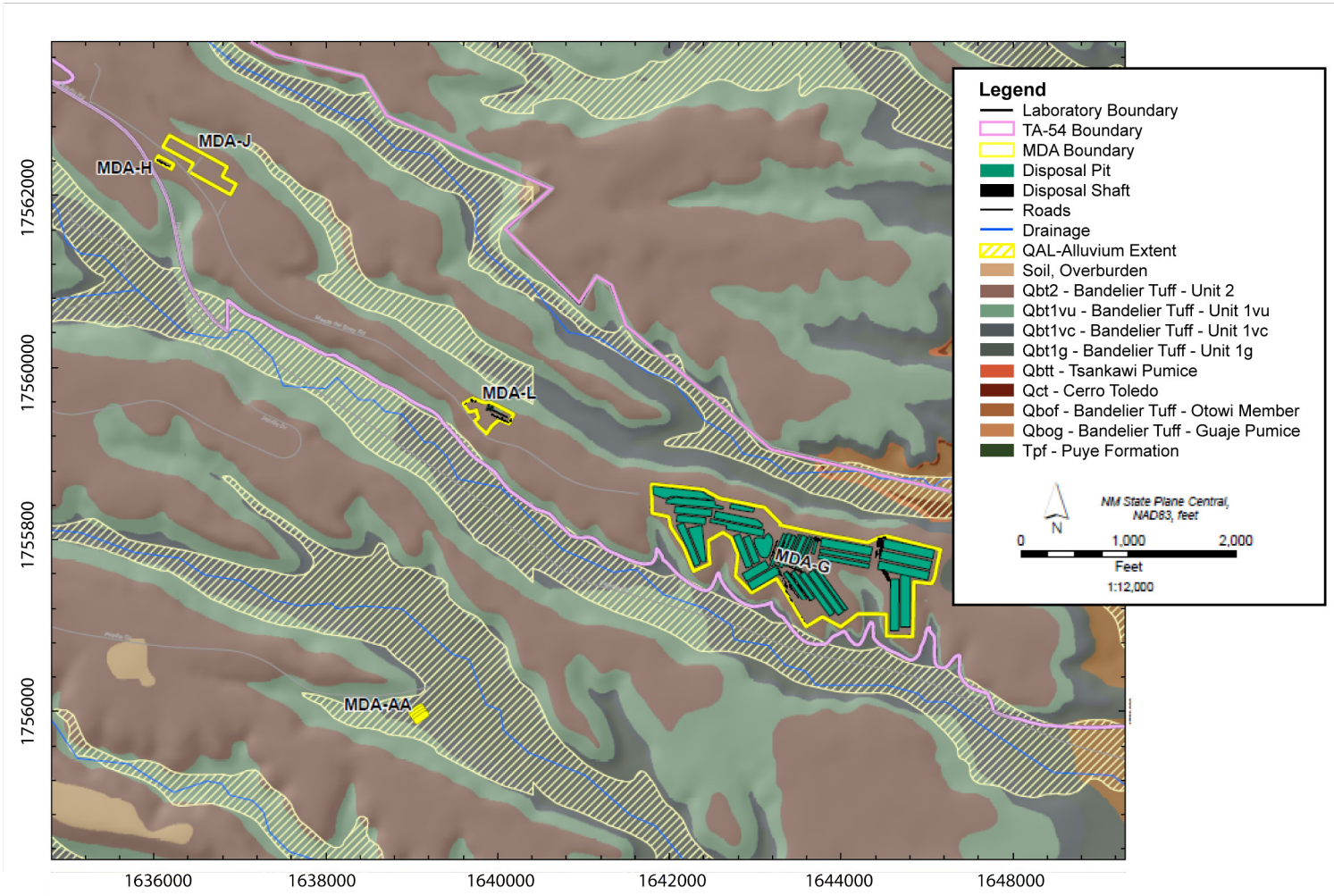

Figure I-2
Surface Geology Predicted by WC09b Geologic Framework Model
(Modified from map created by Weston, 2010)

Structural contours representing the top elevation of each geologic unit are presented in Figures I-3 through I-5 to illustrate the general shape of each layer and differences in the thickness of each model layer relative to the FY03 GFM. The difference is presented as a color flood representing change in layer thickness resulting from alterations to the top and bottom surfaces of each layer. Regions in which elevational changes were less than 0.31 m (1 ft) or where a unit was absent are shown in gray. The figures also indicate the differences (residuals) in elevations between the tops of the modeled surfaces and the contacts observed in boreholes.

Figures I-3 through I-5 illustrate several key points of the WC09b model. The greatest changes between this model and the FY03 model are seen in the two thickest layers, the Cerros del Rio basalts and the Otowi Member (Qbof), both of which exert significant control on the shapes of the remaining layers. The color flooding reveals that the thicknesses of the basalts and the Otowi Member differ by up to 76 m (250 ft) and 46 m (150 ft), respectively, from the earlier estimates. Thicknesses of all other layers differ by less than 15 m (50 ft). The contours of the Puye Formation and Guaje Pumice surfaces are similar in shape to those of the underlying Cerros del Rio, whereas the surface contours of the upper units take their general shape from the surface of the underlying Otowi Member.

Detailed views of most model layers are depicted in Figures I-6 through I-14. These figures provide thickness information, structural contours from the LANL FY09 GFM, and borehole labels to facilitate model inspection. Outcrop data used during the interpolation process are presented where appropriate. Contours are clipped by areas where the layer in question is absent due to pinchout or erosion in the canyons. Borehole data are color coded to reflect the absolute value of the model residuals for each layer. Data appearing in areas without contours are control points that reflect the absence of the layer in the borehole.

The WC09b model incorporates new structural contours for the Cerros del Rio basalts, to reflect a small depression, or paleochannel, in the basalt surface beneath Area G. This paleochannel was inferred by the absence of basalt in borehole 54-24363. According to the contact elevations in surrounding boreholes, the terminal depth of this borehole extends below the elevation at which the basalt should have been encountered. The small basalt paleochannel area centered on borehole 54-24363 is detailed in the inset of Figure I-6. This area contains several boreholes with Tshirege unit 1g lying unconformably above the basalt. Numerous control points were used to force pinchouts of the intermediate layers (Puye Formation, Guaje Pumice, Otowi Member, and Cerro Toledo) in this vicinity. Outside of the paleochannel area, there are very few observations of the Puye Formation within the Area G model domain. The control points used to define the extent of this unit suggest a patchy veneer of Puye Formation above the basalt. The Guaje Pumice and Cerro Toledo Interval display pinchout due to their absence in one or more boreholes. The remaining Tshirege units are continuous beneath the mesa but are absent in areas where they have been eroded away in the canyons. Tshirege unit 2 is shown in Figure I-14; the top elevation for this surface in the Area G domain is dictated by topography rather than by borehole data representing native surface contacts.

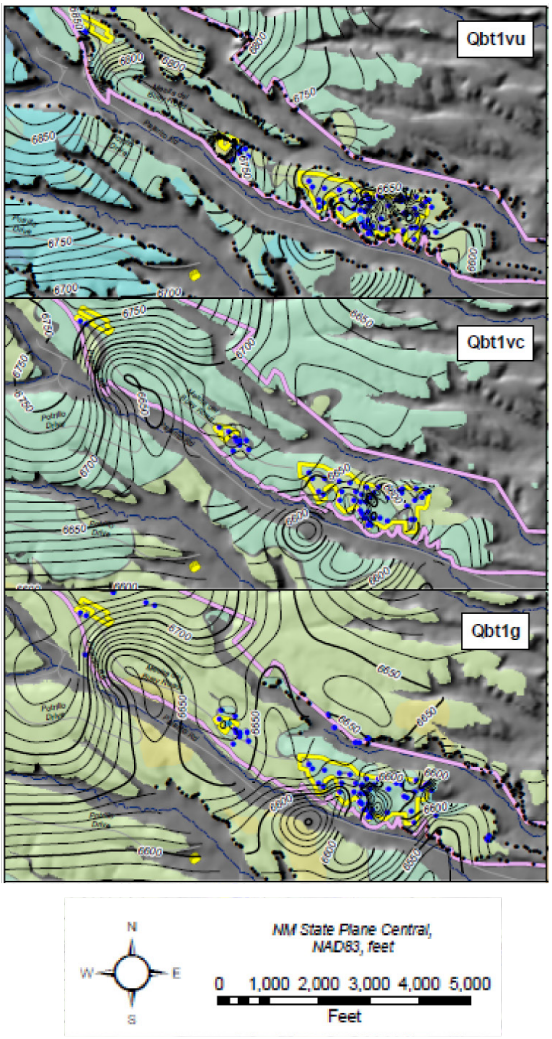

Figure I-3
Top Elevations of Tshirege Member Unit 1 Layers of Bandelier Tuff in the WC09b GFM and Differences in Layer Thickness Relative to the FY03 GFM
(Modified from maps created by Weston, 2010)

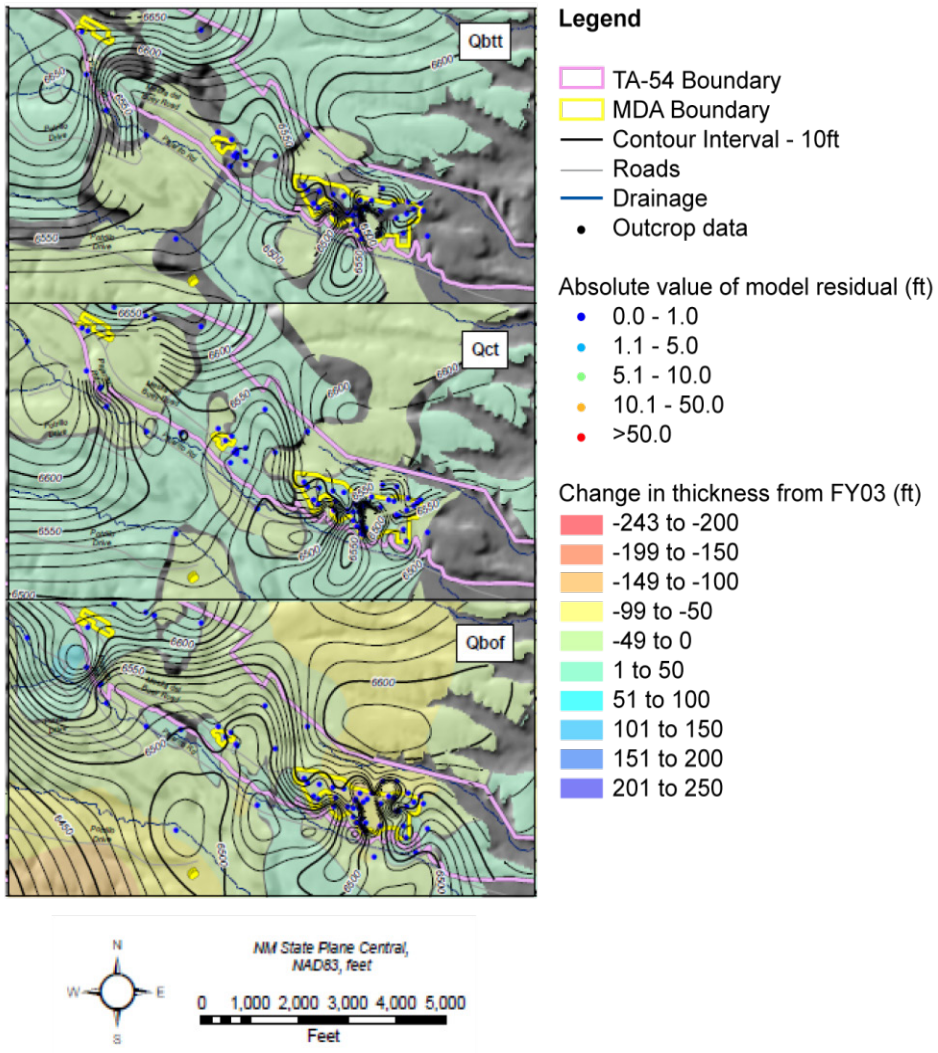

Figure I-4
Top Elevations of the Tsankawi Pumice Bed, Cerro Toledo Interval, and Otowi Member in the WC09b GFM and Differences in Layer Thickness Relative to the FY03 GFM
(Modified from maps created by Weston, 2010)

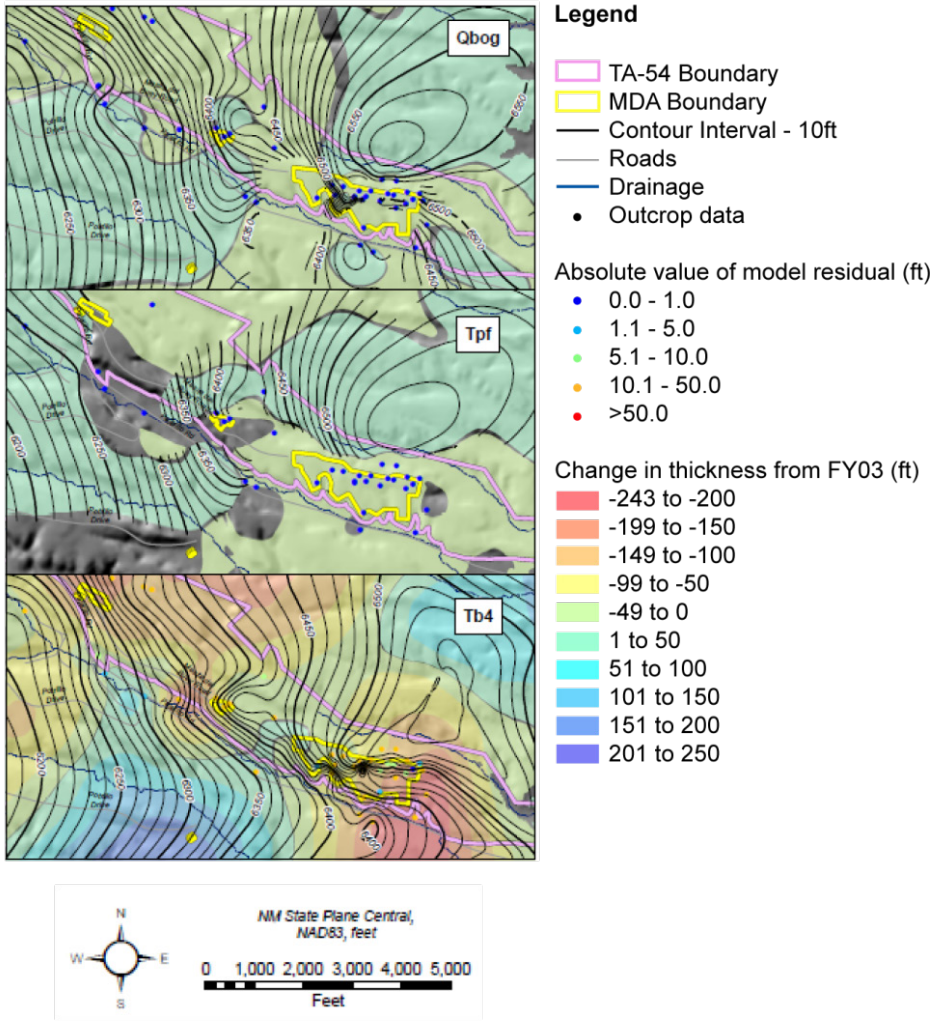

Figure I-5
Top Elevations of the Guaje Pumice Bed, Puye Formation, and Cerros del Rio Basalts in the WC09b GFM and Differences in Layer Thickness Relative to the FY03 GFM
(Modified from maps created by Weston, 2010)

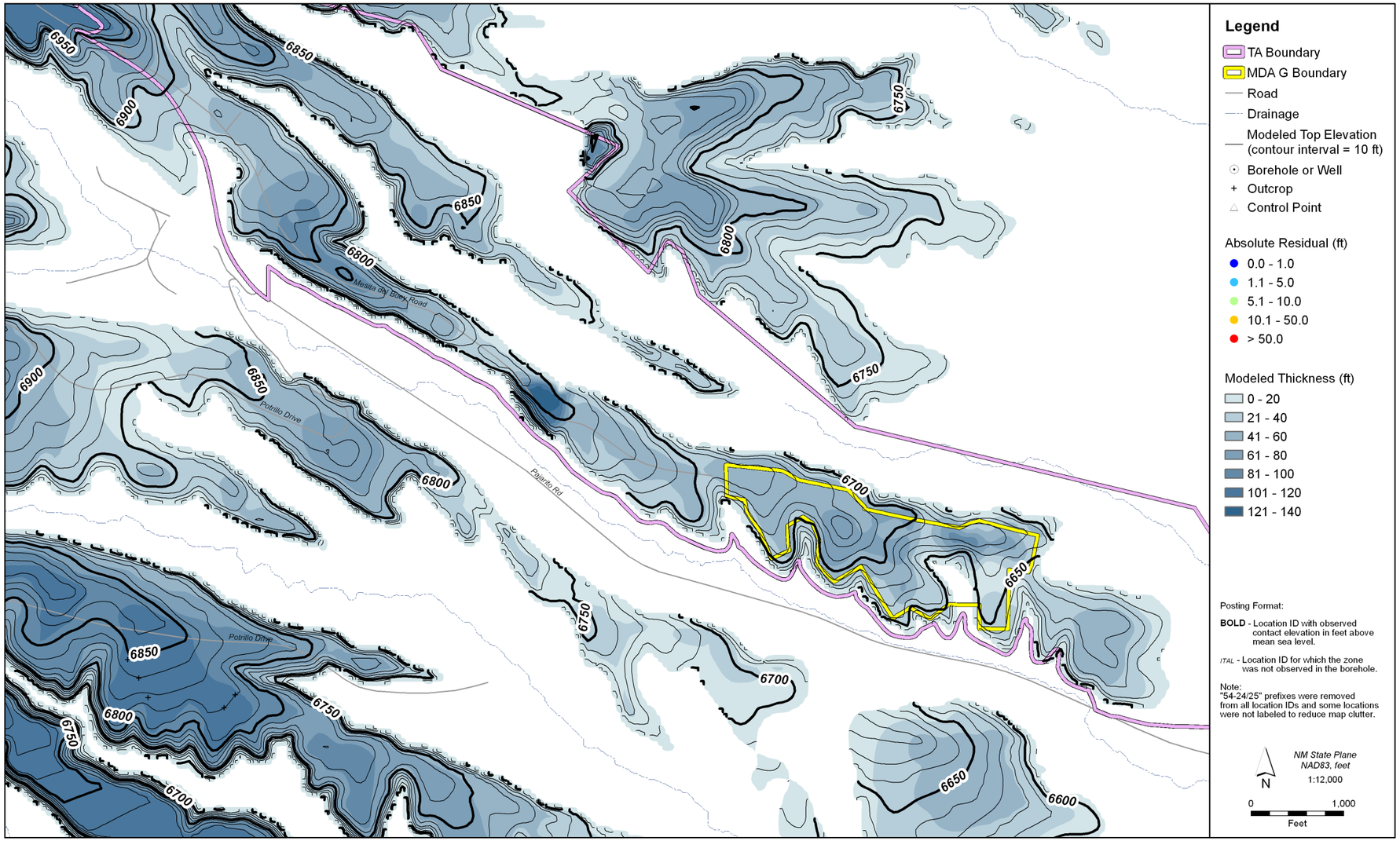

Figure I-6
Thickness and Elevation of Top Surface of Tshirege Unit 2 with Model Residuals

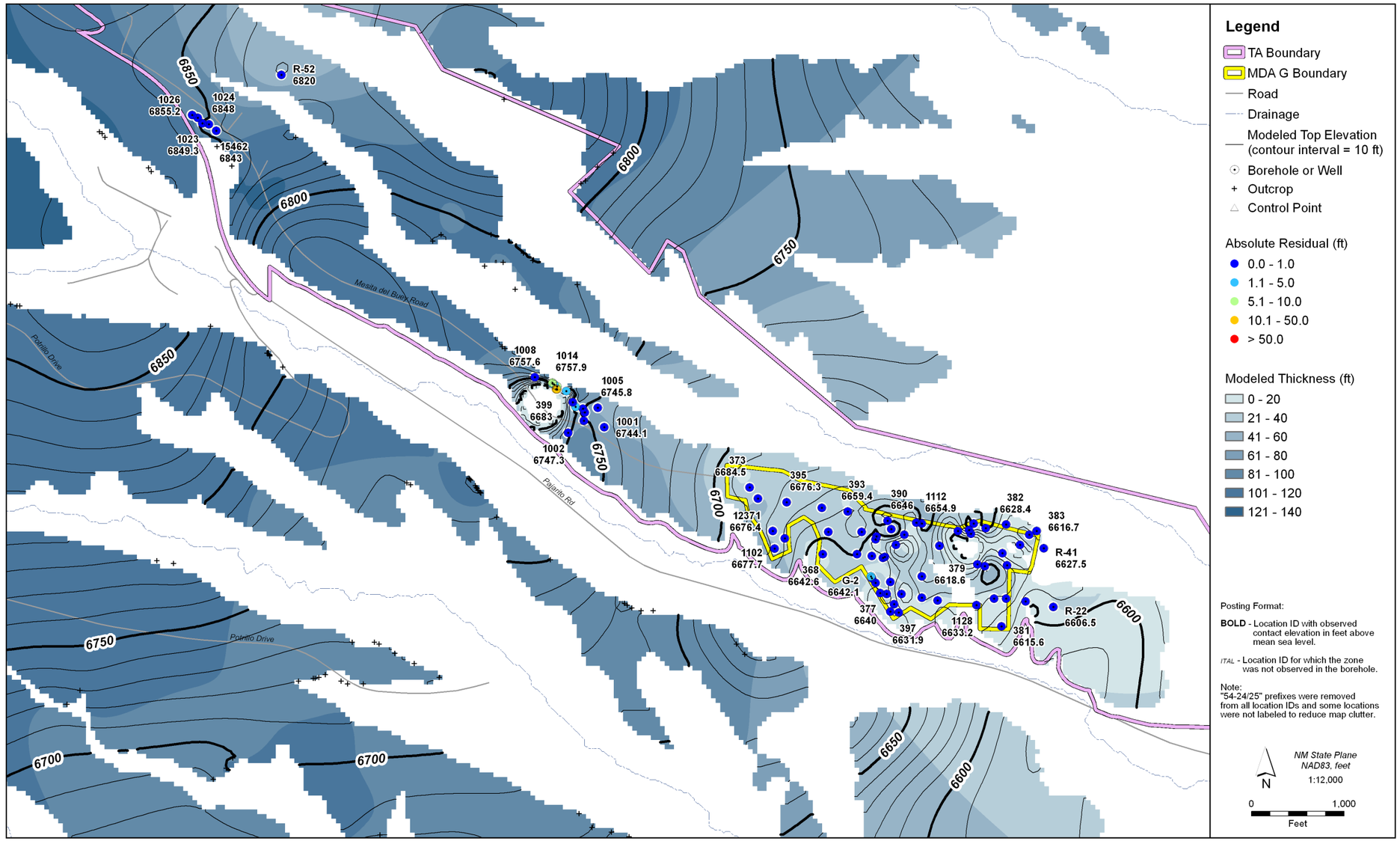

Figure I-7
Thickness and Elevation of Top Surface of Tshirege Unit 1vu with Model Residuals

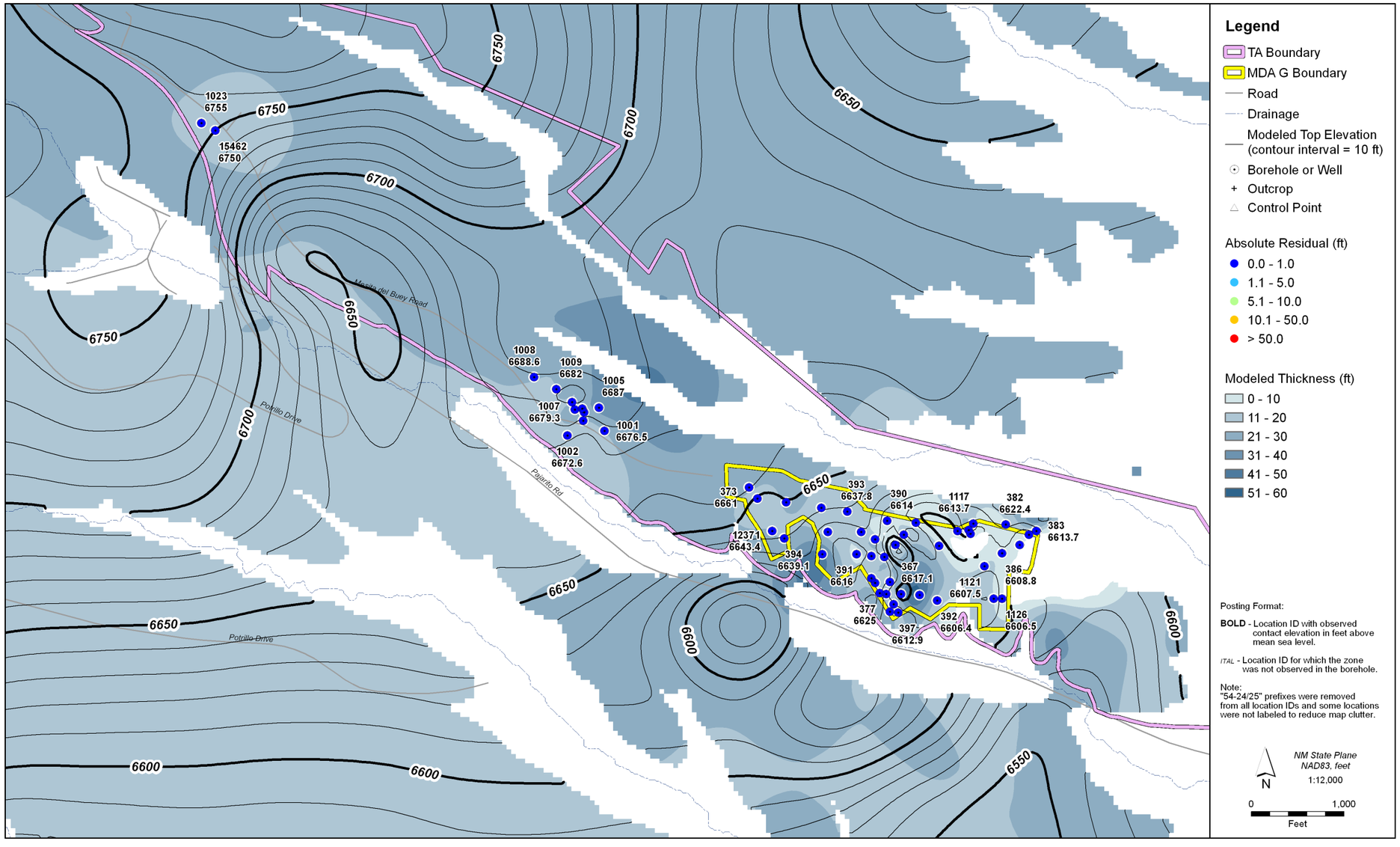

Figure I-8
Thickness and Elevation of Top Surface of Tshirege Unit 1vc with Model Residuals

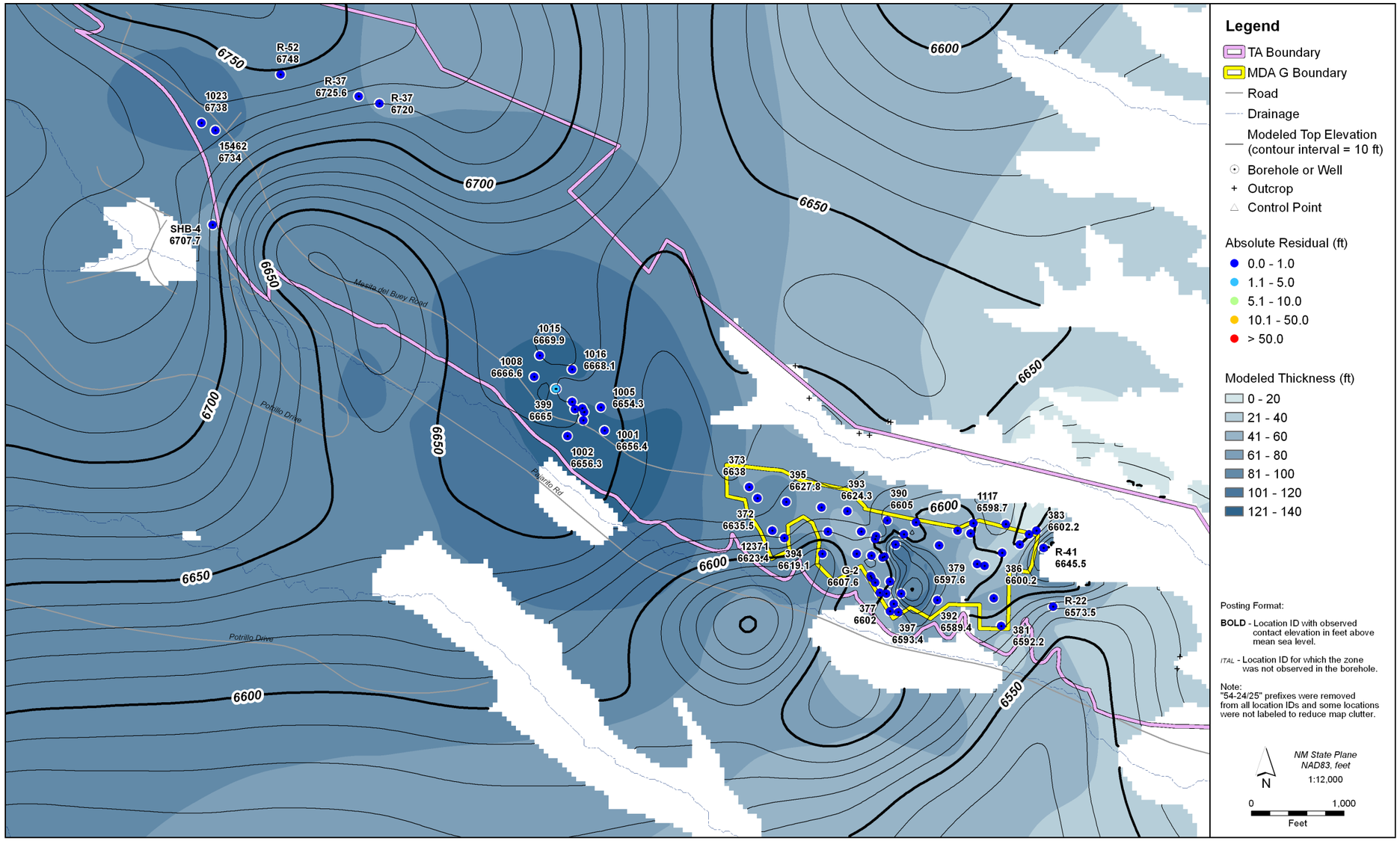

Figure I-9
Thickness and Elevation of Top Surface of Tshirege Unit 1g with Model Residuals

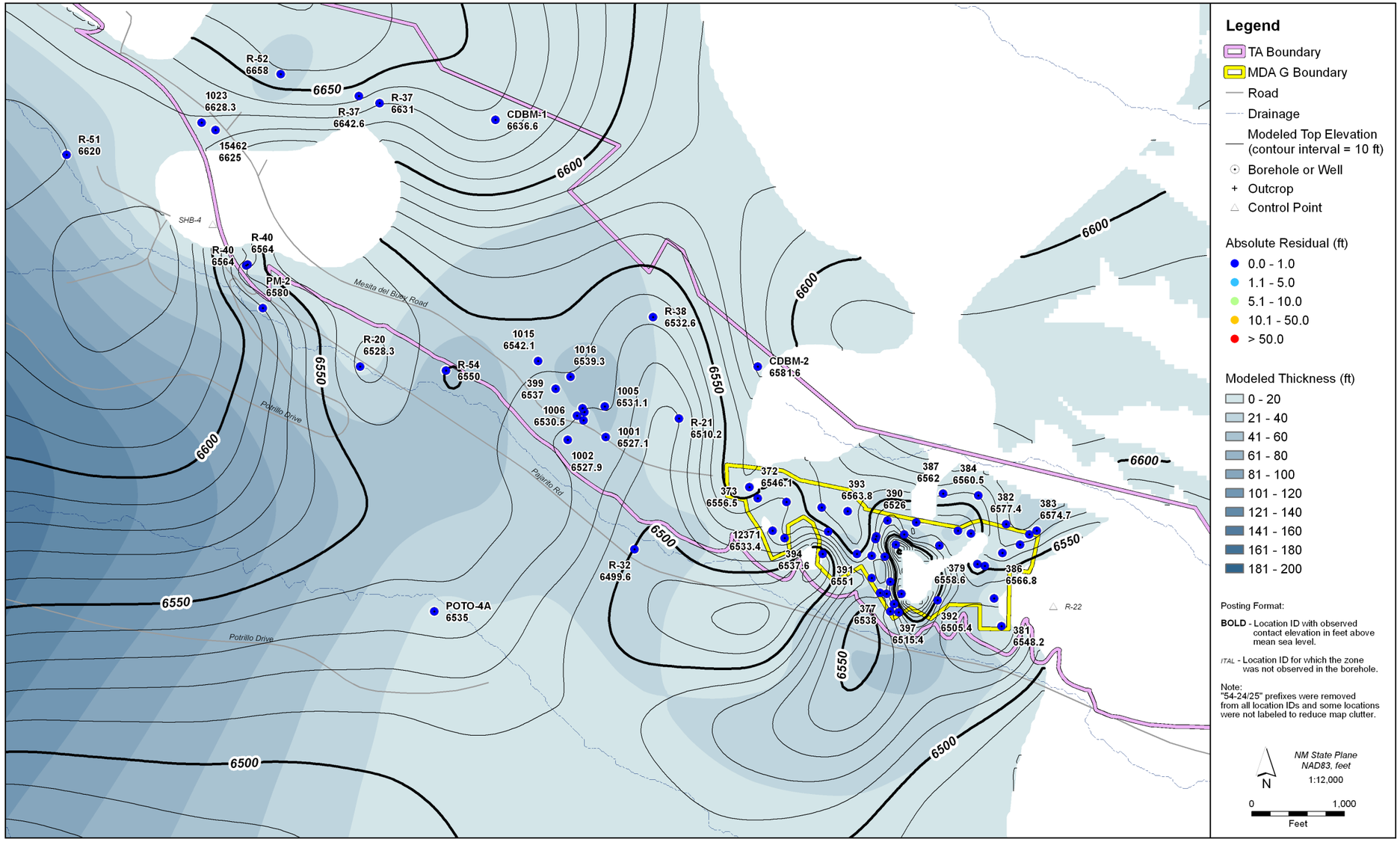

Figure I-10
Thickness and Elevation of Top Surface of Cerro Toledo Interval with Model Residuals

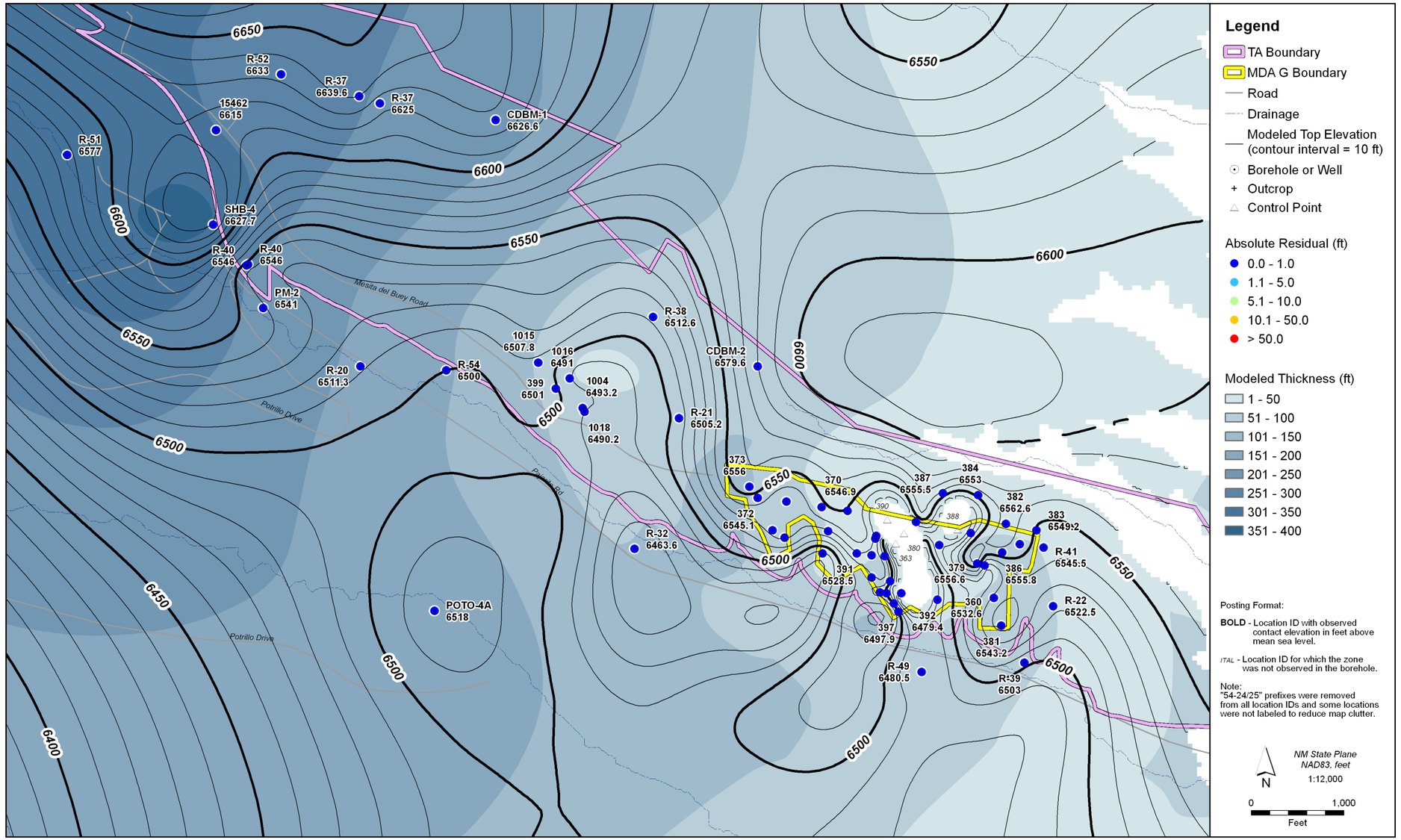

Figure I-11
Thickness and Elevation of Top Surface of Otowi Member with Model Residuals

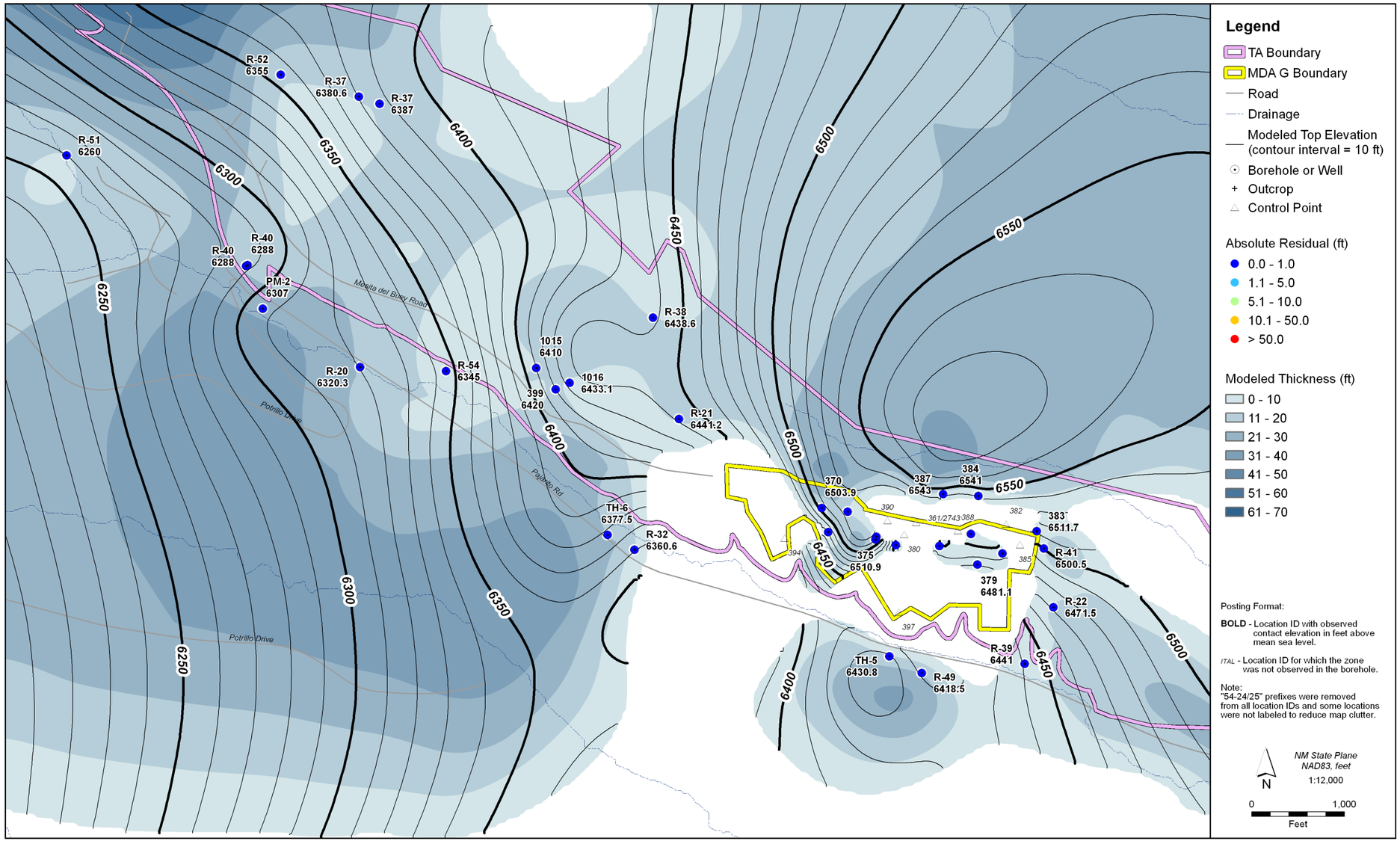

Figure I-12
Thickness and Elevation of Top Surface of Guaje Pumice with Model Residuals

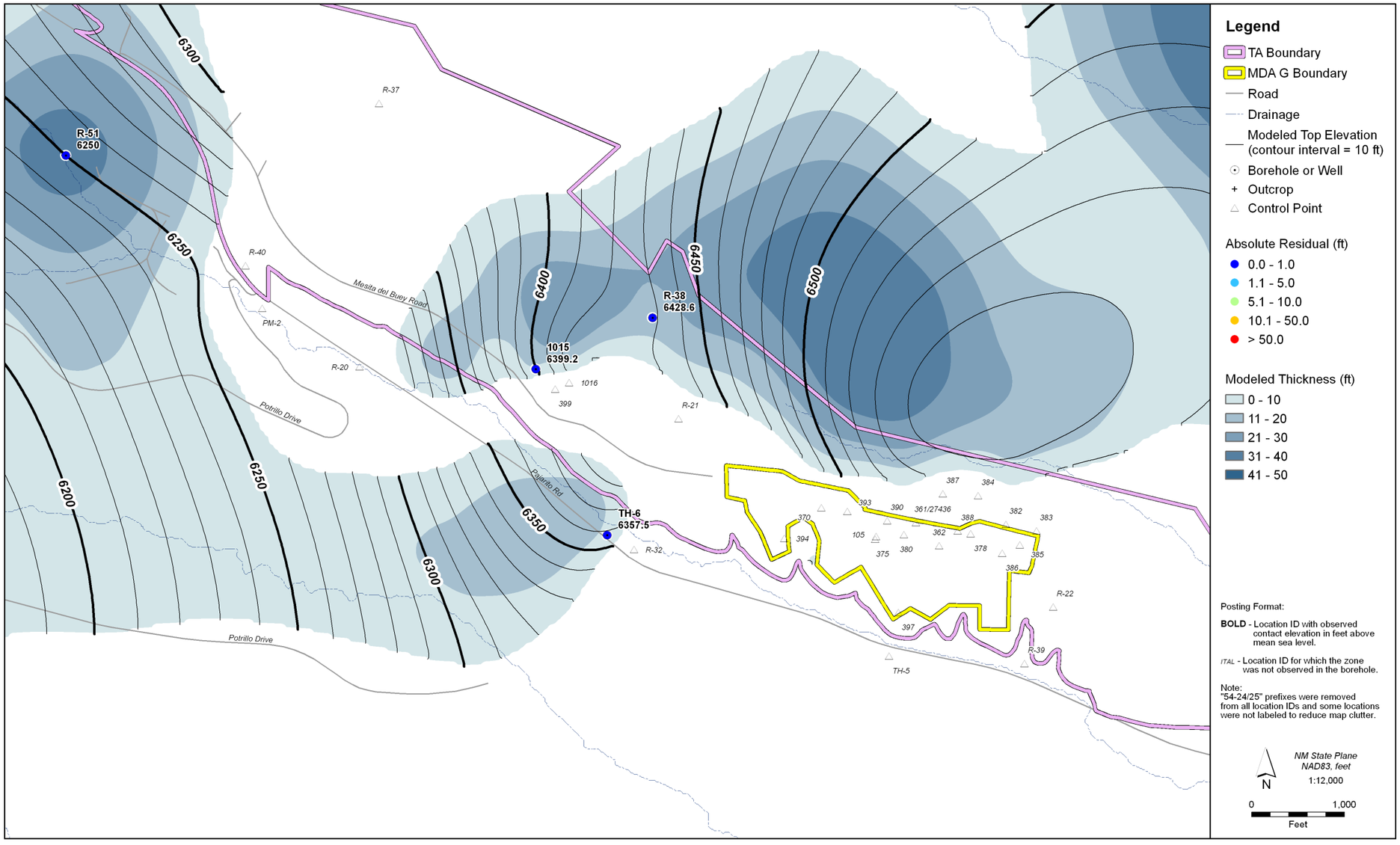

Figure I-13
Thickness and Elevation of Top Surface of Puye Formation with Model Residuals

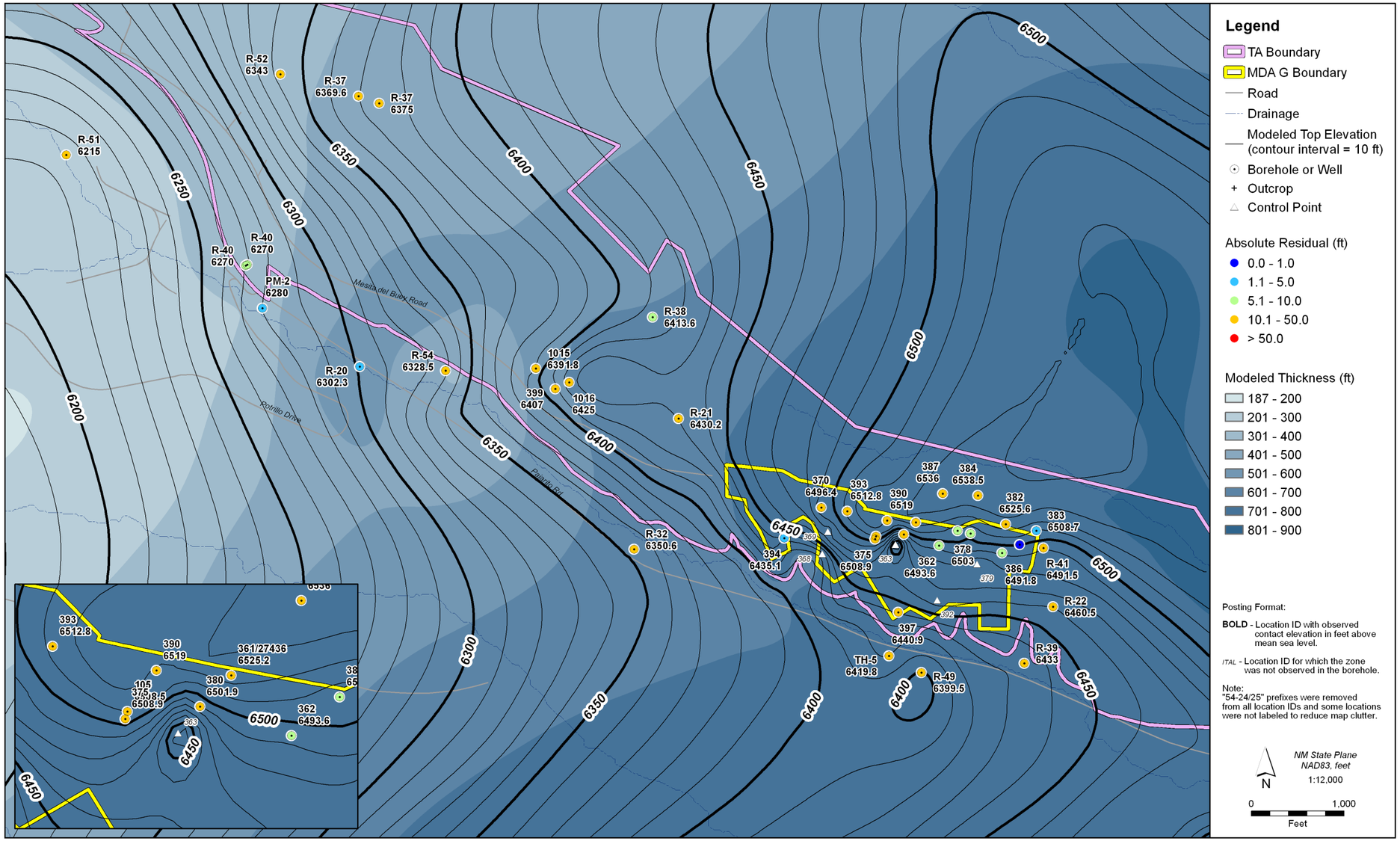

Figure I-14
Thickness and Elevation of Top Surface of Cerros del Rio Basalts with Model Residuals (inset shows paleochannel centered on borehole 54-24363)

I.4 Model Quality Evaluation

Maps and cross sections generated for the WC09b GFM were inspected by LANL geologists and determined to provide a reasonable representation of the Area G geology. In addition, model residuals were determined for the GFM; a summary of these residuals is presented in Table I-1. The majority of the mean absolute residuals for the WC09b GFM are less than 0.31 m (1 ft). The surface for the Cerros del Rio basalts was not forced to fit the full set of clustered data for this formation because of the highly variable nature of the data. Therefore, the residuals for the basalts are higher than those for other units. Model residuals are a measure of how well a model honors the observational data; they are not necessarily indicative of overall model quality. A better measure of model quality is the ability of the model to predict the elevations of various geologic units at unsampled locations; the assessment necessary to validate the model in this manner was not conducted.

Table I-1
Summary of Model Residuals for WC09b GFM

	Top Elevation (ft)		Model Residual				
Lithologic Unit	Min.	Max.	Count	Min. (ft)	Max. (ft)	Avg. (ft)	Standard Deviation (ft)
Cerros del Rio basalts	6215.0	6538.5	46	−44.0	45.2	19.9	13.1
Puye Formation	6250.0	6528.5	36	−0.2	0.1	0.0	0.0
Bandelier Otowi, Guaje Pumice	6260.0	6543.0	45	−0.2	0.2	0.0	0.1
Bandelier Otowi, Ash Flow	6435.7	6700.0	67	−0.4	0.6	0.1	0.1
Cerro Toledo Interval	6450.7	6670.0	72	−0.4	0.8	0.1	0.1
Bandelier Tshirege, Tsankawi Pumice	6451.9	6701.0	55	−0.4	0.8	0.1	0.1
Bandelier Tshirege, Unit 1g	6563.7	6748.0	65	−1.6	0.9	0.1	0.3
Bandelier Tshirege, Unit 1vc	6582.0	6755.0	54	−0.3	0.2	0.1	0.1
Bandelier Tshirege, Unit 1vu	6605.1	6855.2	79	−23.4	33.1	1.2	4.6

I.5 Comparison to Recent GFM Update

The GFM for the Area G domain shown in Figure I-1 continues to evolve as more information about the region is collected and as errors in the current model are discovered. A more recent version of the Area G GFM, WC09d, became available as the groundwater modeling update was

being finalized. Relative to the WC09b GFM, this model adds a dacite unit to the base of the Cerros del Rio basalts and corrects errors to contact information included in the earlier model (Figure I-1). The potential impacts of these changes to the GFM on the groundwater model results presented in this report are discussed below.

The inclusion of the dacite has no impact on the surfaces of interest for the groundwater modeling conducted in support of the Area G performance assessment and composite analysis. Inclusion of this new zone simply represents a differentiation between basalt and dacite at the base of the basalt in a small area defined by five boreholes near the eastern end of Area G.

Two errors in the WC09b model were corrected in the WC09d GFM. First, a detailed analysis of pore gas data at MDA L revealed that a pinchout of Tshirege unit 1v was inadvertently included in the WC09b model. This error was the result of incorporating into the gridding process the terminal depth of a borehole completed in Tshirege unit 1v rather than the contact for unit 1v observed in this borehole. A more significant error was discovered during the analysis of pore gas data at MDA G. Three angled boreholes located near the center of Area G were treated as vertical in the FY09 and WC09b GFMs. The contact information from one of these, borehole 54-24363, was primarily responsible for the inference of a "paleochannel" in the surface of the Cerros del Rio basalts at this location in the WC09b GFM (Figure I-6). Another borehole, 54-24368 had smaller but noticeable impacts on the basalt surface. Correcting the orientations of these boreholes caused the elevations of all observed contacts to increase and eliminated the localized depressions in the corresponding grids. This change smoothes and raises the contour surface of the basalt in the vicinity of borehole 54-24363, which is located near the center of the inset shown in Figure I-14.

Slight adjustments were made to the iterative gridding process used to interpolate the data for each layer. For the WC09b GFM, the LANL FY09 isopach contours were incorporated into the second gridding pass in a multistep process to impose the shape of the LANL FY09 model on the WC09b GFM. In the WC09d model, geologic unit thicknesses were calculated from contacts in boreholes and used to supplement the isopach contours in this gridding pass to reduce extrapolation issues and to incorporate new data that might differ from the original FY09 isopach inferences. In addition, the resolution of the final grids representing each layer was reduced to 61 m (200 ft) from the original 15 m (50 ft) used in the WC09b model. The resolution was reduced in this model because LANL geologists speculate that some of the variability observed in clustered borehole data collected within TA-54 may be caused by improper contact identification for some of the Tshirege units. Honoring all of these variable data yields highly irregular surfaces and may cause potentially significant extrapolation problems near the edges of the mesas. Lowering the resolution effectively produces a moving average of the data that yields undulations where multiple data points suggest that a deflection is real, but smoothes the surface in areas where one or two data values are inconsistent with neighboring points.

The differences between the WC09b and WC09d GFMs are most noticeable in the mapped thicknesses of the Otowi Member and the underlying Cerros del Rio basalts (Figure I-15). The thicknesses of these units change by as much as 23 and 38 m (75 and 125 ft), respectively, near the center of the disposal site; for all other layers, changes in thickness are less than 7.6 m (25 ft). A raised basalt surface and corresponding thinner tuff units near the center of the site will most likely result in decreased travel times for waste disposal region 3.

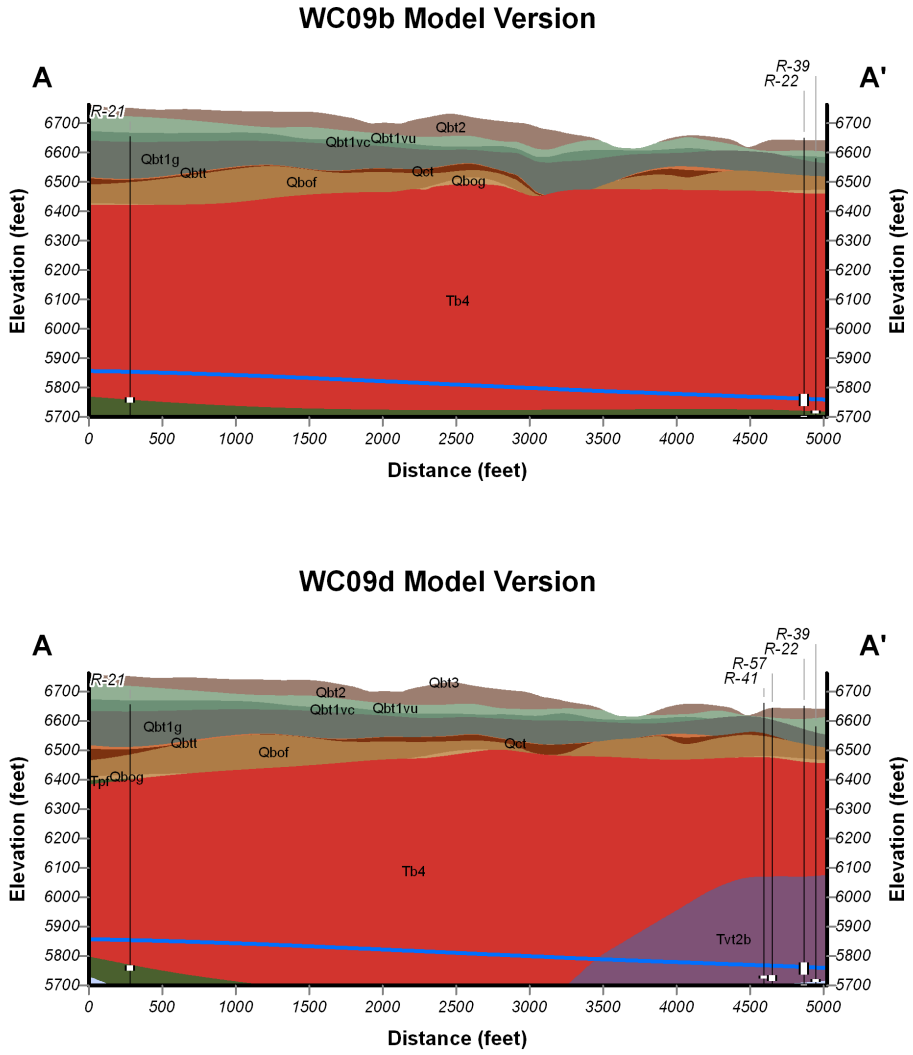

Figure I-15
Comparison of WC09b Model Cross Section to WC09d Model Cross Section

I.6 References

Ball, T., M. Everett, P. Longmire, D. Vaniman, W. Stone, D. Larssen, K. Greene, N. Clayton, and S. McLin, 2002, *Characterization Well R-22 Completion Report*, Los Alamos National Laboratory Report LA-13893-MS.

Cole, G., D. Broxton, S. Reneau, and D. Vaniman, 1997. *Revised Site-Wide Geologic Model for Los Alamos National Laboratory (FY97)*, Los Alamos National Laboratory Report LA-UR-00-2057, Los Alamos, New Mexico.

Cole, G., D. Broxton, S. Reneau, D. Vaniman, R. Warren, and G. WoldeGabriel, 1998. *Revised Site-Wide Geologic Model for Los Alamos National Laboratory (FY98)*, Los Alamos National Laboratory Report LA-UR-00-2058, Los Alamos, New Mexico.

Cole, G., J.W. Carey, L. Burnette, and T. Miller, 2006. *The 2005 Three-Dimensional Geologic Model of the Pajarito Plateau*, Los Alamos National Laboratory Report LA-UR-06-3060, Los Alamos, New Mexico.

Cole, G., A.M. Simmons, D. Coblentz, E. Jacobs, D. Koning, D. Broxton, F. Goff, D. Vaniman, G. WoldeGabriel, and J. Heikoop, 2010. *The 2009 Three-Dimensional Geologic Models of the Los Alamos National Laboratory Site, Southern Española Basin, and Española Basin*, Los Alamos National Laboratory Report LA-UR-09-3701, Los Alamos, New Mexico, April.

Los Alamos National Laboratory (LANL), 2008, *Performance Assessment and Composite Analysis for Los Alamos National Laboratory Technical Area 54, Area G, Revision 4*, Los Alamos National Laboratory Report LA-UR-08—6764, October.

Attachment II
Generation of the Three-Dimensional Computational Mesh for Los Alamos National Laboratory Technical Area 54, Area G

Authors:
Terry Miller, LANL EES-16
Carl Gable, LANL EES-16
Dave Coblentz, LANL EES-16
Philip Stauffer, LANL EES-16
Dan Strobridge, Weston Solutions, Inc.

II.1 Introduction

The development of the Area G flow and transport model requires input data from a number of sources, including water level and head distributions, hydrogeologic unit definitions, recharge and lateral flux distributions within the model domain, geographic information system (GIS) feature locations, and boundary conditions. Incorporation of these inputs into the flow model first requires the generation of a geologic framework and a computational mesh. The geologic framework model (GFM) and known features of the site, described in Attachment I of this report, are used to design a mesh for modeling. Once a computational mesh is formulated, the data inputs can be used to assign the properties to hydrogeologic units and features at node points throughout the mesh.

The computational mesh is designed to be used for coupled unsaturated and saturated zone calculations using the Finite Element Heat and Mass (FEHM) porous flow and transport code. The mesh encompasses an area much larger than the disposal facility to ensure that edge effects do not impact the calculations; its horizontal extents were chosen to match the cells of the Española basin site-scale regional aquifer computational model (Keating et al., 2003). The following criteria have been defined for this mesh.

- To utilize the FEHM particle tracking capability, the mesh must be a uniform, orthogonal finite difference mesh or a balanced octree mesh. The mesh must have adequate hydrogeologic layer resolution to provide accurate streamline particle-tracking solutions.
- Mesh resolution must capture the ground topography accurately enough to locate features in the model area. Features of interest include waste pits, truncated material layers along the mesa, fence boundaries, and the compliance boundary.
- The mesh must use the Weston-Cole 2009b (WC09b) GFM to define the hydrogeologic layers of the model.

Section II.2 discusses the input data used to develop the computational mesh, using the process that is described in Section II.3. Section II.4 compares the mesh presented here to the mesh used to conduct the 2005 groundwater pathway modeling.

II.2 Input Data

Input data for the computational mesh include a GFM based on many types of surface and subsurface data, and GIS surface elevation data. These data are transformed to a common coordinate system for use in creation of the computational mesh.

II.2.1. Geologic Framework Model

The geometry of the GFM was defined with a three-dimensional (3-D) geocellular model of the Pajarito Plateau study area, including Area G. The framework stratigraphy was formed through a process that creates a 3-D model from disparate input data. The process simplifies the large amounts of data available for locations near Area G and extrapolates from sparse data in areas away from the disposal facility. The WC09b GFM adopted for the modeling is a subset of the Los Alamos National Laboratory (LANL) Fiscal Year 2009 (FY09) GFM (Cole et al., 2010), updated to incorporate data collected in 2009. A detailed description of the GFM may be found in Attachment I of this report.

The WC09b GFM represents a significant update to the FY03 GFM used for the 2005 groundwater pathway modeling (Stauffer et al., 2005); the latter GFM was based on the FY98 GFM (Cole et al., 1998), and incorporated data collected through 2003. The most visible difference between the FY03 and WC09b GFMs is the increased thickness of the Cerros del Rio basalts and the modified extents of associated materials such as the Guaje Pumice (Qbog) and the Otowi flow unit (Qbof) of the Bandelier Tuff. New information used in the WC09b GFM for the Cerros del Rio reveals channeling and contour features that were not evident in the earlier GFM. New data also better constrain the location of the Otowi and Cerros del Rio contact, an area critical to understanding the flow system, and better characterize the contours found at the top of the basalt. Special attention was given to this area to be sure the computational mesh captures the updated shape of basalt.

The WC09b GFM was constructed with EarthVision® (Dynamic Graphics Inc., 2005); the EarthVision structure representing geologic units (zones) is used to interpolate hydrogeologic unit identification numbers to the flow and transport computational mesh. The numbers of mesh nodes used in the WC09b GFM to represent the hydrogeologic units found beneath Area G are shown in Table II-1, which also provides the numbers of nodes assigned to these units in the FY03 GFM. Figure II-1 shows a view of the top of the full mesh showing the hydrogeologic units interpolated from the FY03 GFM. Figure II-2 shows the same mesh with units interpolated from the newer WC09b GFM. In each of these figures, the lower portion of the mesh represents geologic units that include the Cerros del Rio basalts, other Cerros del Rio volcanic units, and a small segment of the Puye Formation. These units are modeled using hydrogeologic parameters that are representative of the Cerros del Rio, which is the primary unit located directly beneath the Bandelier Tuff units and the Guaje Pumice at Area G.

II.2.2 GIS Data

Data pertaining to the location of waste burial pits and trenches, the boundaries of Technical Area (TA-54) and Pajarito Road were extracted from the GIS database and utilized as input (see Figure 10, main report, for the locations of many of these features). The locations of pits are

defined by closed polygons. The locations of other features such as TA boundaries and roads are defined by open polylines. The GIS data have no elevation coordinates and are used to identify features on the mesh where the polygons and polylines intersect the top of the mesh representing the ground surface.

Table II-1
Correlation of Geology Represented in the Mesh based on the FY03 GFM and the WC09b GFM

Abbreviation	Hydrogeologic Unit Name and Description	FY03 GFM		WC09b GFM	
		ID	Number of Nodes	ID	Number of Nodes
OB	Soil, overburden	11	5,033	38	9,355
Qbt2	Bandelier Tuff (Tshirege Member), Unit 2	10	15,030	34	15,016
Qbt1vu	Bandelier Tuff (Tshirege Member), Unit 1, vitric portion	9	16,023	33	10,351
Qbt1vc	Bandelier Tuff (Tshirege Member), Unit 1, colonnade portion	8	10,078	32	10,904
Qbt1g	Bandelier Tuff (Tshirege Member), Unit 1, glassy	7	42,755	31	40,578
Qbtt	Bandelier Tuff (Tshirege), Unit 1, Tsankawi Pumice	6	1,065	30	920
Qct	Cerro Toledo interval	5	6,518	29	2,192
Qbof	Bandelier Tuff (Otowi Member), Ash Flow	4	63,522	28	49,336
Qbog	Bandelier Tuff (Otowi Member), Guaje Pumice Bed	3	11,471	27	11,088
Tpf	Puye Formation, fanglomerate	2	2,015	26	318
Tb4	Cerros del Rio basalts			25	225,393
Bottom	Lower unit layers	1	20,1941		
		Total	375,451	*Total*	375,451

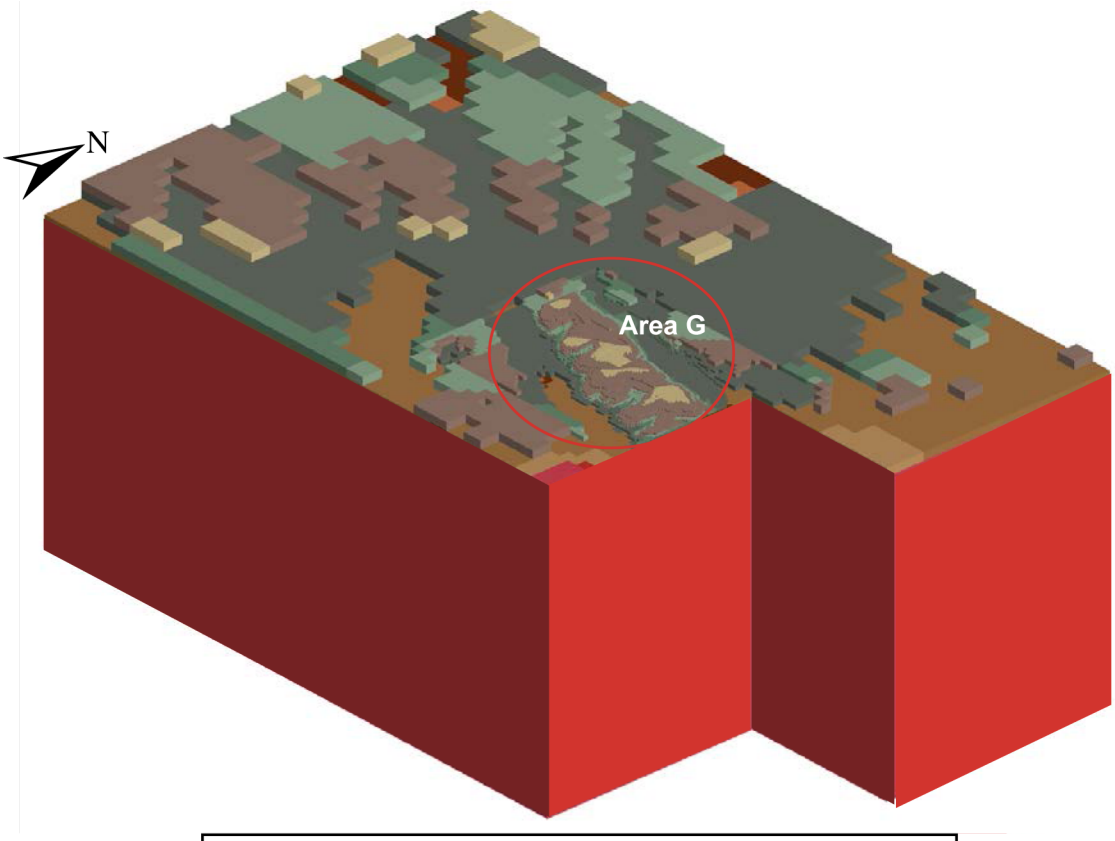

Geologic Unit	
OB	Soil, overburden
Qbt2	Bandelier Tuff (Tshirege Member), Unit 2
Qbt1vu	Bandelier Tuff (Tshirege Member), Unit 1, vitric portion
Qbt1vc	Bandelier Tuff (Tshirege Member), Unit 1, colonnade portion
Qbt1g	Bandelier Tuff (Tshirege Member), Unit 1, glassy
Qbtt	Bandelier Tuff (Tshirege), Unit 1, Tsankawi Pumice
Qct	Cerro Toledo Interval
Qbof	Bandelier Tuff (Otowi Member), Ash Flow
Qbog	Bandelier Tuff (Otowi Member), Guaje Pumice Bed
Tpf	Puye Formation, fanglomerate
Tb4	Cerros del Rio Basalts and other lower units

Figure II-1
Area G Computational Mesh Based on the FY03 GFM, Cut Through Domain at Compliance Boundary

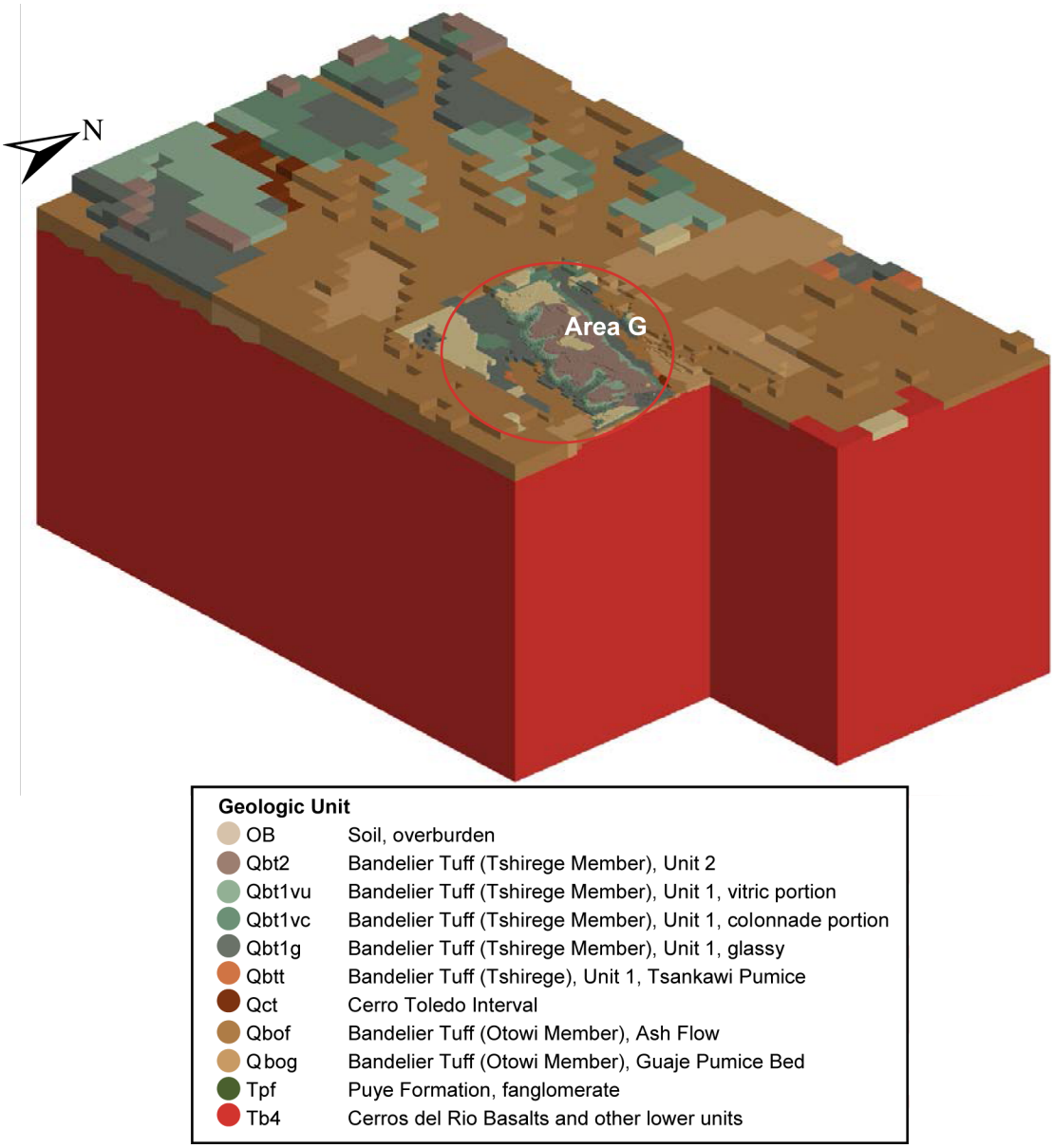

Figure II-2
Area G Computational Mesh Based on the WC09b GFM, Cut Through Domain at Compliance Boundary

II.2.3 Coordinate System

The computational mesh developed for the 2005 groundwater pathway modeling used the same coordinate system as did the Española basin site-scale regional aquifer computational model. However, this coordinate system is based on Stereo Polar (SP) meters, and conversion of the 2003 GFM to this system resulted in layer inversions and unaligned data. Because of these conversion inaccuracies, the mesh for the 2011 modeling was based on the same coordinate system as current GIS data, borehole data, and the GFM, all of which are recorded in State Plane feet or meters using the North American Datum 1983 (NAD 83). Table II-2 shows the boundary coordinates for the Area G computational mesh in State Plane NAD83 meters and the corresponding coordinates for the SP meters used in the 2005 modeling.

Table II-2
Boundary Coordinates for Area G Computations

Coordinate System	East-West (x) Boundary			North-South (y) Boundary			Vertical Boundary (z)		
	Min.	Max.	Diff.	Min.	Max.	Diff.	Min.	Max.	Diff.
State Plane NAD83 (m)	497781.39	502531.39	4750.00	534738.42	537613.42	2875.00	100.00	2150.00	2050.00
Stereo Polar (m)	18500.00	23250.00	4750.00	−133125.00	−130250.00	2875.00	100.00	2150.00	2050.00

II.3 Mesh Generation Process

The computational mesh for the 2011 Area G flow and transport model was developed using the Los Alamos Grid Generation software package (LaGriT) (George, 1997). LaGriT contains a comprehensive set of software macros that use hydrogeologic, GIS, and geometry data to build and optimize computational meshes. LaGriT is also used for mesh analysis and visualization work.

A structured mesh using orthogonal hexahedral elements was chosen for the Area G flow and transport model. The principal reason structured meshes are used for this work is to allow for the use of the streamline particle-tracking transport capability of FEHM. Although a structured mesh is not as flexible as an unstructured mesh in fitting complex geometry, tests have shown that a structured mesh provides accurate solutions as long as there is adequate resolution to represent the geometry of the different materials in each hydrogeologic layer. Moreover, there must be the capability to account for any large gradients present in the flow or transport model. Therefore the mesh needs appropriate resolution along the expected particle paths. Finally, high resolution is needed at the ground surface to correctly locate features such as waste disposal pits.

The following subsections detail the steps used to build the Area G computational mesh. These steps include extraction of the base mesh from the Española basin mesh, refinement of mesh

blocks in areas requiring further resolution, truncation of the mesh top by the topologic surface, optimization of the mesh, assignment of node properties, and the output of FEHM mesh and property files.

II.3.1 Mesh Extent and Resolution

A computational mesh generally evolves from relatively simple, large regions to smaller focus areas with added detail and resolution. For this updated model, a subset was extracted from the Española basin site-scale regional aquifer computational model and then refined to capture features near the waste disposal facility. The coordinates of the subset are listed in Table II-2; the mesh is illustrated in Figure II-3, which includes the eight waste disposal regions that are used in the groundwater modeling as particle release locations.

Table II-3 summarizes the vertical and horizontal resolution adopted for the mesh. The resolution of the mesh in the vertical dimension was selected to accurately represent the geology beneath the disposal facility, while limiting the increased computational resources needed to model the site (Miller et al, 2007). A fine resolution is used between the surface of the facility and the top of the basalts to capture the complexity of the site geology, with a progressively coarser resolution used at greater depths. Figure II-4 illustrates how mesh resolution changes with depth directly beneath Area G.

The Española model has regular orthogonal horizontal node spacing of 125 m (410 ft) in and around TA-54. The horizontal resolution of the mesh was increased in the vicinity of Area G to more accurately represent features (e.g., disposal units) at the facility (Table II-3). A polygon that outlines TA-54 was created using GIS data to define the southern fence line of TA-54; the remainder of the boundary was digitized manually (Figure II-5). Figure II-6 shows a close up of the mesh to illustrate the horizontal transition from low resolution (125 m [410 ft]) to the highest resolution (7.81 m [26 ft]) mesh in the immediate vicinity of Area G.

The top surface of the mesh is an irregular stair-stepped surface created by removing any element whose centroid (average value of the eight corner nodes of a hexahedral element) extends above a digital elevation model (DEM) of the land surface. Additional steps are taken to ensure the ground surface elevations allow for accurate locations of features such as the waste pits. The final truncated mesh has a stair-stepped top surface with some nodes above the DEM. Figure II-7 is an image of the top surface to illustrate how topography is represented in the mesh.

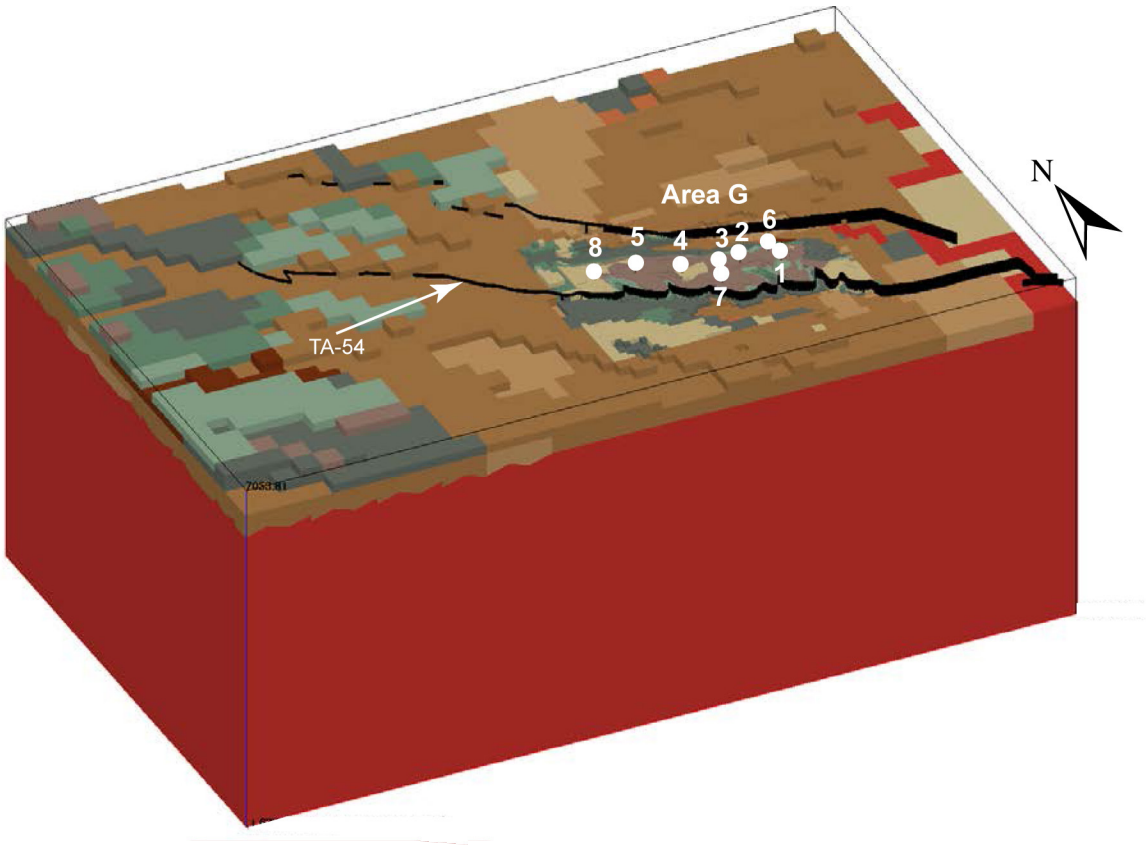

Geologic Unit	
OB	Soil, overburden
Qbt2	Bandelier Tuff (Tshirege Member), Unit 2
Qbt1vu	Bandelier Tuff (Tshirege Member), Unit 1, vitric portion
Qbt1vc	Bandelier Tuff (Tshirege Member), Unit 1, colonnade portion
Qbt1g	Bandelier Tuff (Tshirege Member), Unit 1, glassy
Qbtt	Bandelier Tuff (Tshirege), Unit 1, Tsankawi Pumice
Qct	Cerro Toledo Interval
Qbof	Bandelier Tuff (Otowi Member), Ash Flow
Qbog	Bandelier Tuff (Otowi Member), Guaje Pumice Bed
Tpf	Puye Formation, fanglomerate
Tb4	Cerros del Rio Basalts and other lower units

Figure II-3
Area G Computational Mesh Truncated by Topography, Extended Vertically below the Water Table, and Refined near Area G (based on WC09b GFM)

Table II-3
Spacing Used in the Area G Computational Mesh

Vertical Mesh Spacing			
Elevation of Zone (m above msl)	**Base Mesh (m)**	**Elevation of Zone (m above msl)**	**Refined Mesh (m)**
2075.00–2150.00 (truncated top)	50.00	2075.00–2150.00 (truncated top)	50.00
925.00–2075.00	37.50	2062.50–2075.00	12.50
		1900.00–2062.50	6.25
		1881.25–1900.00	9.38
		1862.50–1881.25	18.75
		925.00–1862.50	37.50
850.00–925.00	75.00	850.00–925.00	75.00
100.00 (bottom)–850.00	150.00	100.00 (bottom)–850.00	150.00

Horizontal Mesh Spacing	
Zone or Region	**Mesh (m)**
Area G	7.81
Transitional Region	15.62
	31.25
	62.5
Base mesh	125.00

msl = mean sea level

.

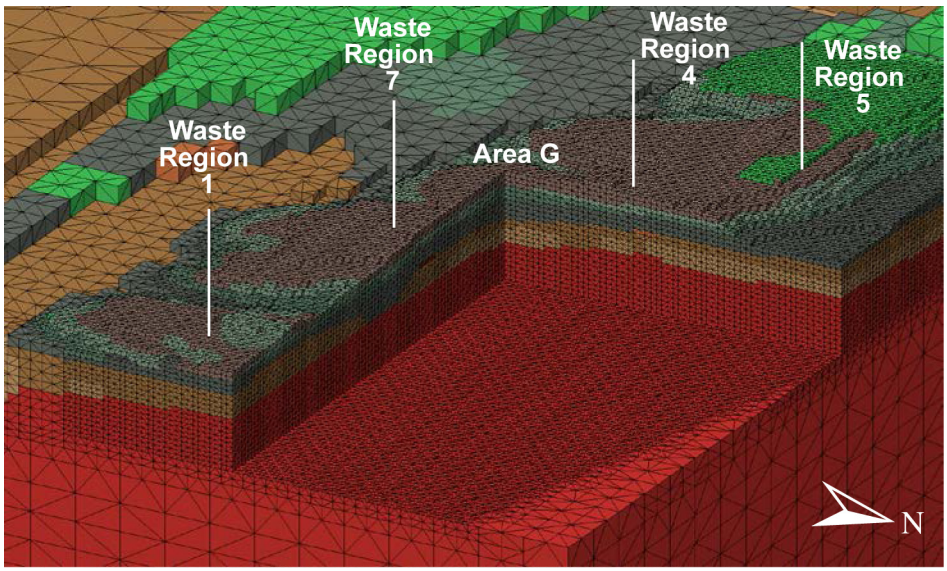

Geologic Unit	
OB	Soil, overburden
Qbt2	Bandelier Tuff (Tshirege Member), Unit 2
Qbt1vu	Bandelier Tuff (Tshirege Member), Unit 1, vitric portion
Qbt1vc	Bandelier Tuff (Tshirege Member), Unit 1, colonnade portion
Qbt1g	Bandelier Tuff (Tshirege Member), Unit 1, glassy
Qbtt	Bandelier Tuff (Tshirege), Unit 1, Tsankawi Pumice
Qct	Cerro Toledo Interval
Qbof	Bandelier Tuff (Otowi Member), Ash Flow
Qbog	Bandelier Tuff (Otowi Member), Guaje Pumice Bed
Tpf	Puye Formation, fanglomerate
Tb4	Cerros del Rio Basalts and other lower units

Figure II- 4
Cutaway of the Refined Portion of the Area G Mesh with Reduction in Vertical and Horizontal Spacing

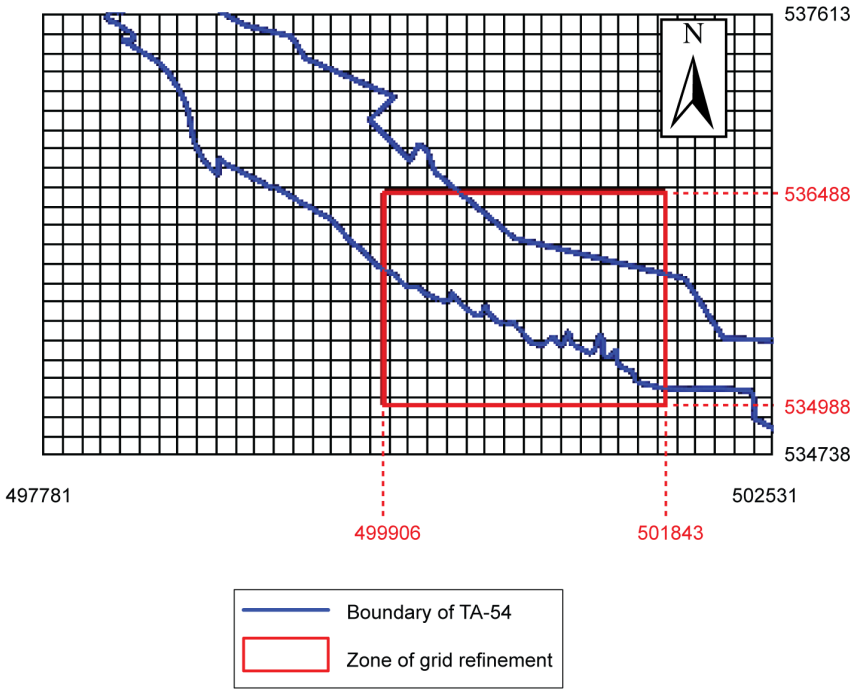

UTM grid coordinates based on State Plane NAD83; coordinates in red indicate the boundaries of the refined grid area.

Figure II-5
Extents of Entire Computational Mesh and Refined Mesh Near Area G

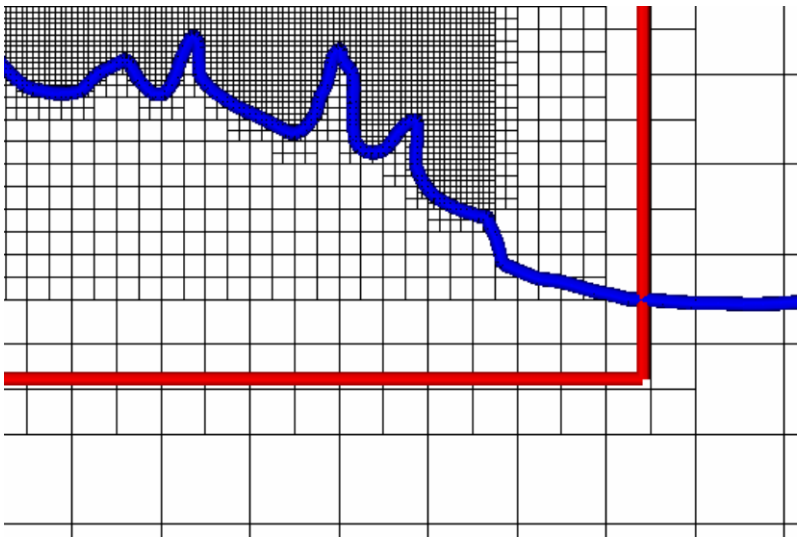

Figure II-6
Close-up of Southeast Portion of Refined Mesh Illustrating Transition in Mesh Resolution

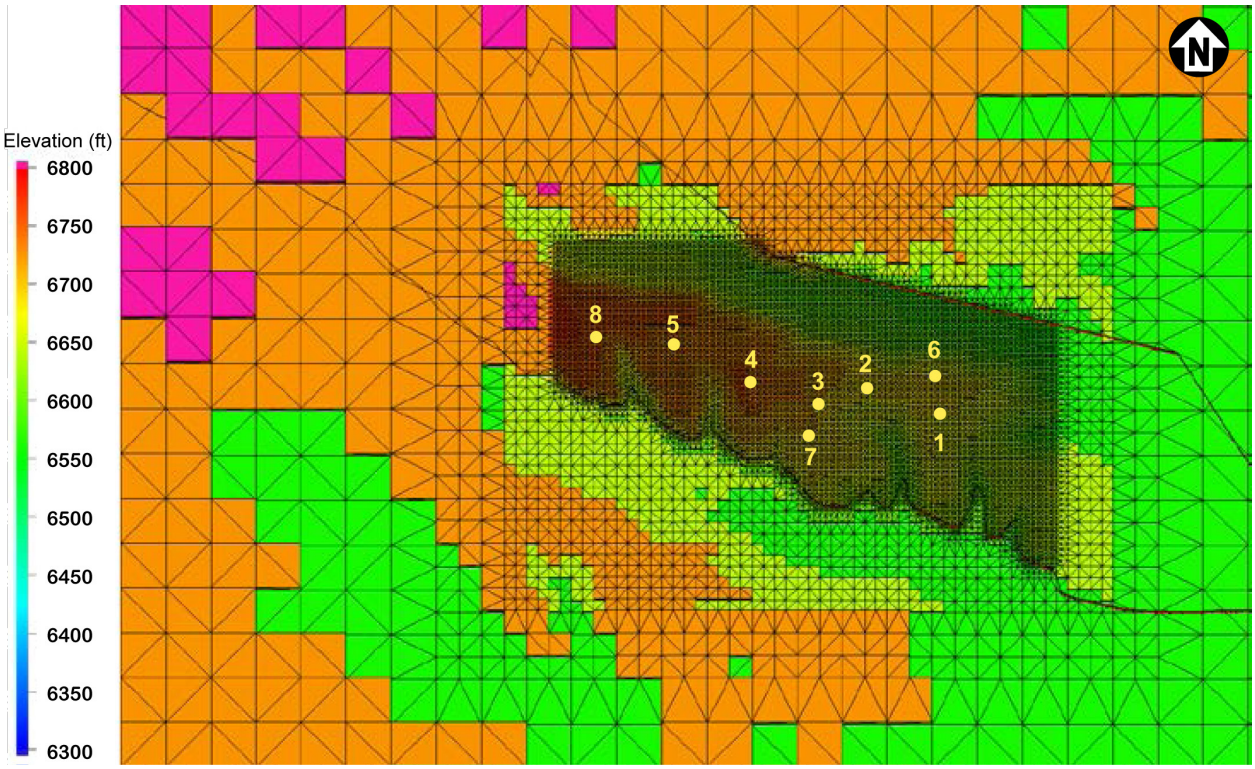

Figure II-7
Surface Elevation of the Computational Mesh

II.3.3 Mesh Properties

A physical hydrogeologic unit was assigned to each node in the computational mesh. The GFM EarthVision geologic structure represents the shape of each hydrogeologic layer. The structured mesh and the hydrogeologic features were imported into LaGriT and were used to identify the hydrogeologic layer designation for each node. Nodes were also identified as falling above or below the water table, and their association with any of the 35 geometrically defined pits was noted by identifying mesh nodes located within each of the pit polygons shown in Figure 10 of the main report.

II.3.4 Output

The control-volume finite element method is used in FEHM to obtain a numerical solution to the groundwater flow equation over the model domain. The mesh node distribution is prepared for use in FEHM: the mesh points are connected, forming a tetrahedral mesh based on a Delauney point connection algorithm that ensures Voronoi control volume discretization. Thus, the tetrahedral elements are also polyhedral Voronoi cells, each cell containing one node. These Voronoi cells are used for the groundwater flow equations, and mesh properties such as permeability and porosity are associated with the mesh nodes.

LaGriT was used to write the FEHM input files listed in Table II-4. The files include the mesh geometry, lists of nodes on external boundaries, and node lists sorted by hydrogeologic unit.

Table II-4
Mesh Generation Output Files for FEHM Modeling

tet_WC09_material.zone	FEHM zone list format for each hydrostratigraphic unit as defined from the WC09b GFM. Updated from the FY03 GFM.
tet_WC09_outside.zone	FEHM zone list format for each face of the model (top, bottom, N, S, E, W). No change.
tet_WC09_outside.area	FEHM area format file with the vector area associated with each exterior node. No change.
tet_WC09_m.fehmn	FEHM 'coor' and 'elem' information for node coordinates and element connectivity. Converted from Stereo Polar to State Plane Meters NAD83.
tet_WC09.stor tet_WC09_unf_linux.stor	FEHM sparse matrix coefficients in ASCII and binary format for linux operating system. No change.
tet_WC09b.inp	For mesh visualization, AVS (Advanced Visual Systems) format graphic file. Updated from FY03 GFM.
tet_WC09b.gmv	For mesh visualization, GMV (General Mesh Viewer) format graphics file. Updated from FY03 GFM.

II.3.5 Mesh Quality

Quality checks were performed to ensure that the final mesh is correct. These include isopach thickness checks of the hydrogeologic surfaces. All nodes were automatically and visually checked to ensure that they were assigned the correct material identification corresponding to the GFM. Lists of the number of nodes associated with each material were compared with the GFM to confirm that the hydrogeologic units were identified correctly. Feature locations were checked against the GFM, and area maps and cross-sections through the mesh were compared to the cross-sections through the GFM.

The accuracy of the represented hydrogeologic units is related to the mesh spacing. The magnitude of the error within the refined area is less than the horizontal mesh block size of 7.8 m (26 ft). Away from the refined area, and beyond the area over which the mesh could influence particles released from Area G, the mesh blocks are large and represent the units only coarsely. Some reasonable mesh simplifications were made. Tshirege Member unit 3 does not occur in the model domain, therefore the few nodes tagged as Tshirege unit 3 during the unit identification process, were reassigned to Tshirege unit 2. Material unit designations below the Bandelier Tuff are currently not differentiated in the numerical modeling, so all layers below the Guaje Pumice were assigned to a single material (the Cerros del Rio basalts).

The horizontal extents of the mesh nodes were compared to the contour maps of each layer (Figures I-6 through I-14 in Attachment I) to ensure the mesh captures the unit layers in an acceptable fashion. This comparison was conducted using Figures II-8 through II-12.

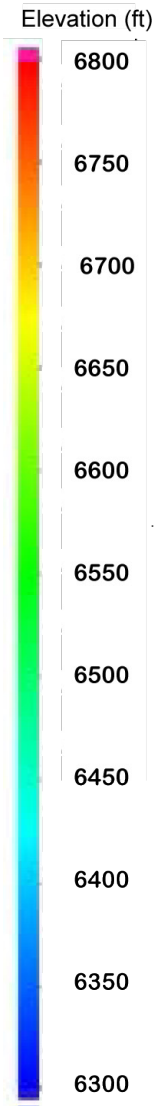

Figure II-8a. Overburden (OB)

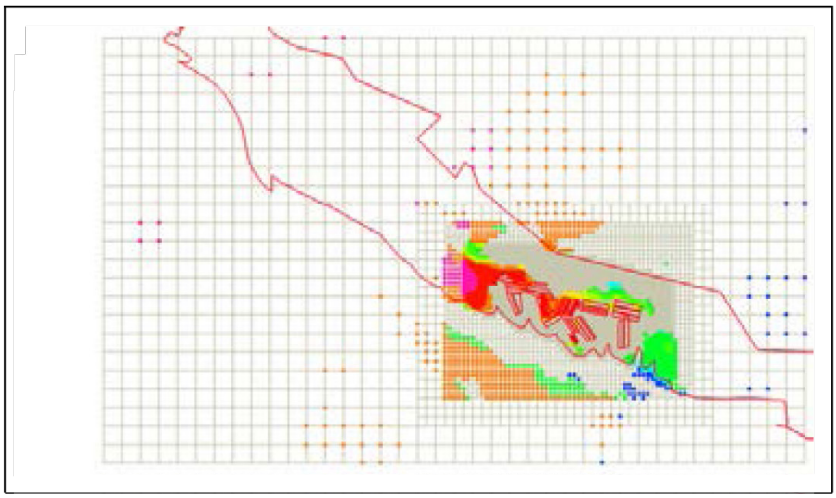

Figure II-8b. Bandelier Tuff, Tshirege Member, Unit 2 (Qbt2)

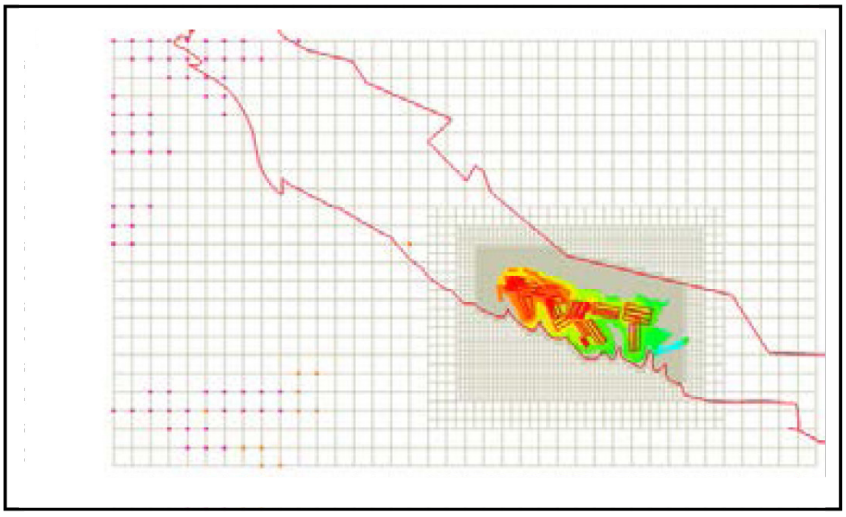

Figure II-8
Elevation of Mesh Nodes for the Top Surfaces of the Overburden and Bandelier Tuff, Tshirege Member Unit 2

Figure II-9a. Bandelier Tuff, Tshirege Member, Unit 1, vitric portion (Qbt1vu)

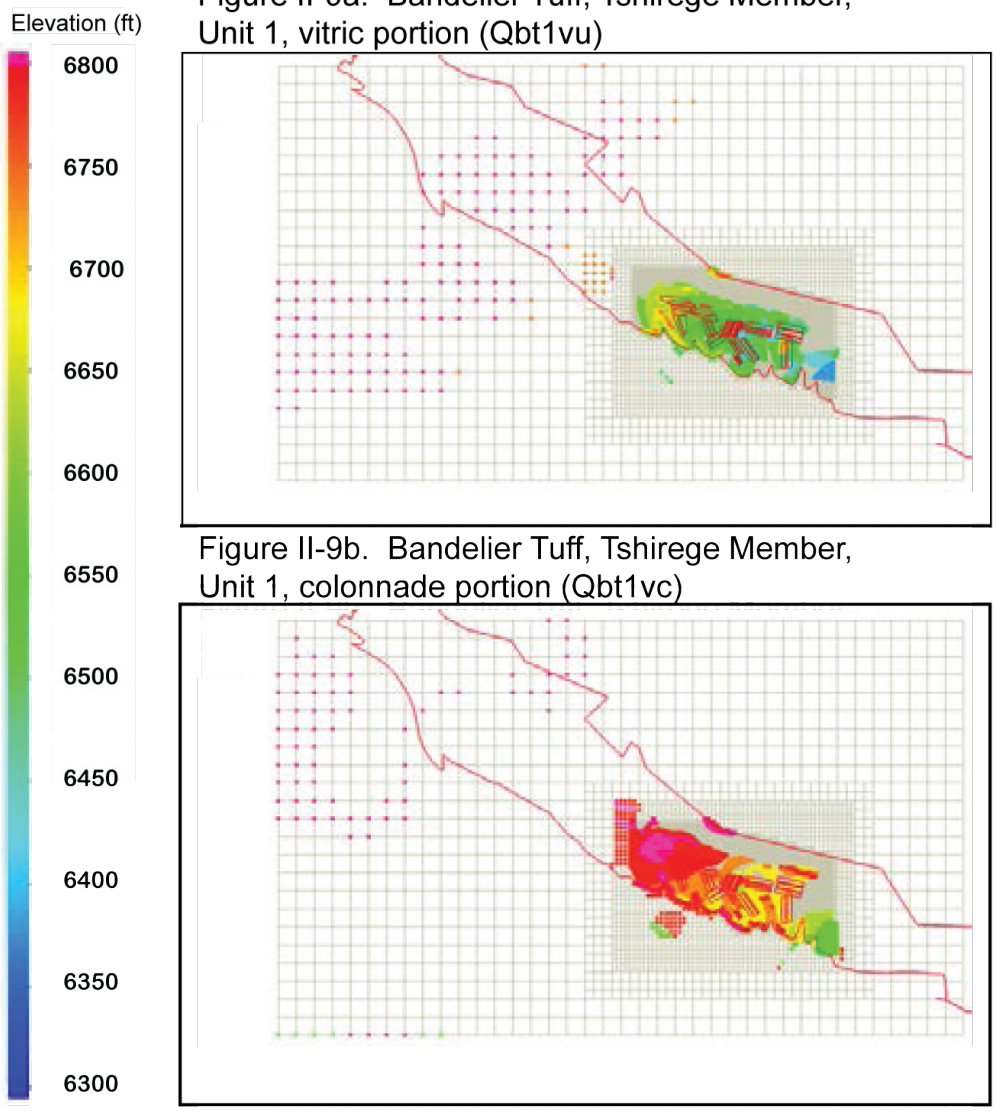

Figure II-9b. Bandelier Tuff, Tshirege Member, Unit 1, colonnade portion (Qbt1vc)

Figure II-9
Elevation of Mesh Nodes for the Top Surfaces of the Bandelier Tuff, Tshirege Member Unit 1vu and Unit 1vc

Figure II-10a. Bandelier Tuff, Tshirege Member, Unit 1, glassy (Qbt1g)

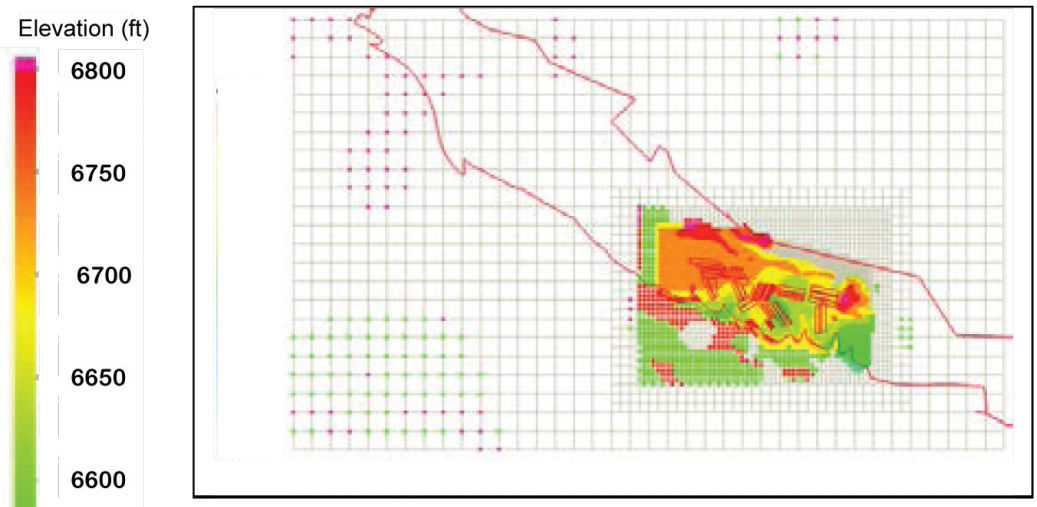

Figure II-10b. Bandelier Tuff, Tshirege Member, Tsankawi Pumice (Qbtt)

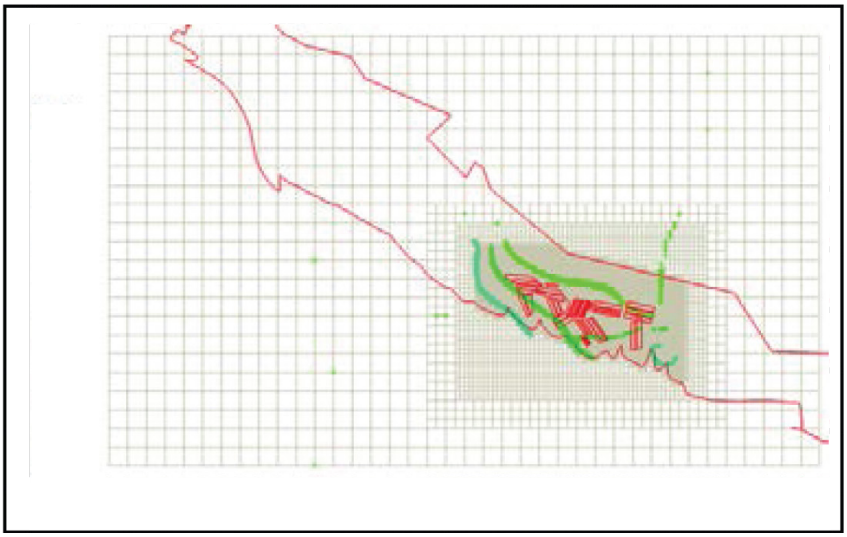

Figure II-10
Elevation of Mesh Nodes for the Top Surfaces of the Bandelier Tuff, Tshirege Member Unit 1g and Tsankawi Pumice

Figure II-11a. Cerro Toledo interval (Qct)

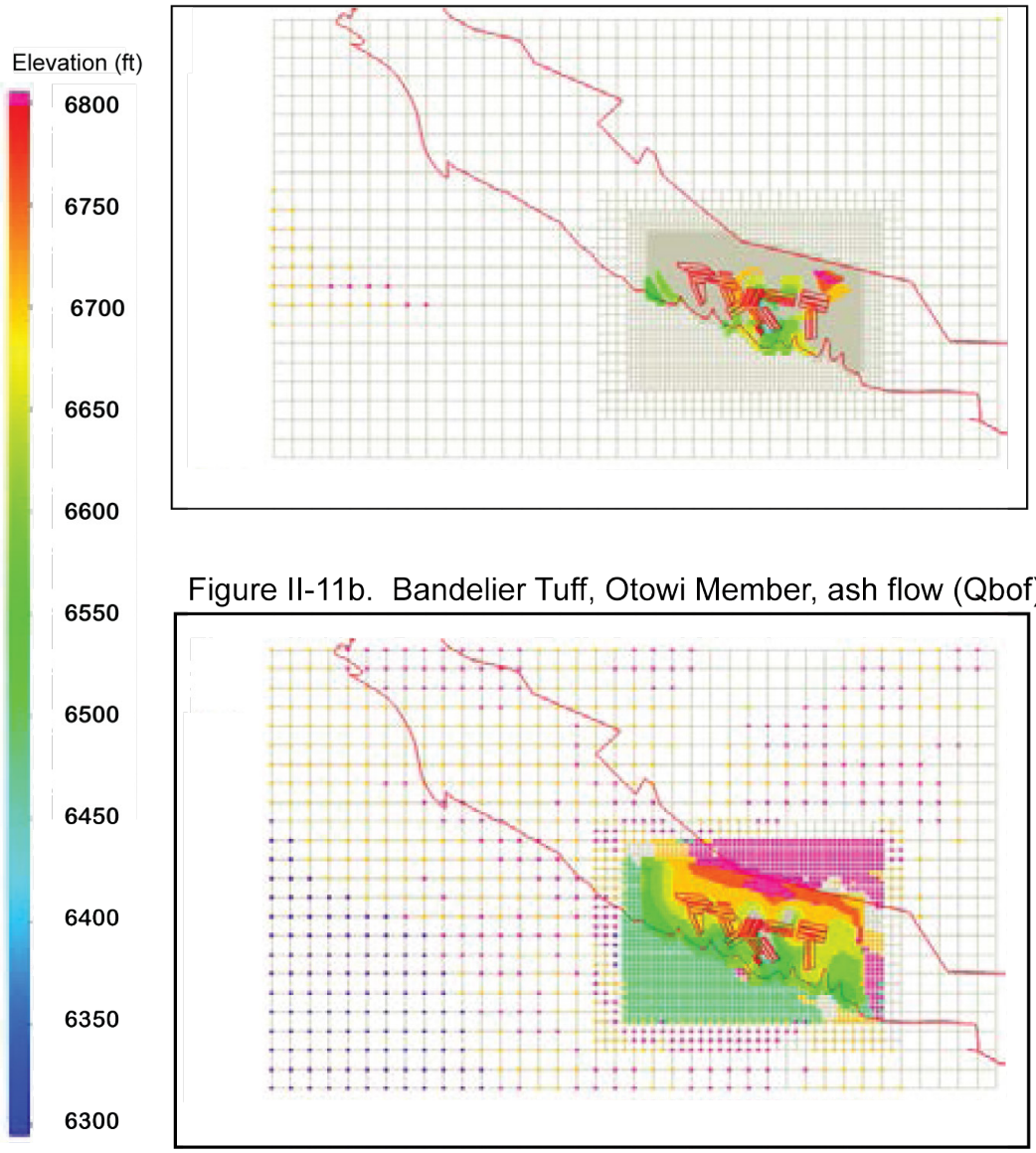

Figure II-11b. Bandelier Tuff, Otowi Member, ash flow (Qbof)

Figure II-11
Elevation of Mesh Nodes for the Top Surfaces of the Cerro Toledo Interval and Bandelier Tuff, Otowi Member

Figure II-12a. Bandelier Tuff, Otowi Member, Guaje Pumice Bed (Qbog)

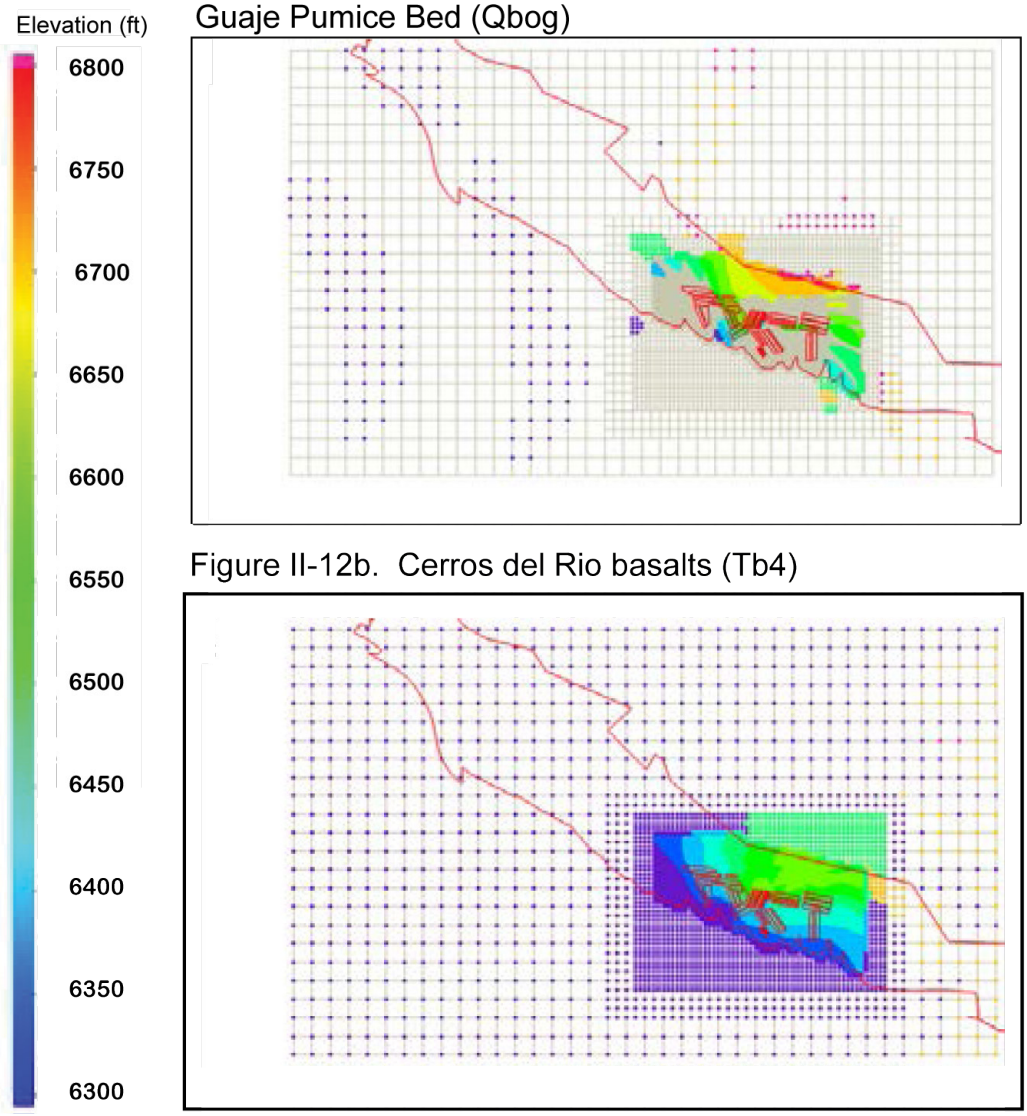

Figure II-12b. Cerros del Rio basalts (Tb4)

Figure II-12
Elevation of Mesh Nodes for the Top Surfaces of the Bandelier Tuff, Otowi Member Guaje Pumice Bed and Cerros del Rio Basalts

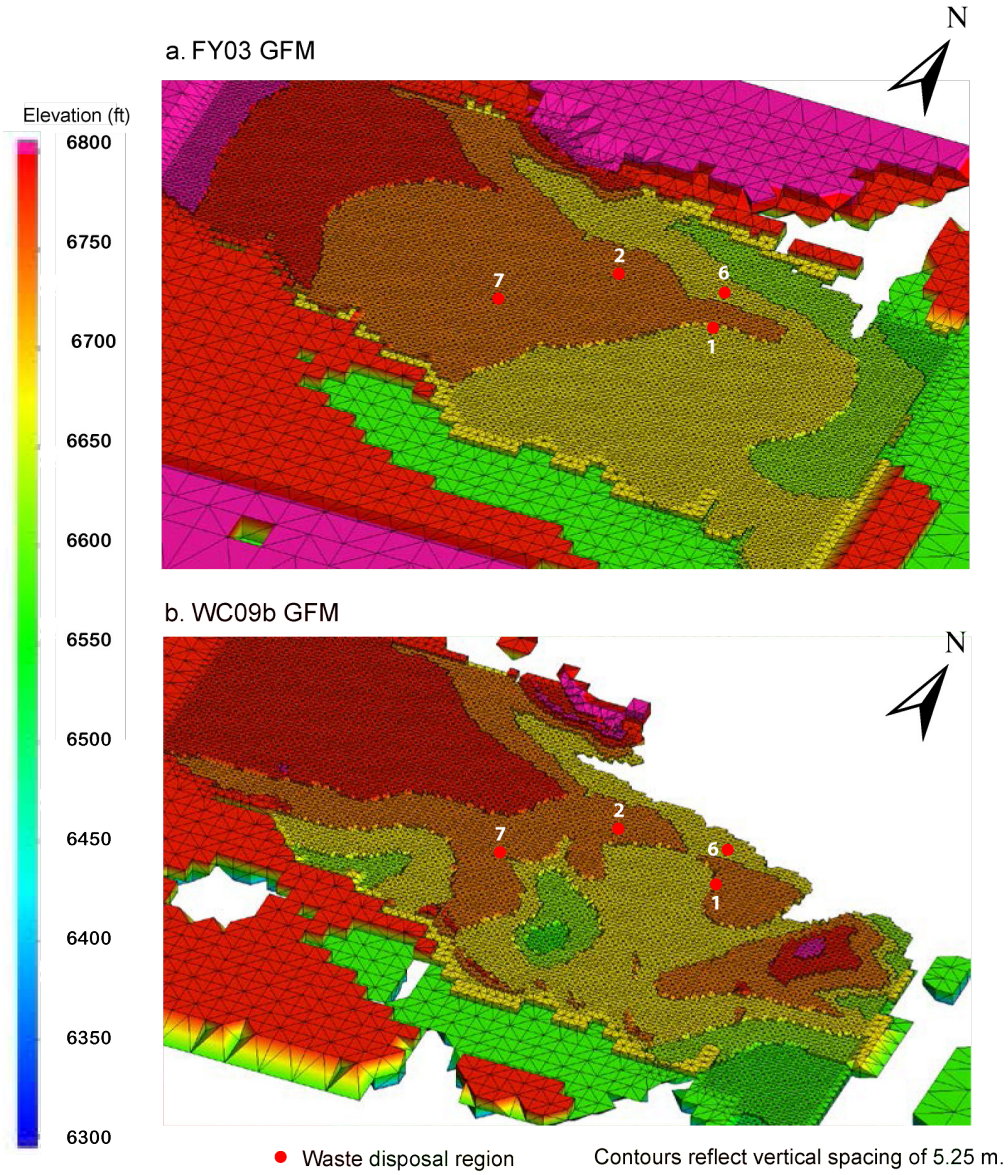

Figure II-13
Mesh Shape and Elevation of the Tshirege Unit 1g

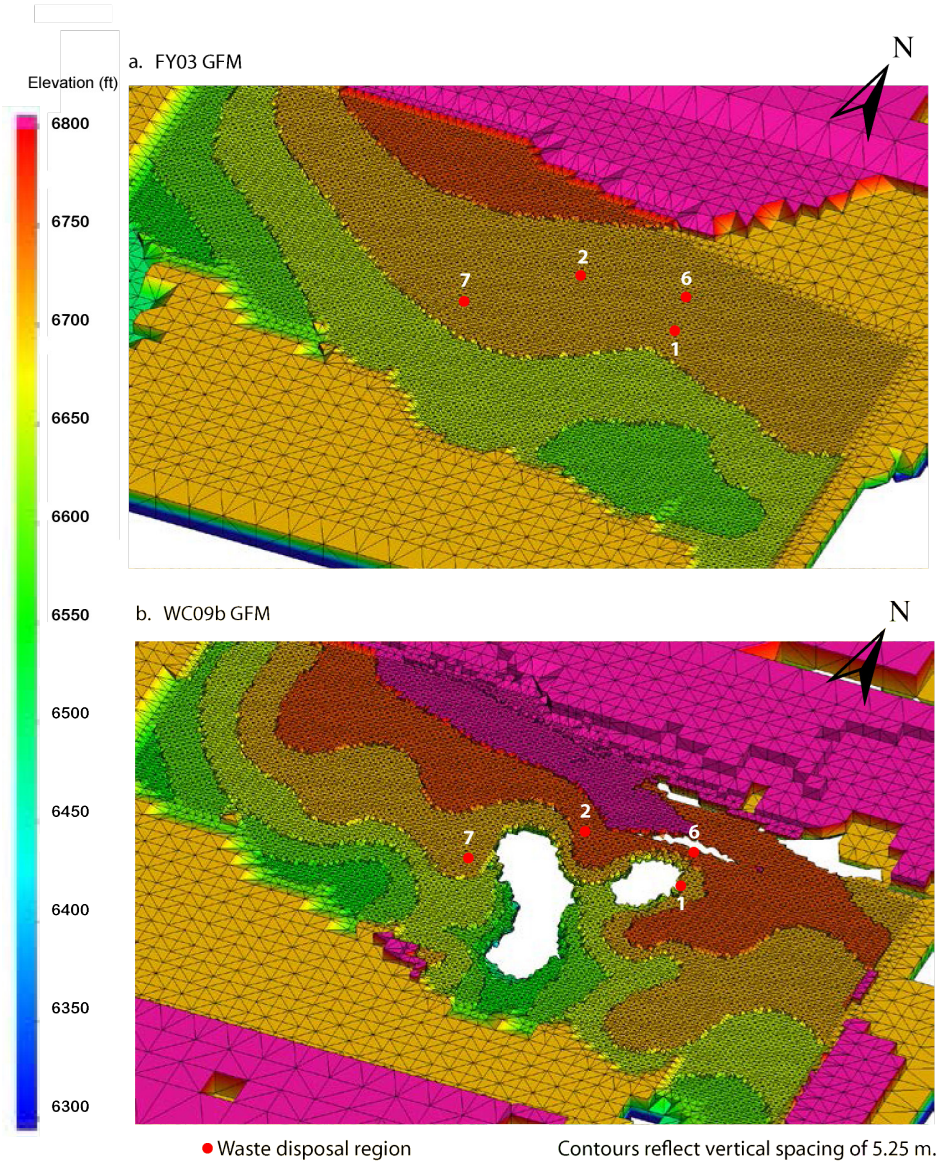

Figure II-14
Mesh Shape and Elevation of the Otowi Member

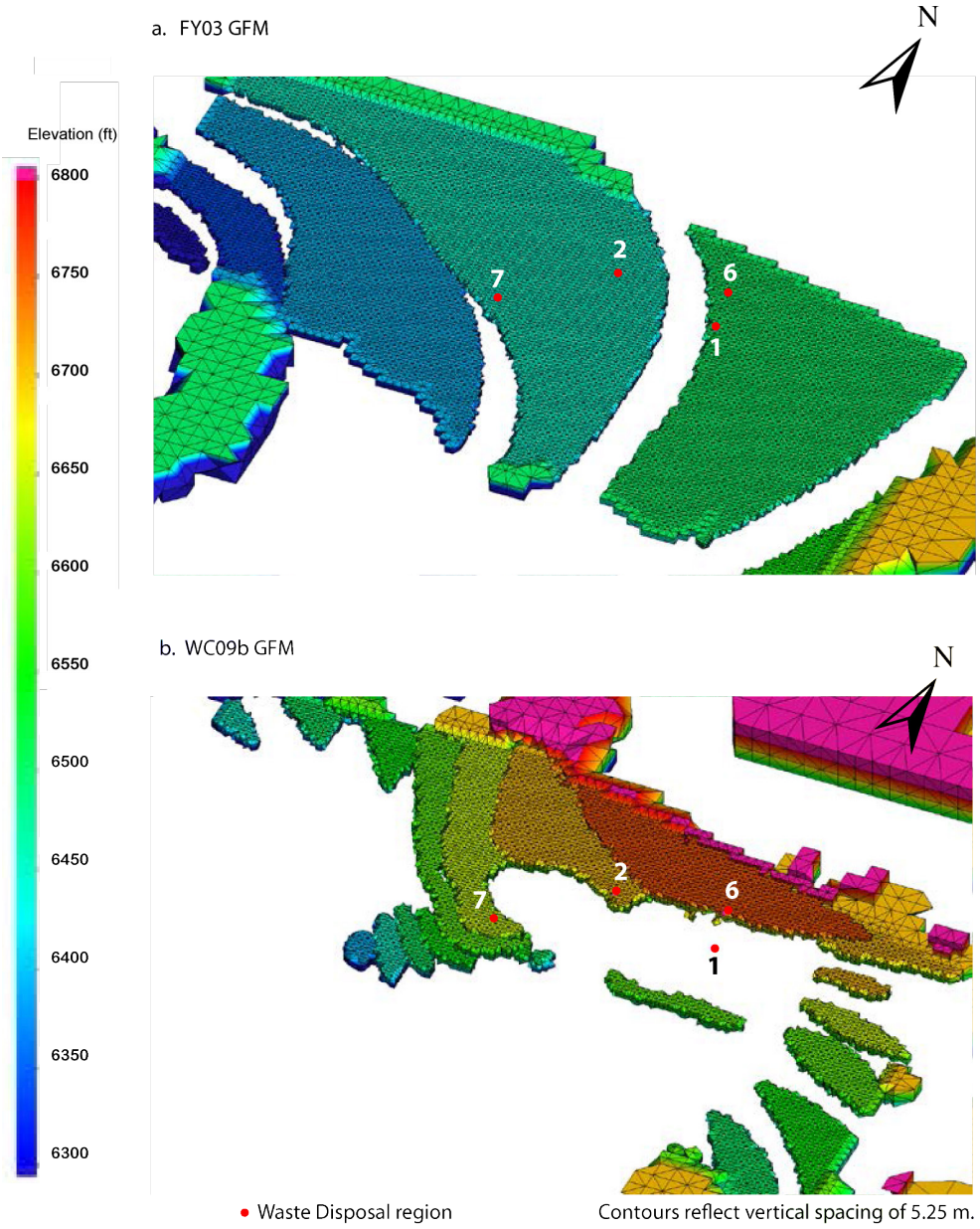

Figure II-15
Mesh Shape and Elevation of the Guaje Pumice Bed

a. FY03 GFM

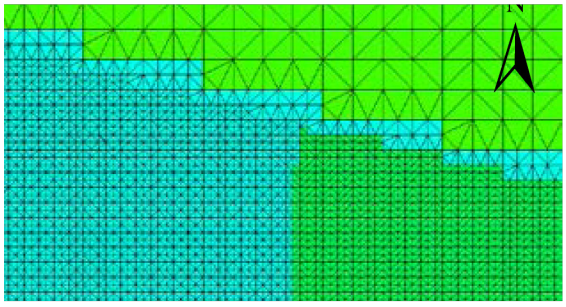

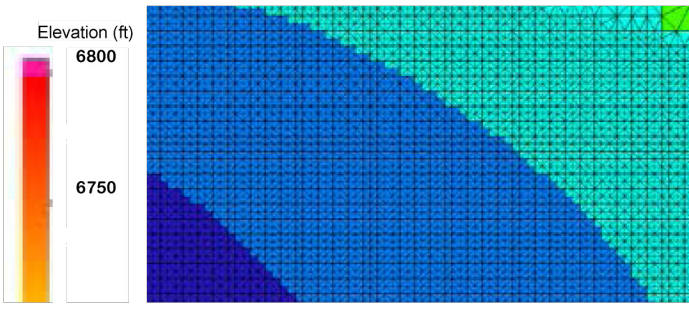

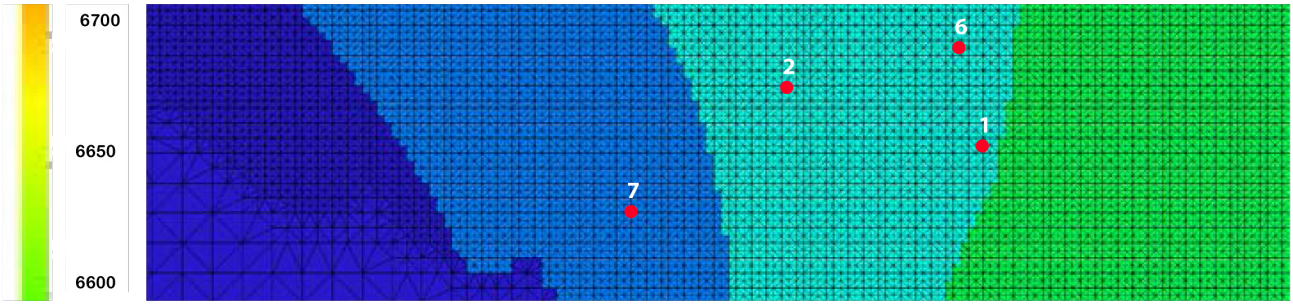

Figure II-16
Mesh Elevation of the Top of the Cerros del Rio Basalts

II.4 Comparison with Previous Mesh

As discussed in Attachment I, the greatest changes between the FY03 GFM and WC09b GFM occur at the top of the Cerros del Rio basalts upwards through Tshirege unit 1g. The two thickest units in the GFM, the Cerros del Rio basalts and the Otowi Member, exert control over the shapes of overlaying layers. The Cerros del Rio (Figure II-16) has increased thickness and its upper surface has a steep slope beneath the center of Area G.

Figures II-13 through II-16 show enlarged views of selected regions of the mesh below Area G for Tshirege unit 1g, the Otowi Member, the Guaje Pumice beds, and the Cerros del Rio basalts. The first three figures show the units in three dimensions; the mesh elements in these views are colored by elevation and allow the viewer to see the shape (thickness, extent, and slope) of each mesh layer. Figure II-16 is a top view showing element and node elevations of the upper surface of the Cerros del Rio basalts.

The mesh for the updated modeling shows thinning of the Otowi Member and the Gujae Pumice bed (Figures II-14 and II-15); discontinuities are present in both of these units, particularly where the thickness of the unit in the GFM is less than the finest mesh spacing of 6.25 m (20.5 ft). Tshirege unit 1g (Figure II-13) shows a thinning trend, but remains continuous below the entire waste repository.

Overall, the computational mesh developed using the WC09b GFM is expected to be a significant improvement over the mesh used in the 2005 modeling. It takes advantage of a large amount of well and borehole data collected between 2003 and 2009 and, as a result, is expected to more accurately represent the geologic heterogeneity in the vicinity of the disposal facility. However, the GFM and, hence, the computational mesh are likely to evolve in the future as additional information is collected at TA-54.

II.5 References

Cole, G., D. Broxton, S. Reneau, D. Vaniman, R. Warren, and G. WoldeGabriel, 1998. *Revised Site-Wide Geologic Model for Los Alamos National Laboratory (FY98),* Los Alamos National Laboratory Report LA-UR-00-2058.

Cole, G., A.M. Simmons, D. Coblentz, E. Jacobs, D. Koning, D. Broxton, F. Goff, D. Vaniman, G. WoldeGabriel, and J. Heikoop, 2010. *The 2009 Three-Dimensional Geologic Models of the Los Alamos National Laboratory Site, Southern Española Basin, and Española Basin*, Los Alamos National Laboratory Report LA-UR-09-3701.

Dynamic Graphics Inc., 2005, Website describing the EarthVision software: http://www.dgi.com/earthvision/evmain.html (accessed on March 13, 2012).

George, D., 1997, Unstructured 3D Grid Toolbox for Modeling and Simulation, Los Alamos National Laboratory Report LA-UR-97-3052, presented at the 1997 Workshop on Computational Electronics and Nanoelectronics, Urbana, Illinois, October 20-22.

Keating, E.H., V.V. Vesselinov, E. Kwicklis, E. and Z. Lu, 2003. "Coupling Basin- and Local-Scale Inverse Models of the Española Basin," *Groundwater*, Vol. 41, No. 2, pp. 200–211.

Miller, T., V. Vesselinov, P. Stauffer, K. Birdsell, and C. Gable, 2007. "Integration of Geologic Frameworks in Meshing and Setup of Computational Hydrogeologic Models, Pajarito Plateau, New Mexico," New Mexico Geologic Society Guidebook, 58th Field Conference, Geology of the Jemez Mountain III.

Stauffer P.H., H.S. Viswanathan, B.A. Robinson, C.W. Gable, G.L. Cole, D.E. Broxton, E.P. Srpinger, and T.G. Schofield, 2005, *Groundwater Pathway Model for the Los Alamos National Laboratory Technical Area 54, Area G,* Los Alamos National Laboratory Report LA-UR-05-7393.

Attachment III
Statistical Description of Vadose-Zone Hydrologic Properties for the Los Alamos National Laboratory TA-54, Material Disposal Area G Groundwater Pathway Model

Author:
Everett P. Springer

III.1 Introduction

Variability in unsaturated-zone flow properties is an important consideration in understanding uncertainty in the travel times of contaminants through the subsurface. Simulation is the most readily available approach to assess flow and transport of contaminants in the unsaturated zone at TA-54 because flow processes are slow and large events are episodic, both of which make measurement difficult. This analysis provides statistical descriptions of the unsaturated-zone hydrologic properties at Technical Area (TA) 54 at Los Alamos National Laboratory (the Laboratory or LANL), using available data to support MDA G groundwater modeling efforts.

III.2 Methods

The methodology used to conduct the statistical analysis of TA-54 hydrologic properties is presented below. Section III.2.1 discusses the sources of data used in the investigation and Section III.2.2 describes the data analyses undertaken.

III.2.1 Data Sources

The data used in the TA-54 investigation were obtained from two sources. The first was a detailed study by Rogers and Gallaher (1995) on the hydrologic properties of Bandelier Tuff found at TA-54 and across the Laboratory. The second source was data from boreholes sampled at TA-54 after the Rogers and Gallaher (1995) report was completed. These data were reported by D.B. Stephens & Associates, Inc. (DBS&A) in two reports. The first report (DBS&A, 1995) presented data for borehole TA-54-G-5 (G-5), while the second (DBS&A, 1996) presented data for boreholes 54-501, 54-502, 54-503, 54-504, 54-1015, 54-1107, 54-1121, G-P38-HH3, and samples from an outcrop of the vapor-phase notch in Mortandad Canyon. The stratigraphy of borehole G-P38-HH3, a horizontal hole drilled from Pit 38, is provided in Puglisi and Vold (1995).

The Broxton and Reneau (1995) nomenclature was used to define the geologic units for the Bandelier Tuff. The stratigraphic correlation provided by Broxton and Reneau was used to map the parameters from Rogers and Gallaher (1995) onto the geologic units.

III.2.2 Data Analysis

The water content and pressure head (retention) data for the boreholes listed above were fitted to the moisture characteristic equation developed by van Genuchten (1980) using the Retention Curve (RETC) computer code (van Genuchten et al., 1991). The water retention relation is described as follows:

$$S_e = \frac{\theta - \theta_r}{\theta_s - \theta_r} = \frac{1}{\left[1 + (\alpha h)^n\right]^m} \qquad 1$$

Where

S_e = effective saturation
θ = volumetric water content (cm^3/cm^3)
θ_r = residual volumetric water content (cm^3/cm^3)
θ_s = saturated volumetric water content (cm^3/cm^3)
h = pressure head (cm)
α = fitting parameter (cm^{-1})
n, m = fitting parameters with $m = 1 - 1/n$

Parameters for Equation 1 were estimated from parameter fitting using the RETC computer code, with the exception of the saturated water content (θ_s). Measured values were used for this parameter because of the limited number of data points for each retention curve. Parameters determined by Rogers and Gallaher (1995) using Equation 1 are included in this report. For a listing of all hydrologic properties and parameter values used for statistical analyses, by geologic unit and borehole, see *Annex IIIa*.

The hydrologic parameters for a geologic unit can also be estimated by the RETC computer code, by pooling data from the given geologic unit. This approach was used to produce the alternative estimates reported in Section III.3.4.

III.3 Results

This section provides the results of the statistical analysis. Section III.3.1 describes the distributions for parameters used for the Bandelier Tuff, Section III.3.2 provides descriptive statistics, and Section III.3.3 discusses correlation among the various parameters.

III.3.1 Distributions of Hydraulic Parameters

Figures III-1 through III-8 are normal probability plots for the saturated water content, residual water content, saturated hydraulic conductivity, and the van Genuchten fitting parameters α and n for unit 1v of the Tshirege Member of the Bandelier Tuff (Qbt 1v). This geologic unit has the largest number of samples so it was used to identify distributions of the unsaturated-zone parameters. By inference, the distributions identified for Qbt 1v should be used in combination with statistical parameters for the other geologic units.

The saturated water content of the Bandelier Tuff appears to follow a normal distribution (Figure III-1), as confirmed by the descriptive statistics presented in Section III.3.2. The

distribution for residual water content, shown on Figure III-2, is discussed in Section III.3.2. The *n* parameter (Figure III-3) appears to follow a normal distribution except for some tailing in the lower values. The α plot (Figure III-4) illustrates how a single value may affect a distribution. The value of α estimated on the basis of the sample taken at a 30-m (99-ft) depth from borehole 54-1107 is 0.29/cm, which is two orders of magnitude greater than the other values of this parameter. The moisture retention data for this sample differed substantially from the other samples, yielding a moisture retention curve that was essentially inverted. When this sample is removed from the analysis, the distribution of the remaining α values is skewed (Figure III-5). Figure III-6 shows the logarithmic transformation of α values (without the sample from borehole 54-1107), which appears to follow a normal distribution. A lognormal distribution has been suggested for saturated hydraulic conductivity (Nielsen et al. 1973; Freeze 1975). The application of a logarithmic transformation to this parameter (Figure III-7) resulted in a normal distribution (Figure III-8).

III.3.2 Descriptive Statistics

The geologic column included in the unsaturated zone beneath TA-54 consists primarily of the Bandelier Tuff and a portion of the underlying Cerros del Rio basalts. The Bandelier Tuff units that occur at TA-54 include the Tshirege Member (consisting here of units 2, 1v, the vapor-phase notch, and unit 1g), Tsankawi Pumice, Cerro Toledo interval, and Otowi Member. Samples from the surface soil and basalt layers at TA-54 are included in this analysis. Tables III-1 through III-8 present statistics for each unit, beginning with the surface soil.

The distribution statistics, skew and kurtosis, are included in the last two columns of Tables III-1 through III-8. Skewness is a measure of the symmetry of the distribution relative to a normal distribution (which has zero skewness). Kurtosis describes the peakedness or flatness of a distribution relative to a normal curve. The kurtosis value for a normal distribution is 3. Distributions with kurtosis values greater than 3 have a relatively greater concentration of the probability near the mean than a normal distribution. Conversely, distributions with a kurtosis less than 3 are flat with a greater portion of the probability away from the mean than a normal distribution. When the number of samples is limited (i.e., when there are fewer than 30 samples), these statistics do not provide very good estimates. For this study, unit 1v (Table III-3) is the only unit with more than 30 samples.

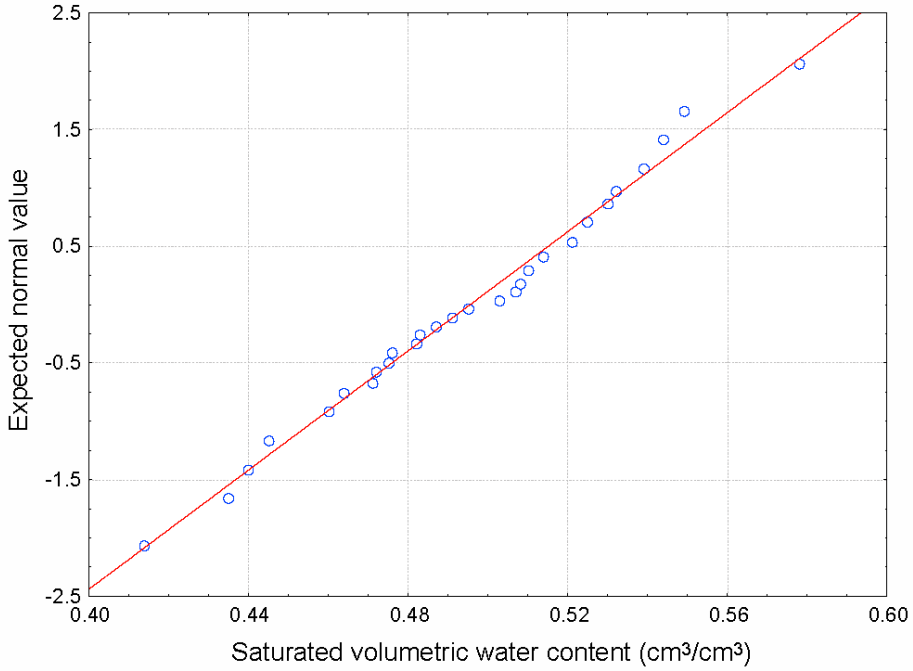

Figure III-1
Normal Probability Plot of Saturated Volumetric Water Content for Bandelier Tuff Tshirege Member Unit 1v

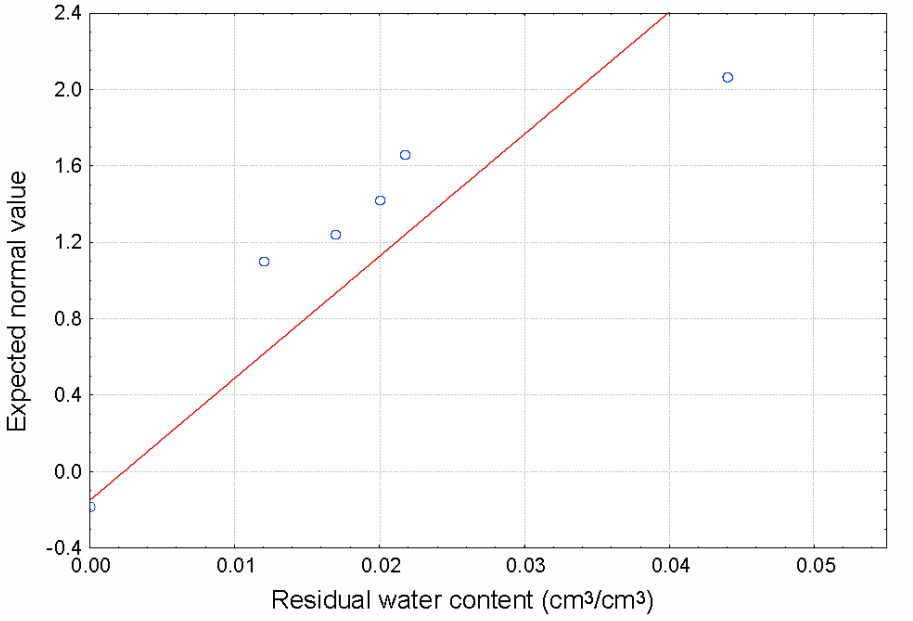

Figure III-2
Normal Probability Plot of Residual Volumetric Water Content for Bandelier Tuff Tshirege Member Unit 1v

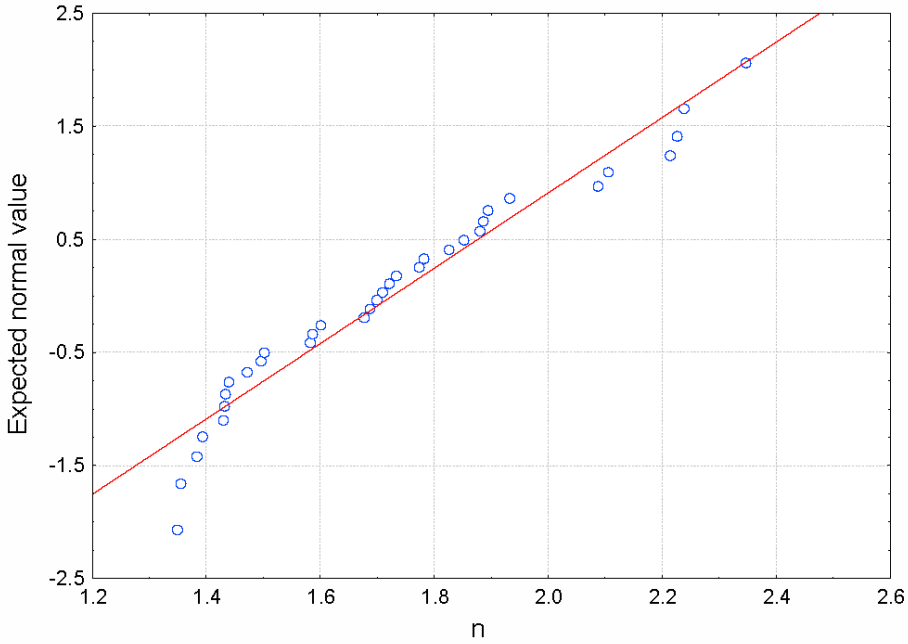

Figure III-3
Normal Probability Plot of van Genuchten *n* Parameter
for Bandelier Tuff Tshirege Member Unit 1v

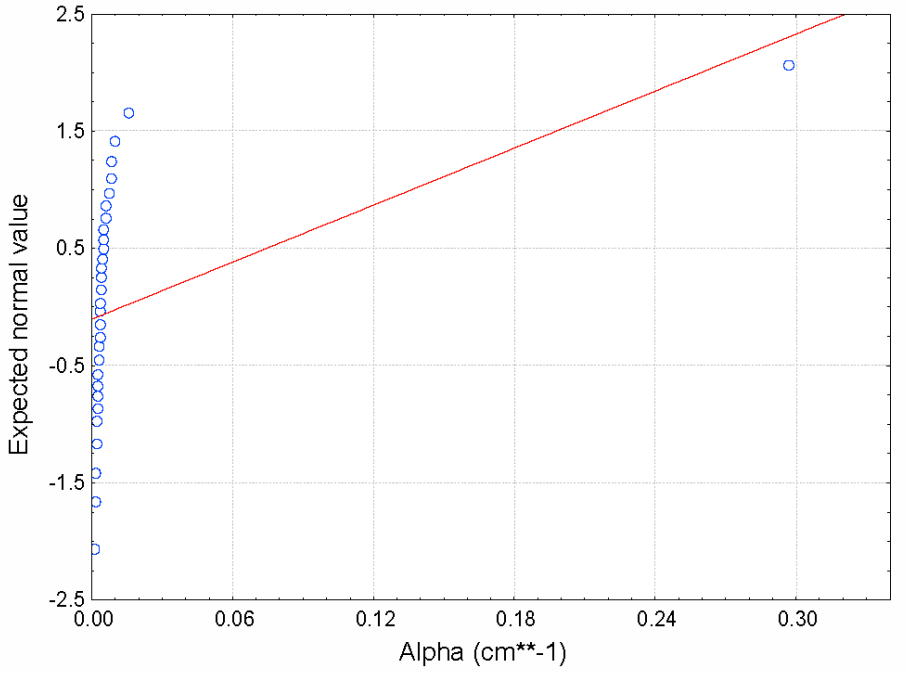

Figure III-4
Normal Probability Plot of van Genuchten α Parameter
for Bandelier Tuff Tshirege Member Unit 1v

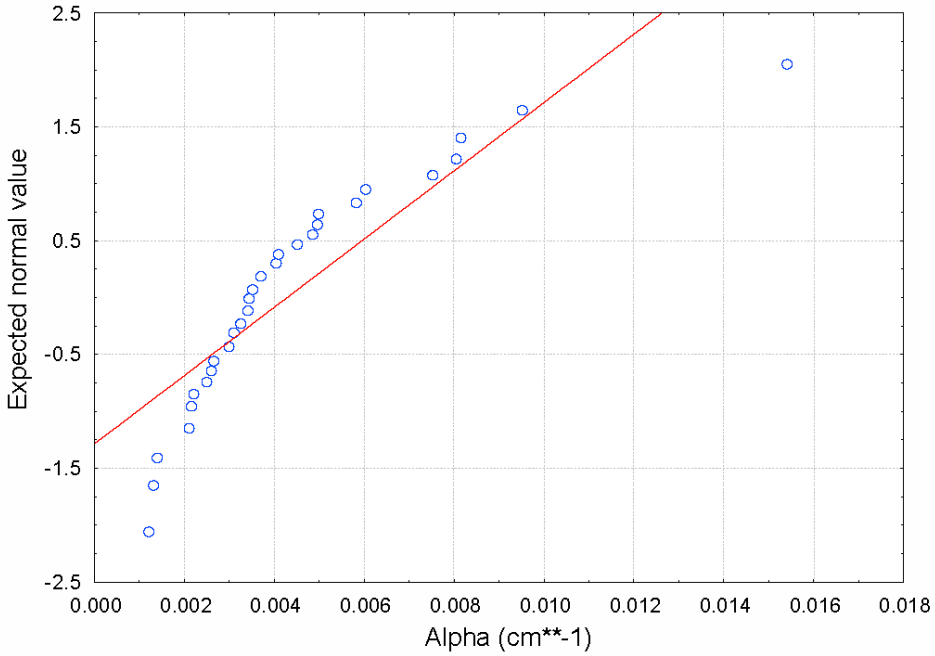

Figure III-5
Normal Probability Plot of van Genuchten α Parameter for Bandelier Tuff Tshirege Member Unit 1v without Data from Borehole 54-1107 (30-m depth)

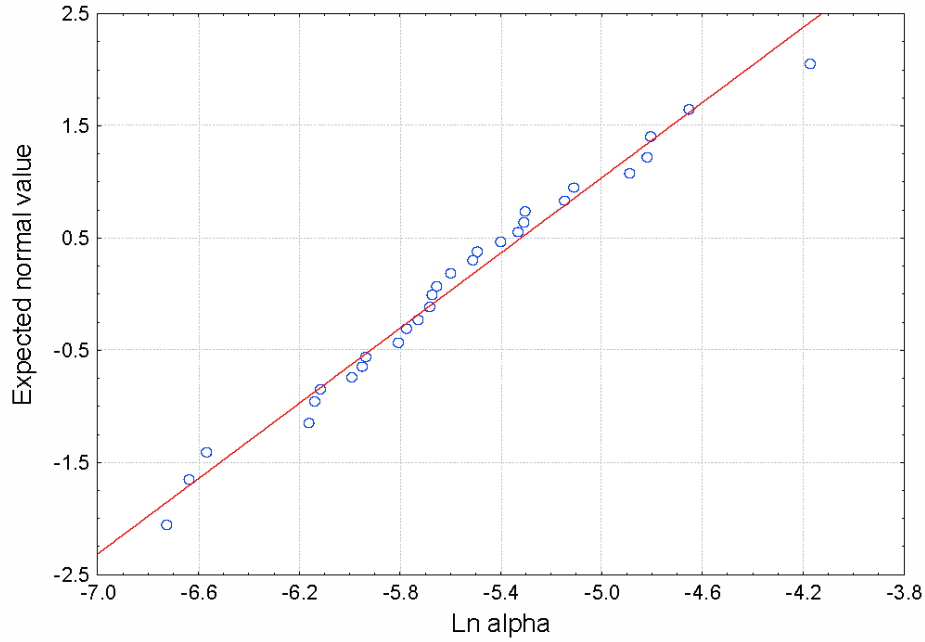

Figure III-6
Normal Probability Plot of Natural-Logarithm-Transformed van Genuchten α Parameter for Bandelier Tuff Tshirege Member Unit 1v without Data from Borehole 54-1107 (30-m depth)

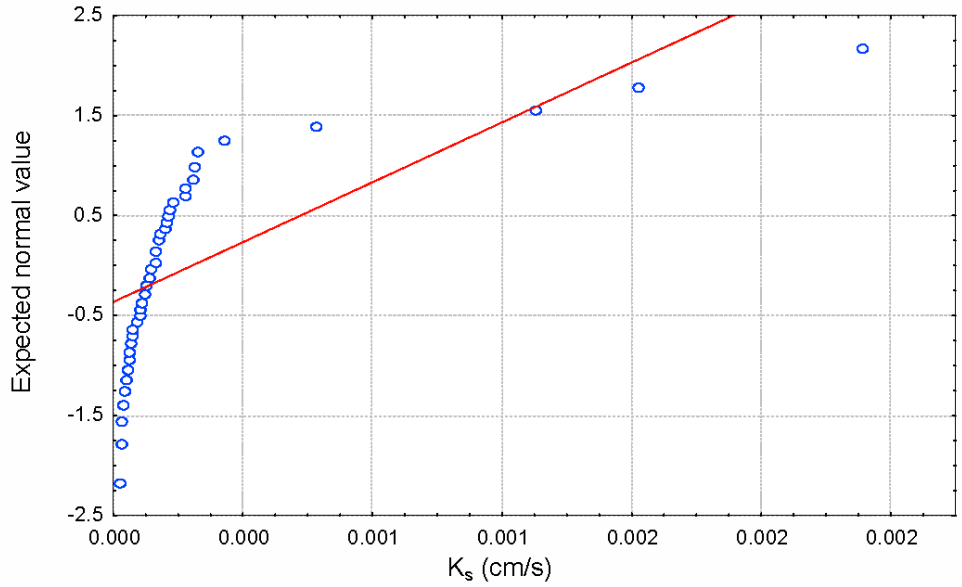

Figure III-7
Normal Probability Plot of Saturated Hydraulic Conductivity for Bandelier Tuff Tshirege Member Unit 1v

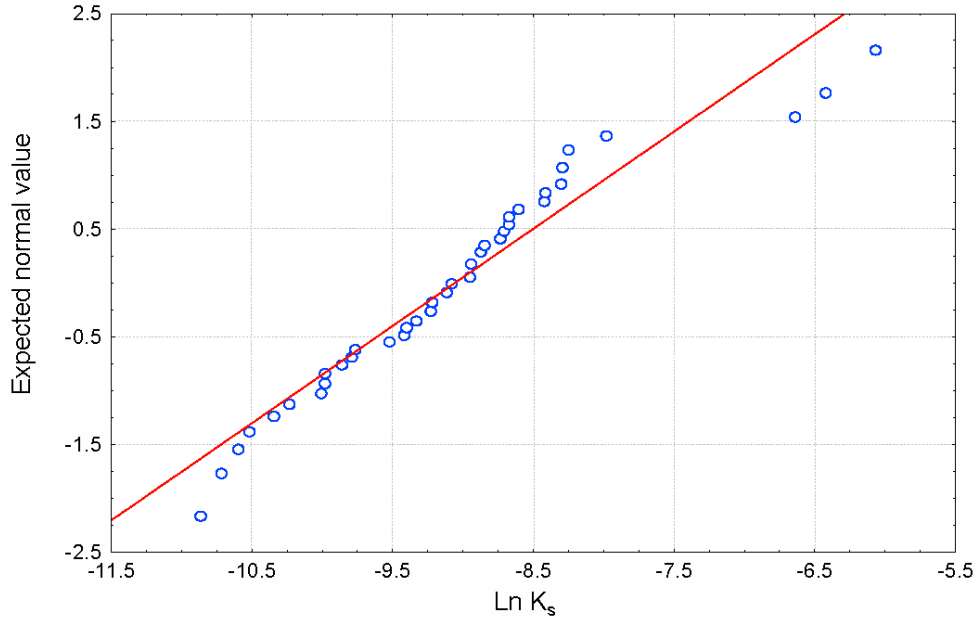

Figure III-8
Normal Probability Plot of Natural-Logarithm-Transformed Saturated Hydraulic Conductivity for Bandelier Tuff Tshirege Member Unit 1v

Table III-1
Statistics for Unsaturated Hydraulic Properties for Soil Unit

Variable	Unit	N	Mean	Standard Deviation	Median	Maximum	Minimum	Skew	Kurtosis
Bulk Density (ρ_b)	g/cm^3	4	1.5E+00	2.4E–02	1.5E+00	1.5E+00	1.4E+00	0.0E+00	–4.3E+00
Saturated Volumetric Water Content (θ_s)	cm^3/cm^3	4	4.1E–01	1,5E–02	4.1E–01	4.3E–01	4.0E–01	2.8E–01	–4.3E+00
Saturated Hydraulic Conductivity (K_s)	cm/s	4	4.7E–06	2.3E–06	5.4E–06	6.5E–06	1.4E–06	–1.7E+00	3.2E+00
Lognormal Saturated Hydraulic Conductivity (Ln K_s)	NA	4	–1.2E+01	7.2E–01	–1.2E+01	–1.2E+01	–1.4E+01	–1.9E+00	3.7E+00
Residual Volumetric Water Content (θ_r)	cm^3/cm^3	4	0.0E+00	0.0E+00	0.0E+00	0.0E+00	0.0E+00	---	---
van Genuchten Fitting Parameter *n*	NA	4	1.2E+00	1.9E–02	1.2E+00	1.3E+00	1.2E+00	–7.4E–01	1.8E+00
van Genuchten Fitting Parameter α	cm^{-1}	4	1.3E–02	4.0E–03	1.2E–02	2.0E–02	9.6E–03	7.6E–01	–1.8E+00
Lognormal α	NA	4	–4.4E+00	3.1E–01	–4.4E+00	–4.0E+00	–4.7E+00	5.3E–01	–3.0E+00

N = Number (of samples) *NA = Not applicable* *--- = Not estimated*

Table III-2
Statistics for Unsaturated Hydraulic Properties for Bandelier Tuff Tshirege Member Unit 2

Variable	Unit	N	Mean	Standard Deviation	Median	Maximum	Minimum	Skew	Kurtosis
Bulk Density (ρ_b)	g/cm^3	8	1.4E+00	7.0E–02	1.4E+00	1.5E+00	1.3E+00	–2.0E–02	–1.9E+00
Saturated Volumetric Water Content (θ_s)	cm^3/cm^3	8	4.1E–01	4.0E–02	4.2E–01	4.6E–01	3.7E–01	2.1E+00	5.8+00
Saturated Hydraulic Conductivity (K_s)	cm/s	17	3.4E–04	3.8E–04	2.2E–04	1.6E–03	2.7E–05	2.6E+00	8.4E+00
Lognormal Saturated Hydraulic Conductivity (Ln K_s)	NA	17	–8.5E+00	1.1E+00	–8.4E+00	–6.4E+00	–1.1E+01	–3.0E–01	–4.8E–01
Residual Volumetric Water Content (θ_r)	cm^3/cm^3	8	1.0E–01	1.3E–02	6.0E–03	3.8–02	0.0E+00	1.4E+00	1.9E+00
van Genuchten Fitting Parameter *n*	NA	8	2.1E+00	5.1E–01	2.0E+00	3.0E+00	1.5E+00	0.8E+00	–3.8E–01
van Genuchten Fitting Parameter α	cm^{-1}	8	6.0E–03	4.0E–03	6.0E–03	1.5E–02	1.9E–03	1.5E+00	3.0E+00
Lognormal α	NA	8	–5.4E+00	7.0E–01	–5.1E+00	–4.2E+00	–6.3E+00	0.01E+00	–6.9–01

N = Number (of samples) *NA = Not applicable*

Table III-3
Statistics for Unsaturated Hydraulic Properties for Bandelier Tuff Tshirege Member Unit 1v

Variable	Unit	N	Mean	Standard Deviation	Median	Maximum	Minimum	Skew	Kurtosis
Bulk Density (ρ_b)	g/cm^3	36	1.17E+00	9.0E–02	1.18E+00	1.32E+00	9.3E–01	–7.0E–01	1.3E–01
Saturated Volumetric Water Content (θ_s)	cm^3/cm^3	33	4.9E–02	4.0E–02	5.0E–01	5.8E–01	4.1E–01	–6.0E–02	–4.5E–01
Saturated Hydraulic Conductivity (K_s)	cm/s	43	2.35E–04	4.40E–04	1.13E–04	2.31E–03	1.90E–05	3.73E+00	1.409E+01
Lognormal Saturated Hydraulic Conductivity (Ln K_s)	NA	43	–9.06E+00	1.04E+00	–9.09E+00	–6.07E+00	–1.087E+01	8.3E–01	1.50E+00
Residual Volumetric Water Content (θ_r)	cm^3/cm^3	33	3.0E–03	9.0E–03	0.0E+00	4.0E–02	0.0E+00	3.74E+00	1.52E+01
van Genuchten Fitting Parameter n	NA	33	1.74E+00	2.8E–01	1.71E+00	2.35E+00	1.35E+00	5.6E–01	–5.6E–01
van Genuchten Fitting Parameter α	cm^{-1}	33	4.0E–03	3.0E–03	3.0E–03	1.5E–02	1.0E–03	2.18E+00	6.31E+00
Lognormal α	NA	33	–5.62E+00	5.7E–01	–5.68E+00	–4.17E+00	–6.73E+00	2.9E–01	3.3E–01

N = Number (of samples) *NA = Not applicable*

Table III-4
Statistics for Unsaturated Hydraulic Properties for Vapor-Phase Notch of the Bandelier Tuff (including values from Mortandad Canyon outcrop)

Variable	Unit	N	Mean	Standard Deviation	Median	Maximum	Minimum	Skew	Kurtosis
Bulk Density (ρ_b)	g/cm^3	5	1.1E+00	5.0E–02	1.1E+00	1.2E+00	1.0E+00	–1.2E+00	1.7E+00
Saturated Volumetric Water Content (θ_s)	cm^3/cm^3	5	4.8E–01	5.0E–02	4.5E–01	5.3E–01	4.3E–01	5.9E–01	–3.2E+00
Saturated Hydraulic Conductivity (K_s)	cm/s	5	9.3E–05	1.4E–04	4.5E–05	3.3E–04	4.8E–06	2.1E+00	4.3E+00
Lognormal Saturated Hydraulic Conductivity (Ln K_s)	NA	5	–1.0E+01	1.6E+00	–1.0E+01	–8.0E+00	–1.2E+01	1.0E–01	–3.0E–02
Residual Volumetric Water Content (θ_r)	cm^3/cm^3	5	3.0E–03	7.0E–03	0.0E+00	2.0E–02	0.0E+00	2.2E+00	5.0E+00
van Genuchten Fitting Parameter *n*	NA	5	1.6E+00	1.6E–01	1.7E+00	1.8E+00	1.4E+00	–5.4E–01	–1.5E+00
van Genuchten Fitting Parameter α	cm^{-1}	5	5.0E–03	5.0E–01	4.0E–03	1.5E–02	2.0E–03	2.1E+00	4.5E+00
Lognormal α	NA	5	–5.6E+00	8.3E–01	–5.6E+00	–4.2E+00	–6.4E+00	1.2E+00	2.4E+00

N = Number (of samples) *NA = Not applicable*

Table III-5
Statistics for Unsaturated Hydraulic Properties for Bandelier Tuff Tshirege Member Unit 1g

Variable	Unit	N	Mean	Standard Deviation	Median	Maximum	Minimum	Skew	Kurtosis
Bulk Density (ρ_b)	g/cm^3	20	1.2E+00	7.0E–02	1.1E+00	1.3E+00	9.4E–01	–5.7E–01	3.2E+00
Saturated Volumetric Water Content (θ_s)	cm^3/cm^3	16	4.6E–01	4.0E–02	4.5E–01	5.2E–01	3.9E–01	–2.9E–01	–7.0E–01
Saturated Hydraulic Conductivity (K_s)	cm/s	24	2.0E–04	1.9E–04	1.4E–04	8.5E–04	3.1E–05	2.2E+00	5.4E+00
Lognormal Saturated Hydraulic Conductivity (Ln K_s)	NA	24	–8.8E+00	8.1E–01	–8.9E+00	–7.1E+00	–1.0E+01	1.6E–01	–1.0E–01
Residual Volumetric Water Content (θ_r)	cm^3/cm^3	16	1.0E–02	2.0E–02	0.0E+00	5.0E–02	0.0E+00	1.5E+00	1.2E+00
van Genuchten Fitting Parameter n	NA	16	1.8E+00	1.8E–01	1.8E+00	2.2E+00	1.4E+00	5.1E–01	8.5E–01
van Genuchten Fitting Parameter α	cm^{-1}	16	6.0E–03	6.0E–03	5.0E–03	2.8E–02	3.0E–03	3.6E+00	1.42E+01
Lognormal α	NA	16	–5.3E+00	5.7E–01	–5.3E+00	–3.6E+00	–6.0E+00	1.9E+00	5.5E+00

N = Number (of samples) *NA = Not applicable*

Table III-6
Statistics for Unsaturated Hydraulic Properties for Bandelier Tuff Tsankawi Pumice/Cerro Toledo Interval

Variable	Unit	N	Mean	Standard Deviation	Median	Maximum	Minimum	Skew	Kurtosis
Bulk Density (ρ_b)	g/cm^3	7	1.2E+00	7.0E–02	1.2E+00	1.3E+00	1.1E+00	–1.8E+00	4.2E+00
Saturated Volumetric Water Content (θ_s)	cm^3/cm^3	7	4.5E–01	4.0E–02	4.4E–01	5.0E–01	4.0E–01	2.5E–01	–1.3E+00
Saturated Hydraulic Conductivity (K_s)	cm/s	7	3.4E–04	5.2E–04	1.3E–04	1.5E–03	6.0E–05	2.5E–01	6.5E+00
Lognormal Saturated Hydraulic Conductivity (Ln K_s)	NA	7	–8.6E+00	1.1E+00	–9.0E+00	–6.5E+00	–9.8E+00	1.3E–01	2.2E+00
Residual Volumetric Water Content (θ_r)	cm^3/cm^3	7	3.0E–03	6.0E–03	0.0E+00	1.6E–02	0.0E+00	2.1E+00	4.5E+00
van Genuchten Fitting Parameter *n*	NA	7	1.5E+00	9.0E–02	1.5E+00	1.6E+00	1.4E+00	4.3E–01	–1.3E+00
van Genuchten Fitting Parameter α	cm^{-1}	7	2.0E–02	7.0E–03	1.3E–02	2.5E–02	7.1E–03	4.3E–01	–1.6E+00
Lognormal α	NA	7	–4.3E+00	5.0E–01	–4.3E+00	–3.7E+00	–5.0E+00	–6.0E–02	1.6E+00

N = Number (of samples) *NA = Not applicable*

Table III-7
Statistics for Unsaturated Hydraulic Properties for Bandelier Tuff Otowi Member

Variable	Unit	N	Mean	Standard Deviation	Median	Maximum	Minimum	Skew	Kurtosis
Bulk Density (ρ_b)	g/cm^3	12	1.2E+00	6.0E–02	1.20E+00	1.3E+00	1.1E+00	1.5E–01	–1.0E–02
Saturated Volumetric Water Content (θ_s)	cm^3/cm^3	12	4.4E–01	1.0E–02	4.4E–01	4.5E–01	4.1E–01	–8.3E–02	–5.4E–01
Saturated Hydraulic Conductivity (K_s)	cm/s	12	2.5E–04	1.2E–04	2.2E–04	5.0E–04	1.0E–04	1.1E+00	7.7E–02
Lognormal Saturated Hydraulic Conductivity (Ln K_s)	NA	12	–8.4E+00	4.5E–01	–8.4E+00	–7.6E+00	–9.2E+00	1.1E–01	–7.0E–02
Residual Volumetric Water Content (θ_r)	cm^3/cm^3	12	1.9E–02	2.0E–02	2.0E–02	4.0E–02	0.0E+00	5.0E–02	–1.3E+00
van Genuchten Fitting Parameter n	NA	12	1.8E+00	2.5E–01	1.7E+00	2.3E+00	1.5E+00	7.7E–01	4.7E–01
van Genuchten Fitting Parameter α	cm^{-1}	12	6.0E–03	1.3E–03	6.0E–03	8.0E–03	3.9E–03	6.0E–01	5.8E–01
Lognormal α	NA	12	–5.1E+00	2.1E–01	–5.1E+00	–4.8E+00	–5.6E+00	–4.0E–02	5.8E–01

N = Number (of samples) *NA = Not applicable*

Table III-8
Statistics for Unsaturated Hydraulic Properties for Cerros del Rio Basalts

Variable	Unit	N	Mean	Standard Deviation	Median	Maximum	Minimum	Skew	Kurtosis
Bulk Density (ρ_b)	g/cm^3	4	2.7E+00	3.1E–01	2.8E+00	2.8E+00	2.2E+00	–2.0E+00	3.8E+00
Saturated Volumetric Water Content (θ_s)	cm^3/cm^3	4	1.0E–01	5.0E–02	1.0E–01	1.6E–01	5.0E–02	4.4E–01	9.5E–01
Saturated Hydraulic Conductivity (K_s)	cm/s	4	2.1E–09	1.6E–09	2.2E–09	3.8E–09	8.7E–11	–5.3E–01	2.8E–01
Lognormal Saturated Hydraulic Conductivity (Ln K_s)	NA	4	–2.1E+01	1.7E+00	–2.0E+01	–1.9E+01	–2.3E+01	–1.8E+00	3.4E+00
Residual Volumetric Water Content (θ_r)	cm^3/cm^3	4	0.0E+00	0.0E+00	0.0E+00	0.0E+00	0.0E+00	---	---
van Genuchten Fitting Parameter *n*	NA	4	1.3E+00	9.0E–02	1.2E+00	1.4E+00	1.2E+00	1.1E+00	1.1E+00
van Genuchten Fitting Parameter α	cm^{-1}	4	3.3E–02	3.5E–2	2.4E–02	8.0E–02	1.0E–03	1.4E+00	2.6E+00
Lognormal α	NA	4	–4.1E+00	1.8E+00	–3.7E+00	–2.5E+00	–6.6E+00	–1.3E+00	2.5E+00

N = Number (of samples) *NA = Not applicable* *--- Not estimated*

The skewness statistics for residual water content, the van Genuchten fitting parameter α, and saturated hydraulic conductivity for unit 1v (Table III-3) indicate that the distributions for these parameters are not normal for unit 1v; this is also seen in the normal probability plots for these parameters (Figures III-2, III-5, and III-7, respectively). A logarithmic transformation was applied to the saturated hydraulic conductivity and α; however, the residual water content was not transformed because its skewness is a result of the fitting by the RETC code, which sets the parameter to zero when its value is below 0.001. The rationale for setting this limit on the residual water content is that this is a fitting parameter and its physical meaning is not clear. For unit 1v, 29 of the 34 total samples had residual water contents equal to zero (Table III-3). A mixed distribution (Yevjevich, 1972) with a probability spike at zero could be used for residual water content, but the analysis for this type of distribution was not performed.

The properties for the Tshirege Member units of the Bandelier Tuff (Tables III-2 through III-5) do not appear to show any demonstrable differences; the properties for the Tsankawi Pumice/Cerro Toledo interval (Table III-6) and the Otowi Member (Table III-7) are also within the range of the means of the other units. The obvious differences between the soil unit (Table III-1) and basalt (Table III-8) properties and the Bandelier Tuff properties are expected because of the material and genesis of these layers as opposed to the tuff.

III.3.3 Correlation

Consideration of the correlation between parameters is important because sampling distributions may not be independent. Correlation may also be used to estimate parameters using more easily measured variables such as soil texture. Correlation matrices were calculated for the aggregated hydraulic parameters for all geologic units at TA-54 (Table III-9) and for each geologic unit (Tables III-10 through 17).

Some of correlations shown in Table III-9 are expected because of functional relationships; these include correlations between saturated conductivity and log-transformed saturated conductivity; α and n; and α and log-transformed α. The RETC code generates a correlation matrix during the fitting process, and α and n are usually highly correlated. Other correlations such as that between the log-transformed saturated conductivity and the saturated water content (θ_s) need to be considered when developing the stochastic simulation for TA-54, as these linear dependencies can affect sampling from distributions when performing Monte Carlo analyses.

Correlations vary among geologic units (Tables III-10 through III-17), as does the number of significant correlations. Again, sample size must be considered when using the correlation coefficients.

Table III-9
Correlation Matrix for Unsaturated Zone Hydraulic Parameters for All Geologic Units

Variable	ρ_b	θ_s	K_s	Ln K_s	θ_r	n	α	Ln α
Bulk Density (ρ_b)	1.0E+00	**–8.8E–01**	–1.6E–01	**–8.6E–01**	–1.2E–01	–2.1E–01	1.3E–01	**2.3E–01**
Saturated Volumetric Water Content (θ_s)	**–8.8E–01**	1.0E+00	**2.1E–01**	**8.3E–01**	4.0E–02	1.6E–01	–7.0E–02	**–2.1E–01**
Saturated Hydraulic Conductivity (K_s)	–1.6E–01	**2.1E–01**	1.0E+00	**4.6E–01**	**3.8E–01**	4.0E–02	1.9E–01	**2.8E–01**
Lognormal Saturated Hydraulic Conductivity (Ln K_s)	**–8.6E–01**	**8.3E–01**	**4.6E–01**	1.0E+00	2.0E–01	**3.2E–01**	–6.0E–02	–1.6E–01
Residual Volumetric Water Content (θ_r)	–1.2E–01	4.0E–02	**3.8E–01**	2.0E–01	1.0E+00	**2.6E–01**	1.2E–01	9.0E–02
van Genuchten Fitting Parameter *n*	–2.1E–01	1.6E–01	4.0E–02	**3.2E–01**	**2.6E–01**	1.0E+00	**–2.5E–01**	**–6.0E–01**
van Genuchten Fitting Parameter α	1.3E–01	–7.0E–02	1.9E–01	–6.0E–02	1.2E–01	**–2.5E–01**	1.0E+00	**6.8E–01**
Lognormal α	**2.3E–01**	**–2.1E–01**	**2.8E–01**	–1.6E–01	9.0E–02	**–6.0E–01**	**6.8E–01**	1.0E+00

Bold *= Correlation is significant at $p < 0.05$, $N = 90$*

Table III-10
Correlation Matrix for Unsaturated Zone Hydraulic Parameters for Soil Layer

Variable	ρ_b	θ_s	K_s	Ln K_s	θ_r	n	α	Ln α
Bulk Density (ρ_b)	1.0E+00	–3.6E–01	4.8E–01	4.5E–01	---	6.5E–01	1.9E–01	1.5E–01
Saturated Volumetric Water Content (θ_s)	–3.6E–01	1.0E+00	6.2E–01	6.2E–01	---	1.9E–01	6.0E–02	1.0E–02
Saturated Hydraulic Conductivity (K_s)	4.8E–01	6.2E–01	1.0E+00	**9.9E–01**	---	8.2E–01	2.0E–02	–5.0E–02
Lognormal Saturated Hydraulic Conductivity (Ln K_s)	4.5E–01	6.2E–01	**9.9E–01**	1.0E+00	---	8.6E–01	–8.0E–02	–1.6E–01
Residual Volumetric Water Content (θ_r)	---	---	---	---	1.0E+00	---	---	---
van Genuchten Fitting Parameter *n*	6.5E–01	1.9E–01	8.2E–01	8.6E–01	---	1.0E+00	–4.0E–01	–4.7E–01
van Genuchten Fitting Parameter α	1.9E–01	6.0E–02	2.0E–02	–8.0E–02	---	–4.0E–01	1.0E+00	**1.0E+00**
Lognormal α	1.5E–01	1.0E–02	–5.0E–02	–1.6E–01	---	–4.7E–01	**1.0E+00**	1.0E+00

Bold *= Correlation is significant at p < 0.05, N = 4* *--- = Not estimated*

Table III-11
Correlation Matrix for Unsaturated Zone Hydraulic Parameters for Bandelier Tuff Tshirege Member Unit 2

Variable	ρ_b	θ_s	K_s	Ln K_s	θ_r	n	α	Ln α
Bulk Density (ρ_b)	1.0E+00	–4.5E–01	1.0E–01	–4.1E–01	6.9E–01	6.0E–01	–5.8E–01	–6.8E–01
Saturated Volumetric Water Content (θ_s)	–4.5E–01	1.0E+00	**7.4E–01**	**9.3E–01**	7.0E–02	–6.3E–01	3.1E–01	5.7E–01
Saturated Hydraulic Conductivity (K_s)	1.0E–01	**7.4E–01**	1.0E+00	**8.4E–01**	6.7E–01	–1.9E–01	1.5E–01	3.2E–01
Lognormal Saturated Hydraulic Conductivity (Ln K_s)	–4.1E–01	**9.3E–01**	**8.4E–01**	1.0E+00	1.9E–01	–5.5E–01	4.9E–01	6.9E–01
Residual Volumetric Water Content (θ_r)	6.9E–01	7.0E–02	6.7E–01	1.9E–01	1.0E+00	5.0E–01	–3.8E–01	–3.6E–01
van Genuchten Fitting Parameter *n*	6.0E–01	–6.3E–01	–1.9E–01	–5.5E–01	5.0E–01	1.0E+00	**–7.3E–01**	**–8.2E–01**
van Genuchten Fitting Parameter α	–5.8E–01	3.1E–01	1.5E–01	4.9E–01	–3.8E–01	**–7.3E–01**	1.0E+00	**9.4E–01**
Lognormal α	–6.8E–01	5.7E–01	3.2E–01	6.9E–01	–3.6E–01	**–8.2E–01**	**9.4E–01**	1.0E+00

Bold *= Correlation is significant at $p < 0.05$, $N = 8$*

Table III-12
Correlation Matrix for Unsaturated Zone Hydraulic Parameters for Bandelier Tuff Tshirege Member Unit 1v

Variable	ρ_b	θ_s	K_s	Ln K_s	θ_r	n	α	Ln α
Bulk Density (ρ_b)	1.0E+00	–1.7E–01	–5.0E–02	9.0E–02	–2.4E–01	**6.0E–01**	–1.1E–01	–2.9E–01
Saturated Volumetric Water Content (θ_s)	–1.7E–01	1.0E+00	**4.3E–01**	**4.6E–01**	1.3E–01	–3.1E–01	1.4E–01	3.1E–01
Saturated Hydraulic Conductivity (K_s)	–5.0E–02	**4.3E–01**	1.0E+00	**8.7E–01**	5.0E–02	–1.5E–01	**7.5E–01**	**6.8E–01**
Lognormal Saturated Hydraulic Conductivity (Ln K_s)	9.0E–02	**4.6E–01**	**8.7E–01**	1.0E+00	–2.5E–01	2.0E–02	**4.0E–01**	**4.2E–01**
Residual Volumetric Water Content (θ_r)	–2.4E–01	1.3E–01	5.0E–02	–2.5E–01	1.0E+00	–7.0E–02	**3.5E–01**	2.6E–01
van Genuchten Fitting Parameter *n*	**6.0E–01**	–3.1E–01	–1.5E–01	2.0E–02	–7.0E–02	1.0E+00	–2.7E–01	**–5.9E–01**
van Genuchten Fitting Parameter α	–1.1E–01	1.4E–01	**7.5E–01**	**4.0E–01**	**3.5E–01**	–2.7E–01	1.0E+00	**8.3E–01**
Lognormal α	–2.9E–01	3.1E–01	**6.8E–01**	**4.2E–01**	2.6E–01	**–5.9E–01**	**8.3E–01**	1.0E+00

Bold *= Correlation is significant at $p < 0.05$, $N = 33$*

Table III-13
Correlation Matrix for Unsaturated Zone Hydraulic Parameters for Bandelier Tuff Vapor-Phase Notch

Variable	ρ_b	θ_s	K_s	Ln K_s	θ_r	n	α	Ln α
Bulk Density (ρ_b)	1.0E+00	2.5E–01	–1.1E–01	–3.6E–01	5.6E–01	–8.1E–01	5.8E–01	5.4E–01
Saturated Volumetric Water Content (θ_s)	2.5E–01	1.0E+00	7.5E–01	7.9E–01	–3.4E–01	–4.9E–01	–1.9E–01	4.0E–02
Saturated Hydraulic Conductivity (K_s)	–1.1E–01	7.5E–01	1.0E+00	8.6E–01	–3.6E–01	1.1E–01	–2.4E–01	–6.0E–02
Lognormal Saturated Hydraulic Conductivity (Ln K_s)	–3.6E–01	7.9E–01	8.6E–01	1.0E+00	–7.2E–01	1.3E–01	–6.1E–01	–3.9E–01
Residual Volumetric Water Content (θ_r)	5.6E–01	–3.4E–01	–3.6E–01	–7.2E–01	1.0E+00	–3.7E–01	**9.9E–01**	**9.0E–01**
van Genuchten Fitting Parameter *n*	–8.1E–01	–4.9E–01	1.1E–01	1.3E–01	–3.7E–01	1.0E+00	–4.4E–01	–5.2E–01
van Genuchten Fitting Parameter α	5.8E–01	–1.9E–01	–2.4E–01	–6.1E–01	**9.9E–01**	–4.4E–01	1.0E+00	**9.6E–01**
Lognormal α	5.4E–01	4.0E–02	–6.0E–02	–3.9E–01	**9.0E–01**	–5.2E–01	**9.6E–01**	1.0E+00

Bold *= Correlation is significant at $p < 0.05$, $N = 5$*

Table III-14
Correlation Matrix for Unsaturated Zone Hydraulic Parameters for Bandelier Tuff Tshirege Member Unit 1g

Variable	ρ_b	θ_s	K_s	Ln K_s	θ_r	n	α	Ln α
Bulk Density (ρ_b)	1.0E+00	–1.9E–01	–2.7E–01	–4.0E–01	–4.0E–02	–4.0E–02	5.0E–02	–1.0E–01
Saturated Volumetric Water Content (θ_s)	–1.9E–01	1.0E+00	3.5E–01	3.4E–01	8.0E–02	–1.0E–02	1.4E–01	8.0E–02
Saturated Hydraulic Conductivity (K_s)	–2.7E–01	3.5E–01	1.0E+00	**9.2E–01**	4.5E–01	**–6.0E–01**	**8.4E–01**	**8.6E–01**
Lognormal Saturated Hydraulic Conductivity (Ln K_s)	–4.0E–01	3.4E–01	**9.2E–01**	1.0E+00	2.1E–01	**–6.8E–01**	**6.6E–01**	**8.1E–01**
Residual Volumetric Water Content (θ_r)	–4.0E–02	8.0E–02	4.5E–01	2.1E–01	1.0E+00	–2.7E–01	**6.1E–01**	4.8E–01
van Genuchten Fitting Parameter *n*	–4.0E–02	–1.0E–02	**–6.0E–01**	**–6.8E–01**	–2.7E–01	1.0E+00	**–6.2E–01**	**–8.0E–01**
van Genuchten Fitting Parameter α	5.0E–02	1.4E–01	**8.4E–01**	**6.6E–01**	**6.1E–01**	**–6.2E–01**	1.0E+00	**9.3E–01**
Lognormal α	–1.0E–01	8.0E–02	**8.6E–01**	**8.1E–01**	4.8E–01	**–8.0E–01**	**9.3E–01**	1.0E+00

Bold *= Correlation is significant at $p < 0.05$, $N = 16$*

Table III-15
Correlation Matrix for Unsaturated Zone Hydraulic Parameters for Tsankawi Pumice/ Cerro Toledo Interval

Variable	ρ_b	θ_s	K_s	Ln K_s	θ_r	n	α	Ln α
Bulk Density (ρ_b)	1.0E+00	–7.5E–01	**–9.3E–01**	**–8.9E–01**	**–7.6E–01**	–1.0E–01	–4.0E–01	–4.8E–01
Saturated Volumetric Water Content (θ_s)	–7.5E–01	1.0E+00	5.7E–01	4.1E–01	5.5E–01	4.0E–02	**7.7E–01**	**7.8E–01**
Saturated Hydraulic Conductivity (K_s)	**–9.3E–01**	5.7E–01	1.0E+00	**9.3E–01**	**9.1E–01**	3.3E–01	1.1E–01	2.0E–01
Lognormal Saturated Hydraulic Conductivity (Ln K_s)	**–8.9E–01**	4.1E–01	**9.3E–01**	1.0E+00	7.0E–01	1.9E–01	6.0E–02	1.8E–01
Residual Volumetric Water Content (θ_r)	**–7.6E–01**	5.5E–01	**9.1E–01**	7.0E–01	1.0E+00	4.9E–01	0.0E+00	7.0E–02
van Genuchten Fitting Parameter *n*	–1.0E–01	4.0E–02	3.3E–01	1.9E–01	4.9E–01	1.0E+00	–4.8E–01	–5.3E–01
van Genuchten Fitting Parameter α	–4.0E–01	**7.7E–01**	1.1E–01	6.0E–02	0.0E+00	–4.8E–01	1.0E+00	**9.9E–01**
Lognormal α	–4.8E–01	**7.8E–01**	2.0E–01	1.8E–01	7.0E–02	–5.3E–01	**9.9E–01**	1.0E+00

Bold *= Correlation is significant at $p < 0.05$, $N = 7$*

Table III-16
Correlation Matrix for Unsaturated Zone Hydraulic Parameters for Bandelier Tuff Otowi Member

Variable	ρ_b	θ_s	K_s	Ln K_s	θ_r	n	α	Ln α
Bulk Density (ρ_b)	1.0E+00	2.0E–02	**–6.9E–01**	**–7.7E–01**	1.7E–01	7.0E–02	**–7.6E–01**	**–7.9E–01**
Saturated Volumetric Water Content (θ_s)	2.0E–02	1.0E+00	2.3E–01	2.8E–01	–3.5E–01	–4.3E–01	4.3E–01	4.5E–01
Saturated Hydraulic Conductivity (K_s)	**–6.9E–01**	2.3E–01	1.0E+00	**9.7E–01**	2.4E–01	2.2E–01	**6.8E–01**	**6.7E–01**
Lognormal Saturated Hydraulic Conductivity (Ln K_s)	**–7.7E–01**	2.8E–01	**9.7E–01**	1.0E+00	1.9E–01	1.8E–01	**7.2E–01**	**7.4E–01**
Residual Volumetric Water Content (θ_r)	1.7E–01	–3.5E–01	2.4E–01	1.9E–01	1.0E+00	**9.5E–01**	–4.4E–01	–4.4E–01
van Genuchten Fitting Parameter *n*	7.0E–02	–4.3E–01	2.2E–01	1.8E–01	**9.5E–01**	1.0E+00	–5.0E–01	–4.8E–01
van Genuchten Fitting Parameter α	**–7.6E–01**	4.3E–01	**6.8E–01**	**7.2E–01**	–4.4E–01	–5.0E–01	1.0E+00	**9.9E–01**
Lognormal α	**–7.9E–01**	4.5E–01	**6.7E–01**	**7.4E–01**	–4.4E–01	–4.8E–01	**9.9E–01**	1.0E+00

Bold *= Correlation is significant at $p < 0.05$, $N = 12$*

Table III-17
Correlation Matrix for Unsaturated Zone Hydraulic Parameters for Cerros del Rio Basalts

Variable	ρ_b	θ_s	K_s	Ln K_s	θ_r	n	α	Ln α
Bulk Density (ρ_b)	1.0E+00	–8.2E–01	1.8E–01	–1.0E–01	---	5.0E–02	1.6E–01	–2.1E–01
Saturated Volumetric Water Content (θ_s)	–8.2E–01	1.0E+00	4.1E–01	6.6E–01	---	2.3E–01	1.0E–01	1.6E–01
Saturated Hydraulic Conductivity (K_s)	1.8E–01	4.1E–01	1.0E+00	9.3E–01	---	3.8E–01	5.1E–01	4.0E–02
Lognormal Saturated Hydraulic Conductivity (Ln K_s)	–1.0E–01	6.6E–01	9.3E–01	1.0E+00	---	5.7E–01	2.7E–01	–1.3E–01
Residual Volumetric Water Content (θ_r)	---	---	---	---	1.0E+00	---	---	---
van Genuchten Fitting Parameter *n*	5.0E–02	2.3E–01	3.8E–01	5.7E–01	---	1.0E+00	–6.0E–01	–8.8E–01
van Genuchten Fitting Parameter α	1.6E–01	1.0E–01	5.1E–01	2.7E–01	---	–6.0E–01	1.0E+00	8.4E–01
Lognormal α	–2.1E–01	1.6E–01	4.0E–02	–1.3E–01	---	–8.8E–01	8.4E–01	1.0E+00

Bold *= Correlation is significant at p < 0.05, N = 4* *--- = Not estimated*

III.3.4 Alternative Estimates

An alternative approach to provide parameter estimates for a geologic unit is to combine the retention data for the geologic unit and obtain a single set of parameter estimates using the RETC code. The RETC geologic unit fitted curve for Tshirege Member unit 2 is shown in Figure III-9. The saturated volumetric water content (θ_s) was a fitting parameter for this curve. Figure III-9 also shows curves for Tshirege Member unit 2 using mean and median parameter values from Table III-2. The curves for mean and median parameter values appear similar, but both diverge from the geologic unit fitted curve over the range of 100 cm to 1.0×10^4 cm (39 to 3,900 in.).

The RETC code generates statistics including 95 percent confidence intervals for fitted parameters; Table III-18 lists these statistics for Tshirege Member unit 2. A comparison of the estimated parameters in Table III-18 to the mean and median estimates in Table III-2 shows that both the saturated volumetric water content (θ_s) and α fall inside the 95 percent confidence intervals, but the mean and median estimates for n (Table III-2) lie outside the 95 percent confidence limits given in Table III-18. The limited sample size for unit 2 makes it virtually impossible to determine which set of parameters is more appropriate for unit 2; however, the values in Table III-18 provide another estimate that can be used in Monte Carlo analyses of flow and transport at TA-54.

Table III-18
Parameter Estimates and Statistics for RETC Fit to All Retention Data for Bandelier Tuff Tshirege Member Unit 2

Parameter	Value	Standard Error of Coefficient	95% Confidence Limit	
			Lower	Upper
Saturated Volumetric Water Content (θ_s)	4.1E–01	1.0E–02	3.9E–01	4.3E–01
van Genuchten Fitting Parameter α	5.0E–03	1.0E–03	3.0E–03	7.0E–03
van Genuchten Fitting Parameter n	1.7E+00	9.0E–02	1.5E+00	1.9E+00

The alternative estimates of hydrologic parameters developed for unit 1v are provided in Figure III-10 and Table III-19. Figure III-10 shows an obvious bias for the saturated volumetric water volume (θ_s) estimated from all the data; this bias results from setting the zero-pressure values in the data to 0.10 cm. These initial data values are weighted heavily in fitting the saturated volumetric water content values. Comparison of the all-data parameter estimates shown in Table III-19 with the mean and median estimates in Table III-3 reveal the bias in saturated volumetric water content; the median values for both α and n lie within the 95 percent confidence intervals. The mean values for α and n from Table III-3 lie at the upper range of the 95 percent confidence limit for these parameters (Table III-19).

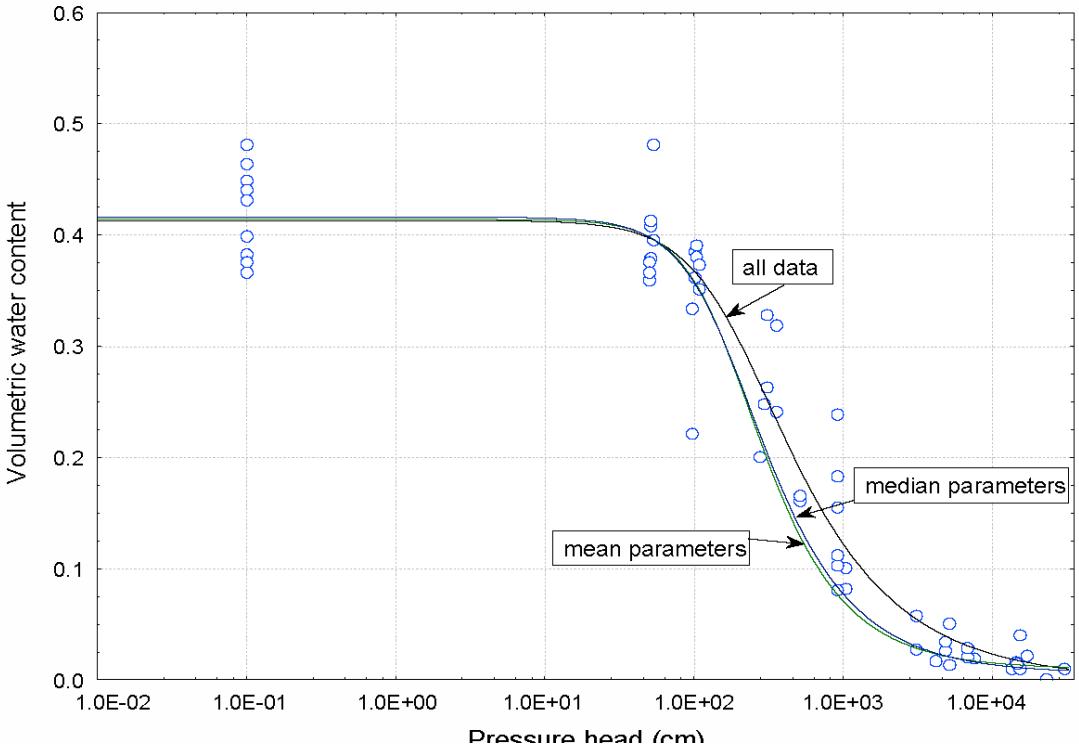

Figure III-1
Comparison of van Genuchten Retention Curve Fits for Bandelier Tuff Tshirege Member Unit 2: Curves for All Retention Data, Mean Values, and Median Values

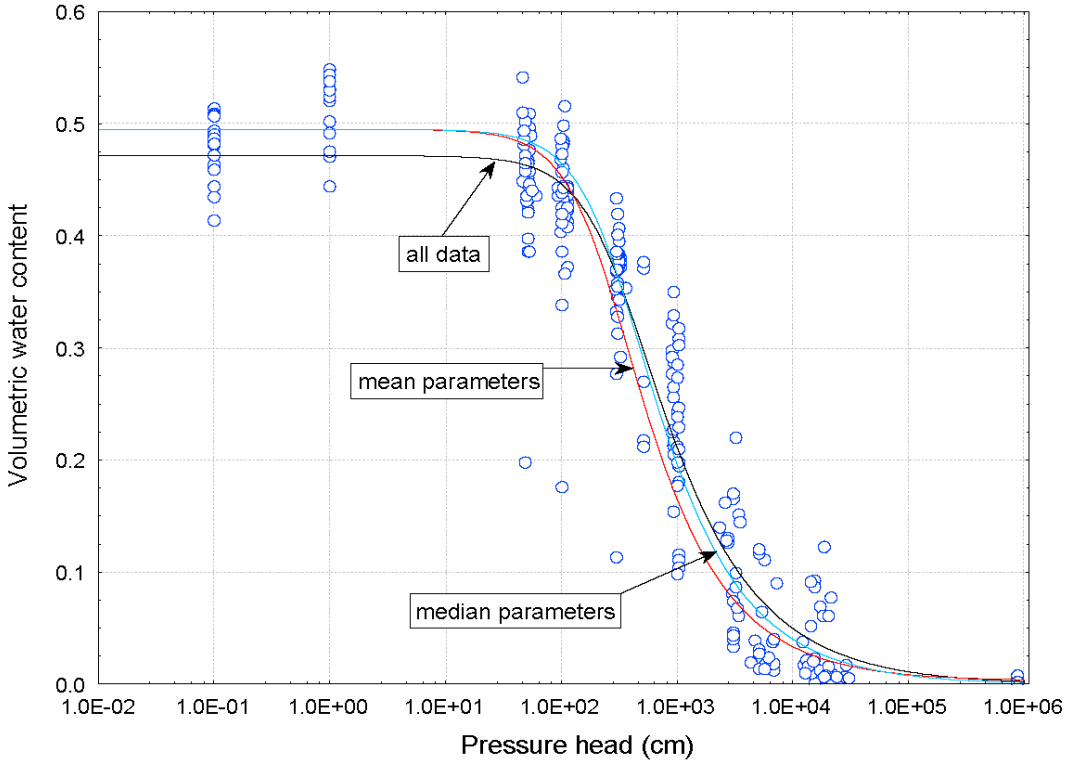

Figure III-2
Comparison of van Genuchten Retention Curve Fits for Bandelier Tuff Tshirege Member Unit 1v: Curves for All Retention Data, Mean Values, and Median Values

Table III-19
Parameter Estimates and Statistics for RETC Fit to All Retention Data for Bandelier Tuff Tshirege Member Unit 1v

Parameter	Value	Standard Error of Coefficient	95% Confidence Limit	
			Lower	Upper
Saturated Volumetric Water Content (θ_s)	4.7E–01	1.0E–02	4.6E–01	4.8E–01
van Genuchten Fitting Parameter α	3.0E–03	3.0E–04	3.0E–03	4.0E–03
van Genuchten Fitting Parameter *n*	1.7E+00	4.0E–02	1.6E+00	1.7E+00

Tables III-20 and III-21 and Figures III-11 and III-12 present results of the all-data RETC-fitted curve for unit 1g and the Otowi Member, respectively. Again, comparisons can be made with the mean and median estimates for these units (Tables III-5 and III-7). For Tshirege Member unit 1g, mean and median *n* parameter values exceed the upper 95 percent confidence limits of the parameters fitted to all retention values. Mean and median parameter values for the Otowi Member (Table III-7) are within the 95 percent confidence interval of the parameters fitted to all retention data (Table III-21).

Table III-20
Parameter Estimates and Statistics for RETC Fit to All Retention Data for Bandelier Tuff Tshirege Member Unit 1g

Parameter	Value	Standard Error of Coefficient	95% Confidence Limits	
			Lower	Upper
Saturated Volumetric Water Content (θ_s)	4.6E–01	1.0E–02	4.4E–01	4.7E–01
van Genuchten Fitting Parameter α	5.0E–03	5.0E–04	4.0E–03	6.0E–03
van Genuchten Fitting Parameter *n*	1.7E+00	4.0E–02	1.6E+00	1.7E+00

Table III-21
Parameter Estimates and Statistics for RETC Fit to All Retention Data for Bandelier Tuff Otowi Member

Parameter	Value	Standard Error of Coefficient	95% Confidence Limits	
			Lower	Upper
Residual Volumetric Water Content (θ_r)	1.6E–02	8.0E–03	1.0E–03	3.1E–02
Saturated Volumetric Water Content (θ_s)	4.3E–01	4.0E–03	4.2E–01	4.4E–01
van Genuchten Fitting Parameter α	6.0E–03	4.0E–04	5.0E–03	7.0E–03
van Genuchten Fitting Parameter *n*	1.7E+00	6.0E–02	1.6E+00	1.8E+00

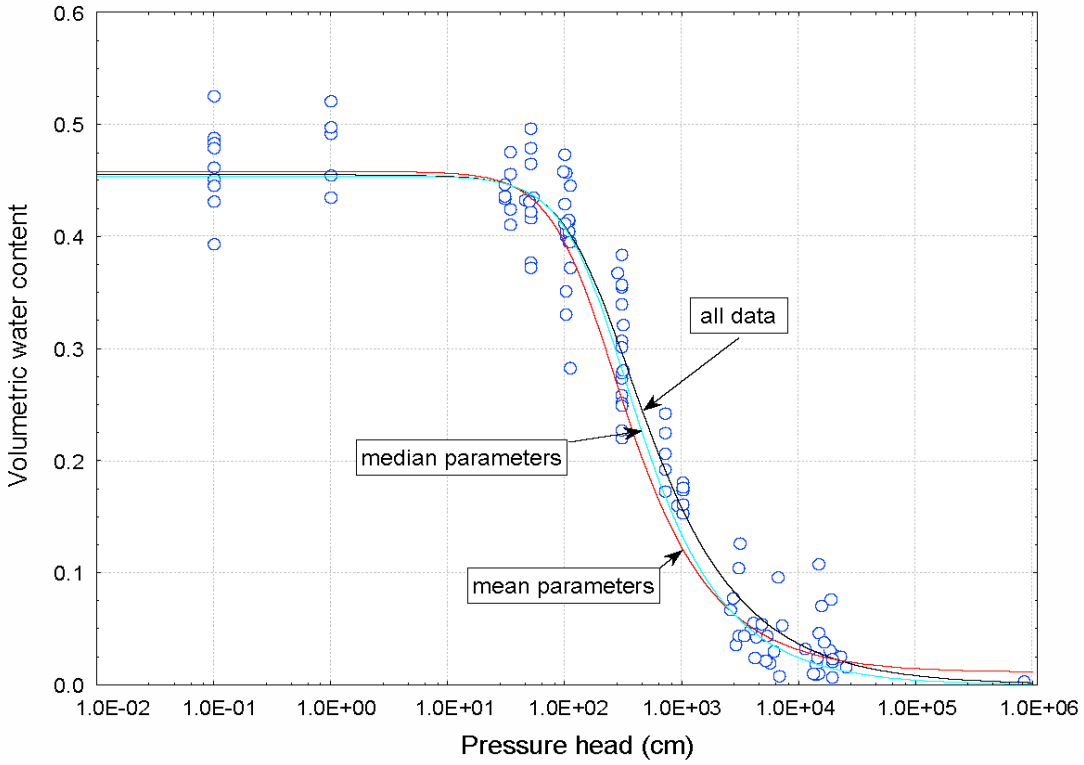

Figure III-3
Comparison of van Genuchten Retention Curve Fits for Bandelier Tuff Tshirege Member Unit 1g: Curves for All Retention Data, Mean Values, and Median Values

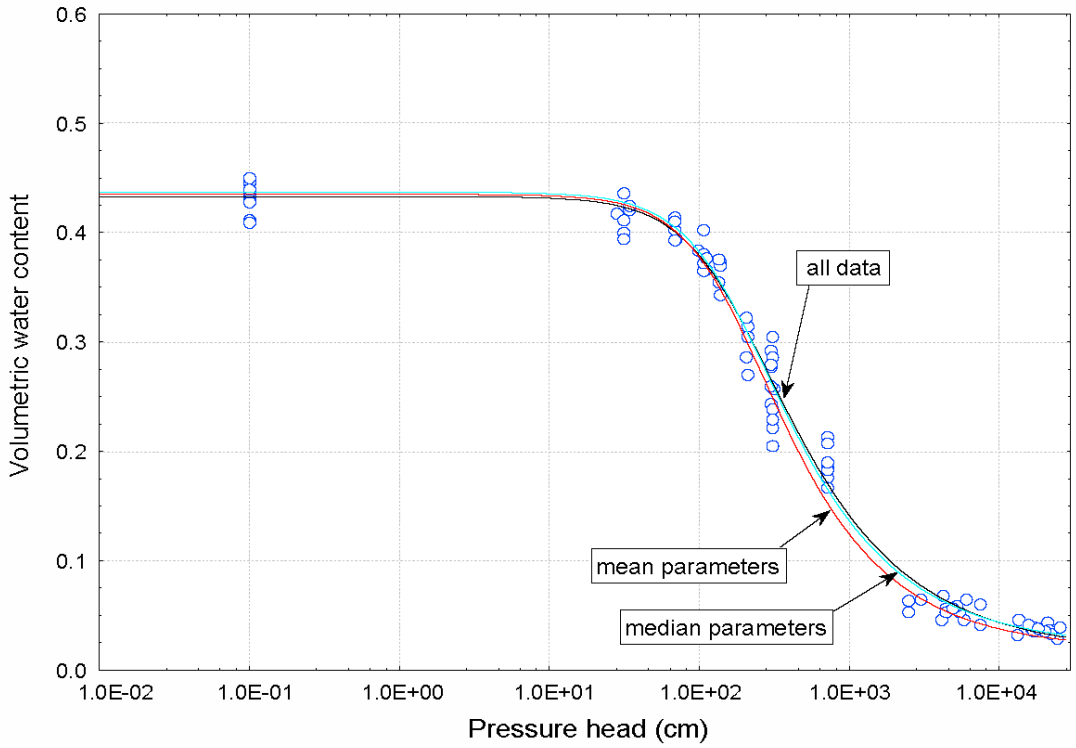

Figure III-4
Comparison of van Genuchten Retention Curve Fits for Bandelier Tuff Otowi Member: Curves for All Retention Data, Mean Values, and Median Values

III.4 Summary and Conclusions

This study provided a statistical analysis of hydrologic properties of geologic units from TA-54 to estimate parameters for stochastic analyses of groundwater flow and transport. Descriptive statistics and correlation properties were calculated both by geologic unit and for the aggregated data. Distribution plots and the skew statistic indicated that saturated hydraulic conductivity and the van Genuchten α parameter were not described by a normal distribution; consequently, natural logarithmic transformations were performed on these two parameters. Correlation analyses revealed some linear relationships between parameters that are important when generating distributions for Monte Carlo analysis. Retention data were pooled and fitted to Equation 1 by geologic unit to provide additional estimates of the hydrologic parameters.

The parameters estimated in this report pertain to core samples that represent matrix properties of the materials. At high saturation, features such as fractures or macropores can change hydrologic behavior substantially. The parameters presented in this study will not accurately represent these features at high saturation conditions.

There were a limited number of samples for the geologic units included in this study, which prevents meaningful comparative analyses among units and makes it difficult to define statistics such as parameter correlation within a single unit. The lack of spatial correlation data, in both the vertical and lateral directions, is also a limiting factor in terms of using this information for flow and transport simulation.

III.5 References

Broxton, D.E. and S.L. Reneau, 1995, *Stratigraphic Nomenclature of the Bandelier Tuff for the Environmental Restoration Project at Los Alamos National Laboratory*, Los Alamos National Laboratory Report, LA-13010-MS.

DBS&A, 1995, *Laboratory Analysis of Soil Hydraulic Properties of G-5 Soil Samples*, Daniel B. Stephens & Associates, Inc., Contract completion Report to Los Alamos National Laboratory, January.

DBS&A, 1996, *Hydraulic Properties of Los Alamos National Laboratory Soil Samples*, Contract completion Report to Los Alamos National Laboratory, October.

Freeze, R.A., 1975, "A Stochastic-Conceptual Analysis of One-Dimensional Groundwater Flow in Nonuniform Homogeneous Media," *Water Resources Res*., Vol. 11, pp. 725–741.

Nielsen, D. R., J.W. Biggar, and K.T. Erh, 1973, "Spatial Variability of Field-Measured Soil-Water Properties," *Hilgardia*, Vol. 42, pp. 215–259.

Puglisi, C.V. and E.L. Vold, 1995, "Low-Impact Sampling under an Active Solid Low-Level Radioactive Waste Disposal Unit Using Horizontal Drilling Technology," *Symposium on the Scientific Basis for Nuclear Waste Management*, Materials Research Society, Boston, MA, November 27, 1995.

Rogers, D.B. and B.M. Gallaher, 1995, *The Unsaturated Hydraulic Characteristics of the Bandelier Tuff*, Los Alamos National Laboratory Report LA-12968-MS, September.

van Genuchten, M.Th., 1980, "A Closed Form Equation for Predicting the Hydraulic Conductivity of Unsaturated Soil," *Soil Science Soc. Am. J*., Vol. 44, pp. 892–898.

van Genuchten, M.Th., F.J. Leij, and S.R. Yates, 1991, *The RETC Code for Quantifying the Hydraulic Functions of Unsaturated Soils*, U.S. Environmental Protection Agency Rep. No. EPA/600/2-91/065, 85p.

Yevjevich, V.M., 1972, "Probability and Statistics in Hydrology," *Water Resources Publication*, Fort Collins, Co. 276p.

Annex IIIa
Parameters and Data Used for Statistical Analyses

The following table contains the parameters and other data used for the statistical analyses reported above. Values have been rounded to three significant digits (except for sampling depths).

Annex IIIa:
Parameters and Data Used for Statistical Analyses

Unit	Borehole	Depth (ft)	Depth (m)	ρ_b (g/cm³)	θ_s (cm³/cm³)	Porosity (cm³/cm³)	K_s (cm/s)	Ln K_s	θ_r (cm³/cm³)	n	α (cm^{-1})	Ln α
soil	54-501 [a]	0	0.0	1.47E+00	4.00E–01	4.44E–01	5.45E–06	–1.21E+01	0.00E+00	1.26E+00	9.58E–03	–4.65E+00
	54-502 [a]	0	0.0	1.42E+00	4.29E–01	4.66E–01	5.43E–06	–1.21E+01	0.00E+00	1.24E+00	9.73E–03	–4.63E+00
	54-503 [a]	0	0.0	1.46E+00	4.20E–01	4.51E–01	6.52E–06	–1.19E+01	0.00E+00	1.24E+00	1.83E–02	–4.00E+00
	54-504 [a]	0	0.0	1.43E+00	3.98E–01	4.62E–01	1.39E–06	–1.35E+01	0.00E+00	1.21E+00	1.42E–02	–4.26E+00
2	54-1006[d]	42	12.8	1.28E+00	4.49E–01		4.10E–04	–7.80E+00	0.00E+00	1.76E+00	6.40E–03	–5.05E+00
	TA-54-G-5 [b]	9	2.7	1.35E+00	3.99E–01	4.74E–01	2.10E–04	–8.47E+00	0.00E+00	1.56E+00	1.46E–02	–4.23E+00
		21.5	6.6	1.37E+00	4.32E–01	4.67E–01	1.30E–04	–8.95E+00	0.00E+00	1.49E+00	6.84E–03	–4.99E+00
		32.5	9.9	1.45E+00	3.67E–01	4.37E–01	3.10E–05	–1.04E+01	1.22E–02	2.63E+00	2.85E–03	–5.86E+00
		42.5	13.0	1.49E+00	3.83E–01	4.20E–01	2.70E–05	–1.05E+01	1.22E–02	2.19E+00	1.86E–03	–6.29E+00
		52.5	16.0	1.43E+00	3.76E–01	4.43E–01	4.00E–05	–1.01E+01	1.85E–02	2.95E+00	2.04E–03	–6.20E+00
	LGM-85-06 [d]	29	8.8		4.25E–01		4.80E–04	–7.64E+00				
		51	15.5		4.02E–01		8.40E–05	–9.39E+00				
	LGM-85-11 [d]	3	0.9		5.40E–01	5.40E–01	5.40E–04	–7.52E+00				
		30	9.1		5.15E–01	5.15E–01	2.80E–04	–8.18E+00				
	LLC-85-14 [d]	30	9.1	1.37E+00	4.41E–01		4.20E–04	–7.78E+00	0.00E+00	1.89E+00	6.00E–03	–5.12E+00
	LLC-85-15 [d]	10.5	3.2	1.46E+00	4.64E–01		1.60E–03	–6.44E+00	3.80E–02	2.04E+00	6.00E–03	–5.12E+00
	LLM-85-01 [d]	30	9.1		3.96E–01	3.96E–01	1.10E–04	–9.12E+00				

vpn= Vapor-phase notch

[a] *Parameters for these boreholes obtained and/or calculated from data in DBS&A (1996).*

[b] *Parameters for this borehole obtained and/or calculated from data in DBS&A (1995).*

[c] *Parameters for this borehole obtained and/or calculated from data in DBS&A (1996); stratigraphy from Puglisi and Vold (1995)*

[d] *Parameters from Rogers and Gallaher (1995)*

Annex IIIa: (Continued)
Parameters and Data Used for Statistical Analyses for

Unit	Borehole	Depth (ft)	Depth (m)	ρ_b (g/cm^3)	θ_s (cm^3/cm^3)	Porosity (cm^3/cm^3)	K_s (cm/s)	Ln K_s	θ_r (cm^3/cm^3)	n	α (cm^{-1})	Ln α
2 (cont.)	LLM-85-02 [d]	7	2.1		4.15E–01	4.15E–01	4.40E–04	–7.73E+00				
		36	11.0		4.65E–01	4.65E–01	1.20E–04	–9.03E+00				
	LLM-85-05 [d]	15	4.6		5.26E–01	5.26E–01	5.60E–04	–7.49E+00				
		36	11.0		7.36E–01	7.36E–01	2.20E–04	–8.42E+00				
1v	54-1001 [d]	68	20.7	1.20E+00	4.14E–01		1.30E–04	–8.95E+00	0.00E+00	1.89E+00	3.40E–03	–5.68E+00
		83	25.3	1.25E+00	4.60E–01		1.10E–04	–9.12E+00	0.00E+00	2.23E+00	2.20E–03	–6.12E+00
		102	31.1	1.19E+00	5.14E–01		1.60E–04	–8.74E+00	0.00E+00	1.78E+00	3.40E–03	–5.68E+00
		122	37.2	1.18E+00	4.64E–01		2.20E–05	–1.07E+01	0.00E+00	1.58E+00	4.10E–03	–5.50E+00
		142	43.3	1.20E+00	4.82E–01		8.20E–05	–9.41E+00	0.00E+00	1.43E+00	3.70E–03	–5.60E+00
	54-1002 [d]	92.5	28.2	1.26E+00	4.60E–01		8.10E–05	–9.42E+00	0.00E+00	2.21E+00	1.20E–03	–6.73E+00
		122	37.2	1.23E+00	4.95E–01		4.60E–05	–9.99E+00	0.00E+00	1.77E+00	3.10E–03	–5.78E+00
		142.5	43.4	1.19E+00	4.91E–01		2.50E–05	–1.06E+01	1.70E–02	1.39E+00	1.54E–02	–4.17E+00
	54-1003 [d]	102	31.1	1.22E+00	5.10E–01		1.30E–04	–8.95E+00	0.00E+00	1.73E+00	3.00E–03	–5.81E+00
		119.5	36.4	1.22E+00			9.90E–05	–9.22E+00				
	54-1006 [d]	76.9	23.4	1.28E+00	4.45E–01		9.80E–05	–9.23E+00	0.00E+00	1.88E+00	3.00E–03	–5.81E+00
		124.5	38.0	1.22E+00	4.35E–01		4.50E–05	–1.00E+01	0.00E+00	2.09E+00	3.50E–03	–5.66E+00
		136.7	41.7	1.28E+00	4.72E–01		5.70E–05	–9.77E+00	0.00E+00		1.40E–03	–6.57E+00
	54-1107 [a]	93.2	28.4	1.16E+00	5.49E–01	4.98E–01	1.29E–04	–8.96E+00	0.00E+00	1.47E+00	6.02E–03	–5.11E+00

vpn= Vapor-phase notch

[a] *Parameters for these boreholes obtained and/or calculated from data in DBS&A (1996).*

[b] *Parameters for this borehole obtained and/or calculated from data in DBS&A (1995).*

[c] *Parameters for this borehole obtained and/or calculated from data in DBS&A (1996); stratigraphy from Puglisi and Vold (1995)*

[d] *Parameters from Rogers and Gallaher (1995)*

Annex IIIa: (Continued)
Parameters and Data Used for Statistical Analyses for

Unit	Borehole	Depth (ft)	Depth (m)	ρ_b (g/cm^3)	θ_s (cm^3/cm^3)	Porosity (cm^3/cm^3)	K_s (cm/s)	Ln K_s	θ_r (cm^3/cm^3)	n	α (cm^{-1})	Ln α
1v (cont.)	54-1107 [a] (cont.)	96.25	29.3	1.18E+00	5.21E–01	4.89E–01	1.13E–04	–9.09E+00	0.00E+00	1.35E+00	9.51E–03	–4.66E+00
		98.2	29.9	9.30E–01	4.45E–01	6.01E–01	4.61E–05	–9.99E+00	0.00E+00	1.43E+00	5.82E–03	–5.15E+00
		99.2	30.2	1.13E+00	5.21E–01	5.11E–01	6.25E–04	–7.38E+00	2.18E–02	1.35E+00	2.97E–01	–1.21E+00
		101.3	30.9	1.20E+00	5.03E–01	4.83E–01	3.20E–05	–1.04E+01	0.00E+00	1.43E+00	2.64E–03	–5.94E+00
	54-1121 [a]	64.25	19.6	1.09E+00	5.32E–01	5.30E–01	2.21E–04	–8.42E+00	0.00E+00	1.50E+00	7.52E–03	–4.89E+00
		67.75	20.7	1.18E+00	5.44E–01	4.89E–01	1.64E–04	–8.72E+00	0.00E+00	1.70E+00	4.04E–03	–5.51E+00
		70.25	21.4	1.07E+00	5.25E–01	5.39E–01	1.43E–04	–8.85E+00	0.00E+00	1.44E+00	8.05E–03	–4.82E+00
		75.25	22.9	1.20E+00	4.71E–01	4.83E–01	7.32E–05	–9.52E+00	0.00E+00	1.68E+00	3.24E–03	–5.73E+00
		77.75	23.7	1.08E+00	5.39E–01	5.32E–01	1.71E–04	–8.67E+00	0.00E+00	1.38E+00	8.16E–03	–4.81E+00
	TA-54-G-5 [b]	60.5	18.4	1.17E+00	5.78E–01	5.42E–01	2.20E–04	–8.42E+00	0.00E+00	1.85E+00	4.97E–03	–5.30E+00
		70	21.3	1.17E+00	4.75E–01	5.45E–01	8.80E–05	–9.34E+00	0.00E+00	2.10E+00	1.31E–03	–6.64E+00
		82.5	25.2	1.18E+00	4.40E–01	5.43E–01	3.60E–05	–1.02E+01	0.00E+00	1.83E+00	2.15E–03	–6.14E+00
	G-P38-HH3 [c]	70.25	21.4	1.03E+00		5.58E–01	1.62E–03	–6.43E+00				
		122.25	37.3	1.02E+00		5.59E–01	2.31E–03	–6.07E+00				
		129.25	39.4	1.32E+00	5.39E–01	4.32E–01	2.47E–04	–8.31E+00	0.00E+00	1.89E+00	2.49E–03	–6.00E+00
		144.25	44.0	1.06E+00	5.25E–01	5.42E–01	3.42E–04	–7.98E+00	0.00E+00	1.69E+00	3.43E–03	–5.68E+00
		204.25	62.3	1.17E+00	5.30E–01	4.95E–01	1.82E–04	–8.61E+00	0.00E+00	1.49E+00	4.84E–03	–5.33E+00
		257.27	78.4	1.09E+00	4.76E–01	5.32E–01	5.58E–05	–9.79E+00	0.00E+00	1.60E+00	4.94E–03	–5.31E+00

vpn= Vapor-phase notch

[a] *Parameters for these boreholes obtained and/or calculated from data in DBS&A (1996).*

[b] *Parameters for this borehole obtained and/or calculated from data in DBS&A (1995).*

[c] *Parameters for this borehole obtained and/or calculated from data in DBS&A (1996); stratigraphy from Puglisi and Vold (1995)*

[d] *Parameters from Rogers and Gallaher (1995)*

Annex IIIa: (Continued)
Parameters and Data Used for Statistical Analyses for

Unit	Borehole	Depth (ft)	Depth (m)	ρ_b (g/cm^3)	θ_s (cm^3/cm^3)	Porosity (cm^3/cm^3)	K_s (cm/s)	Ln K_s	θ_r (cm^3/cm^3)	n	α (cm^{-1})	Ln α
1v (cont.)	LGM-85-06 [d]	99	30.2		5.26E–01		1.30E–03	–6.65E+00				
	LGM-85-11 [d]	94	28.7		6.43E–01	6.43E–01	1.10E–04	–9.12E+00				
	LLC-86-22 [d]	54.5	16.6	1.26E+00	5.10E–01		5.20E–05	–9.86E+00	2.00E–02	2.24E+00	3.70E–03	–5.60E+00
		54.5	16.6	1.26E+00	4.83E–01		2.50E–04	–8.29E+00	0.00E+00	1.93E+00	4.50E–03	–5.40E+00
		65	19.8	1.27E+00	4.87E–01		1.40E–04	–8.87E+00	0.00E+00	2.35E+00	2.60E–03	–5.95E+00
		131.5	40.1	1.05E+00	5.07E–01		1.90E–05	–1.09E+01	1.20E–02	1.59E+00	2.10E–03	–6.17E+00
		131.5	40.1	1.05E+00	5.08E–01		2.70E–05	–1.05E+01	4.40E–02	1.71E+00	2.10E–03	–6.17E+00
	LLM-85-01 [d]	52	15.9		6.44E–01	6.44E–01	2.60E–04	–8.26E+00				
		101	30.8		6.21E–01	6.21E–01	2.50E–04	–8.29E+00				
	LLM-85-02 [d]	67	20.4		4.33E–01	4.33E–01	9.80E–05	–9.23E+00				
		117	35.7		4.85E–01	4.85E–01	1.70E–04	–8.68E+00				
		76	23.2		7.42E–01	7.42E–01	1.30E–04	–8.95E+00				
vpn	TA-54-G-5 [b]	92.5	28.2	1.13E+00	5.25E–01	5.58E–01	6.80E–05	–9.60E+00	0.00E+00	1.40E+00	3.54E–03	–5.64E+00
	MC-1 [a]		0.0	1.09E+00	5.33E–01	5.31E–01	3.29E–04	–8.02E+00	0.00E+00	1.67E+00	3.96E–03	–5.53E+00
	MC-2 [a]		0.0	1.01E+00	4.39E–01	5.65E–01	4.54E–05	–1.00E+01	0.00E+00	1.80E+00	2.72E–03	–5.91E+00
	MC-4 [a]		0.0	1.15E+00	4.45E–01	5.03E–01	4.77E–06	–1.23E+01	1.48E–02	1.52E+00	1.48E–02	–4.21E+00
	MC-5 [a]		0.0	1.10E+00	4.33E–01	5.27E–01	1.54E–05	–1.11E+01	0.00E+00	1.73E+00	1.59E–03	–6.44E+00
1g	54-1002 [d]	179.3	54.7	1.16E+00	3.93E–01		6.50E–05	–9.64E+00	0.00E+00	1.82E+00	4.30E–03	–5.45E+00

vpn= Vapor-phase notch

[a] *Parameters for these boreholes obtained and/or calculated from data in DBS&A (1996).*

[b] *Parameters for this borehole obtained and/or calculated from data in DBS&A (1995).*

[c] *Parameters for this borehole obtained and/or calculated from data in DBS&A (1996); stratigraphy from Puglisi and Vold (1995)*

[d] *Parameters from Rogers and Gallaher (1995)*

Annex IIIa: (Continued)
Parameters and Data Used for Statistical Analyses for

Unit	Borehole	Depth (ft)	Depth (m)	ρ_b (g/cm^3)	θ_s (cm^3/cm^3)	Porosity (cm^3/cm^3)	K_s (cm/s)	Ln K_s	θ_r (cm^3/cm^3)	n	α (cm^{-1})	Ln α
1g (cont.)	54-1002 [d] (cont.)	244	74.4	1.14E+00	3.93E–01		1.70E–04	–8.68E+00	0.00E+00	1.75E+00	6.20E–03	–5.08E+00
	54-1003 [d]	157	47.9	1.14E+00	4.32E–01		1.30E–04	–8.95E+00	2.50E–02	1.77E+00	4.00E–03	–5.52E+00
		207	63.1	1.18E+00	4.28E–01		1.50E–04	–8.81E+00				
		261	79.6	1.11E+00	4.88E–01		2.70E–04	–8.22E+00				
		271.5	82.8	1.31E+00	4.10E–01		2.60E–04	–8.26E+00				
	54-1006 [d]	161	49.1	1.13E+00	5.26E–01		1.20E–04	–9.03E+00				
	54-1107 [a]	104.3	31.8	1.13E+00	4.92E–01	5.12E–01	8.06E–05	–9.43E+00	0.00E+00	2.00E+00	2.64E–03	–5.94E+00
		108.25	33.0	1.15E+00	5.21E–01	5.05E–01	4.61E–04	–7.68E+00	0.00E+00	1.77E+00	4.61E–03	–5.38E+00
	54-1121 [a]	80.25	24.5	1.18E+00	4.35E–01	4.93E–01	3.71E–05	–1.02E+01	4.31E–02	1.80E+00	3.04E–03	–5.80E+00
		82.75	25.2	1.14E+00	4.98E–01	5.09E–01	1.22E–04	–9.01E+00	1.59E–02	1.59E+00	5.94E–03	–5.13E+00
		87.75	26.8	1.14E+00	4.55E–01	5.10E–01	1.02E–04	–9.19E+00	0.00E+00	1.67E+00	5.06E–03	–5.29E+00
	CDBM-1 [d]	24	7.3	1.17E+00	4.88E–01		6.20E–05	–9.69E+00	0.00E+00	1.94E+00	2.90E–03	–5.84E+00
		34	10.4	1.07E+00	4.62E–01		2.20E–04	–8.42E+00	0.00E+00	1.63E+00	5.50E–03	–5.20E+00
		44	13.4	1.26E+00	4.45E–01		7.00E–05	–9.57E+00	0.00E+00	1.68E+00	4.10E–03	–5.50E+00
		54	16.5	1.09E+00	4.46E–01		4.60E–04	–7.68E+00	0.00E+00	1.52E+00	7.00E–03	–4.96E+00
		64	19.5	1.23E+00	4.51E–01		1.20E–04	–9.03E+00	5.00E–03	1.72E+00	5.30E–03	–5.24E+00
	CDBM-2 [d]	28	8.5	1.19E+00	4.79E–01		8.50E–04	–7.07E+00	5.10E–02	1.43E+00	2.81E–02	–3.57E+00
		38	11.6	9.40E–01	4.84E–01		4.50E–04	–7.71E+00	2.60E–02	1.79E+00	7.10E–03	–4.95E+00

vpn= Vapor-phase notch

[a] *Parameters for these boreholes obtained and/or calculated from data in DBS&A (1996).*

[b] *Parameters for this borehole obtained and/or calculated from data in DBS&A (1995).*

[c] *Parameters for this borehole obtained and/or calculated from data in DBS&A (1996); stratigraphy from Puglisi and Vold (1995)*

[d] *Parameters from Rogers and Gallaher (1995)*

Annex IIIa: (Continued)
Parameters and Data Used for Statistical Analyses for

Unit	Borehole	Depth (ft)	Depth (m)	ρ_b (g/cm^3)	θ_s (cm^3/cm^3)	Porosity (cm^3/cm^3)	K_s (cm/s)	Ln K_s	θ_r (cm^3/cm^3)	n	α (cm^{-1})	Ln α
1g (cont.)	TA-54-G-5 [b]	102.5	31.3	1.14E+00	4.52E–01	5.30E–01	3.10E–05	–1.04E+01	8.25E–03	2.16E+00	2.60E–03	–5.95E+00
	LGM-85-06 [d]	115	35.1		5.63E–01		9.10E–05	–9.31E+00				
	LGM-85-11 [d]	115	35.1		6.01E–01	6.01E–01	1.80E–04	–8.62E+00				
	LLM-85-01 [d]	124	37.8		4.89E–01	4.89E–01	2.20E–04	–8.42E+00				
	LLM-85-05 [d]	123	37.5		6.56E–01	6.56E–01	1.60E–04	–8.74E+00				
Tsankawi	54-1121 [a]	121.25	37.0	1.21E+00	4.86E–01	4.69E–01	1.16E–04	–9.06E+00	0.00E+00	1.52E+00	2.46E–02	–3.70E+00
	54-1123 [a]	89.25	27.2	1.20E+00	4.64E–01	4.63E–01	8.30E–05	–9.40E+00	0.00E+00	1.36E+00	2.39E–02	–3.74E+00
	CDBM-1 [d]	89	27.1	1.20E+00	4.42E–01		2.30E–04	–8.38E+00	0.00E+00	1.43E+00	1.31E–02	–4.34E+00
		94	28.7	1.05E+00	5.03E–01		1.50E–03	–6.50E+00	1.60E–02	1.59E+00	1.73E–02	–4.06E+00
Cerro Toledo	54-1121 [a]	124.75	38.0	1.28E+00	4.26E–01	4.74E–01	5.60E–05	–9.79E+00	5.41E–03	1.57E+00	8.05E–03	–4.82E+00
		134.75	41.1	1.24E+00	4.15E–01	4.72E–01	1.25E–04	–8.99E+00	0.00E+00	1.61E+00	6.86E–03	–4.98E+00
	54-1123 [a]	91.75	28.0	1.23E+00	3.98E–01	4.73E–01	2.77E–04	–8.19E+00	0.00E+00	1.45E+00	1.10E–02	–4.51E+00
Otowi	CDBM-1 [d]	104	31.7	1.20E+00	4.46E–01		2.30E–04	–8.38E+00	0.00E+00	1.49E+00	6.40E–03	–5.05E+00
		114	34.8	1.29E+00	4.51E–01		1.60E–04	–8.74E+00	2.50E–02	1.78E+00	4.50E–03	–5.40E+00
		124	37.8	1.10E+00	4.37E–01		2.90E–04	–8.15E+00	0.00E+00	1.45E+00	8.20E–03	–4.80E+00
		134	40.9	1.24E+00	4.47E–01		1.60E–04	–8.74E+00	1.20E–02	1.65E+00	5.70E–03	–5.17E+00
		144	43.9	1.14E+00	4.28E–01		4.20E–04	–7.78E+00	4.20E–02	2.31E+00	5.50E–03	–5.20E+00
		154	47.0	1.29E+00	4.10E–01		1.00E–04	–9.21E+00	2.70E–02	1.89E+00	3.90E–03	–5.55E+00

vpn= Vapor-phase notch

[a] *Parameters for these boreholes obtained and/or calculated from data in DBS&A (1996).*

[b] *Parameters for this borehole obtained and/or calculated from data in DBS&A (1995).*

[c] *Parameters for this borehole obtained and/or calculated from data in DBS&A (1996); stratigraphy from Puglisi and Vold (1995)*

[d] *Parameters from Rogers and Gallaher (1995)*

Annex IIIa: (Continued)
Parameters and Data Used for Statistical Analyses for

Unit	Borehole	Depth (ft)	Depth (m)	ρ_b (g/cm^3)	θ_s (cm^3/cm^3)	Porosity (cm^3/cm^3)	K_s (cm/s)	Ln K_s	θ_r (cm^3/cm^3)	n	α (cm^{-1})	Ln α
Otowi (cont.)	CDBM-1 [d] (cont.)	164	50.0	1.21E+00	4.36E–01		1.70E–04	–8.68E+00	0.00E+00	1.49E+00	6.10E–03	–5.10E+00
		174	53.0	1.18E+00	4.12E–01		2.10E–04	–8.47E+00	3.00E–02	1.90E+00	5.30E–03	–5.24E+00
		184	56.1	1.18E+00	4.32E–01		3.00E–04	–8.11E+00	2.60E–02	1.89E+00	6.20E–03	–5.08E+00
		189	57.6	1.19E+00	4.30E–01		1.80E–04	–8.62E+00	8.00E–03	1.65E+00	5.70E–03	–5.17E+00
	CDBM-2 [d]	67	20.4	1.16E+00	4.46E–01		5.00E–04	–7.60E+00	1.70E–02	1.60E+00	8.40E–03	–4.78E+00
		68	20.7	1.22E+00	4.40E–01		2.70E–04	–8.22E+00	3.90E–02	1.99E+00	6.00E–03	–5.12E+00
Basalts	54-1015 [a]	384.65	117.3	2.19E+00	1.62E–01	2.52E–01	1.80E–09	–2.01E+01	0.00E+00	1.26E+00	2.37E–02	–3.74E+00
		464.25	141.5	2.77E+00	4.50E–02	5.50E–02	8.74E–11	–2.32E+01	0.00E+00	1.17E+00	2.52E–02	–3.68E+00
		465.75	142.0	2.84E+00	8.70E–02	3.00E–02	2.65E–09	–1.97E+01	0.00E+00	1.38E+00	1.31E–03	–6.64E+00
		521.25	158.9	2.81E+00	1.05E–01	4.20E–02	3.75E–09	–1.94E+01	0.00E+00	1.21E+00	8.25E–02	–2.50E+00

vpn= Vapor-phase notch

[a] *Parameters for these boreholes obtained and/or calculated from data in DBS&A (1996).*

[b] *Parameters for this borehole obtained and/or calculated from data in DBS&A (1995).*

[c] *Parameters for this borehole obtained and/or calculated from data in DBS&A (1996); stratigraphy from Puglisi and Vold (1995)*

[d] *Parameters from Rogers and Gallaher (1995)*

Attachment IV
Incorporation of Sorption in the Micromixing Model for the Los Alamos National Laboratory Technical Area-54, Area G Groundwater Pathway Model

Prepared by
Bruce Robinson
Hari Viswanathan
Phil Stauffer
Shaoping Chu

IV.1 Introduction

In a complex numerical model such as the groundwater transport model for Area G, spatial variability in hydrologic and transport properties, and nonpoint-source regions over which contaminants enter the system give rise to a distribution of reactive travel times through the system. Particle-tracking calculations provide a straightforward means for representing this variability for a simple source term such as a pulse. However, particle-tracking approaches become cumbersome for more complex sources and in cases where chemical transformations, sorption, or radioactive decay must be taken into account.

A simplified approach has been developed for obtaining a solute mass-flux model for reactive chemical species using particle-tracking results obtained from a groundwater flow and transport model of arbitrary complexity. Information extracted from particle-tracking simulations using the complex, multidimensional model are used to construct a simplified model that reproduces the residence time distribution (RTD) of a conservative solute using the theory introduced by Robinson and Viswanathan (2003). For conservative solutes or solutes with reactions that do not vary spatially, this mixing model can be used directly to simulate time-dependent solute-release functions or sorption and kinetic parameters. This model, called an abstracted or reduced model, can be run at a small fraction of the computational burden of the original groundwater flow model. When reactions possess spatially dependent properties, the situation becomes more complex. However, by treating the particle-tracking information statistically, reasonable abstraction models can be constructed for those situations as well.

IV.2 Numerical Formulation

The micromixing model of Robinson and Viswanathan (2003) may be used to simulate a solute molecule traveling through a system with a conservative (nonreactive) travel time of t_p. This molecule is subject to advective and dispersive transport so that, in general, there is a distribution of arrival times at a downstream location for an ensemble of particles released from a source. The micromixing model constructs a simple one-dimensional (1-D) pathway that reproduces an arbitrary RTD for this conservative transport situation. This simplified model can be used in place of the original model to reproduce the distribution of travel times, while incorporating specified source terms and chemical reactions. The goal of this study, which extends the 2003 work of Robinson and Viswanathan, is to incorporate sorption into the model in a manner that reproduces the original model's sorption behavior.

For a particle traveling with a conservative travel time of t_p, the corresponding reactive travel time (t_r) for a species undergoing equilibrium, linear sorption (the so-called K_d model) can be expressed as follows:

$$t_r = \int_0^t R(t')dt' \quad (1)$$

Where

t_r = the reactive travel time
$R(t')$ = the path-dependent retardation factor (i.e., the local retardation factor for the portion of the flow path traveled between times t' and $t' + dt'$)

In terms of reproducing a given transit time of a particle, the final arrival time is all that matters. Therefore, one approach is to define an effective retardation factor R_p for a particle as follows:

$$R_p = t_r / t_p = \int_0^t R(t')dt' / t_p \quad (2)$$

Where

t_p = the conservative (nonreactive) travel time
R_p = the effective retardation factor

These expressions divide the particle path into discrete intervals (at the resolution of the numerical model) of computed travel times to obtain an average retardation factor. Numerically, the integral in Equation 2 is computed as follows:

$$t_r = \int_0^t R(t')dt' = \sum_{i=1}^{N} R_i(t_{p,i} - t_{p,i-1}) \quad (3)$$

Where

i = the i^{th} segment of the particle path
R_i = the local retardation factor along the i^{th} segment

The time difference included in this equation represents the conservative travel time along a given segment.

Equation 4 can be used to calculate the local retardation factor for segment *i*:

$$R_i = 1 + \frac{\rho_i K_{d,i}}{\theta_i} \quad (4)$$

Where

ρ_i = the bulk rock density
$K_{d,i}$ = the sorption coefficient
θ_i = the volumetric water content

Although the development above holds for a single particle, complications arise when an ensemble of particles of different travel times are considered. The complications arise from the fact that all paths of conservative residence time t_p need not possess the same sorbing travel time because the paths may not have equivalent R_p. Therefore, in the most general sense, the transport times of conservative and sorbing species must be described using a joint probability distribution function. Using this approach, the following relations apply:

$$\int_0^\infty h(t_p, t_r)dt_r = f(t_p)dt_p \quad 5$$

and

$$\int_0^\infty h(t_p, t_r)dt_p = g(t_r)dt_r \quad 6$$

Where

$h(t_p, t_r)dt_p dt_r$ = the fraction of the particle trajectories with conservative residence times between t_p and $t_p + dt_p$ and sorbing residence times between t_r and $t_r + dt_r$
$f(t_p)dt_p$ = the fraction of conservative particles leaving the system with residence times between t_p and $t_p + dt_p$
$g(t_r)dt_r$ = the fraction of sorbing particles leaving the system with residence times between t_r and $t_r + dt_r$

As discussed earlier, particle-tracking information from a complex model provides the means for determining $h(t_p, t_r)$, as each particle passing through a model possesses a unique t_p and t_r. To proceed from this information to a simplified mixing model that includes sorption, it is recognized that the exact order in which the sorption takes place within the mixing reactor is relatively unimportant, as long as the appropriate RTDs are reproduced. Furthermore, for linear, equilibrium sorption, Robinson and Viswanathan (2003) showed that both early and late mixing models yield an identical result. In the present study, the reduced model is assembled on the basis of the maximum mixedness model developed in Robinson and Viswanathan (2003), but it is recognized that the minimum mixedness model would yield the same results. The goal is to

populate the maximum mixedness model with a variable sorption coefficient along the flow path in a manner that approximates the behavior of the complex model.

Because all particles of a given conservative travel time do not necessarily have the same sorptive travel time, it is impossible in a single mixing model such as this to exactly replicate the behavior of the complex system. However, reasonable approximations are possible, and these can be verified simply by performing a comparison to the results from the original model. In this study, the approximation is to define $\bar{t}_r(t_p)$, the mean sorptive travel time for a given conservative travel time t_p, so as to yield a reasonable average sorptive travel time that applies for a given t_p:

$$\bar{t}_r(t_p) = \int_0^\infty \frac{t_r h(t_p, t_r)}{f(t_p)} dt_r \qquad 7$$

Where

$\bar{t}_r(t_p)$ = the mean sorptive travel time for a given conservative travel time t_p

Equation 7 prescribes that the arithmetic average of the t_r values be used for all particles of conservative travel time t_p (i.e., values between t_p and $t_p + dt_p$). Subject to checks using the original model, this travel time abstraction is postulated to yield a reactive RTD that is close to that of the original model.

Next, the function $\bar{t}_r(t_p)$ is used to populate the maximum mixedness model with sorption parameters along its length. Because the internal flow in the model is plug flow, the sorption parameters at all locations less than $x(t_p)$ (the location along the model associated with residence time t_p) must be accounted for when the value is assigned at the corresponding location in order to reproduce $\bar{t}_r(t_p)$ for a particular travel time t_p. In other words, the local retardation factor that yields the proper reactive travel time must be incrementally determined. The following expressions from Robinson and Viswanathan (2003) describe the construction of the mixedness model:

$$x(t_p) = \frac{Q}{\theta A_x} \int_0^{t_p} [1 - F(t_p)] dt_p \qquad 8$$

and

$$q(t_p) = Q f(t_p) dt_p \qquad 9$$

Where

$x(t_p)$ = the location along the model associated with residence time t_p

Q = the volumetric flow rate in the mixing model

θ = the volumetric water content (assumed constant along the model)
A_x = the cross-sectional area of the equivalent 1-D path
$F(t_p)$ = the cumulative RTD, and
$q(t_p)$ = the incremental flow rate entering the model at $x(t_p)$

One way to approach this problem is to compute a spatially dependent retardation factor $R_f(t_p)$ as the local retardation factor for the interval within the model corresponding to residence times between t_p and $t_p + dt_p$ using the following expression:

$$\bar{t}_r(t_p) = \int_0^{t_p} R(t_p)dt_p \qquad 10$$

Numerically, this integration can be carried out along the model. Starting at $t_p = 0$ (the model outlet), the following is assigned: $R(t_p \le t_{p,\min}) = \bar{t}_r(t_{p,\min})/t_{p,\min}$. This allows the desired sorptive travel time for the mass arriving at the outlet to be achieved with the absolute shortest conservative travel time. Then, for each successive interval in the mixing model,

$$R(t_p + dt_p) = \frac{\bar{t}_r(t_p + dt_p) - \bar{t}_r(t_p)}{dt_p} \qquad 11$$

Equation 11 prescribes the incremental sorbing travel time needed to attain the "correct" overall retardation factor and travel time for the mass entering the system at the location corresponding to $t_p + dt_p$.

The above approach takes advantage of a simplifying assumption to facilitate the construction of the mixing model for sorption, namely that the distribution of t_r values at a given t_p be used to compute an average sorptive travel time function $\bar{t}_r(t_p)$, as shown in Equation 7. Nevertheless, this approach still requires the cell-by-cell definition of the retardation factor to reproduce this function in the model. A further simplification may be possible that allows the entire model to be reduced to a uniform retardation factor. For systems in which the function $\bar{t}_r(t_p)$ versus t_p is a straight line, it is observed that the slope of the straight line is an effective retardation factor that would apply for all travel times, and therefore a uniform retardation factor throughout the mixing model would be applicable.

The validity of each of these successively more restrictive approximations must be evaluated on a case-by-case basis. To evaluate a particular flow field and transport scenario, particle-tracking runs can be conducted in which, for each particle trajectory, t_p and t_r are computed, and a scatter plot of t_r and t_p is produced. If the series of points follows a relatively tight, confined

curve (all particles of time t_p have approximately the same value of t_r), then the mixing model can be assigned retardation factors along its length using Equation 11. If that curve is a straight line, then the retardation factor that applies throughout the entire mixing model is computed as t_r / t_p.

IV.3 Transformation of Sorption Parameters to 1-D Abstractions

This section presents an analysis that demonstrates the relationship between sorption parameters in the three-dimensional (3-D) site-scale Area G model and sorption parameters in the 1-D abstraction models. Sorption of radionuclides in the 3-D site-scale model is limited to the Bandelier Tuff, and thus a single sorption distribution coefficient, K_d, is assigned to all units above the Cerros del Rio basalt. The relationship between K_d and the amount of retardation experienced by a radionuclide in the system is given by the following equation:

$$R_f = 1 + \frac{K_d \rho_b}{s\phi} \qquad 12$$

Where

R_f = the retardation factor
K_d = the distribution coefficient
ρ_b = bulk rock density
s = saturation
ϕ = porosity

In the 3-D model, s, ρ_b, ϕ, and K_d may vary spatially throughout the model.

The K_d for the 3-D model is divided by the K_d for the 1-D model to calculate a transformation factor (Table IV-1); this factor is used to transform the stochastic K_d chosen by the GoldSim® software for each realization and species into the correct K_d for input into the 1-D Finite Element Heat and Mass (FEHM) abstraction model. The transformation factor calculated for a given infiltration rate and release location is not sensitive to the value of K_d, allowing the 80 values presented in Table IV-1 to be applied to all values of K_d that may be used in the stochastic GoldSim simulations. Figure IV-1 compares a 3-D particle breakthrough simulation to a 1-D abstraction simulation (with and without the transformation factor applied) for a release from waste disposal region 1 with an infiltration rate of 1.5 mm/yr (0.06 in.), a 3-D model K_d of 0.1, and a 1-D model transformation factor for K_d of 1.5. All 80 transformation factors in Table IV-1 (i.e., 8 waste disposal regions × 10 infiltration rates) are estimated using this method.

Table IV-1
Transformation Factor Matrix Used to Convert Distribution Coefficients to Values Used in the GoldSim One-Dimensional Abstraction Models

Infiltration (mm/yr)	FFindex	Distribution Coefficient Value by Waste Disposal Region [a]							
		1	2	3	4	5	6	7	8
0.10	1	2.3	2.3	2.8	2.7	2.5	2.0	2.2	2.4
0.25	2	2.0	2.0	2.5	2.2	2.2	1.8	2.0	2.1
0.50	3	1.5	1.8	2.1	2.0	2.0	1.6	1.8	1.9
1.00	4	1.5	1.5	1.8	1.8	1.7	1.4	1.5	1.7
1.50	5	1.5	1.5	1.8	1.6	1.6	1.4	1.4	1.6
2.00	6	1.3	1.4	1.7	1.5	1.5	1.3	1.3	1.5
4.00	7	1.2	1.2	1.5	1.3	1.4	1.1	1.2	1.3
6.00	8	1.1	1.2	1.4	1.3	1.3	1.1	1.1	1.3
8.00	9	1.1	1.1	1.3	1.2	1.2	1.0	1.1	1.2
10.00	10	1.0	1.1	1.2	1.1	1.1	1.0	1.0	1.1

FFindex = Flow-field index used by GoldSim to select the 10 different infiltration scenarios

[a] Numbers are rounded to two significant digits.

Similarities in peak breakthrough times for releases from waste disposal regions 1 and 3 can be seen in Figures IV-2 and IV-3, respectively. The fits between the 1-D abstraction breakthrough curves and the 3-D particle breakthrough distributions are quite good when the K_d is low. As the distribution coefficient increases, the scatter in the 3-D breakthrough distributions becomes more pronounced and the fit is not as accurate. In general, low values of K_d and higher infiltration rates lead to better matches between the 3-D and 1-D models. The algorithm used to create the 1-D abstraction leads to some smoothing of the scattered data and approximations of the shape and peak value of the 3-D data. Although the fits appear less good at longer times, these times fall well beyond the end of the 1,000-year compliance period and the approximate fit is acceptable for the analysis. More importantly, the 1-D and 3-D results for times less than 5,000 years match well and provide confidence that the 1-D abstraction retains the information embedded in the 3-D model.

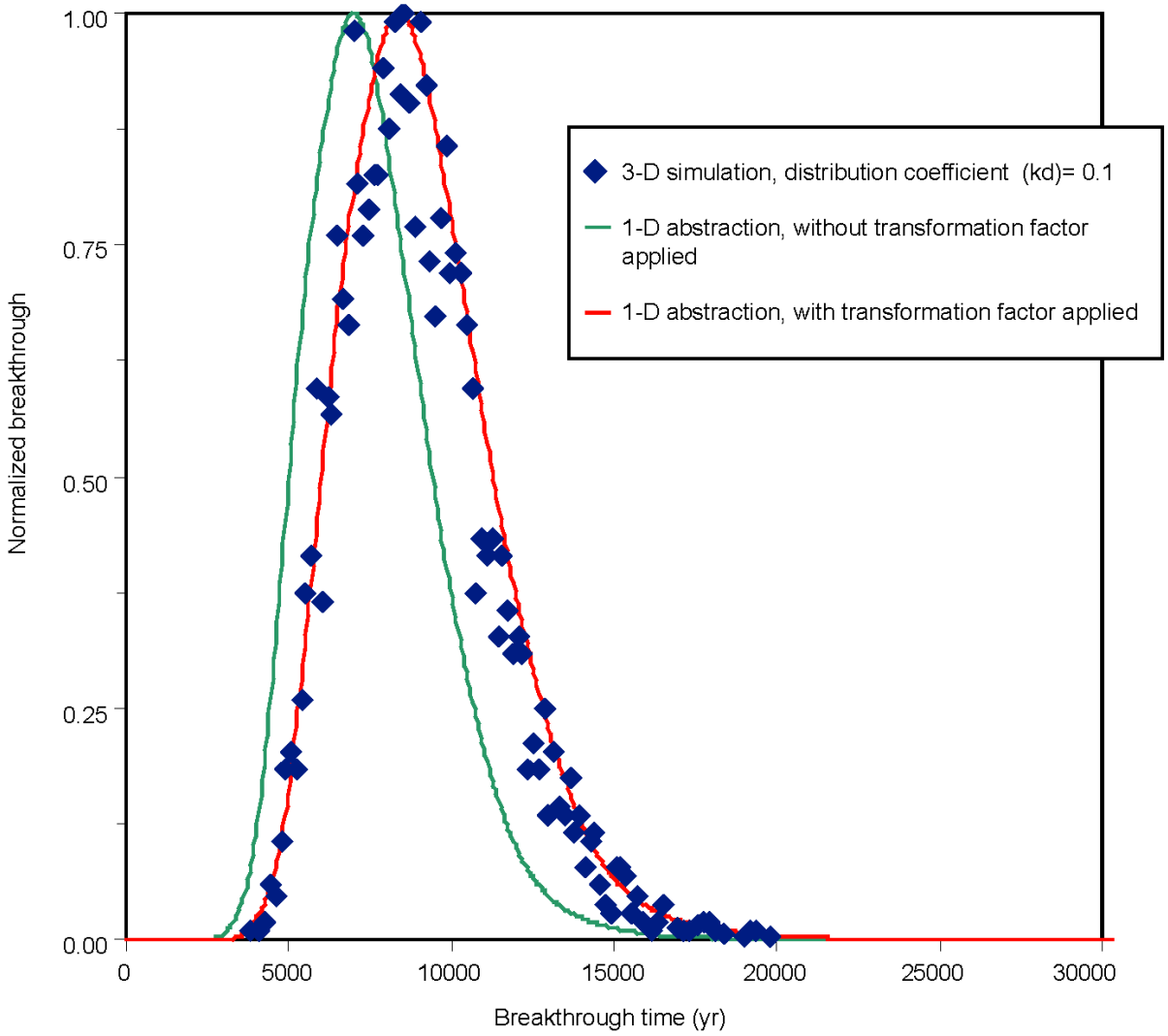

Figure IV-1
1-D Abstraction vs. 3-D Simulation
for Waste Disposal Region 1 (infiltration rate = 1.5 mm/yr)

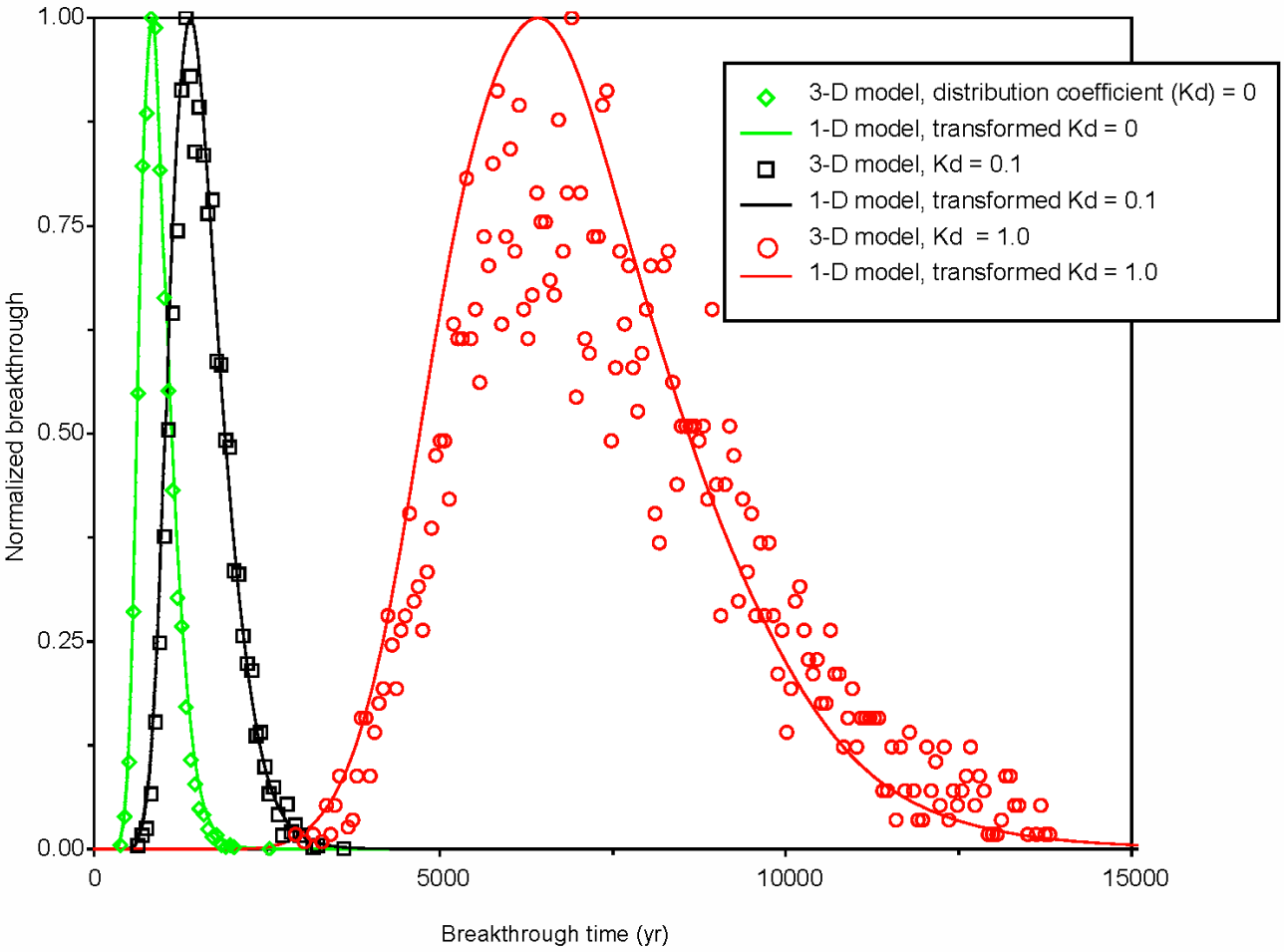

Figure IV-2
1-D Plume vs. 3-D Particle Breakthrough Curves for Waste Disposal Region 1 (infiltration rate = 10 mm/yr)

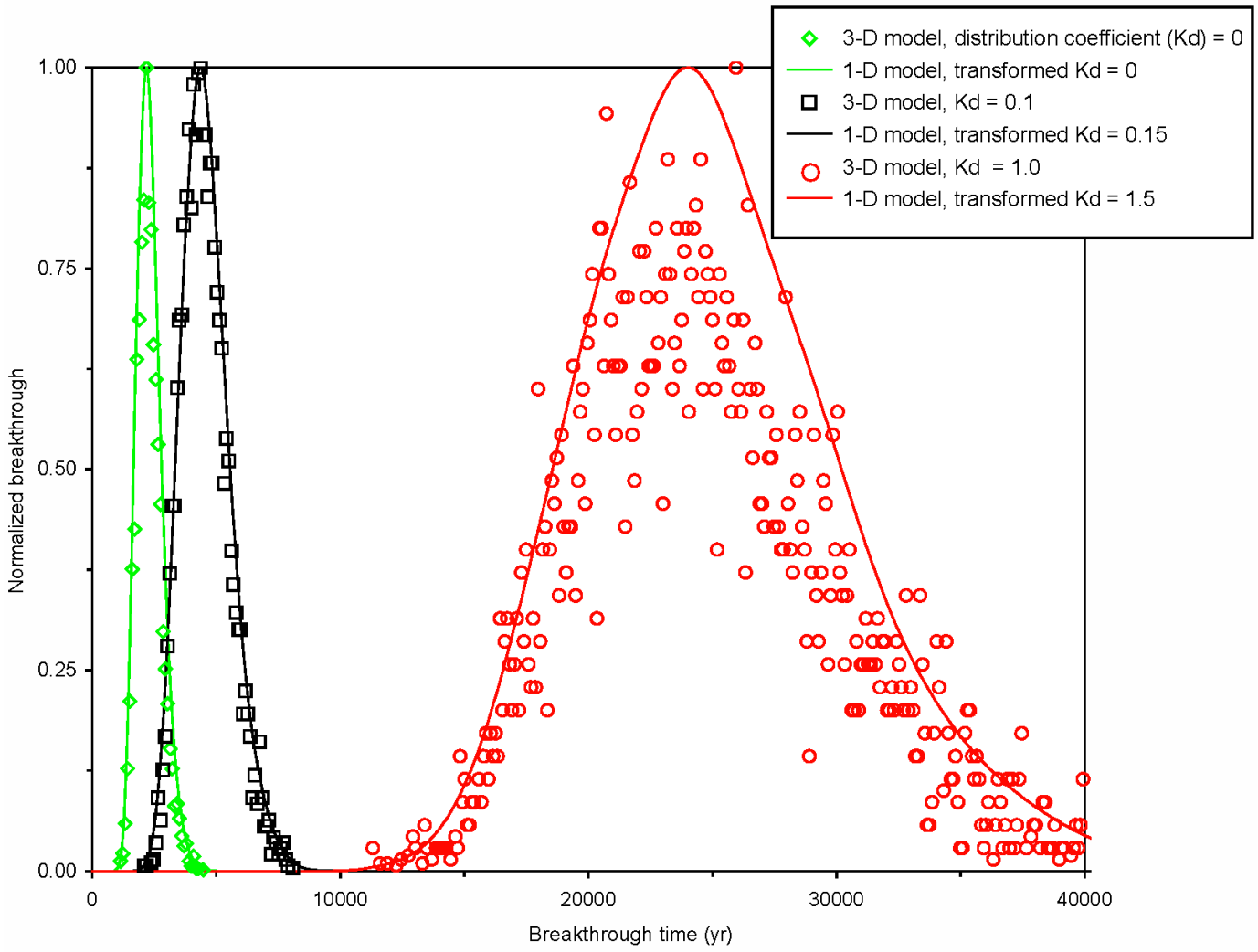

Figure IV-3
1-D Plume vs. 3-D Particle Breakthrough Curves for Waste Disposal Region 3 (infiltration rate = 4 mm/yr)

IV.4 References

Robinson, B.A. and H. Viswanathan, 2003, "Application of the Theory of Micromixing to Groundwater Reactive Transport Models," *Water Resources Res*., Vol. 39, No. 11.

Attachment V
Details on the Coupling of GoldSim and the Finite Element Heat and Mass Transfer Code for the Los Alamos National Laboratory TA-54, Area G Groundwater Pathway Model

Authors:
Philip Stauffer
Hari Viswanathan
Shaoping Chu
Zora Dash

V.1 Introduction

This attachment describes the manner in which the system-level GoldSim® model of Area G is coupled with the process-level Finite Element Heat and Mass (FEHM) model of the groundwater pathway. Section V-2 provides background information on how the personal computer environment is configured to run the coupled models. Section V-3 describes the parameters that are passed from the GoldSim model to FEHM to control the groundwater simulations and to maintain compatibility with the logic structure embedded in FEHM. Details about the FEHM data file that are specific to the Area G model are presented in Section V-4. Finally, Section V-5 provides pieces of the FEHM source code that have been modified and describe how these changes allow FEHM and GoldSim to communicate. Throughout this attachment, the GoldSim working directory refers to the directory that contains the GoldSim Area G performance assessment and composite analysis model.

V.2 Directory Structure and File Requirements for the GoldSim Coupling

The GoldSim model calls FEHM eight times simultaneously during the model simulations. Several modifications were made to FEHM to ensure that file-sharing violations and memory management errors do not occur. The first step was to develop a subdirectory structure that organizes the parameter files associated with each possible combination of waste disposal region and flow-field index. The structure consists of eight subdirectories (clusters 1 through 8) located in the GoldSim working directory; these subdirectories correspond to the eight waste disposal regions. Each subdirectory contains 10 *Flowfield index* subdirectories (A through J). Starting with directory A, these correspond to infiltration rates of 0.1, 0.25, 0.5, 1.0, 1.5, 2.0, 4.0, 6.0, 8.0, and 10 mm/yr (0.0039, 0.0098, 0.02, 0.039, 0.059, 0.079, 0.16, 0.24, 0.32, and 0.39 in./yr). These directories and the FEHM input files they contain were built using a shell script and two FORTRAN codes (see *Attachment VI*). Each of the 80 individual subdirectories located within the GoldSim working directory contains the three files required to set up and run a single FEHM simulation (i.e., fehmn.files, goldfehm.dat, and areag.rtd).

To avoid memory management errors, a copy of the FEHM executable (i.e., fehm_01.dll through fehm_08.dll) must be located in each of the eight cluster subdirectories. A template batch file (Copy_RELEASE_dll.bat) is provided that copies a master FEHM executable to the correct file names in the correct cluster subdirectories.

The coupling between GoldSim and FEHM allows the user to specify how many parameters are passed to each FEHM simulation from the GoldSim model. This is done using the file fehmn.gold. The first number in this file is the total number of user-specified inputs found in the

GoldSim model. These inputs are specified in the FEHM external pathway element in GoldSim; the values of these parameters are explained in the next section.

The output from the eight simultaneous FEHM simulations is written to separate files in the eight cluster subdirectories. The generic names for these files are fehmn.err, a_in_array.txt, and fehmn.log; the actual files for each cluster include the cluster number (e.g., fehm8.err, a_in8.txt, and fehm8.log for cluster 8). This was done so that each file has a unique name to avoid any possible memory violations when running eight simultaneous FEHM simulations.

V.3 Parameter-Sharing between GoldSim and FEHM

GoldSim passes a string of variables to FEHM to initialize each simulation and at each time step of the system-level simulation. These variables include *time*, *Flowfield index*, *cluster*, the *number of species* that FEHM will be simulating, the K_d sorption parameter for each species, and the *amount of mass* entering the groundwater pathway from each waste disposal region (Table V-1). The GoldSim Area G performance assessment and composite analysis model uses a stochastic variable called *flowfield* to pick an infiltration scenario for each realization. This value is passed to FEHM, which then sets up and runs the correct residence time distribution (RTD) function from the subdirectories cluster 1 through cluster 8 and the 10 infiltration subdirectories A through J. This process is repeated eight times, corresponding to the eight waste disposal regions, to activate the eight FEHM external pathways in the system model; each external pathway contains a call to the FEHM dynamic link library (dll).

Once the appropriate files for the randomly chosen *Flowfield index* have been assembled by FEHM, GoldSim initializes the simulation by passing the first time increment to FEHM. In each simultaneous FEHM simulation, GoldSim passes into FEHM the amount of mass entering the groundwater pathway for a given waste disposal region. FEHM accepts the incoming mass and adds it to the ongoing calculation of transport through the subsurface to the compliance boundary using the abstraction model described in *Attachment IV*. Within each of the eight simultaneous FEHM simulations, the cumulative transport of each species is modeled, taking into account sorption, radioactive decay, and ingrowth. FEHM takes many small time steps for each GoldSim time step to ensure that the tracer transport solution converges to the correct answer. At the end of each GoldSim time step, FEHM passes any mass reaching the compliance boundary back to GoldSim. Mass reaching the compliance boundary represents radionuclides that have migrated from the waste inventory or daughter products formed as a result of ingrowth during transport along the groundwater pathway. Simulations performed to test the GoldSim coupling included radioactive decay, ingrowth, and sorption.

Table V-1
Variables Passed from GoldSim to FEHM during System-Level Simulations

IN Array Index	GoldSim Variable	Range of Values	FEHM Variable	Comments
1	*Etime*	0 to final time	in(1)	---
2	*Flowfield index*	1 to 10; generated within GoldSim from a stochastic distribution	in(2)	---
3	Realization	1 to N realizations	in(3)	---
4	Area G Flag for FEHM	666	in(4)	Fixed value
5	Timestep_Length (yrs)	Variable	in(5)	---
6	Cluster	1 to 8	in(6)	Cluster index
7	Number of FEHM species	Currently fixed at 19	in(7)	Number of FEHM species
8 to (8 + in(7) -1)	GoldSim Species number for each of the 19 FEHM species	1 to the total number of GoldSim species	in(8) through in(8 + in(7) -1)	Species in FEHM are numbered 1 to 19
(8 + in(7)) to (8 + 2 × in(7) -1)	Sorption parameter K_d for each FEHM species	Generated within GoldSim from stochastic distributions	in(8 + in(7)) through in(8 + 2 × in(7) -1)	---
(8 + 2 × in(7))	Number of GoldSim species	Set within GoldSim (80+)	in(8 + 2 × in(7))	Value provided directly by GoldSim
(8 + 2 × in(7) + 1)	Mass input flag	---	in(1)	Not used
(8 + 2 × in(7) + 2)	# input buffer	---	in(1)	Not used
(8 + 2 × in(7) + 3)	# output buffer	---	in(1)	Not used
(8 + 2 × in(7) + 4) through (8 + 2 × in(7) + 4+ in(7)-1)	Mass of each GoldSim species entering the groundwater pathway	Variable	in(1)	Value provided directly by GoldSim

--- = *None*

The number of radionuclides or species included in the FEHM modeling is much smaller than the total number of contaminants included in the performance assessment and composite analysis. Screening calculations were performed to remove radionuclides that do not pose a risk by means of groundwater pathway exposures.

Although parameters are shared by GoldSim and FEHM, there are no files common to both programs. The parameters passed to FEHM from GoldSim via the IN array described in Table V-1 contain all the necessary information to instruct FEHM to set up a 1-D pipe pathway representative of the conditions specified for a particular GoldSim realization. Continued parameter sharing through the IN array during a realization allows mass to be moved from

GoldSim to FEHM. Finally, the OUT array, which is also passed between GoldSim and FEHM at each time step, allows mass to move back to GoldSim from FEHM.

V.4 FEHM Data File Modifications

Each data file (areag.dat) created by the Datamaker.f program (see *Attachment VI*) contains a path to the correct RTD for a given pipe with a given *Flowfield index*. The only other changes to the areag.dat file specific to the Area G performance assessment and composite analysis model are found in the TRAC macro. First, after the keyword "trac," a line has been added that contains the keyword "rip" to tell FEHM that this is a simulation controlled by GoldSim. Second, when the first number in Group 12 of the TRAC macro is set to 66, FEHM recognizes that GoldSim will provide the K_d for each species as part of the IN array that GoldSim passes into FEHM.

An example of an FEHM data file is shown in Table V-2. This particular file pertains to *cluster 5* and *Flowfield index F*. Experienced FEHM users will notice a new residence time distribution macro (RTDM) that is currently being documented for inclusion in the next version of the user's manual. The RTDM instructs FEHM to set up and use a 1-D abstraction model to recreate a conservative RTD breakthrough curve. This RTD curve can be specified either through statistical parameters (e.g., mean and standard deviation) or the RTD can be read in from a file. For the Area G modeling, the RTD is read from a file called cluster5/F/areag.rtd. The example shown in Table V-2 has 19 species in FEHM; this number is listed just before the beginning of the TRAC macro in a comment section.

Several parameters are common to all of the 1-D abstraction simulations. The water saturation in the entire domain is set to 1 (fully saturated), the permeability is fixed at 1×10^{-10} m^2 (1.1×10^{-9} ft^2), porosity is fixed at 0.3, rock density is fixed at 2,000 kg/m^3 (125 lb/ft^3), and the temperature is fixed at 20°C (68°F). The tracer concentration in the entire domain is initially zero, and the first number in Unit 12 of TRAC is set to 66 for all species to indicate that GoldSim is controlling the K_d. Although the input deck appears to assign an injection for each species over all nodes for the entire simulation (1 0 0 1 0. 1.0×10^9), FEHM has been changed to inject the incoming mass (passed through the IN array) into only the first node of the 1-D abstraction pathway. The mass flux conversion from the IN array is performed in the FEHM subroutine userc.f (see Section V.5.3). The tolerance in the tracer concentration is set at 1.0×10^{-8} to counter infrequently observed instabilities.

Table V-2
Example FEHM Data File for Cluster 5 and Flowfield Index F

```
MDA G  19 Species 5/24/2011
cond
1 0 0 2.7 2.7 2.7

init
1. 20 20 0 1000 20 0 0
node
3
1 10 50
perm
1 0 0 1.e-10 1.e-10 1.e-10

rock
1 0 0  2000.0  0.1E+31  0.3000

sol
1 -1
time
1.0e9 1.0e9 1000 1 92 11 0.

ctrl
50 1e-6 8
1 0 0 1

1 0 0.5
25 2. 1 1.e20
1 1
rflo
rest
rtdm
min
0.3     1000.
file
cluster6\A\areag.rtd

#-------------------------------------------------
# 19 species,
#  Species   Half-Life (yr)
#  1 Pu-242  3.750e5
#  2 Pu-240  6.560e3
#  3 Pu-239  2.410e4
#  4 Np-237  2.140e6
#  5  U-238  4.470e9
#  6  U-236  2.342e7
#  7  U-235  7.040e8
#  8  U-234  2.460e5
#  9  U-233  1.592e5
# 10 Pa-231  3.280e4
# 11 Th-232  1.400e10
# 12 Th-230  7.540e4
# 13 Th-229  7.300e3
# 14 Th-228  1.912
# 15 Ra-228  5.760
```

Table V-2 (Continued)
Example FEHM Data File for Cluster 5 and Flowfield Index F

```
# 16 Ra-226  1.599e3
# 17 Ac-227  2.177e1
# 18 Pb-210  2.230e1
# 19 C-14    5.715e3
trac
rip
1
0 1 1.e-8 1.
0. 1.e20 1.e20 1.e20
50 2.0 2000.  73000.
19
1
 66 0. 0. 1. 1.e-30 1.e-30 1.e-30 1.e-30

1 0 0 1

1 0 0 0.

1 0 0 1. 0. 1.e9

1
 66 0. 0. 1. 1.e-30 1.e-30 1.e-30 1.e-30

1 0 0 1

1 0 0 0.

1 0 0 1. 0. 1.e9

1
 66 0. 0. 1. 1.e-30 1.e-30 1.e-30 1.e-30

1 0 0 1

1 0 0 0.

1 0 0 1. 0. 1.e9

1
 66 0. 0. 1. 1.e-30 1.e-30 1.e-30 1.e-30

1 0 0 1

1 0 0 0.

1 0 0 1. 0. 1.e9

1
 66 0. 0. 1. 1.e-30 1.e-30 1.e-30 1.e-30

1 0 0 1

1 0 0 0.

1 0 0 1. 0. 1.e9
```

Table V-2 (Continued)
Example FEHM Data File for Cluster 5 and Flowfield Index F

```
1
 66 0. 0. 1. 1.e-30 1.e-30 1.e-30 1.e-30

1 0 0 1

1 0 0 0.

1 0 0 1. 0. 1.e9

1
 66 0. 0. 1. 1.e-30 1.e-30 1.e-30 1.e-30

1 0 0 1

1 0 0 0.

1 0 0 1. 0. 1.e9

1
 66 0. 0. 1. 1.e-30 1.e-30 1.e-30 1.e-30

1 0 0 1

1 0 0 0.

1 0 0 1. 0. 1.e9

1
 66 0. 0. 1. 1.e-30 1.e-30 1.e-30 1.e-30

1 0 0 1

1 0 0 0.

1 0 0 1. 0. 1.e9

1
 66 0. 0. 1. 1.e-30 1.e-30 1.e-30 1.e-30

1 0 0 1

1 0 0 0.

1 0 0 1. 0. 1.e9
```

Table V-2 (Continued)
Example FEHM Data File for Cluster 5 and Flowfield Index F

```
1
 66 0. 0. 1. 1.e-30 1.e-30 1.e-30 1.e-30

 1 0 0 1

 1 0 0 0.

 1 0 0 1. 0. 1.e9

 1
 66 0. 0. 1. 1.e-30 1.e-30 1.e-30 1.e-30

 1 0 0 1

 1 0 0 0.

 1 0 0 1. 0. 1.e9

 1
 66 0. 0. 1. 1.e-30 1.e-30 1.e-30 1.e-30

 1 0 0 1

 1 0 0 0.

 1 0 0 1. 0. 1.e9

 1
 66 0. 0. 1. 1.e-30 1.e-30 1.e-30 1.e-30

 1 0 0 1

 1 0 0 0.

 1 0 0 1. 0. 1.e9

 1
 66 0. 0. 1. 1.e-30 1.e-30 1.e-30 1.e-30

 1 0 0 1

 1 0 0 0.

 1 0 0 1. 0. 1.e9

 1
```

Table V-2 (Continued)
Example FEHM Data File for Cluster 5 and Flowfield Index F

```
 66 0. 0. 1. 1.e-30 1.e-30 1.e-30 1.e-30

 1 0 0 1

 1 0 0 0.

 1 0 0 1. 0. 1.e9

 1
 66 0. 0. 1. 1.e-30 1.e-30 1.e-30 1.e-30

 1 0 0 1

 1 0 0 0.

 1 0 0 1. 0. 1.e9

 rxn
 ** NCPLX, NUMRXN
 0, 19
 ** Coupling of the aqueous components for computing efficency(dRi/dUj)
 19
 1 0 0 0 0 0 0 0 0 0 0 0 0 0 0 0 0 0 0
 0 1 0 0 0 0 0 0 0 0 0 0 0 0 0 0 0 0 0
 0 0 1 0 0 0 0 0 0 0 0 0 0 0 0 0 0 0 0
 0 0 0 1 0 0 0 0 0 0 0 0 0 0 0 0 0 0 0
 0 0 0 0 1 0 0 0 0 0 0 0 0 0 0 0 0 0 0
 0 0 0 0 0 1 0 0 0 0 0 0 0 0 0 0 0 0 0
 0 0 0 0 0 0 1 0 0 0 0 0 0 0 0 0 0 0 0
 0 0 0 0 0 0 0 1 0 0 0 0 0 0 0 0 0 0 0
 0 0 0 0 0 0 0 0 1 0 0 0 0 0 0 0 0 0 0
 0 0 0 0 0 0 0 0 0 1 0 0 0 0 0 0 0 0 0
 0 0 0 0 0 0 0 0 0 0 1 0 0 0 0 0 0 0 0
 0 0 0 0 0 0 0 0 0 0 0 1 0 0 0 0 0 0 0
 0 0 0 0 0 0 0 0 0 0 0 0 1 0 0 0 0 0 0
 0 0 0 0 0 0 0 0 0 0 0 0 0 1 0 0 0 0 0
 0 0 0 0 0 0 0 0 0 0 0 0 0 0 1 0 0 0 0
 0 0 0 0 0 0 0 0 0 0 0 0 0 0 0 1 0 0 0
 0 0 0 0 0 0 0 0 0 0 0 0 0 0 0 0 1 0 0
 0 0 0 0 0 0 0 0 0 0 0 0 0 0 0 0 0 1 0
 0 0 0 0 0 0 0 0 0 0 0 0 0 0 0 0 0 0 1
 ** IDCPNT(IC),CPNTNAM(IC),IFXCONC(IC),CPNTPRT(IC),CPNTGS
        1   Pu-242    0    0 1e-9
        2   Pu-240    0    0 1e-9
        3   Pu-239    0    0 1e-9
        4   Np-237    0    0 1e-9
        5    U-238    0    0 1e-9
        6    U-236    0    0 1e-9
        7    U-234    0    0 1e-9
        8    U-233    0    0 1e-9
        9    U-232    0    0 1e-9
       10   Pa-231    0    0 1e-9
       11   Th-232    0    0 1e-9
       12   Th-230    0    0 1e-9
       13   Th-229    0    0 1e-9
```

Table V-2 (Continued)
Example FEHM Data File for Cluster 5 and Flowfield Index F

```
      14   Th-228    0    0 1e-9
      15   Ra-228    0    0 1e-9
      16   Ra-226    0    0 1e-9
      17   Ac-227    0    0 1e-9
      18   Pb-229    0    0 1e-9
      19    C-14     0    0 1e-9
** Aqueous Complex Identification: IDCPLX(IX), CPLXNAM(IX),CPLXPRT(IX)
** Immobile Compoenet Identification:  IDIMM(IM), IMMNAM(IM),IMMPRT(IM):
** IDVAP(IV), VAPNAM(IM), VAPPRT(IV) (ID # and name of vapor spec, NVAP rows)
** skip nodes? for chemical speciation calculation
  0
** RSDMAX tolerance for equil. speciation calculation
  1.0e-8  1
******  Chemical reaction information group 9-11 omitted if NCPLX=0 *******
** Group 9  LOGKEQ (=0 if stability constants are given as K, =1 if given as log
** Group 10 CKEQ(IX) (Stability constants, NCPLX rows)
** Group 11 STOIC(IX,IC) (Stoichiometric coeff: NCPLX rows, NCPNT columns)
**============================================================
      5
** Group 13 Where does the reaction take place? **
  1 0 0

** GROUP 14   HALF LIFE (years)       1    **  Pu242 to U238
3.75e5
** Group 15 RXNTYPE
1
** GROUP 16  Parent Daughter
   1     5
**============================================================
      5
** Group 13 Where does the reaction take place? **
  1 0 0

** GROUP 14   HALF LIFE (years)       2    **  U238 to U234
4.47e9
** Group 15 RXNTYPE
1
** GROUP 16  Parent Daughter
   5     8
**============================================================
      5
** Group 13 Where does the reaction take place? **
  1 0 0

** GROUP 14   HALF LIFE (years)       3    **  U234 to Th230
2.46e5
** Group 15 RXNTYPE
1
** GROUP 16  Parent Daughter
   8     12
**============================================================
      5
** Group 13 Where does the reaction take place? **
  1 0 0
```

Table V-2 (Continued)
Example FEHM Data File for Cluster 5 and Flowfield Index F

```
** GROUP 14   HALF LIFE (years)        4    **  Th230 to Ra226
7.54e4
** Group 15 RXNTYPE
1
** GROUP 16  Parent Daughter
   12     16
**=========================================================
       5
** Group 13 Where does the reaction take place? **
  1 0 0

** GROUP 14   HALF LIFE (years)        5    **  Ra226 to Pb210
1.599e3
** Group 15 RXNTYPE
1
** GROUP 16  Parent Daughter
   16   18
**=========================================================
       5
** Group 13 Where does the reaction take place? **
  1 0 0

** GROUP 14   HALF LIFE (years)        6    **  Pb210 to Dummy
22.3
** Group 15 RXNTYPE                    END OF Pu242 Chain
1
** GROUP 16  Parent Daughter
   18    0
**=========================================================
       5
** Group 13 Where does the reaction take place? **
  1 0 0

** GROUP 14   HALF LIFE (years)        7    ** Pu240 tto U236
6.56e3
** Group 15 RXNTYPE
1
** GROUP 16  Parent Daughter
   2      6
**=========================================================
       5
** Group 13 Where does the reaction take place? **
  1 0 0

** GROUP 14   HALF LIFE (years)        8    **  U236 to Th232
2.342e7
** Group 15 RXNTYPE
1
** GROUP 16  Parent Daughter
   6      11
**=========================================================
       5
** Group 13 Where does the reaction take place? **
  1 0 0
```

Table V-2 (Continued)
Example FEHM Data File for Cluster 5 and Flowfield Index F

```
** GROUP 14   HALF LIFE (years)        9    **  Th232 to Ra228
1.4e10
** Group 15 RXNTYPE
1
** GROUP 16  Parent Daughter
   11     15
**=========================================================
       5
** Group 13 Where does the reaction take place? **
  1 0 0

** GROUP 14   HALF LIFE (years)        10   ** Ra228 to Th228
5.76
** Group 15 RXNTYPE
1
** GROUP 16  Parent Daughter
   15    14
**=========================================================
       5
** Group 13 Where does the reaction take place? **
  1 0 0

** GROUP 14   HALF LIFE (years)        11   **  Th228 to Dummy
1.912
** Group 15 RXNTYPE
1
** GROUP 16  Parent Daughter              END of Pu240 Chain
  14  0
**=========================================================
       5
** Group 13 Where does the reaction take place? **
  1 0 0

** GROUP 14   HALF LIFE (years)        12   **  Pu239 to U235
2.41e4
** Group 15 RXNTYPE
1
** GROUP 16  Parent Daughter
   3  7
**=========================================================
       5
** Group 13 Where does the reaction take place? **
  1 0 0

** GROUP 14   HALF LIFE (years)        13   **  U235 to Pa231
7.04e8
** Group 15 RXNTYPE
1
** GROUP 16  Parent Daughter
   7     10
**=========================================================
       5
** Group 13 Where does the reaction take place? **
  1 0 0
```

Table V-2 (Continued)
Example FEHM Data File for Cluster 5 and Flowfield Index F

```
** GROUP 14   HALF LIFE (years)        14   **  Pa231 to Ac227
3.28e4
** Group 15 RXNTYPE
1
** GROUP 16  Parent Daughter
   10   17
**=========================================================
       5
** Group 13 Where does the reaction take place? **
  1 0 0

** GROUP 14   HALF LIFE (years)        15   ** Ac227 to Dummy
21.77
** Group 15 RXNTYPE
1
** GROUP 16  Parent Daughter              END of Pu239 Chain
   17     0
**=========================================================
       5
** Group 13 Where does the reaction take place? **
  1 0 0

** GROUP 14   HALF LIFE (years)        16   **  Np237 to U233
2.14e6
** Group 15 RXNTYPE
1
** GROUP 16  Parent Daughter
   4     9
**=========================================================
       5
** Group 13 Where does the reaction take place? **
  1 0 0

** GROUP 14   HALF LIFE (years)        17   **  U233 Th229
1.592e5
** Group 15 RXNTYPE
1
** GROUP 16  Parent Daughter
   9    13
**=========================================================
       5
** Group 13 Where does the reaction take place? **
  1 0 0

** GROUP 14   HALF LIFE (years)        18   **  Th229 to Dummy
7.3e3
** Group 15 RXNTYPE
1
** GROUP 16  Parent Daughter              END of Np237 Chain
   13   0
**=========================================================
       5
** Group 13 Where does the reaction take place? **
  1 0 0
```

Table V-2 (Continued)
Example FEHM Data File for Cluster 5 and Flowfield Index F

```
 ** GROUP 14   HALF LIFE (years)        19   **  C14 to Dummy
 5.715e3
 ** Group 15 RXNTYPE
 1
 ** GROUP 16  Parent Daughter
   19   0
stop
```

V.5 FEHM Code Modifications

Modifications of the FEHM code were needed to allow the GoldSim model to communicate with FEHM. These changes are outlined in the following sections. The coupling underwent a major modification in April to July of 2011 and these changes are reflected below. Although many permanent changes have been made to FEHM source code subroutines to allow the Area G simulations to function, only those changes specific to the Area G simulations that require separate files to be compiled into the main source code are described below. The code changes that are specific to the Area G model are located in the EES-16 files space at:

/scratch/fwo/stauffer/Fortran/ MDAG\MDAG_DLL_April_2011\Fortran_mods_4_2011

V.5.1 Modifications to fehmn.f

The fehmn.f subroutine was modified to remove nearly all Yucca Mountain/GoldSim specific code and streamline the coupling of FEHM to GoldSim as related to Area G. A counter (loopstart) is used to track the point in the main time stepping loop of FEHM (the l loop) at which control of the modeling passes to GoldSim, thereby allowing the groundwater modeling to resume at the same point in time when GoldSim cedes control. When Method = 1, GoldSim is in time stepping mode and will pass mass into FEHM.

A brief description of each significant change to fehmn.f followed by the source code that represents the change is presented below. The changes are provided in outline style and each change is bracketed by a set of red plus signs (+) to allow the reader to more easily follow the flow of information.

++

1. The organization of fehmn.f has been modified to clearly state the GoldSim method calls in the order in which they occur during a GoldSim simulation, mainly Method = 2, 3, 99, 2, 3, 99, 2, 3, 0, 1.

```
c-------------------------------------------------------------------------------
c-----------------------------------------------      Method = 2
      if(method.eq.2) then
        out(1) = 3.0
            end if
c-------------------------------------------------------------------------------
c - - - - - - - - - - - - - - - - - - - - - - -      Method = 3
      if(method.eq.3) then
        ripfehm = 1
c - - - - - fehmn.gold has num of incoming and out (minus species mass)
              inquire(7777,opened=it_is_open)
        if(.not.it_is_open) then
```

```
                        open(7777,file='fehmn.gold', status='unknown')
       end if
              rewind(7777)
        read(7777,*) n_input_arguments, out_flag
              close(7777)
       out(1) = n_input_arguments
       out(2) = 0
            end if
c-------------------------------------------------------------------------------
c - - - - - - - - - - - - - - - - - - - - - - -                Method = 99
     if(irun.NE.0.AND.method.EQ.99) then
c    Cleanup - close  files at the end of the realizations
       if (isave .ne. 0) call diskwrite
c     Close log err and a_in_array.txt files
              inquire(unit = ierr,opened=it_is_open)
       if(it_is_open) close (ierr)
              inquire(unit = iptty,opened=it_is_open)
       if(it_is_open) close (iptty)
              inquire(unit = iaunit, opened=it_is_open)
       if(it_is_open) close (iaunit)
c    Release all dynamic array memory at the beginning of a realization
              call releasemem
              irun = 0
c      Phil removed much YMP stuff in the following section
     end if
c-------------------------------------------------------------------------------

c - - - - - - - - - - - - - - - - - - - - PHS 4/20/2011              Method = 0

     if(method.eq.0) then

      continue

     end if       ! END IF  Method = 2,3,99,0
```

++

2. Another important modification is that the incoming ING array is mapped to the IN array which is now loaded into a common block so that it can be passed wherever it is needed. The IN array is first loaded when Method = 1 and the time of the simulation is 0, and is updated at each time step to reflect changes in the parameters passed from GoldSim (e.g., Etime and realization number).

```
c - - - - - - - - - - - - - - - - - - - - PHS 4/20/2011     time=0   Method = 1
c                                      Beginning of new Realization
     if((method.eq.1).AND.(ing(1).EQ.0)) then
c    ----------------------------------------------------------
c     GoldSim Initialization Stuff
c      Allocate memory for the in array and
c        load values of IN for Time=0
       size_of_in = n_input_arguments + 4 + ing(n_input_arguments + 1)
       if (not(allocated(in))) then
         allocate(in(size_of_in))
```

```
        end if
        do j = 1,size_of_in
   in(j)=ing(j)
        end do
++++++++++++++++++++++++++++++++++++++++++++++++++++++++++++++++++++++++++++++++
```

3. The diagnostic file output by the previous performance assessment and composite analysis modeling, a_inarray.txt, has been modified; one file is now written to each of the cluster directories for more precise diagnostics. The ERR and LOG files are also written for each cluster FEHM simulation to the cluster directory with a unique name and file ID number; initial diagnostic information is written to each of these files.

```
c - - - - - PHS moving open err,log,a_inarray files to here.4/20/11

      cluster = int(in(6))
              clus(1) = '1'
              clus(2) = '2'
              clus(3) = '3'
              clus(4) = '4'
              clus(5) = '5'
              clus(6) = '6'
              clus(7) = '7'
              clus(8) = '8'

      logfile = 'clusterX/fehmn.log'
      errfile = 'clusterX/fehmn.err'
      ainfile = 'clusterX/a_in_array.txt'
      logfile(8:8) = clus(cluster)
              errfile(8:8) = clus(cluster)
              ainfile(8:8) = clus(cluster)
      logfile(14:14) = clus(cluster)
              errfile(14:14) = clus(cluster)
              ainfile(14:14) = clus(cluster)

      ierr = 6555 + cluster
      inquire(unit = ierr,opened=it_is_open)
      if(.not.it_is_open) then
        open (ierr, file = errfile, status='unknown')
      end if

      iptty = 6666 + cluster
      inquire(unit = iptty,opened=it_is_open)
      if(.not.it_is_open) then
               open(iptty,file = logfile, status='unknown')
       end if

      iaunit = 6777 + cluster
              inquire(unit = iaunit, opened=it_is_open)
      if(.not. it_is_open) then
               open(iaunit,file = ainfile,status='unknown')
              end if

              write(ierr,*) 'cluster ',cluster , 'method = ',method,
     x           'realiz ',int(in(3))
```

```
      write(iaunit,*)  'cluster ',cluster , 'method = ',method,
     x             'realiz ',int(in(3))
            write(iptty,*) 'cluster ',cluster , 'method = ',method,
     x             'realiz ',int(in(3))

      write(iaunit,*) '----------------------------------------'
            write(iaunit,*) 'IN array values  -  size of in' , size_of_in
            do j = 1,7+int(in(7))
       write(iaunit,720) j,int(in(j))
            end do
            do j = 8+int(in(7)) , 7+2*int(in(7))
              write(iaunit,721) j, in(j)
            end do
            do j = 8+2*int(in(7)),size_of_in-int(in(n_input_arguments + 1))
              write(iaunit,720) j, int(in(j))
            end do
            do j = size_of_in-int(in(n_input_arguments+1))+ 1, size_of_in
              write(iaunit,721) j, in(j)
            end do
      write(iaunit,*) '----------------------------------------'

 720    format(I5,I5)
 721    format(I5,G12.3)
++++++++++++++++++++++++++++++++++++++++++++++++++++++++++++++++++++++++++++++++
```

4. The OUT array is then set to zero to avoid any problems with very small numbers that can be introduced by GoldSim:

```
            do j = 1, in(8+in(7)*2)
        out(j) = 0.0
            end do
++++++++++++++++++++++++++++++++++++++++++++++++++++++++++++++++++++++++++++++++
```

5. Next, the namefiles subroutine is called to find the name of the fehmn.files file that will be used for a given simulation.

```
call namefiles
```

The following subroutine in fehmn.f points to the correct fehmn.files file in the subdirectories to initialize each of the eight simultaneous FEHM simulations. This routine now accounts for GoldSim having either 1 or 19 species so that a single directory structure can be used for all simulations. This new capability was added in January of 2012. For a given stochastic *Flowfield index*, FEHM calls the following:

```
c - - - - - Subroutine namefiles  Names the .files file
c- - - - - - SPC for multi cluster run

      subroutine namefiles
      implicit none

      integer ncase, open_file
```

```
        character*1  cluster(8), infil(10)
        character*2 species(19)
    character*74 zzout


     infil(1) = 'A'
     infil(2) = 'B'
     infil(3) = 'C'
     infil(4) = 'D'
     infil(5) = 'E'
     infil(6) = 'F'
     infil(7) = 'G'
     infil(8) = 'H'
     infil(9) = 'I'
     infil(10) = 'J'

     cluster(1) = '1'
     cluster(2) = '2'
     cluster(3) = '3'
     cluster(4) = '4'
     cluster(5) = '5'
     cluster(6) = '6'
     cluster(7) = '7'
     cluster(8) = '8'

           species(1)  = '01'
           species(19) = '19'

     zzout(1:28) = 'cluster1/A/fehmn_1_01.files '
     zzout(8:8) = cluster(int(in(6)))
           zzout(10:10) = infil(int(in(2)))
           zzout(18:18) = cluster(int(in(6)))
           zzout(20:21) = species(int(in(7)))

     nmfil(1) = zzout

    return
     end subroutine namefiles
```

++

6. If ING(1) = 0 at the beginning of each realization, the variables that are used to control the FEHM/GoldSim coupling are initialized:

```
c      --------------------------------
c      Set GoldSim specific values for
c      beginning of new realization
            qcout_old = 0.0
            jumpflag = 0
            loopstart = 1
            loopflag = 0
            nstep = 100000
c      Phil adding TS control for MDA G fixes
c      reset time parameters at new realization
```

```
            days = 0.0
            day  = 1.0
            daymin = 1.e-4
c       ----------------------------------
++++++++++++++++++++++++++++++++++++++++++++++++++++++++++++++++++++++++++++++++
```

7. Several changes occur in the main time stepping portion of FEHM when the simulation time in GoldSim is greater than 0 (ING(1) > 0). At the start of each new GoldSim time step, the ING(x) array is remapped onto the IN(x) array, the maximum time step in FEHM is set to the lesser of the GoldSim time step or 10 years, and the loop counter (1) of the main FEHM time step loop is set to ensure the loop is entered at the correct time after returning from GoldSim.

```
c     - - - - - - - - - - - - - - - - - -
c       load values of IN for Time GT 0,
c        set goldtime and
c        daymax = goldtime OR 10yrs whichever is smaller
              do j = 1,size_of_in
                in(j)=ing(j)
              end do
        goldtime = in(1)*365.25
              if(in(5).GT.10) then
                daymax = 365.25*10
              else
                daymax = in(5)*365.25
              end if
c     - - - - - - - - - - - - -
c     WRITE OUT to a_in_array the values of tracer coming in from GoldSim
       write(iaunit,*) '**********************************'
       write(iaunit,*) '  Species coming in from GoldSim  '
       write(iaunit,*) ' FEHM#   GS#   in_location    Mass    '

       do j = 1, int(in(7))
                k =  size_of_in - int(in(8+in(7)*2)) + int(in(7+j))
         write(iaunit,737)  j, int(in(7+j)) , k,  in(k)
              end do
 737    format(3I7,G12.3)
c      -------------------------------
c      Maintain loop count when coming in and out of GoldSim  PHS 5/11/2011
              if(jumpflag.EQ.666) then
                loopstart = loopflag
       else
                loopstart = 1
              end if
c      -------------------------------
c      -------------------------------
c      Maintain loop count when coming in and out of GoldSim  PHS 5/11/2011
              if(jumpflag.EQ.666) then
                loopstart = loopflag
       else
                loopstart = 1
              end if
c      -------------------------------
```

++

8. The following changes to fehmn.f occur within the major time step loop on (l). First, the loop proceeds from loopstart to nstep, to ensure that time stepping in FEHM is not impacted by the GoldSim coupling. Next, code has been added to force the FEHM and GoldSim time steps to synchronize with one another. Finally, at the end of the major time step loop, a check is made to determine if the process needs to jump out of the major time step loop and return to GoldSim. This jump is set in motion when the FEHM time is equal to or greater than the current GoldSim time. If this condition is met, the code first calls subroutine loadoutarray_trac to calculate the masses to send to GoldSim. Next, the loop flag is indexed and the jumpflag is set to 666 to signal to FEHM that it is at the end of a GoldSim time step. The jump out of the major loop is accomplished using a GOTO statement that leaves the major time stepping loop and jumps to line 9999.

```
      do l = loopstart, nstep

c        ------------------------------------
c        PHS 5/11/2011  adding to force final time to = GoldSim timestep
                        if(days.GT.goldtime) then
                          day = day - (days-goldtime)
                  days = goldtime
                  if(day.LT.1.) day = 1.0
                          daymax = day
                  write(iaunit,*) '---------------------------'
                  write(iaunit,*) 'day daymax years goldtime-yrs '
                  write(iaunit,778) day,daymax,days/365.25,goldtime/365.25
                  write(iaunit,*) '---------------------------'
                 end if
 778       format(4(F9.3,' -- '))
c        ------------------------------------

c- - - - - - - - - - - - - - - - - - - - - - - - - - - - - - - Jump Back to GS
                 if(days.GE.goldtime) then
                  call loadoutarray_trac
                  loopflag = l+1
                  jumpflag = 666
            goto 9999
                 end if
c- - - - - - - - - - - - - - - - - - - - - - - - - - - - - - - Jump Back to GS
```

++

9. The subroutine loadoutarray_trac, shown below, calculates the contaminant masses (moles) to send to GoldSim when FEHM reaches the end of each GoldSim time step.

```
      subroutine loadoutarray_trac
cHari compute conc values to pass back to goldsim
      implicit none
```

```
      real*8, allocatable :: out_save(:)
      real*8, allocatable :: time_dump(:)
      integer ispecies
      integer number_of_species
      integer ns2,izones, sflag, node1, node393
      integer nflow_frac, number_of_zones,indexout,indexmzone
      integer add_spots, add_spots2
      real*8 cur_time, prev_time, del_time
      real*8 :: cur_time_save = 0.
      save out_save, time_dump, cur_time_save

c     index_in_species= 4 + 6 +
c     number_of_species = int(in(index_in_species))
c     Changing SUPER INDEX CHANGE  9/28/04 in(8+in(7)*2))
cSPC note: for not using index 66 for Kd, here should be in(8+in(7))

      write(iaunit,*) 'loadoutarray - species loaded',in(8+in(7)*2)
      do jjj = 1, in(8+in(7)*2)
        out(jjj) = 0.0
      end do

      write(iaunit,*) '------------------------------'
      write(iaunit,*) 'sflag goldsp mass_out'
      do sflag = 1, in(7)
        out(in(7+sflag)) = qcout(sflag) - qcout_old(sflag)
        qcout_old(sflag) = qcout(sflag)
        write(iaunit,*) sflag,int(in(7+sflag)),out(in(7+sflag))
 775    format(2I6,E12.4)
 776    format(I6,2E12.4)
      end do
            write(iaunit,*) '------------------------------'
            write(iaunit,*) ' node1 conc    node393 conc   sp13'
            do sflag = 1, int(in(7))
              node1 = (sflag - 1 )* neq + 1
              node393 = sflag*(neq-1) + 393
              write(iaunit,776) sflag, anl(node1) , anl(node393)
            end do
      write(iaunit,*) '------------------------------'

      return
      end subroutine loadoutarray_trac
```

++

10. After the major time stepping loop is exited with a GOTO jump to line 9999, FEHM closes all files with index numbers less than 500 and returns to GoldSim.

```
9999   continue
       state = 0
       if((method.EQ.1).AND.(iptty.GT.1000)) then
         write(iptty,*) 'Return fehmn.f  Cluster Method Realiz ',
     x                  int(in(6)),method, int(in(3))
       end if

       do i = 1, 500
```

```
      inquire(unit=i,opened=it_is_open)
      if(it_is_open) then
        close(i)
      end if
     end do

    return
++++++++++++++++++++++++++++++++++++++++++++++++++++++++++++++++++++++++++++++++
```

V.5.2 Modifications to Other FEHM Subroutines

In this iteration of the Area G coupling of FEHM to GoldSim, care was taken to reduce the number of subroutines that must be recompiled when switching from the standard version of FEHM to the adapted version of FEHM that is used for the Area G groundwater modeling. In the current coupling, fehmn_pc_dll_MDAG.f (dated 1/26/2012) is the only file that must be swapped (for fehmn_pc.f) whenever a new version of FEHM is built for use with the Area G performance assessment and composite analysis model. This file is located in:

/scratch/fwo/stauffer/Fortran/ MDAG\MDAG_DLL_Jan_2012\Fortran_mods_Jan_2012

```
++++++++++++++++++++++++++++++++++++++++++++++++++++++++++++++++++++++++++++++++
```

V.5.3 Modifications to userc.f

Subroutine userc.f was modified to allow the K_d values to be set by GoldSim and to convert the radionuclide mass (moles) supplied by GoldSim to the fluxes used in FEHM (moles/time). The mass of a given species coming from GoldSim, in(11+nspeci+sflag) is divided by the associated GoldSim time step (deltat = in(5) × 3600. × 24. × 365.25) to yield getflux and rcss, which are molar flow rates with units of moles per second.

This section is hard-wired to input mass only into the first node (1), and assumes that the mixing model is of the minimum-mixedness variety described in *Attachment IV*.

```
      save flag_kd2,in3_old,tf1
      save transform_kd,flag_kd, flag_gsmass, ii, jj

cSPC  add for transformation factor
      real*8 transform_kd(8,10)
      integer flag_kd, i1,j1, ii, jj
      save flag_kd2,in3_old
      save transform_kd,flag_kd, ii, jj
c-------------------------------------------------------------
c   Phil and Hari  6/2004 - 4/2011
c   This section is for Tracer transport coupled
c   with Goldsim.  The input flux is calculated from
c   the mass/time
Ci  also, feed in kd from in(*) array
c   AND check to see if deltat is negative and reset
c   meaning that a new realization is underway!
c-------------------------------------------------------------
```

```
c--- Changes to SUPER INDEXING  9 28 04  IN(8+in(7)-1+nsp)

      if(in(4).EQ.666) then

c - - - - - - only open and read the transform matrix once.
               if (flag_kd.NE.666) then
         open(222,file='transformation_matrix.txt')
                read(222,*)
c                  ii=cluster  jj=flowfield
                read(222,*) ii,jj
                write(iaunit,*) 'Transform Matrix  column=cluster row=FF '
         do j1 = 1,jj
                 read(222,*) (transform_kd(i1,j1) , i1=1,ii)
                 write(iaunit,771) (transform_Kd(i1,j1), i1=i,ii)
         end do
         close(222)
         flag_kd=666
        end if

       if(in3_old.NE.in(3)) flag_kd2 = 0

       if((i.eq.1).AND.(in(1).GT.0)) then

        if(flag_kd2.NE.1) then
                 write(iaunit,*) 'Transformation in USERC.f '
                 write(iaunit,*) 'Cluster Flowfield NSP Kd Factor'
                 tf1 = 666
                end if

                if((iadsfl(nsp,1).eq.66).and.(flag_kd2.ne.1))then
                          a1adfl(nsp,1) = in(7+in(7)+nsp)*
   &               transform_kd(int(in(6)),int(in(2)))
         write(iaunit,772) int(in(6)),int(in(2)),nsp,
   &        a1adfl(nsp,1), transform_kd(int(in(6)),int(in(2)))
                  if(nsp.eq.nspeci) then
                           flag_kd2 = 1
                  in3_old = in(3)
                  end if
                endif

 771    format(10(F6.3))
 772    format(3I6,2x,2G9.3)

c-------- 4/27/2011  in(5) is now delta T direct from GS in yrs

        deltat = in(5)*3600.*24.*365.25

cSPC comment: this is for areaG run with Kd specified
cSPC comment: With no Kd option, shall use follow line
c         getflux = in(11+ nspeci+sflag)/deltat

        sflag = int(in(7+nsp))
        getflux = in(11+2*nspeci+sflag)/deltat

        rc_ss   = -getflux
        drc_ss  = 0.

             endif    ! i EQ 1
```

```
        endif               ! in(4) EQ 666
    endif
```

++

V.5.4 Modifications to iofile.f

Several lines in subroutine iofile.f are skipped when using the Area G version of FEHM to avoid overwriting the fehmn.files and *.err files that are named in fehmn_pc_dll_MDAG_7_2011.f. In the code below, in(4) = 666 when the Area G version of FEHM is used. The following code change has been incorporated into the main version of FEHM.

```
    if(in(4).NE.666) nmfil( 1) = 'fehmn.files'

   if(in(4).NE.666) then
     nargc = iargc()
     if (nargc .ge. 1) then
       call getarg(1, cmdline)
       len = len_trim(cmdline)
       inquire (file = cmdline(1:len), exist = ex)
       if (ex) nmfil(1) =  cmdline(1:len)
     end if
    end if

    if(in(4).NE.666) ierr = nufilb(14)
    inquire (ierr, opened = opnd)
    if (.not. opnd) then
      open (ierr, file = nmfil(14), status = cstats(14),
   *       form = cform(14))
      write (ierr, 1000)  verno, jdate, jtime
    end if
```

Attachment VI
Summary of Pre- and Post-Processing Codes for the Los Alamos National Laboratory TA-54, Area G Groundwater Pathway Model

Author:
Philip H. Stauffer

VI.1 Introduction

This attachment lists the source code for the pre- and postprocessor codes that were used in conjunction with the Area G groundwater pathway model. Section VI.2 presents the preprocessor codes gwtable.f, points.f, run_directory_builder, FILEmaker.f, and Datmaker.f. The postprocessor codes histo.f, satchopg.f, and well.f are provided in Section VI.3. Brief descriptors are given for each code with explanations of input and output so a future user can recreate the analysis using the same logic.

VI.2 Preprocessing Codes

Five preprocessor codes were used to conduct the groundwater pathway modeling. Listings of these codes are provided below.

VI.2.1 gwtable.f

```
      program gwtable

c------------------
c     code to take the  xyz coordinates
c     work with the xyz coordinates
c     and assign macro to create a water
c     table set that lies below the plane
c     with z = 5900 W  to z = 5700. E
c
c     Also creates the E and W boundaries
c     flow macros
c-----------------------------------------

      implicit none

      integer nd,i

      real*8 x, y,z, pg
      real*8 pres, heade, headw, rol, tope, topw
      real*8 topn, xdum , xe, xw, rolt, rolb, depth

c--------------------  Head on east and west boundary

      heade = 5700. * .3048
      headw = 5900. * .3048

c----------------------------- density of water
```

```
c                          gage pressure
      rolt = 998.6023
      rolb = 1007.235
      pg  = 0.08

c--------------  elevation of gw

      topw = 5900. * .3048
      tope = 5700. * .3048

      xe = 23250.
      xw = 18500.
c------------

      open(unit=7,file='areag.10001_geo')
      open(unit=16,file='gwpres_try2.macro')
      open(unit=17,file='gwflow_try2.macro')
      open(unit=18,file='gw_above2.zone')
      open(unit=19,file='gw_below2.zone')

      write(16,329)
      write(17,328)
      write(18,327)
      write(19,327)

c------   Read in the Geo file

      read(7,*)

c------------   Decide if node is below
c              water table plane: set to correct P

      do i=1 , 375451
        read(7,*) nd,x,y,z
        xdum = x - xw
        topn = topw - (topw-tope)*(xdum/4750.)
        if(topn.GT.z) then
          depth = topn - z
          rol = rolt + 0.5*(depth/1698.)*(rolb-rolt)
          pres = pg + (depth*rol*9.81 / 1.e6)
          write(16,330)  nd,nd, pres
          write(19,*) nd
          if((x.EQ.xe).OR.(x.EQ.xw)) then
            write(17,331)  nd,nd, pres
          end if
        else
          write(18,*) nd
        endif
      enddo
```

```
      write(16,*)
      write(17,*)
      write(18,*)
      write(18,332)
      write(19,*)
      write(19,332)

c-----------------------------------------
       close(7)
       close(8)
       close(16)

 327   format('zone')
 328   format('flow')
 329   format('pres')
 330   format(2x,I10,2x,I10,'  1  ',e16.9,2x,' 15.00  1')
 331   format(2x,I10,2x,I10,' 1 ',e16.9,2x,' -15.00 1000')
 332   format('stop')

      end
```

VI.2.2 points.f

```
      program points

c------------------
c     code to  distribute points at each pit node
c      for each cluster for input to the sptr macro.
C      Used in the Well Capture Analysis
c-----------------------------------------

      implicit none

      character*24 filein
      character*12 fileout

      integer index, npart, i, j, k , n, pnum(40), numn
      integer pnode, count, nybin, bin(1000), flag
      integer pit_node(66,2000), pit(40), npits , dum
      integer m1,m2

      real*8  x(400000), y(400000), zdum,  zfix, z(400000)
      real*8  xmin, xmax, ymin, ymax
      real*8  ybin(1000) , xshift, yshift

c---------------------------------------
c     pit_node(pit_number,node number)
c---------------------------------------
      write(6,*) 'what is the input file '
```

```
      read(5,*) filein

      fileout = 'points_x.out'

      fileout(8:8) = filein(9:9)

      open(unit=7,file=
     2 '/scratch/fwo/stauffer/G/Grid/areag_lev4b_pits_RENUMBERD.zone')
      open(unit=8,file='/scratch/fwo/stauffer/G/Grid/areag.10001_geo')
      open(unit=9,file=filein)
      open(unit=17,file=fileout)
      open(unit=18,file='points_bin.out')

c-----------------------------------------------------
c   read in the geo file and store nodal x,y information
c-----------------------------------------------------

      read(8,*) numn
      do i = 1, numn
        read(8,*) dum, x(i), y(i), z(i)
      end do

c--------------------------------------
c    read in the pit_node(pit_number,node number)
c    and
c    pnum(n) which are the number of nodes in pit n
c    and
c    remove any duplicate x,y points (take only the second)
c    set the bad node to node = zero
c-----------------------------------------------

      flag = 0
      read(7,*)
      do i = 1,36
       read(7,*) j
       read(7,*)
       read(7,*) pnum(j)
       read(7,*) (pit_node(j,k) , k=1,pnum(j))

       do k = 1,pnum(j)-2
         m1 = pit_node(j,k)
         if(m1.NE.0) then
          do n = k+1 , pnum(j)
           m2 = pit_node(j,n)
           if((x(m1).EQ.x(m2)).AND.(y(m1).EQ.y(m2))) then
            pit_node(j,n) = 0
           end if
          end do
         end if
       end do
```

```
      end do

c-----------------------------------------------------
c   assign variables
c   npart = number of particles per node
c   pit(n) = pit# of the nth pit
c   pnode = node number of the nth node in a given pit
c   pit_node(pit_number,node number)
c   xshift yshift to set center of cluster on well
c-----------------------------------------------------

c   THINGS TO  READ IN DEPENDING ON CLUSTER
c    set in   file=9   cluster_info.in
c-----------------------------------------------

      read(9,*)
      read(9,*)
      read(9,*)

      read(9,*) npart
      read(9,*) npits
      do i = 1,npits
        read(9,*) pit(i)
      end do

      read(9,*)

      read(9,*) xshift
      read(9,*) yshift
      read(9,*) zfix
c-------------------------------------------

      count = 0

      xmin=1.e6
      xmax=0.
      ymin=0.
      ymax=-140000.

      do i = 1, npits
        index = pit(i)
        do j = 1,pnum(index)
          pnode = pit_node(index,j)
          if(pnode.NE.0) then
           do k = 1,npart
             write(17,666) count,x(pnode)+xshift,
     2                     y(pnode)+yshift,zfix
            count = count + 1
           end do
           if(x(pnode).LT.xmin) xmin = x(pnode)
```

```
          if(x(pnode).GT.xmax) xmax = x(pnode)
          if(y(pnode).LT.ymin) ymin = y(pnode)
          if(y(pnode).GT.ymax) ymax = y(pnode)
         end if
        end do
       end do

       write(6,*) 'surface nodes in cluster ', count
       write(6,*) 'Min dist to well ', 22000. - (xmax+xshift)
       write(6,*) 'Max dist to well ', 22000. - (xmin+xshift)
       write(6,*) 'xmax ymax ', xmax,ymax
       write(6,*) 'xmin ymin ', xmin,ymin

c-------------------------------------------------
c   search pnode's y values and place into ybin(1..nybin)
c   then add a number to the bin(1..nybin)
c-------------------------------------------------

       write(6,*) xmin, xmax, ymin, ymax
       do i = 1,200
        bin(i) = 0
        ybin(i) = 0
       end do

       count = 0
       nybin = 1
       ybin(1) = ymin

       do i = 1, npits
        index = pit(i)
        do j = 1,pnum(index)
         pnode = pit_node(index,j)
         if(pnode.NE.0) then
          flag = 0
          do k = 1,nybin
           if(y(pnode).EQ.ybin(k)) flag = 1
          end do
          if(flag.NE.1) then
           nybin = nybin + 1
           ybin(nybin) = y(pnode)
          end if
          do k = 1,nybin
           if(y(pnode).EQ.ybin(k)) then
            bin(k) = bin(k) + 1
            n = k
            count = count + 1
           end if
          end do
         end if
        end do
```

```
      end do

      write(6,*) count, nybin, (bin(n), n=1,nybin)

c-----------------------------------------------
c  write out the x for each bin and the number of
c  particles per bin
c-----------------------------------------------
      count = 0
      do i = 1,nybin
        write(18,667)  ybin(i), bin(i)
        count = count + bin(i)
      end do
        write(6,*) 'Surface nodes in cluster ', count

 666  format(i6,x,F9.1,x,F12.1,x,F8.1)
 667  format(F12.1, x, I5)

      End
```

Example input for this program for Cluster 5:

```
====================================
points to write at each node
number of pits in cluster
pits 1 - n
10
6
32
33
35
36
37
38
Shift in x and y
-250.
-125.
1750.
```

VI.2.3 Run_directory_builder

This shell script creates a directory called Cluster_Directories then fills it with the 80 subdirectories necessary for use in the GoldSim system-level model. Once the directory structure is built, each of the 80 subdirectories gets an fehmn.files file, an goldfehm.dat file, and an areag.rtd file. The two FORTRAN codes that follow this script (FILEmaker.f and Datmaker) are used to change characters in the fehmn.files and goldfehm.dat files so that thy have the correct information regarding pathways to the data files and correct rtd files for a given cluster at a given flow-rate. The shell script below is designed to be run from /scratch/fwo/stauffer/G/Filemaker and requires the FILEmaker.f, Datmaker.f, goldfehm.dat. The FILEmaker.f program is set up to create the directory structure that Rob Shuman requires for GoldSim on his PC.

```
cd /scratch/fwo/stauffer/G

rm -r Cluster_Directories
mkdir Cluster_Directories
cd Cluster_Directories

mkdir cluster1
mkdir cluster2
mkdir cluster3
mkdir cluster4
mkdir cluster5
mkdir cluster6
mkdir cluster7
mkdir cluster8

cd cluster1
mkdir A
mkdir B
mkdir C
mkdir D
mkdir E
mkdir F
mkdir G
mkdir H
mkdir I
mkdir J
cd ../cluster2
mkdir A
mkdir B
mkdir C
mkdir D
mkdir E
mkdir F
mkdir G
mkdir H
mkdir I
mkdir J
cd ../cluster3
mkdir A
mkdir B
mkdir C
mkdir D
mkdir E
mkdir F
mkdir G
mkdir H
mkdir I
mkdir J
cd ../cluster4
mkdir A
```

```
mkdir B
mkdir C
mkdir D
mkdir E
mkdir F
mkdir G
mkdir H
mkdir I
mkdir J
cd ../cluster5
mkdir A
mkdir B
mkdir C
mkdir D
mkdir E
mkdir F
mkdir G
mkdir H
mkdir I
mkdir J
cd ../cluster6
mkdir A
mkdir B
mkdir C
mkdir D
mkdir E
mkdir F
mkdir G
mkdir H
mkdir I
mkdir J
cd ../cluster7
mkdir A
mkdir B
mkdir C
mkdir D
mkdir E
mkdir F
mkdir G
mkdir H
mkdir I
mkdir J
cd ../cluster8
mkdir A
mkdir B
mkdir C
mkdir D
mkdir E
mkdir F
mkdir G
```

```
mkdir H
mkdir I
mkdir J

cp /scratch/fwo/stauffer/G/bg0.1/cluster1/areag.rtd /scratch/fwo/stauffer/G/Cluster_Directories/cluster1/A/.
cp /scratch/fwo/stauffer/G/bg0.1/cluster2/areag.rtd /scratch/fwo/stauffer/G/Cluster_Directories/cluster2/A/.
cp /scratch/fwo/stauffer/G/bg0.1/cluster3/areag.rtd /scratch/fwo/stauffer/G/Cluster_Directories/cluster3/A/.
cp /scratch/fwo/stauffer/G/bg0.1/cluster4/areag.rtd /scratch/fwo/stauffer/G/Cluster_Directories/cluster4/A/.
cp /scratch/fwo/stauffer/G/bg0.1/cluster5/areag.rtd /scratch/fwo/stauffer/G/Cluster_Directories/cluster5/A/.
cp /scratch/fwo/stauffer/G/bg0.1/cluster6/areag.rtd /scratch/fwo/stauffer/G/Cluster_Directories/cluster6/A/.
cp /scratch/fwo/stauffer/G/bg0.1/cluster7/areag.rtd /scratch/fwo/stauffer/G/Cluster_Directories/cluster7/A/.
cp /scratch/fwo/stauffer/G/bg0.1/cluster8/areag.rtd /scratch/fwo/stauffer/G/Cluster_Directories/cluster8/A/.

cp /scratch/fwo/stauffer/G/bg0.25/cluster1/areag.rtd /scratch/fwo/stauffer/G/Cluster_Directories/cluster1/B/.
cp /scratch/fwo/stauffer/G/bg0.25/cluster2/areag.rtd /scratch/fwo/stauffer/G/Cluster_Directories/cluster2/B/.
cp /scratch/fwo/stauffer/G/bg0.25/cluster3/areag.rtd /scratch/fwo/stauffer/G/Cluster_Directories/cluster3/B/.
cp /scratch/fwo/stauffer/G/bg0.25/cluster4/areag.rtd /scratch/fwo/stauffer/G/Cluster_Directories/cluster4/B/.
cp /scratch/fwo/stauffer/G/bg0.25/cluster5/areag.rtd /scratch/fwo/stauffer/G/Cluster_Directories/cluster5/B/.
cp /scratch/fwo/stauffer/G/bg0.25/cluster6/areag.rtd /scratch/fwo/stauffer/G/Cluster_Directories/cluster6/B/.
cp /scratch/fwo/stauffer/G/bg0.25/cluster7/areag.rtd /scratch/fwo/stauffer/G/Cluster_Directories/cluster7/B/.
cp /scratch/fwo/stauffer/G/bg0.25/cluster8/areag.rtd /scratch/fwo/stauffer/G/Cluster_Directories/cluster8/B/.

cp /scratch/fwo/stauffer/G/bg0.5/cluster1/areag.rtd /scratch/fwo/stauffer/G/Cluster_Directories/cluster1/C/.
cp /scratch/fwo/stauffer/G/bg0.5/cluster2/areag.rtd /scratch/fwo/stauffer/G/Cluster_Directories/cluster2/C/.
cp /scratch/fwo/stauffer/G/bg0.5/cluster3/areag.rtd /scratch/fwo/stauffer/G/Cluster_Directories/cluster3/C/.
cp /scratch/fwo/stauffer/G/bg0.5/cluster4/areag.rtd /scratch/fwo/stauffer/G/Cluster_Directories/cluster4/C/.
cp /scratch/fwo/stauffer/G/bg0.5/cluster5/areag.rtd /scratch/fwo/stauffer/G/Cluster_Directories/cluster5/C/.
cp /scratch/fwo/stauffer/G/bg0.5/cluster6/areag.rtd /scratch/fwo/stauffer/G/Cluster_Directories/cluster6/C/.
cp /scratch/fwo/stauffer/G/bg0.5/cluster7/areag.rtd /scratch/fwo/stauffer/G/Cluster_Directories/cluster7/C/.
cp /scratch/fwo/stauffer/G/bg0.5/cluster8/areag.rtd /scratch/fwo/stauffer/G/Cluster_Directories/cluster8/C/.

cp /scratch/fwo/stauffer/G/bg1/cluster1/areag.rtd /scratch/fwo/stauffer/G/Cluster_Directories/cluster1/D/.
cp /scratch/fwo/stauffer/G/bg1/cluster2/areag.rtd /scratch/fwo/stauffer/G/Cluster_Directories/cluster2/D/.
cp /scratch/fwo/stauffer/G/bg1/cluster3/areag.rtd /scratch/fwo/stauffer/G/Cluster_Directories/cluster3/D/.
cp /scratch/fwo/stauffer/G/bg1/cluster4/areag.rtd /scratch/fwo/stauffer/G/Cluster_Directories/cluster4/D/.
cp /scratch/fwo/stauffer/G/bg1/cluster5/areag.rtd /scratch/fwo/stauffer/G/Cluster_Directories/cluster5/D/.
cp /scratch/fwo/stauffer/G/bg1/cluster6/areag.rtd /scratch/fwo/stauffer/G/Cluster_Directories/cluster6/D/.
cp /scratch/fwo/stauffer/G/bg1/cluster7/areag.rtd /scratch/fwo/stauffer/G/Cluster_Directories/cluster7/D/.
cp /scratch/fwo/stauffer/G/bg1/cluster8/areag.rtd /scratch/fwo/stauffer/G/Cluster_Directories/cluster8/D/.

cp /scratch/fwo/stauffer/G/bg1.5/cluster1/areag.rtd /scratch/fwo/stauffer/G/Cluster_Directories/cluster1/E/.
cp /scratch/fwo/stauffer/G/bg1.5/cluster2/areag.rtd /scratch/fwo/stauffer/G/Cluster_Directories/cluster2/E/.
cp /scratch/fwo/stauffer/G/bg1.5/cluster3/areag.rtd /scratch/fwo/stauffer/G/Cluster_Directories/cluster3/E/.
cp /scratch/fwo/stauffer/G/bg1.5/cluster4/areag.rtd /scratch/fwo/stauffer/G/Cluster_Directories/cluster4/E/.
cp /scratch/fwo/stauffer/G/bg1.5/cluster5/areag.rtd /scratch/fwo/stauffer/G/Cluster_Directories/cluster5/E/.
cp /scratch/fwo/stauffer/G/bg1.5/cluster6/areag.rtd /scratch/fwo/stauffer/G/Cluster_Directories/cluster6/E/.
cp /scratch/fwo/stauffer/G/bg1.5/cluster7/areag.rtd /scratch/fwo/stauffer/G/Cluster_Directories/cluster7/E/.
cp /scratch/fwo/stauffer/G/bg1.5/cluster8/areag.rtd /scratch/fwo/stauffer/G/Cluster_Directories/cluster8/E/.

cp /scratch/fwo/stauffer/G/bg2/cluster1/areag.rtd /scratch/fwo/stauffer/G/Cluster_Directories/cluster1/F/.
```

cp /scratch/fwo/stauffer/G/bg2/cluster2/areag.rtd /scratch/fwo/stauffer/G/Cluster_Directories/cluster2/F/.
cp /scratch/fwo/stauffer/G/bg2/cluster3/areag.rtd /scratch/fwo/stauffer/G/Cluster_Directories/cluster3/F/.
cp /scratch/fwo/stauffer/G/bg2/cluster4/areag.rtd /scratch/fwo/stauffer/G/Cluster_Directories/cluster4/F/.
cp /scratch/fwo/stauffer/G/bg2/cluster5/areag.rtd /scratch/fwo/stauffer/G/Cluster_Directories/cluster5/F/.
cp /scratch/fwo/stauffer/G/bg2/cluster6/areag.rtd /scratch/fwo/stauffer/G/Cluster_Directories/cluster6/F/.
cp /scratch/fwo/stauffer/G/bg2/cluster7/areag.rtd /scratch/fwo/stauffer/G/Cluster_Directories/cluster7/F/.
cp /scratch/fwo/stauffer/G/bg2/cluster8/areag.rtd /scratch/fwo/stauffer/G/Cluster_Directories/cluster8/F/.

cp /scratch/fwo/stauffer/G/bg4/cluster1/areag.rtd /scratch/fwo/stauffer/G/Cluster_Directories/cluster1/G/.
cp /scratch/fwo/stauffer/G/bg4/cluster2/areag.rtd /scratch/fwo/stauffer/G/Cluster_Directories/cluster2/G/.
cp /scratch/fwo/stauffer/G/bg4/cluster3/areag.rtd /scratch/fwo/stauffer/G/Cluster_Directories/cluster3/G/.
cp /scratch/fwo/stauffer/G/bg4/cluster4/areag.rtd /scratch/fwo/stauffer/G/Cluster_Directories/cluster4/G/.
cp /scratch/fwo/stauffer/G/bg4/cluster5/areag.rtd /scratch/fwo/stauffer/G/Cluster_Directories/cluster5/G/.
cp /scratch/fwo/stauffer/G/bg4/cluster6/areag.rtd /scratch/fwo/stauffer/G/Cluster_Directories/cluster6/G/.
cp /scratch/fwo/stauffer/G/bg4/cluster7/areag.rtd /scratch/fwo/stauffer/G/Cluster_Directories/cluster7/G/.
cp /scratch/fwo/stauffer/G/bg4/cluster8/areag.rtd /scratch/fwo/stauffer/G/Cluster_Directories/cluster8/G/.

cp /scratch/fwo/stauffer/G/bg6/cluster1/areag.rtd /scratch/fwo/stauffer/G/Cluster_Directories/cluster1/H/.
cp /scratch/fwo/stauffer/G/bg6/cluster2/areag.rtd /scratch/fwo/stauffer/G/Cluster_Directories/cluster2/H/.
cp /scratch/fwo/stauffer/G/bg6/cluster3/areag.rtd /scratch/fwo/stauffer/G/Cluster_Directories/cluster3/H/.
cp /scratch/fwo/stauffer/G/bg6/cluster4/areag.rtd /scratch/fwo/stauffer/G/Cluster_Directories/cluster4/H/.
cp /scratch/fwo/stauffer/G/bg6/cluster5/areag.rtd /scratch/fwo/stauffer/G/Cluster_Directories/cluster5/H/.
cp /scratch/fwo/stauffer/G/bg6/cluster6/areag.rtd /scratch/fwo/stauffer/G/Cluster_Directories/cluster6/H/.
cp /scratch/fwo/stauffer/G/bg6/cluster7/areag.rtd /scratch/fwo/stauffer/G/Cluster_Directories/cluster7/H/.
cp /scratch/fwo/stauffer/G/bg6/cluster8/areag.rtd /scratch/fwo/stauffer/G/Cluster_Directories/cluster8/H/.

cp /scratch/fwo/stauffer/G/bg8/cluster1/areag.rtd /scratch/fwo/stauffer/G/Cluster_Directories/cluster1/I/.
cp /scratch/fwo/stauffer/G/bg8/cluster2/areag.rtd /scratch/fwo/stauffer/G/Cluster_Directories/cluster2/I/.
cp /scratch/fwo/stauffer/G/bg8/cluster3/areag.rtd /scratch/fwo/stauffer/G/Cluster_Directories/cluster3/I/.
cp /scratch/fwo/stauffer/G/bg8/cluster4/areag.rtd /scratch/fwo/stauffer/G/Cluster_Directories/cluster4/I/.
cp /scratch/fwo/stauffer/G/bg8/cluster5/areag.rtd /scratch/fwo/stauffer/G/Cluster_Directories/cluster5/I/.
cp /scratch/fwo/stauffer/G/bg8/cluster6/areag.rtd /scratch/fwo/stauffer/G/Cluster_Directories/cluster6/I/.
cp /scratch/fwo/stauffer/G/bg8/cluster7/areag.rtd /scratch/fwo/stauffer/G/Cluster_Directories/cluster7/I/.
cp /scratch/fwo/stauffer/G/bg8/cluster8/areag.rtd /scratch/fwo/stauffer/G/Cluster_Directories/cluster8/I/.

cp /scratch/fwo/stauffer/G/bg10/cluster1/areag.rtd /scratch/fwo/stauffer/G/Cluster_Directories/cluster1/J/.
cp /scratch/fwo/stauffer/G/bg10/cluster2/areag.rtd /scratch/fwo/stauffer/G/Cluster_Directories/cluster2/J/.
cp /scratch/fwo/stauffer/G/bg10/cluster3/areag.rtd /scratch/fwo/stauffer/G/Cluster_Directories/cluster3/J/.
cp /scratch/fwo/stauffer/G/bg10/cluster4/areag.rtd /scratch/fwo/stauffer/G/Cluster_Directories/cluster4/J/.
cp /scratch/fwo/stauffer/G/bg10/cluster5/areag.rtd /scratch/fwo/stauffer/G/Cluster_Directories/cluster5/J/.
cp /scratch/fwo/stauffer/G/bg10/cluster6/areag.rtd /scratch/fwo/stauffer/G/Cluster_Directories/cluster6/J/.
cp /scratch/fwo/stauffer/G/bg10/cluster7/areag.rtd /scratch/fwo/stauffer/G/Cluster_Directories/cluster7/J/.
cp /scratch/fwo/stauffer/G/bg10/cluster8/areag.rtd /scratch/fwo/stauffer/G/Cluster_Directories/cluster8/J/.

cd /scratch/fwo/stauffer/G/Filemaker

FILEmaker

Datmaker

VI.2.3.1 FILEmaker.f

```
c- --- - - - ------------------------------------------------------------------
c-------- program to  make the fehmn.files files for all
c-------- 80 subdirectories in the MDA G GoldSim Model..
c- --- - - - ------------------------------------------------------------------

      program filemaker

      implicit none

    character*1  cluster(8), infil(10), slash
      character*74 zzout
    integer   i,   j, k

      infil(1) = 'A'
      infil(2) = 'B'
      infil(3) = 'C'
      infil(4) = 'D'
      infil(5) = 'E'
      infil(6) = 'F'
      infil(7) = 'G'
      infil(8) = 'H'
      infil(9) = 'I'
      infil(10) = 'J'

      cluster(1) = '1'
      cluster(2) = '2'
      cluster(3) = '3'
      cluster(4) = '4'
      cluster(5) = '5'
      cluster(6) = '6'
      cluster(7) = '7'
      cluster(8) = '8'

c ----------------------------  44 characters plus  24 characters
c  1234567890         2         3         4
c  /scratch/fwo/stauffer/G/Cluster_Directories/
c  ------- character 52=cluster  54=infil  62=cluster
c--------------------------------------------------------------------

      zzout(1:44)  = '/scratch/fwo/stauffer/G/Cluster_Directories/'
      zzout(45:68) = 'cluster1/A/fehmn_1.files'
      slash = '/'

      do i = 1,8
       zzout(52:52) = cluster(i)
       zzout(62:62) = cluster(i)
```

```
      do j = 1,10
        zzout(54:54) = infil(j)
        open(11,file=zzout)

        write(11,20) cluster(i),slash,infil(j)
        write(11,21)
        write(11,20) cluster(i),slash,infil(j)
        write(11,22)
          do k=1,6
            write(11,*)
          end do
        write(11,23)
        write(11,24)
        write(11,25)
        write(11,26)
        write(11,*)

        close(11)
      end do
    end do


c--------0---------2---------3---------4---------5---------6---------7--

 20   format("c:/Program Files/GTG/GoldSim/MDA G PA-CA Model/cluster",
  x       A1,A1,A1, "/goldfehm.dat")
 21   format("c:/Program Files/GTG/GoldSim/MDA G PA-CA Model/",
  x        "grid/grid.fehmn")
 22   format('goldfehm.out')
 23   format("c:/Program Files/GTG/GoldSim/MDA G PA-CA Model/",
  x        "grid/grid.stor")
 24   format('goldfehm.chk')
 25   format('none')
 26   format('0')
  END
```

VI.2.3.2 Datmaker.f

```
c- --- - - - ------------------------------------------
c-------- program to change the .dat file for each case
c-------- 80 subdirectories in the MDA G GoldSim model.
c---------  independent of pc directory pathway
c          uses only clusterX/Y/*.dat subdirectories
c- --- - - - ------------------------------------------

      program filemaker

      implicit none
```

```
      character*1  cluster(8), infil(10), slash
        character*80 dumchar
        character*67 zzout
      integer   i,   j, k

        infil(1) = 'A'
        infil(2) = 'B'
        infil(3) = 'C'
        infil(4) = 'D'
        infil(5) = 'E'
        infil(6) = 'F'
        infil(7) = 'G'
        infil(8) = 'H'
        infil(9) = 'I'
        infil(10) = 'J'

        cluster(1) = '1'
        cluster(2) = '2'
        cluster(3) = '3'
        cluster(4) = '4'
        cluster(5) = '5'
        cluster(6) = '6'
        cluster(7) = '7'
        cluster(8) = '8'

        open(12,file='/scratch/fwo/stauffer/G/Filemaker/goldfehm.dat')

c ----------------------------  44 characters plus  23 characters
c  ------- character 52=cluster  54=infil
c-----------------------------------------------------------------

        zzout(1:44)  = '/scratch/fwo/stauffer/G/Cluster_Directories/'
        zzout(45:67) = 'cluster1/A/goldfehm.dat'
        slash = '/'

       do i = 1,8
         zzout(52:52) = cluster(i)
         do j = 1,10
           zzout(54:54) = infil(j)
           open(11,file=zzout)
           rewind(12)
             do k = 1,1000
               read(12,20,end=81,err=81) dumchar
               if(dumchar(1:4).EQ.'clus') then
                 dumchar(8:8) = cluster(i)
                 dumchar(10:10) = infil(j)
               end if
             write(11,20) dumchar
           end do
 81        continue
```

```
        close(11)
       end do
      end do


c--------0---------2---------3---------4---------5---------6---------7--

 20    format(A80)

   END
```

VI.3 Postprocessing Codes

Three postprocessing codes were used in conjunction with the groundwater pathway model. The codes are listed below.

VI.3.1 histo.f

This program creates the rtd file (areag.rtd) for input to the 1-D abstraction model used in GoldSim. Also created are two files containing histogram information for particle breakthrough.

```
      program histo

c------------------
c     code to take the sptr 3  file and
c     and convert the output to a histogram
c     of breakthrough in a series of bins.
c----------------------------------------

      implicit none

      integer part(25000),index, partTot
      integer i, flag, sump ,  bindex, dp

      real*8 time(25000), dtdum, sumt, normp(25000), partr
      real*8 maxc

c-------------------------------------
c   partr = ratio of particles to total particles
c   normp = partr normalized to the size of dtdum
c------------

      open(unit=7,file='areag.sptr3')
      open(unit=16,file='areag.rtd')
      open(unit=17,file='areag.hist3')
      open(unit=18,file='areag.hist_norm')
```

```
c------  read in particles and times
      read(7,*)
      read(7,*)
      read(7,*)

      index = 1
      do while(flag.NE.1)
       read(7,*,err=100) time(index), part(index)
       partTot = part(index)
       index = index + 1
      end do

 100  continue
c--------------------  Write particles per bin

      bindex = 1
      flag = 0
      sump = 0
      sumt = 0.

      write(6,*) ' Total Particles ' , partTot
c     write(16,*) 'Time(s)   part/(partTot*dt)    '
      write(17,*) 'Time(yrs)   particles bin  dT(days)'
      write(18,*) 'Time(s) Time(yrs) Norm1 part/(partTot*dt)  '

      maxc = 0.
      do i=2, index - 1
        dtdum = time(i) - time(i-1)
        dp = part(i) - part(i-1)
        partr = dreal(dp)/dreal(partTot)
        normp(i) = partr / (dtdum/365.25)
        write(16,*) time(i)*86400., normp(i)
        write(17,*) time(i)/365.25, dp, i-1, dtdum
        if(normp(i).GT.maxc) maxc = normp(i)
        sump = sump + dp
        sumt = sumt + dtdum
      end do

      do i=2, index - 1
        write(18,*) time(i)*86400.,time(i)/365.25,normp(i)/maxc,normp(i)
      end do

      write(16,*)
c-----------------------------------------

        close(7)
        close(16)
        close(17)
```

```
      end
```

VI.3.2 satchopg.f

```
c-------- program to take data from  '.sca'  file and put
c---------   depth vs  sat  for R20,  R21 R32, 1121,1107, and pit 36
,
      program schop

     character*80  zzin
     integer  node(1000,6),  i, nn(6),  n
     real*8   x,y,z(1000,6),sat, x1,x2,x3,x5
       write(6,*) 'What is the name of the file to format'
       read *, zzin

       open(16,file=zzin)
       open(18,file='/scratch/fwo/stauffer/G/Grid/1121_borehole.zone')
       open(19,file='/scratch/fwo/stauffer/G/Grid/R20_borehole.zone')
       open(20,file='/scratch/fwo/stauffer/G/Grid/R21_borehole.zone')
       open(21,file='/scratch/fwo/stauffer/G/Grid/R32_borehole.zone')
       open(22,file='/scratch/fwo/stauffer/G/Grid/1107_borehole.zone')
       open(23,file='/scratch/fwo/stauffer/G/Grid/Pit36_borehole.zone')
       open(24,file='zzSat_1121')
       open(25,file='zzSat_R20')
       open(26,file='zzSat_R21')
       open(27,file='zzSat_R32')
       open(28,file='zzSat_1107')
       open(29,file='zzSat_Pit36')
       open(30,file='zzSat_Hari')

       read(18,*)
       read(18,*) nn(4)
       read(19,*)
       read(19,*) nn(1)
       read(20,*)
       read(20,*) nn(2)
       read(21,*)
       read(21,*) nn(3)
       read(22,*)
       read(22,*) nn(5)
       read(23,*)
       read(23,*) nn(6)

       do i = 1,nn(1)
        read(19,*)  node(i,1) , x, y, z(i,1)
       end do
       do i = 1,nn(2)
        read(20,*)  node(i,2) , x, y, z(i,2)
       end do
```

```
do i = 1,nn(3)
 read(21,*)  node(i,3) , x, y, z(i,3)
end do
do i = 1,nn(4)
 read(18,*)  node(i,4) , x, y, z(i,4)
end do
do i = 1,nn(5)
 read(22,*)  node(i,5) , x, y, z(i,5)
end do
do i = 1,nn(6)
 read(23,*)  node(i,6) , x, y, z(i,6)
end do

write(6,*) nn(1)  , x, y
write(6,*) nn(2)  , x, y
write(6,*) nn(3)  , x, y
write(6,*) nn(4)  , x, y
write(6,*) nn(5)  , x, y
write(6,*) nn(6)  , x, y

  read(16,*)

write(24,*) 'Node1121 Elev(m) Elev(ft) Sat1121 '
write(25,*) 'NodeR20 Elev(m) Elev(ft) SatR20 '
write(26,*) 'NodeR21 Elev(m) Elev(ft) SatR21 '
write(27,*) 'NodeR32 Elev(m) Elev(ft) SatR32 '
write(28,*) 'Node1107 Elev(m) Elev(ft) Sat1107 '
write(29,*) 'NodePit36 Elev(m) Elev(ft) SatPit36 '

s1  = 1
s2  = 1
s3  = 1
s4 =  1
s5  = 1
s6 =  1

do i = 1,  375451
  read(16,665) n,x1, x2, x3, sat
  write(30,*) sat

  if(i.EQ.node(s1,1)) then
    zd = z(s1,1)
    write(25,20) node(s1,1), zd, zd/.3048, sat
    s1 = s1 + 1
  end if

  if(i.EQ.node(s2,2)) then
    zd = z(s2,2)
    write(26,20) node(s2,2), zd, zd/.3048, sat
    s2 = s2 + 1
```

```
      end if

      if(i.EQ.node(s3,3)) then
        zd = z(s3,3)
        write(27,20) node(s3,3), zd, zd/.3048, sat
        s3 = s3 + 1
      end if

      if(i.EQ.node(s4,4)) then
        zd = z(s4,4)
        write(24,20) node(s4,4), zd, zd/.3048, sat
        s4 = s4 + 1
      end if

      if(i.EQ.node(s5,5)) then
        zd = z(s5,5)
        write(28,20) node(s5,5), zd, zd/.3048, sat
        s5 = s5 + 1
      end if

      if(i.EQ.node(s6,6)) then
        zd = z(s6,6)
        write(29,20) node(s6,6), zd, zd/.3048, sat
        s6 = s6 + 1
      end if

    end do

 10     format(i8,1x,6g13.4)
 20     format(i10,f10.3,1x,f10.3,1x,f8.2)
665     format(i10.10,2x,4(' : ',e16.9,x))
666     format(i10.10,5(' : ',e16.9))


      close(16)
      close(25)
      close(26)
    close(27)
      close(30)


    END
```

Example input for this code is the list of nodes in the approximate x-y location of Borehole 1121. The header line is for reference, the second line is the number of nodes in the file and the next 23 nodes are the numerical representation of the well.

```
=====================================================
Borehole 1121   top at 6685 ft
23
0000062729      0.219843750E+05  -0.132164062E+06   0.190000000E+04
```

0000077832	0.219843750E+05	-0.132164062E+06	0.190625000E+04
0000091771	0.219843750E+05	-0.132164062E+06	0.191250000E+04
0000105758	0.219843750E+05	-0.132164062E+06	0.191875000E+04
0000120315	0.219843750E+05	-0.132164062E+06	0.192500000E+04
0000134792	0.219843750E+05	-0.132164062E+06	0.193125000E+04
0000148731	0.219843750E+05	-0.132164062E+06	0.193750000E+04
0000162718	0.219843750E+05	-0.132164062E+06	0.194375000E+04
0000177629	0.219843750E+05	-0.132164062E+06	0.195000000E+04
0000192732	0.219843750E+05	-0.132164062E+06	0.195625000E+04
0000206671	0.219843750E+05	-0.132164062E+06	0.196250001E+04
0000220658	0.219843750E+05	-0.132164062E+06	0.196875001E+04
0000235215	0.219843750E+05	-0.132164062E+06	0.197500001E+04
0000249692	0.219843750E+05	-0.132164062E+06	0.198125001E+04
0000263631	0.219843750E+05	-0.132164062E+06	0.198750001E+04
0000277618	0.219843750E+05	-0.132164062E+06	0.199375001E+04
0000292529	0.219843750E+05	-0.132164062E+06	0.200000001E+04
0000307631	0.219843750E+05	-0.132164062E+06	0.200625001E+04
0000321290	0.219843750E+05	-0.132164062E+06	0.201250001E+04
0000333891	0.219843750E+05	-0.132164062E+06	0.201875001E+04
0000345275	0.219843750E+05	-0.132164062E+06	0.202500001E+04
0000354487	0.219843750E+05	-0.132164062E+06	0.203125001E+04
0000361096	0.219843750E+05	-0.132164062E+06	0.203750001E+04

VI.3.3 well.f

```
      program well

c------------------
c    Code to take the sptr 2  file and
c    find the particles entering the well, output to areag.wellout.
c    All particles last points are output to the file areag.allout.
c    Also creates areag.sptr2_capture file that
c    contains a flag so the particles pathways can be colored
c    from the release point to the well.
c----------------------------------------

      implicit none

      integer part,zone,old,new, flag, index, count
      integer numpart, i, partn(50000), parts(50000)
      integer capt(50000)

      real*8 x,y,z,time
      real*8 xs(50000), ys(50000), zs(50000),times(50000)
c--------------------------------------

      open(unit=7,file='areag.sptr2')
      open(unit=17,file='areag.wellout')
```

```
      open(unit=18,file='areag.allout')
      open(unit=19,file='areag.sptr2_capture')

      write(17,*) 'part x y z time zone old new'
      write(19,*) 'part x y z t zone old new capture'
c------  read in particles and other info
      read(7,*)
      read(7,*)
      read(7,*)

      do while(flag.NE.1)
       read(7,*,err=100) part,x,y,z,time,zone,old,new
       if(time.EQ.0.0) numpart = numpart + 1
       partn(part) = new
       xs(part) = x
       ys(part) = y
       zs(part) = z
       times(part) = time
       parts(part) = part

       if(new.EQ.0) index = index + 1
      end do

 100  continue

      write(6,*) numpart
      do i = 1,numpart
         capt(i) = -1
         write(6,555) parts(i),xs(i),ys(i),zs(i),times(i),partn(i)
         write(18,555) parts(i),xs(i),ys(i),zs(i),times(i),partn(i)
         if(partn(i).LT.0) then
         write(17,555) parts(i),xs(i),ys(i),zs(i),times(i),partn(i)
         count = count + 1
         capt(i) = 1
       end if
      end do

      index = index + count

      write(17,*) count, index , dreal(count)/dreal(index)
      write(6,*) count, index , dreal(count)/dreal(index)

c-----------------------------------------
c    WRite out new sptr2 file with the capture flag set +1 -1

c       rewind(7)
c       read(7,*)
c       read(7,*)
c       read(7,*)
```

```
c       do while(flag.NE.1)
c         read(7,*,err=101) part,x,y,z,time,zone,old,new
c         write(19,556) part,x,y,z,time,zone,old,new,capt(part)
c       end do

c 101   continue

c----------------------------------------

     close(7)
       close(17)

 555  format(I5,x,F12.1,xF9.1,x,F6.1,x,F9.1,x,I6,x,I6,x,I6)
 556  format(I5,x,F12.1,xF9.1,x,F6.1,x,F9.1,4(x,I6))

      end
```

Attachment VII
Comparison of 2005 and 2011 Results for the Los Alamos National Laboratory TA-54, Area G Groundwater Pathway Model

*Author*s
Shaoping Chu
Philip H. Stauffer

VII.1 Introduction

As discussed in the main report, the Area G groundwater modeling was updated, primarily, to incorporate a more accurate understanding of the geology beneath and in the vicinity of the disposal facility. Section VII-2 of this attachment compares the geologic cross-sections that were used in the 2005 groundwater model to represent the eight waste disposal regions to the cross-sections used in the updated 2011 model. Changes in the geologic cross-sections affect projections of particle breakthrough; Section VII-3 compares the breakthrough curves projected by the modeling for the eight disposal regions.

VII.2 Geologic Cross-Sections

Figures VII-1 through VII-4 compare the geologic cross-sections adopted for the eight waste disposal regions in 2005 to the cross-sections developed using the WC09b geologic framework model (GFM), which was the basis for the 2011 groundwater modeling. Examination of these figures reveals that the nature and magnitude of the differences between the cross-sections vary widely across the disposal site. For all waste disposal regions, one or more geologic units are found in the earlier cross-sections but not in the 2011 model. For example, the Cerro Toledo interval (Qct) occurs in the 2005 cross-section for disposal region 1 but is not found in the 2011 cross-section. The Guaje Pumice (Qbog) occurs in the earlier cross-sections for disposal regions 2, 3, 5, 6, and 7 but not in the later cross-sections.

The other notable difference between the cross-sections used in the 2005 and 2011 groundwater models concerns the overall thickness of the Bandelier Tuff and the underlying Cerros del Rio (Tb4) basalts. In general, the tuff tends to be thinner in the 2011 cross-sections, accompanied by a corresponding increase in the thickness of the basalts. Exceptions occur, as shown for disposal region 3, where the thickness of the basalt is nearly identical for the 2005 and 2011 cross-sections, and disposal region 8, which was projected to have a thinner basalt layer in the 2011 cross-section. The magnitude of the differences in tuff and basalt thickness ranges from moderate (disposal region 5) to large (disposal region 4).

In general, the presence of geologic units beneath Area G is established, and the thicknesses of those units assigned, by interpolating observations between sampling points (boreholes and wells). Data generated from boreholes and wells that have been drilled since the 2005 modeling provide greater insight into actual subsurface conditions and provide an opportunity to improve upon the accuracy of previous interpolations. For example, in some cases the new boreholes and wells reveal the absence of a unit under portions of the disposal site that was not evident from the more widely spaced boreholes and wells used for the earlier modeling. In other cases, the additional boreholes and wells enable more accurate estimates of a given unit's thicknesses. Additional details about the GFMs used in the 2005 and 2011 modeling are provided in *Attachment I*.

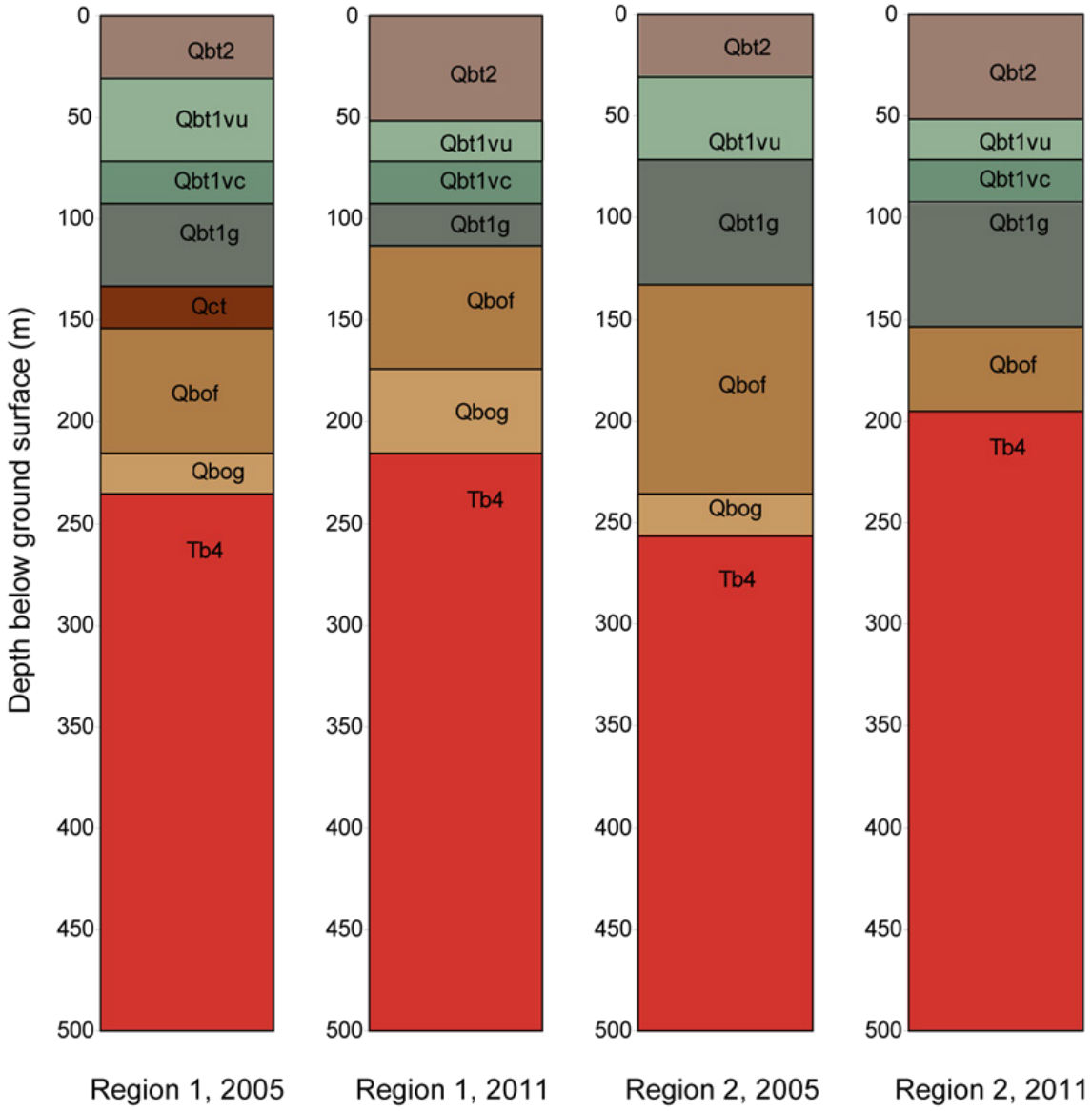

Figure VII-1
Comparison of Geologic Cross-sections for Waste Disposal Regions 1 and 2 in the 2005 and 2011 Groundwater Models

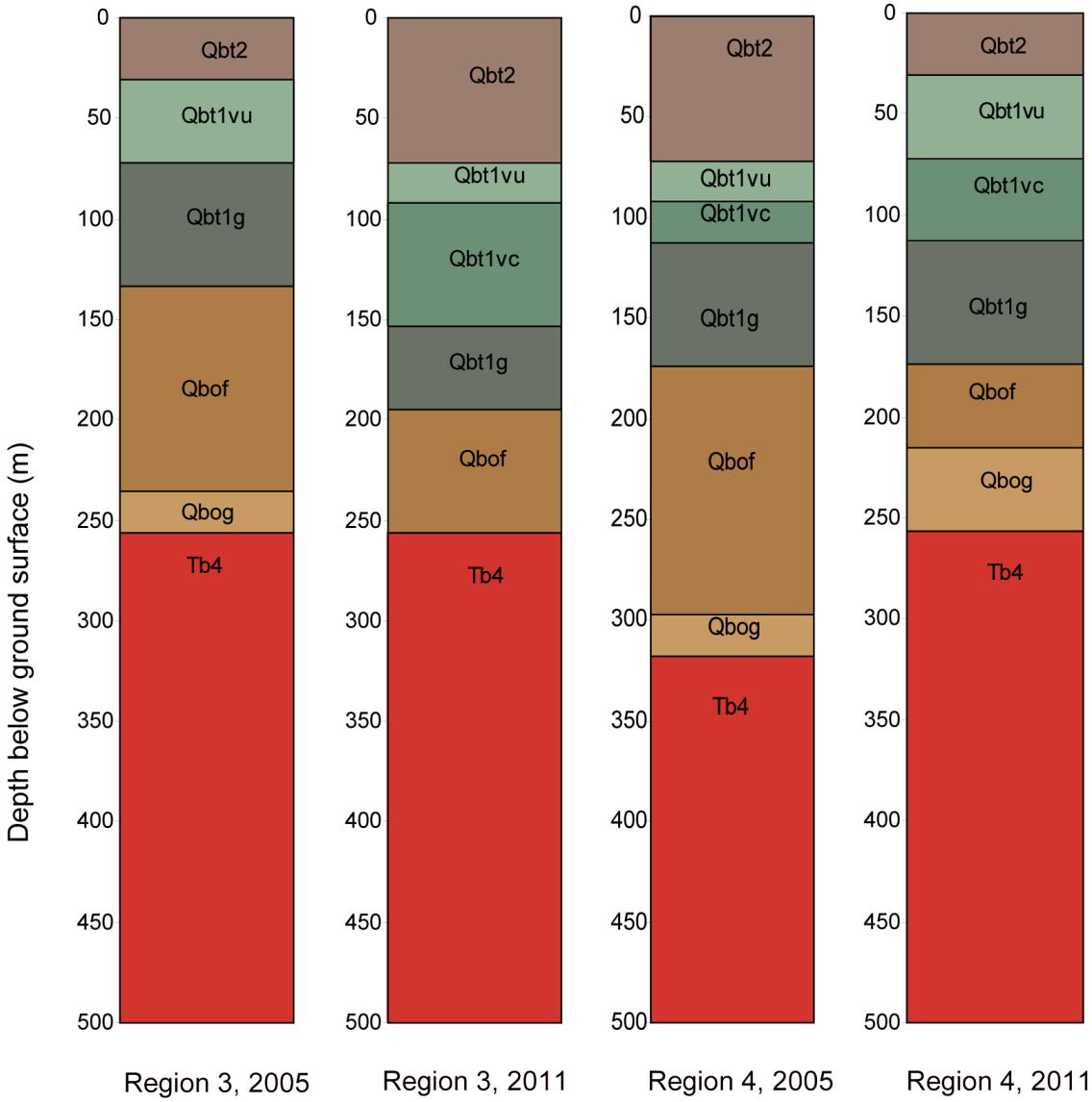

Figure VII-2
Comparison of Geologic Cross-sections for Waste Disposal Regions 3 and 4 in the 2005 and 2011 Groundwater Models

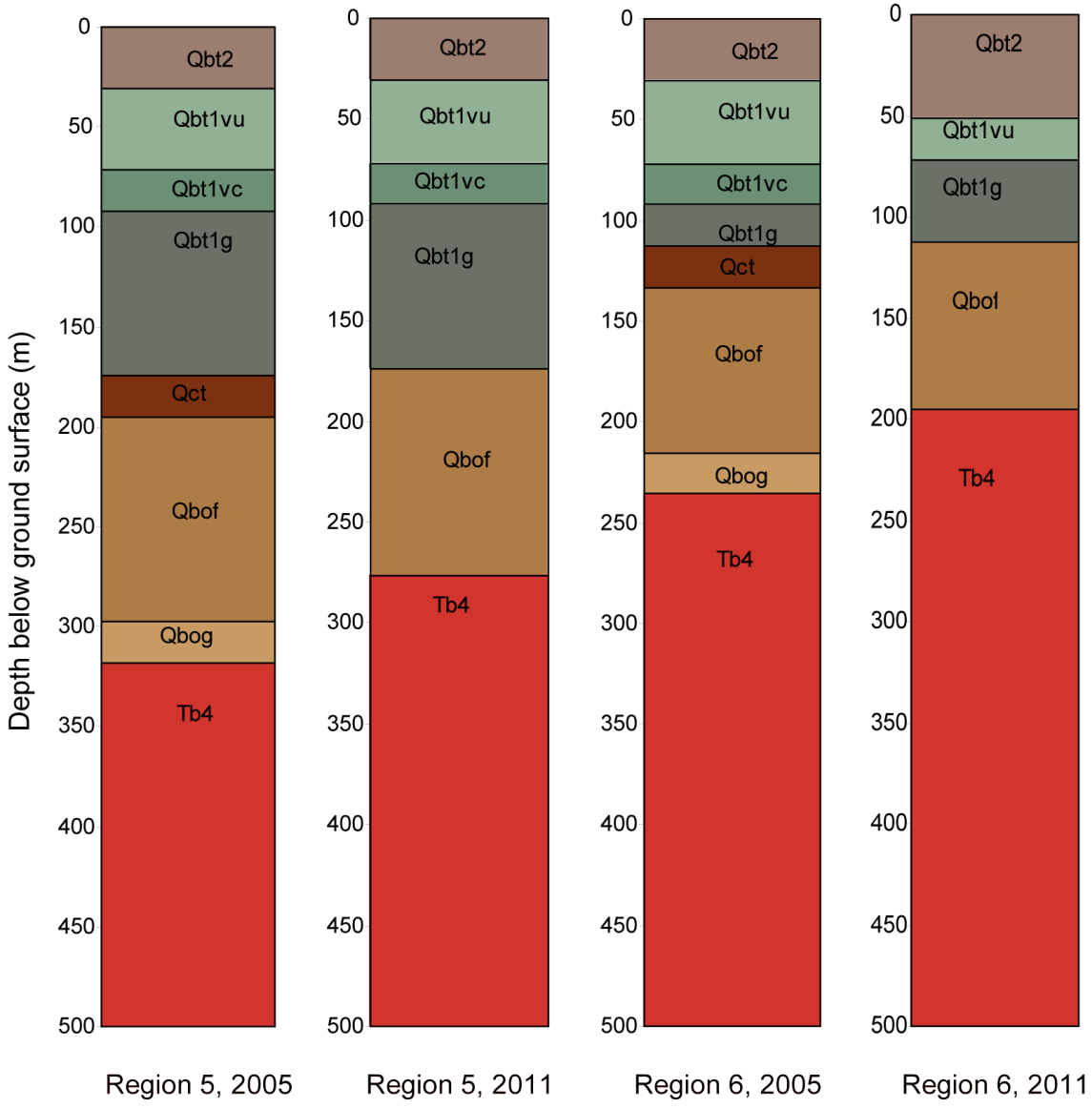

Figure VII-3
Comparison of Geologic Cross-sections for Waste Disposal Regions 5 and 6 in the 2005 and 2011 Groundwater Models

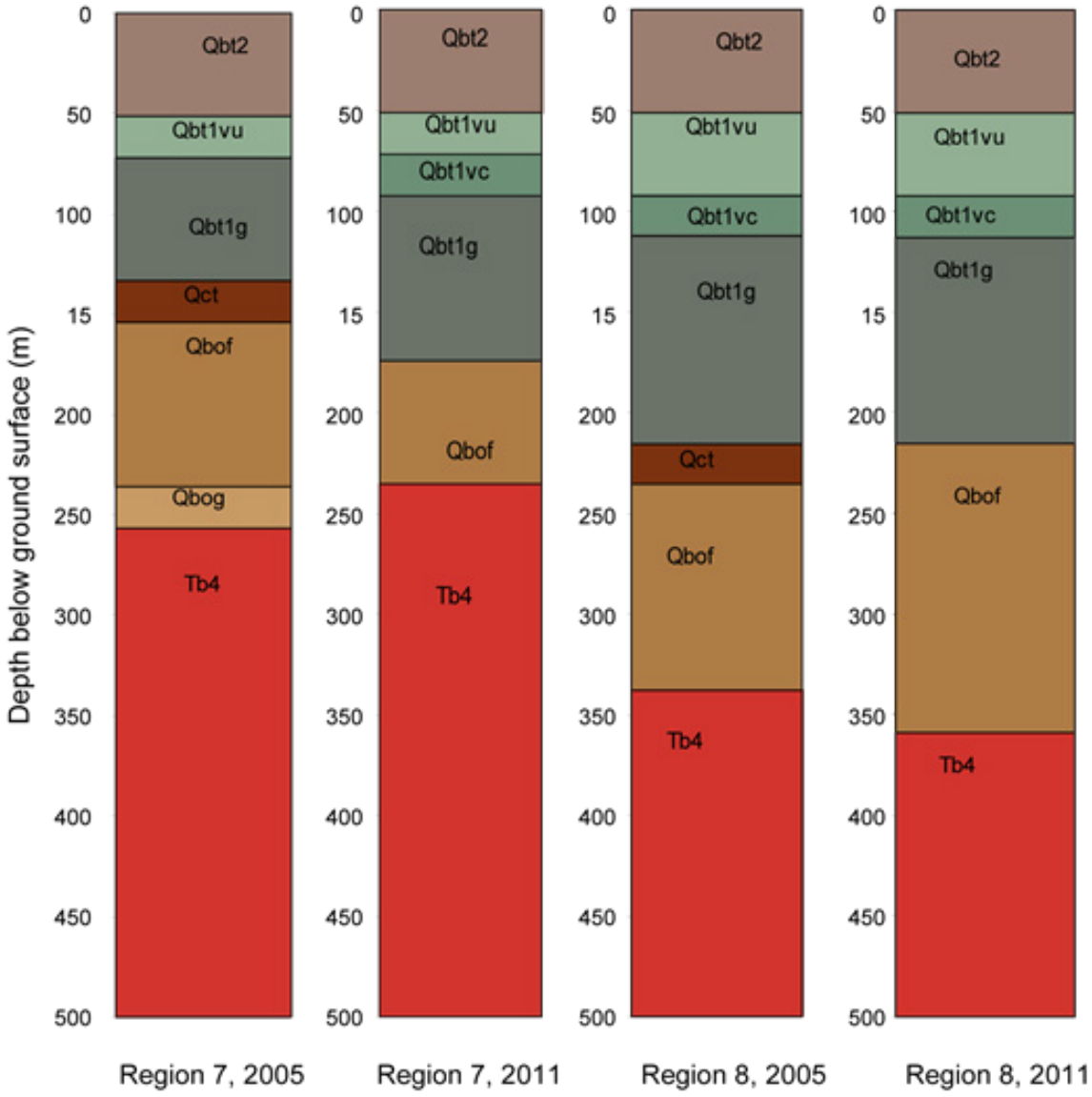

Figure VII-4
Comparison of Geologic Cross-sections for Waste Disposal Regions 7 and 8 in the 2005 and 2011 Groundwater Models

VII.3 Normalized Breakthrough Curves

The changes in thicknesses of the Bandelier Tuff and Cerros del Rio basalts have a significant impact on the rate at which water flows through the unsaturated zone to the regional aquifer beneath Area G. In general, travel times in the tuff are slow compared to those through the highly porous basalts. Consequently, the general trend towards thinner tuff and thicker basalts in the 2011 groundwater modeling suggest a reduction in the breakthrough times projected using the Finite Element Heat and Mass (FEHM) transport code.

Table VII-1 summarizes the approximate peak breakthrough times projected using the 2005 and 2011 models. The 2005 and 2011 breakthrough curves projected for the eight waste disposal regions are compared in Figures VII-5 through VII-12; breakthrough curves are shown for two infiltration rates, 1 and 10 mm/yr (0.039 and 0.39 in./yr). The breakthrough curves are normalized to 1.0 to facilitate comparison of the time histories projected by the two models. The 2011 model projects earlier particle breakthrough than the 2005 model at all locations; differences in breakthrough times are similar for both infiltration rates.

Table VII-1
Approximate Peak Breakthrough Times by Waste Disposal Region, 2005 vs. 2011

	Peak Breakthrough Time			
	Infiltration 1 mm/yr		Infiltration 10 mm/yr	
Waste Disposal Region	2005	2011	2005	2011
1	7050	6000	1000	840
2	8120	5120	1180	760
3	7840	6680	1210	1050
4	8680	5890	1320	950
5	9420	7320	1260	1100
6	6210	3500	950	570
7	7110	6000	1050	830
8	9170	8220	1440	1330

Consistent with the discussion in Section VII-2, differences in breakthrough behavior are smaller for some waste disposal regions. For example, breakthrough times projected for disposal regions 1, 3, 7, and 8 are the most similar; the thickness of the tuff in these regions remained relatively constant between 2005 and 2011. On the other hand, breakthrough times are quite different for disposal regions 2, 4, and 6 because the tuff in these regions is much thinner in the 2011 model.

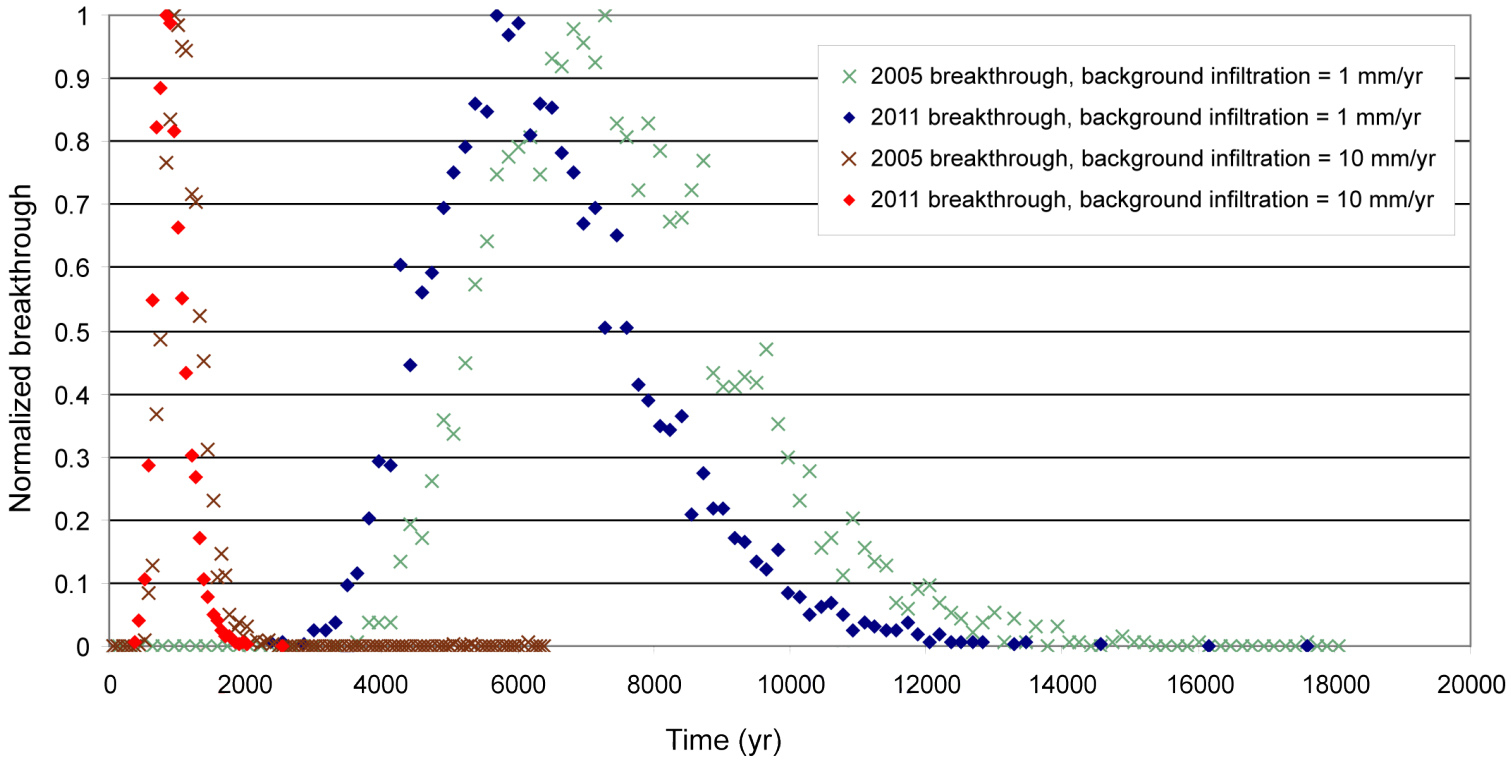

Figure VII-5
Comparison of 2005 and 2011 Model Breakthrough Curves for Waste Disposal Region 1 (infiltration rate = 1 mm/yr and 10 mm/yr)

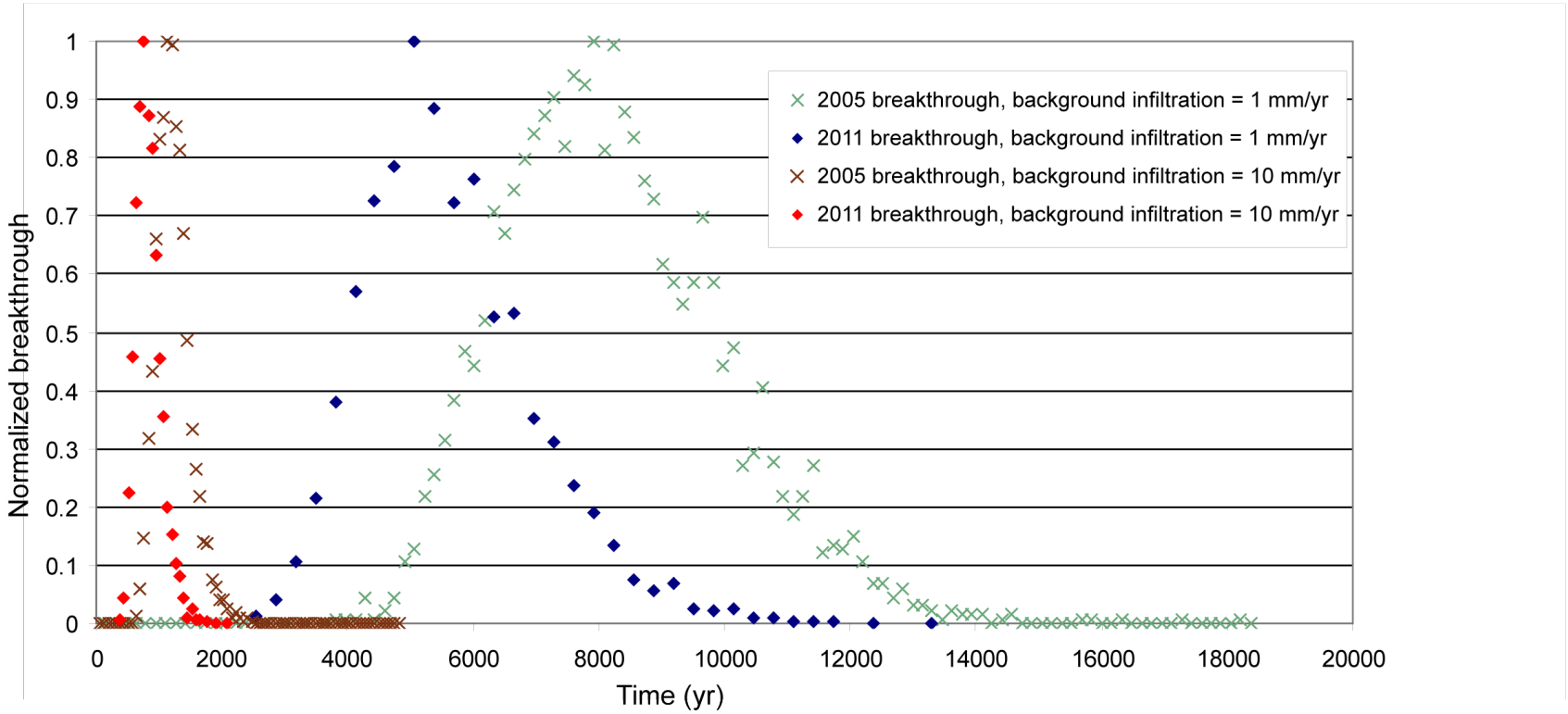

Figure VII-6
Comparison of 2005 and 2011 Model Breakthrough Curves for Waste Disposal Region 2 (infiltration rate = 1 mm/yr and 10 mm/yr)

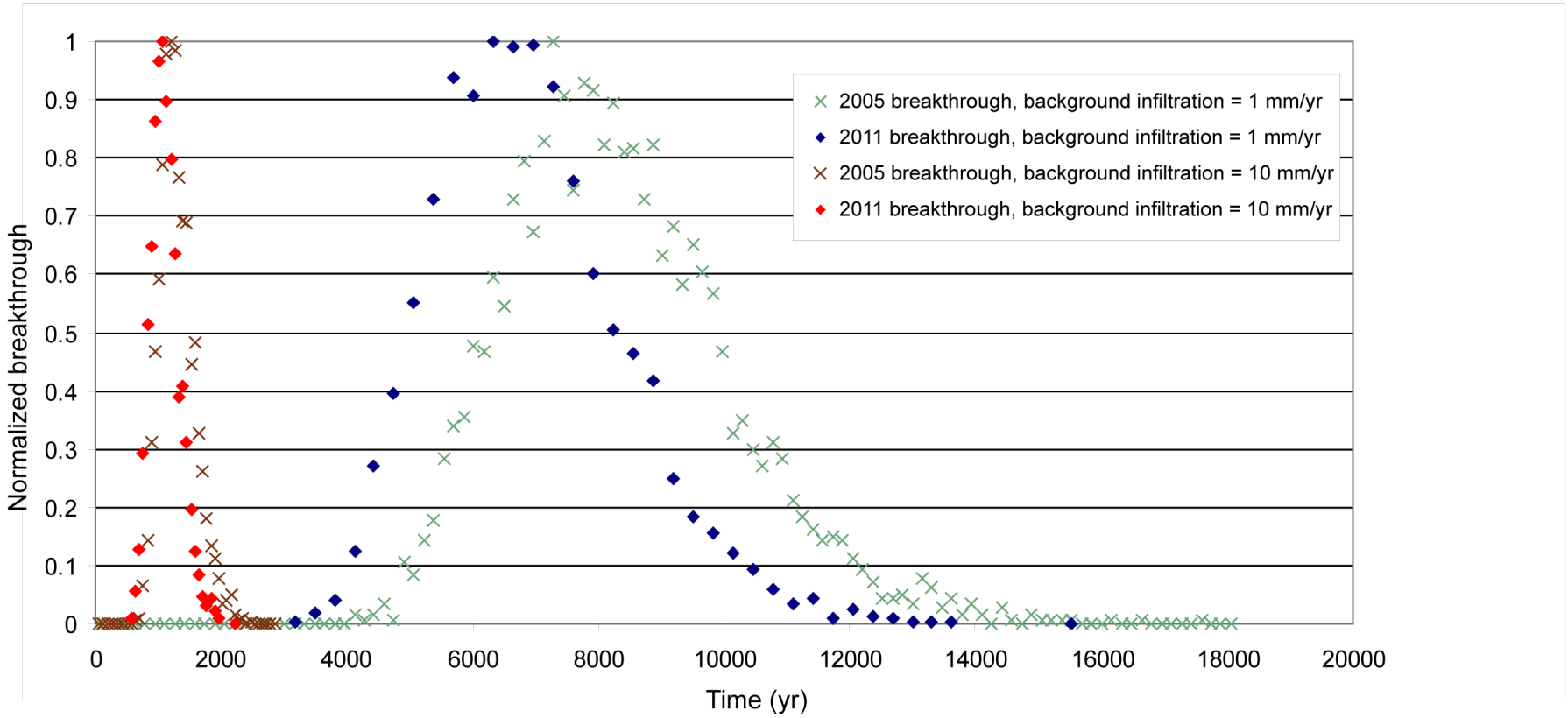

Figure VII-7
Comparison of 2005 and 2011 Model Breakthrough Curves for Waste Disposal Region 3 (infiltration rate = 1 mm/yr and 10 mm/yr).

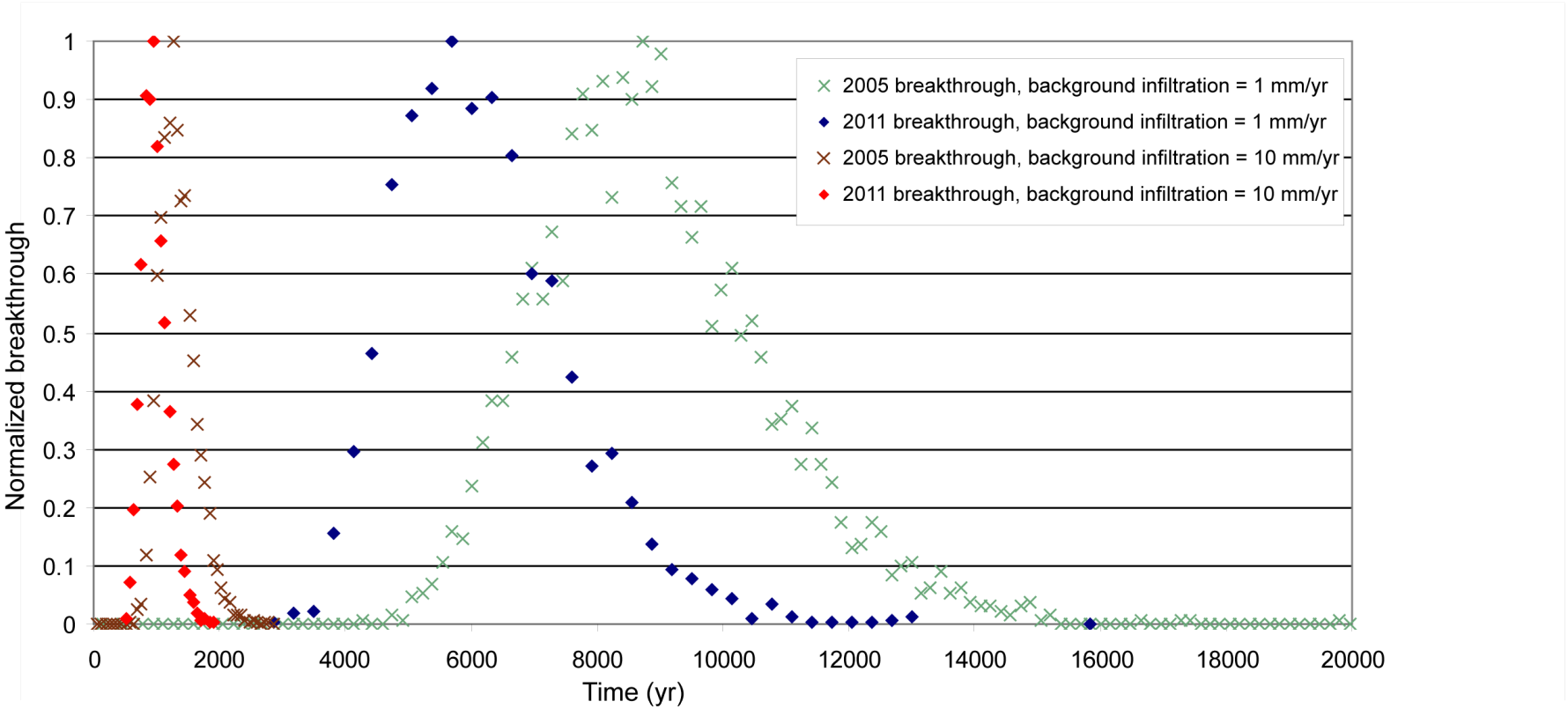

Figure VII-8
Comparison of 2005 and 2011 Model Breakthrough Curves for Waste Disposal Region 4 (infiltration rate = 1 mm/yr and 10 mm/yr)

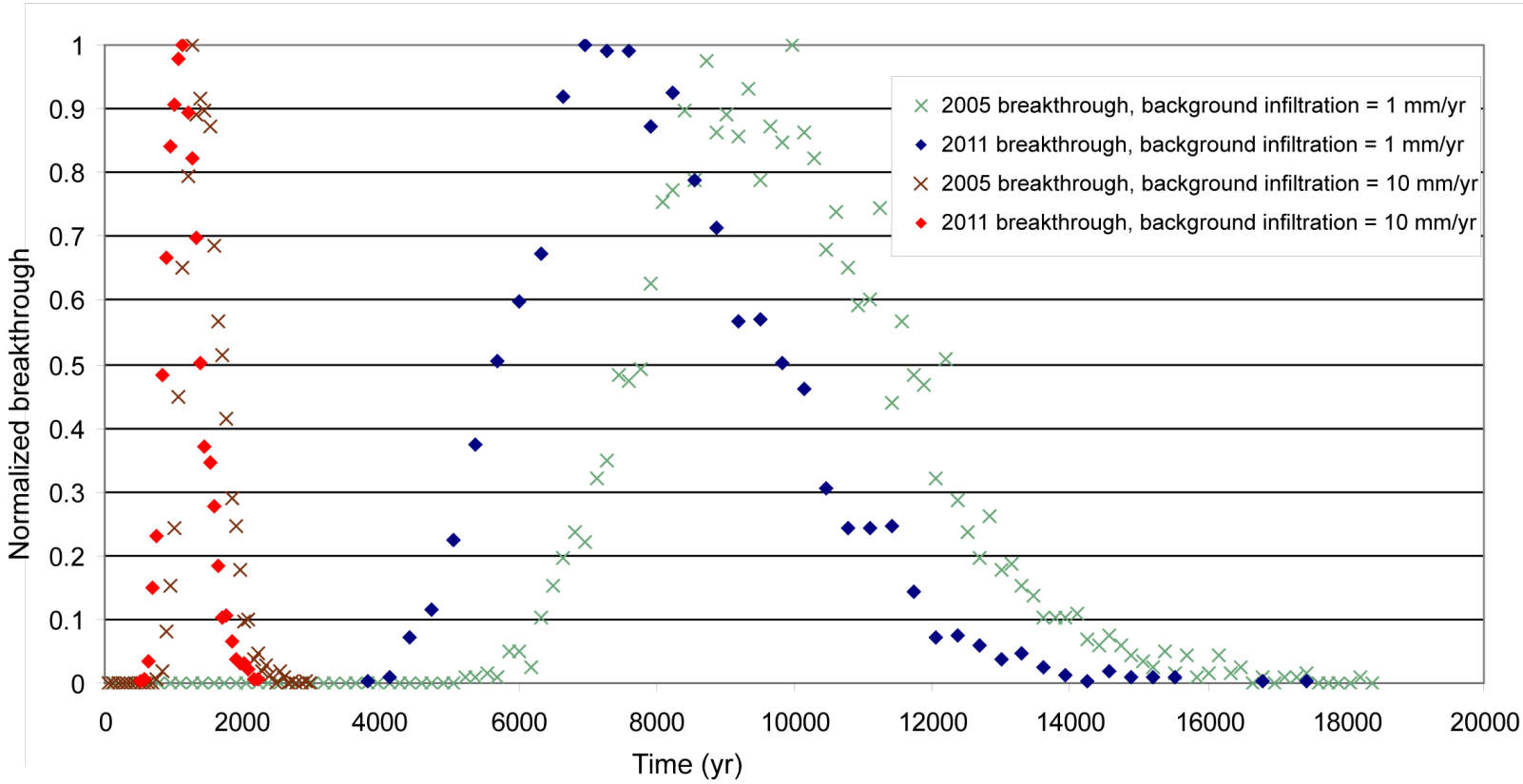

Figure VII-9
Comparison of 2005 and 2011 Model Breakthrough Curves for Waste Disposal Region 5 (infiltration rate = 1 mm/yr and 10 mm/yr)

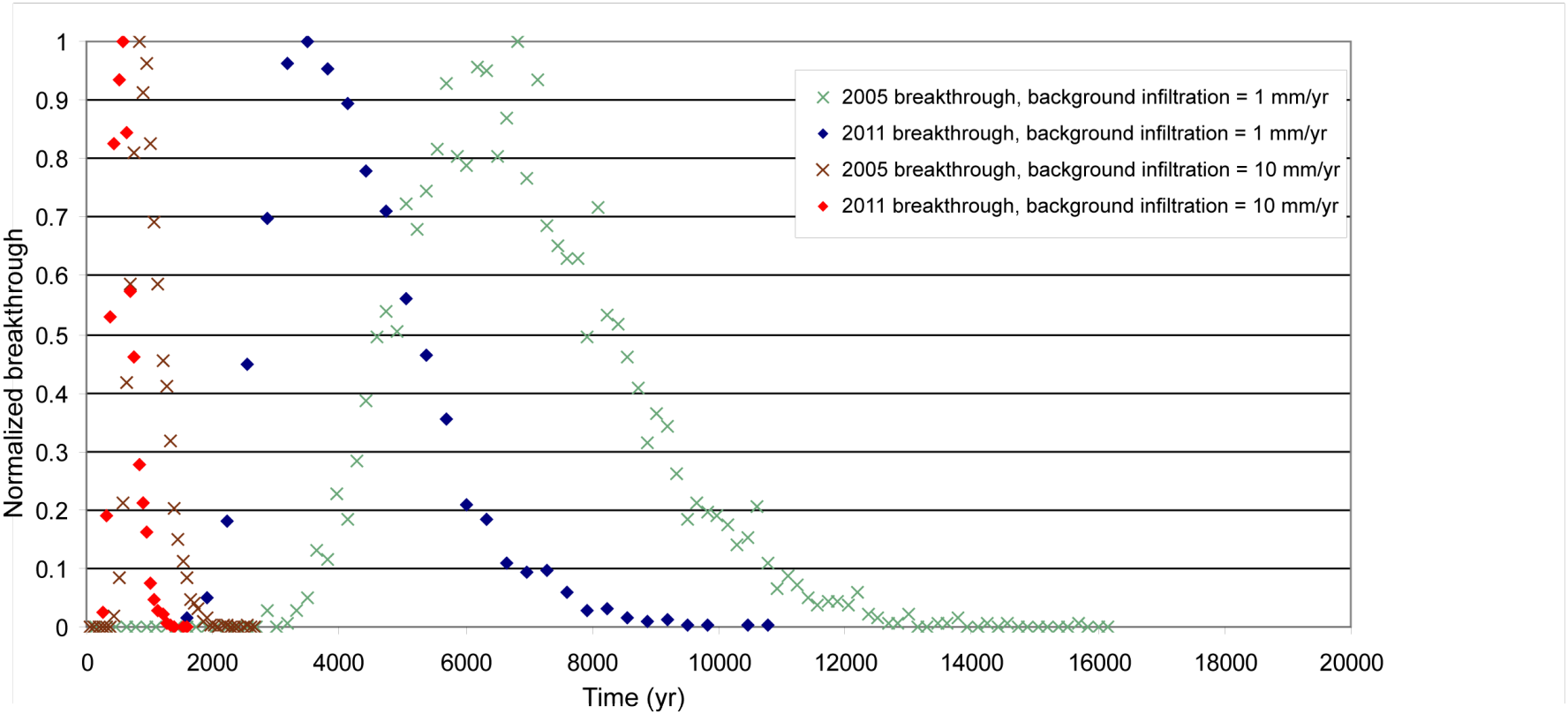

Figure VII-10
Comparison of 2005 and 2011 Model Breakthrough Curves for Waste Disposal Region 6 (infiltration rate = 1 mm/yr and 10 mm/yr)

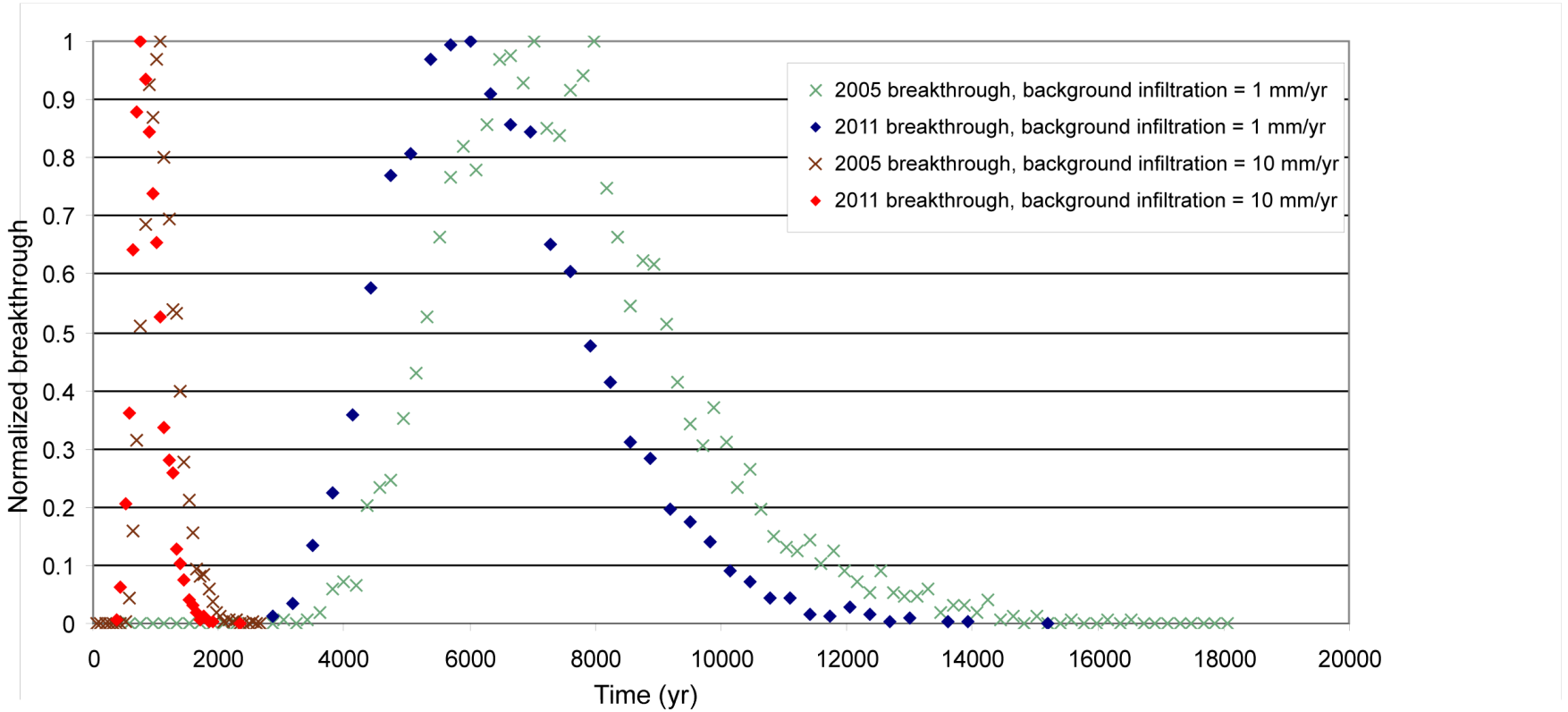

Figure VII-11
Comparison of 2005 and 2011 Model Breakthrough Curves for Waste Disposal Region 7 (infiltration rate = 1 mm/yr and 10 mm/yr)

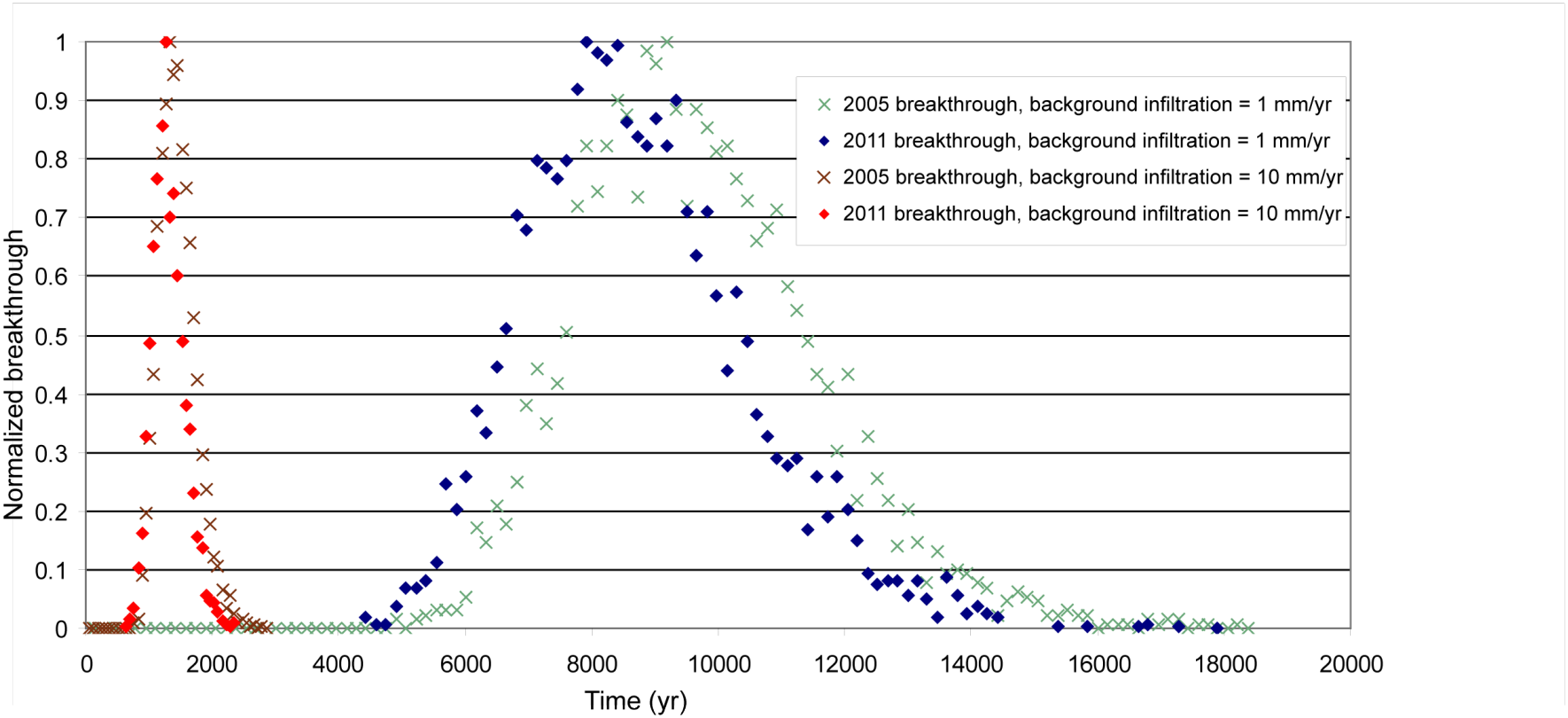

Figure VII-12
Comparison of 2005 and 2011 Model Breakthrough Curves for Waste Disposal Region 8 (infiltration rate = 1 mm/yr and 10 mm/yr)

The results shown in Figures VII-5 through VII-12 indicate that the thickness of the Bandelier Tuff is the primary determinant of breakthrough times beneath Area G, with the longest travel times occurring where the tuff is thickest (e.g., disposal regions 5 and 8). However, the permeability reduction present at the top of the Cerros del Rio basalts (see Section 3.2.3 of the main report) also plays a role in determining breakthrough behavior. This reduced permeability causes water to spread laterally at the contact before it flows downward to the water table, delaying breakthrough in the process. For waste disposal region 8, lateral spreading at the top of the basalt is about 30 m (98 ft) in the 2011 model, much less than the 100 m (328 ft) spread projected in the 2005 model. Thus, even though the Bandelier Tuff is slightly thicker at this location in the 2011 model (Figure VII-4), breakthrough occurs at times earlier than those projected in 2005.

Attachment VIII
Quantifying Transport Uncertainty in Unsaturated Soil using Monte Carlo Sampling of Retention Curves for the Los Alamos National Laboratory Technical Area-54, Area G Groundwater Pathway Model

Authors
Zhiming Lu
Philip H. Stauffer

VIII.1 Introduction

The groundwater pathway modeling conducted in support of the Area G performance assessment and composite analysis uses mean hydrologic properties of geologic strata to estimate rates of water flow and contaminant transport in the vadose zone below the disposal facility. Variability in these properties introduces uncertainty into the model projections. The analysis presented below describes how the variability in the media properties affects the breakthrough curves estimated by the modeling. Additional details can be found in Stauffer and Lu (In Press).

VIII.2 Methods

Monte Carlo simulations can be used to understand the effects that uncertainties in hydrologic properties have upon groundwater or contaminant breakthrough times estimated by means of models. In such simulations, hydrologic properties are sampled from input distributions and used to implement flow and transport equations for a large number of realizations. Breakthrough curve statistics are then computed from these realizations. Researchers often use a simple arithmetic average of breakthrough curves to describe the mean behavior of the system; deviations from the mean are calculated using typical statistical methods. This approach, however, tends to distort the system behavior by producing earlier estimates of initial breakthrough and longer tails than the individual breakthrough curves suggest.

A disadvantage of Monte Carlo simulations is their heavy computational demands. These demands are especially great for unsaturated flow models which solve nonlinear flow equations. A different approach to evaluating uncertainty is introduced here that requires much less computational time to conduct probabilistic groundwater model simulations. Rather than sampling distributions of the basic hydrologic properties, this approach samples distributions of soil retention curves directly. The retention curve distributions are developed easily and quickly from the hydrologic properties using Monte Carlo techniques. Sampling retention curves rather than the component hydrologic properties greatly reduces the number of realizations needed to understand the model's behavior, while retaining reasonable accuracy.

VIII.2.1 Model Description

The Area G groundwater model used to conduct the uncertainty analysis is described in the main body of this report. Developed using the Finite Element Heat and Mass (FEHM) transport code, the model uses a three-dimensional (3-D) numerical grid to represent the topography and geology of the disposal facility and its environs. The grid offers high resolution near the disposal facility to permit accurate location of important features such as disposal units, truncated material layers along the mesa edges, and facility and compliance boundaries.

All lateral boundaries in the vadose zone are assumed to be no-flow boundaries; no mass may enter or leave the system via these boundaries. Water in the regional aquifer flows from west to

east, towards the Rio Grande. A constant hydraulic head is maintained on the east and west faces of the model within the saturated zone; the northern and southern boundaries are no-flow boundaries. A constant infiltration rate of 1 mm/yr (0.039 in./yr) was applied at the top boundary of the model for the purposes of investigating model uncertainty. Dispersion is fixed, with longitudinal dispersivity equal to 2 m (6.6 ft), transverse dispersivity fixed to zero, and diffusion set to zero.

VIII.2.2 Hydrologic Properties of Geologic Strata

Unsaturated flow is described using the constitutive relationships of unsaturated hydraulic conductivity versus pressure head, and effective water content versus pressure head. The FEHM modeling adopts the van Genuchten–Mualem model (van Genuchten, 1980):

$$K(\boldsymbol{x},t) = K_s(\boldsymbol{x})\sqrt{S(\boldsymbol{x},t)}\{1-[1-S^{1/m}(\boldsymbol{x},t)]^m\}^2 \quad (1)$$

$$S(\boldsymbol{x},t) = \{1+[-\alpha(\boldsymbol{x})\psi(\boldsymbol{x},t)]^n\}^{-m} \quad (2)$$

Where

ψ = pressure head
$K_S(x)$ = saturated hydraulic conductivity (m/s)
$S(x,t)$ = effective saturation, $\theta_e/(\theta_s-\theta_r)$, where
θ_e = effective water content, $\theta_r \le \theta_e \le \theta_s$
θ_r = residual (irreducible) water content
θ_s = saturated water content
α = pore-size distribution parameter (m^{-1})
n = fitting parameter
m = $1 - 1/n$

Springer (2005) examined geographical differences among vadose-zone hydrologic properties across the Laboratory as a means of estimating vadose-zone model parameters for the Bandelier Tuff. These hydrologic properties include bulk density, saturated water content, saturated hydraulic conductivity, fitted parameters such as the van Genuchten parameters (α and n), and residual water content. Nonparametric analyses were used to identify differences in the measured hydrologic properties for different lithologic units within various LANL technical areas and mesa-top versus canyon settings.

The uncertainty analysis treats hydrologic properties for four lithologic units of the Bandelier Tuff (units 2, 1v, and 1g of the Tshirege Member, and the Otowi Member) as random variables. The saturated hydraulic conductivity K_s, the pore size distribution parameter α, fitting parameter n, the saturated water content θ_s, and residual water content θ_r are treated as piece-wise random functions, which vary from unit to unit but are constants within each unit. Information provided

in Springer (2005) was used to estimate distributions for these input parameters; the parameter statistics provided in Springer and the distributions assigned to the hydrologic properties of the four units are summarized in Table VIII-1. The parameters K_S and α are described using log-normal distributions, n is assumed to follow a truncated normal distribution (with a lower bound of 1.0), and θ_s and θ_r are assumed to be normally distributed.

Table VIII-1
Parameter Statistics and Assigned Distributions for Bandelier Tuff Stratigraphic Units

Parameter	Unit	No. of Samples	Mean	Standard Deviation	Lower Bound	Upper Bound
ln K_s (m/s)	Tshirege Member unit 2 (Qbt2)	17	–13.12	1.13		
	Tshirege Member unit 1v (Qbt1v)	44	–13.63	1.06		
	Tshirege Member unit 1g (Qbt1g)	17	–13.59	0.69		
	Otowi Member (Qbof)	12	–12.89	0.46		
ln α (1/m)	Qbt2	8	–0.76	0.69	–6.91	4.61
	Qbt1v	34	–0.87	0.94	–6.91	4.61
	Qbt1g	9	–0.90	0.32	–6.91	4.61
	Qbof	12	–0.53	0.21	–6.91	4.61
n	Qbt2	8	2.06	0.51	1	5
	Qbt1v	34	1.73	0.28	1	5
	Qbt1g	9	1.81	0.17	1	5
	Qbof	12	1.76	0.25	1	5
θ_s	Qbt2	10	0.41	0.03	0	0.6
	Qbt1v	35	0.5	0.04	0	0.6
	Qbt1g	14	0.46	0.05	0	0.6
	Qbof	12	0.43	0.01	0	0.6
θ_r	Qbt2	8	0.01	0.013	0	0.05
	Qbt1v	34	0.003	0.009	0	0.05
	Qbt1g	9	0.01	0.015	0	0.05
	Qbof	12	0.019	0.015	0	0.05

Monte Carlo simulations were conducted using the hydrologic property distributions presented in Table VIII-1 to generate a series of retention curves for each geologic unit. The realizations were conducted using the Latin Hypercube Sampling (LHS) method. First described by McKay (1979), and further elaborated upon by Iman et al. (1981), this sampling scheme is a form of

stratified sampling that can be applied to multiple variables. The method is commonly used to reduce the number of realizations that are required to achieve a reasonably accurate random distribution.

A series of 1,000 retention curves (see Equation 1) was developed for each geologic unit for saturations ranging from zero to 1. The curves for each unit were sorted on the basis of capillary pressure at a saturation of 0.5, and the sorted curves were divided into groups of 5, 10, 20, and 40 retention curves. The subsets of the retention curves were developed to allow evaluation of the number of realizations required to achieve convergence of the breakthrough modeling results and to explore the efficiency of different retention curve sampling approaches.

VIII 2.3 Particle Breakthrough Modeling

Monte Carlo simulations were conducted using the Area G groundwater model to estimate the impacts of variability in hydrologic properties on particle breakthrough. Two approaches for conducting these simulations were used. First, parameters were sampled from the distributions of hydrologic properties shown in Table VIII-1 and used in FEHM simulations of particle breakthrough; four simulations were conducted, using 25, 50, 100, and 1,000 realizations. In these simulations, 15,625 particles were uniformly distributed within, and released from, a 1-m (3.3-ft) cube; the particles were tracked until they reached the groundwater pathway compliance boundary, 100 m (330 ft) downgradient of the Area G fence line. The number of particles reaching the compliance boundary was recorded and normalized cumulative breakthrough curves were developed. All simulations were conducted using LHS.

The second series of Monte Carlo simulations sampled the retention curves distributions described in Section VIII.2.2 and used these curves in FEHM to estimate particle breakthrough. Four simulations were conducted using 25, 50, 100, and 200 realizations. Each simulation used three methods for sampling the retention curves. As explained earlier, the 1,000 retention curves for each geologic unit were ordered on the basis of capillary pressure at a saturation of 0.5 and divided into groups of 5, 10, 20, and 40 curves. For each unit, the first sampling approach selected the middle retention curve from each interval; the selected curves were then used to conduct one model realization. This sequence was repeated until all realizations for the simulation were completed. For example, the first realization of a 50-realization simulation would select the middle retention curve for unit 2 of the Tshirege Member from one of the 20 groups of retention curves. Curves for the other three units would be selected similarly and the realization would be implemented. Retention curves were sampled randomly from each group in the second sampling approach. In the third approach, retention curves were randomly selected from the entire population of 1,000 curves, without regard to the group in which they occurred.

VIII.3 Results and Discussion

The results of the uncertainty analysis are presented below. The distributions of the retention curves are presented and discussed in Section VIII.3.1, followed by a discussion of the impacts of hydrologic parameter variability on projected breakthrough times in Section VIII.3.2.

VIII.3.1 Retention Curve Distributions

Figure VIII-1 presents the 1,000 retention curves for the four geologic units. The heavy red and blue curves represent the fifth and ninety-fifth percentiles of the distribution when the retention curves are ordered by capillary pressure at a saturation of 0.5; the symbols shown in the figure are capillary pressures calculated using measurements of gravimetric moisture content and matric potential taken from Springer (2005). The distributions of the retention curves are not uniform across the range of saturations; curves for low saturations tend to be more widely dispersed than the curves observed at higher water contents. Most of the capillary pressures calculated from measurements of saturation and matric potential lie between the fifth and ninety-fifth percentile curves shown in Figure VIII-1.

The retention curves for units 2 and 1v of the Tshirege Member exhibit the greatest spread throughout the range of saturations, a result of the high variability seen in the units' hydrologic properties. It is interesting to note that spreading of retention curves for Qbt1g is smaller than that of Qbo, even though all Qbt1g rock properties except *n* (the van Genuchten fitting parameter) have greater variability than do the properties for Qbo. This result indicates that the variability of *n* has a large impact on the degree of spreading of retention curves. This observation is consistent with stochastic analysis (Lu and Zhang, 2002).

VIII 3.2 Modeling Results

The results of the 1,000-realization Monte Carlo simulation are provided in Figure VIII-2; mean, median, fifth, and ninety-fifth percentile breakthrough curves are indicated in the figure as well. These results were obtained by sampling the hydrologic property distributions and using the sampled values in the FEHM groundwater model. Examination of the figure reveals substantial variability in the breakthrough curves. In general, projected travel times range over an order of magnitude, from thousands to tens of thousands of years; a small number of realizations exhibit extremely long travel times, caused by very high suction (low unsaturated conductivity) in some units. The mean breakthrough curves do not take into account the small number of realizations with very long travel times.

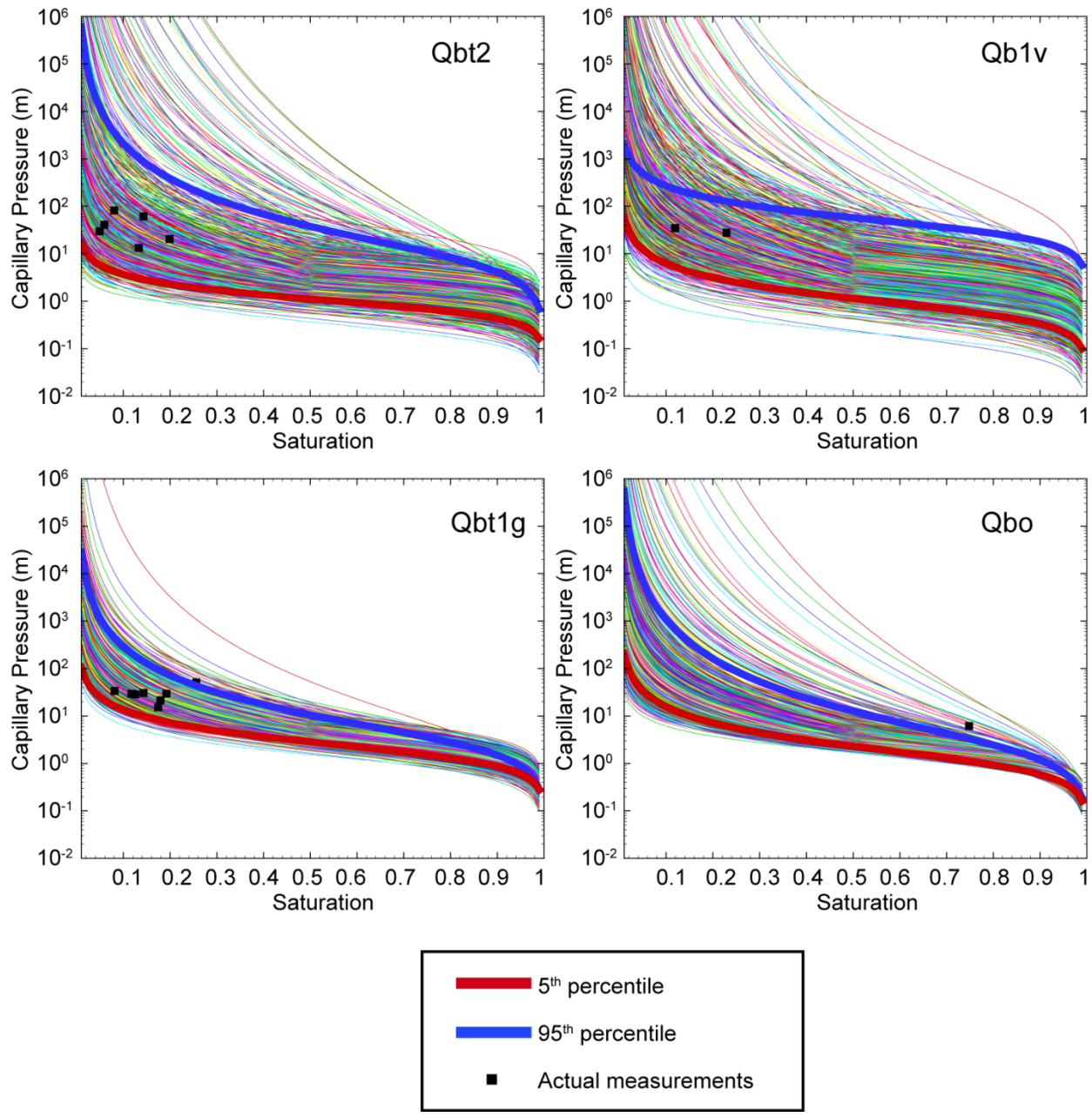

Figure VIII-1
Retention Curves for Bandelier Tuff Units Based on 1000 Realizations (generated from the Latin Hypercube Sampling method)

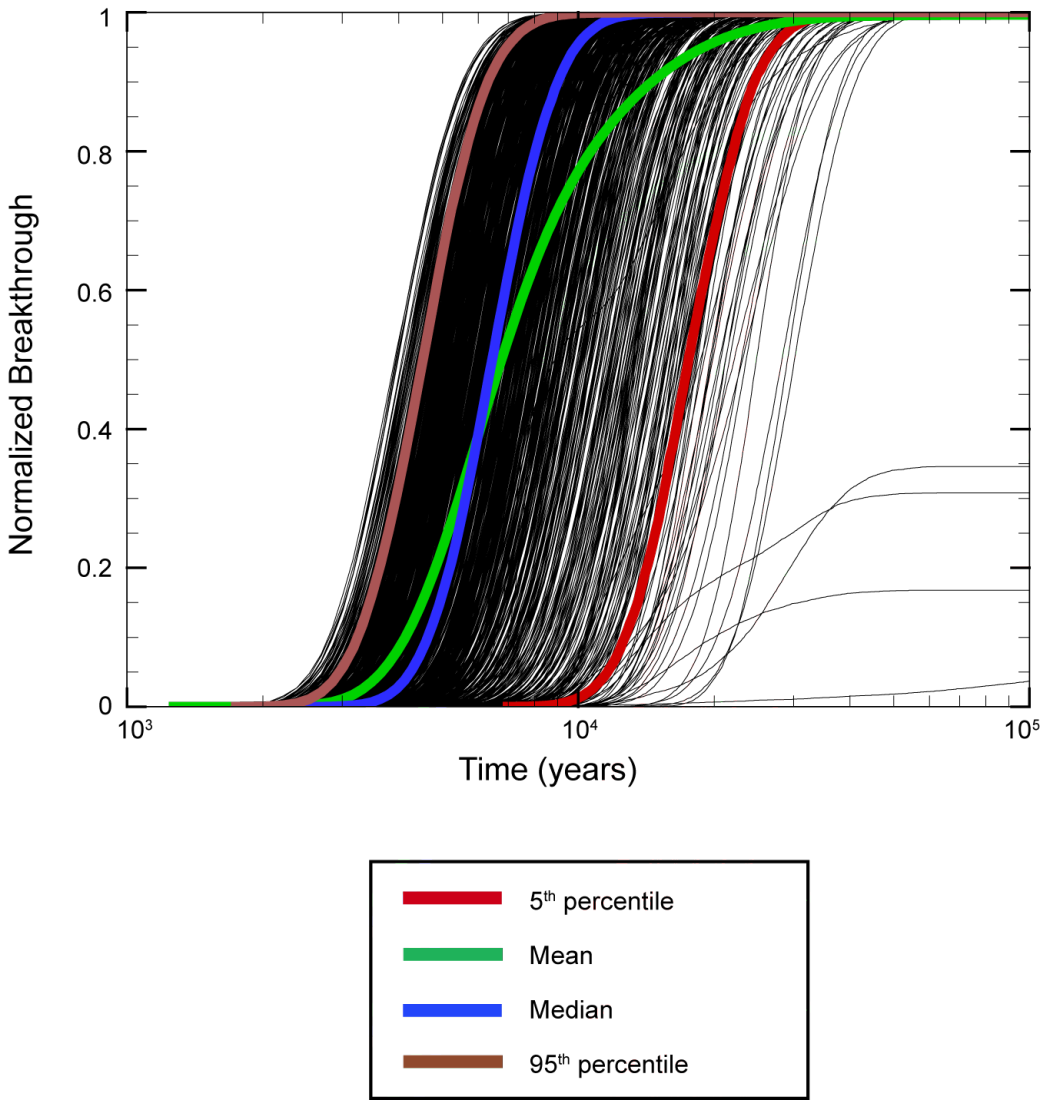

Figure VIII-2
Normalized Cumulative Breakthrough Curves from 1000 Monte Carlo Realizations Using Sampled Hydrologic Properties

The fifth, fiftieth (median), and ninety-fifth percentile breakthrough curves shown in Figure VIII-2 represent the results of actual model realizations. The mean curve represents the average behavior of the modeled system across all realizations and, as such, deviates significantly from actual breakthrough curves projected by the modeling. Examination of the figure suggests the mean curve will likely overestimate mass fluxes at early times in a simulation, but underestimate actual fluxes at later times. More importantly, the mean curve may underestimate the peak of the mass flux. These shortcomings suggest that the use of the median breakthrough curve may be preferable if an accurate understanding of the groundwater system is desired.

The results of the four simulations that sampled the hydrologic properties directly were used to determine how quickly the model results converged. This analysis was conducted by comparing the fifth percentile, mean, median, and ninety-fifth percentile breakthrough curves projected by these simulations; the results of the comparisons are provided in Figure VIII-3. The mean breakthrough curves shown for these simulations represent the average of the breakthrough curves across all realizations. The fifth, fiftieth, and ninety-fifth percentile curves represent the appropriate rank of normalized breakthrough at each time during the simulation. For example, the fifth percentile curve represents the fifth percentile of all realization results at each time during the 1,000-year simulation period. Curves estimated in this manner may or may not coincide with any of the actual breakthrough curves estimated for the simulation. Also shown in two of the four frames of Figure VIII-3 is the breakthrough curve estimated using the mean hydrologic properties listed in Table VIII-1.

The convergence analysis indicates that the fifth and ninety-fifth percentile, mean, and median breakthrough curves estimated using 100 realizations closely resemble the results seen for a simulation that includes 1,000 realizations. These results suggest that the use of 100 realizations in Monte Carlo simulations that use LHS may adequately represent the variability in the projected breakthrough curves. Separately, it is interesting to note that the breakthrough curve estimated using the mean hydrologic properties of the geologic units (Table VIII-1) is nearly identical to the median breakthrough curve estimated by the probabilistic modeling; however, it differs substantially from the mean breakthrough curve that is calculated by averaging breakthrough behavior over all realizations.

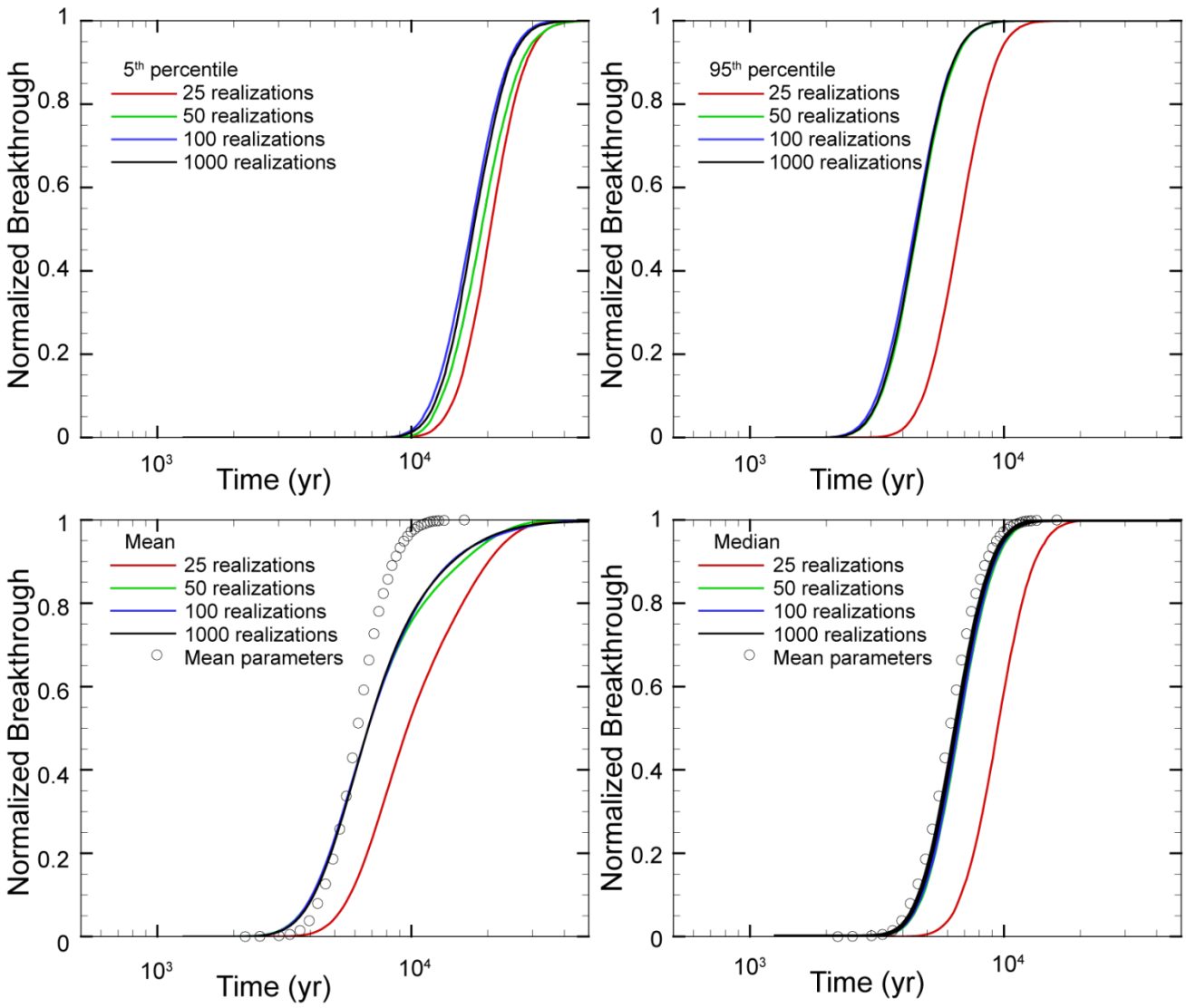

Figure VIII-3
Comparison of Fifth Percentile, Mean, Median, and Ninety-fifth Percentile Breakthrough Curves Estimated using Different Numbers of LHS Realizations

The results shown in Figures VIII-2 and VIII-3 provide a basis for quantifying the uncertainty associated with the groundwater and contaminant travel times projected for the Area G performance assessment and composite analysis. Examination of the model projections for the 1,000-realization simulation indicates that particles will first appear at the compliance boundary at about two-thirds of the time projected when mean hydrologic properties are used for the geologic strata. For example, the time required for half of the particle mass to arrive at the compliance boundary is projected to be approximately 6,500 years when mean hydrologic properties and an infiltration rate of 1 mm/yr (0.039 in./yr) are assumed. Examination of Figure VIII-2 reveals that the minimum arrival time for half of the particle mass is on the order of 4,000 years. Consistent with the information provided above, a much greater difference is observed between the arrival time estimated using mean hydrologic properties and the maximum travel time estimated by the uncertainty analysis. The time required for half of the particle mass to reach the compliance boundary increases from 6,500 years to about 30,000 years.

The results of the Monte Carlo simulations that were conducted by sampling the retention curves were compared to projections based on the sampling of hydrologic properties. Figure VIII-4 compares the median breakthrough curves estimated by sampling hydrologic properties directly to those projected using sampled retention curves; results are provided for simulations using 25 to 1,000 realizations. The three frames included in the figure correspond to the different methods used to sample the retention curves.

Looking first at Figure VIII-4a, the median breakthrough curves estimated by all but one simulation agree with the 1,000-realization model run that used sampled hydrologic properties; only the 25-realization simulation that used sampled hydrologic properties diverges from the results of the 1,000-realization simulation. These results confirm that the approach that samples retention curves directly yields results consistent with simulations that sample hydrologic properties of the geologic media. Sampling retention curves directly appears to confer an advantage in simulations with a small number of realizations, as shown by the results for the 25-realization model runs. This may reflect the fact that the retention curves calculated from small samples of hydrologic properties do not address the probability space of the retention curves as completely as sampling the curves directly.

The median breakthrough curves estimated when the retention curve intervals are sampled randomly (Figure VIII-4b) are the same as those seen when the central curve of each interval is selected (Figure VIII-4a). However, the median curves estimated when retention curves are sampled without using LHS diverge significantly from the 1,000-realization results (Figure VIII-4c). In this case, the median breakthrough curves estimated by all of the simulations that used sampled retention curves imply later breakthrough times than the 1,000-realization result, and fare poorly when compared to the results of simulations that sample hydrologic properties directly over small numbers of realizations.

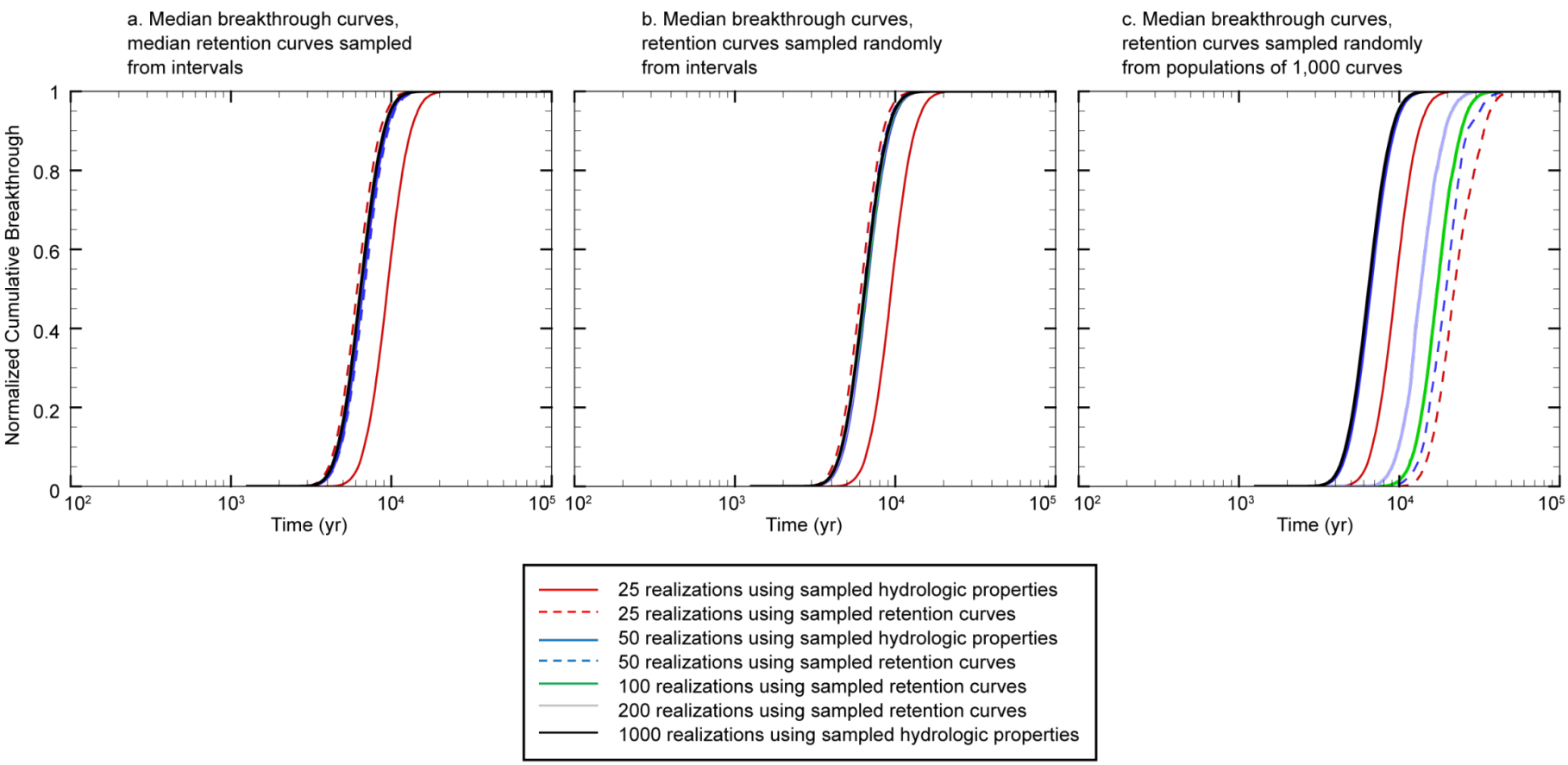

Figure VIII-4
Breakthrough Curves Estimated Using Sampled Hydrologic Properties vs. Sampled Retention Curves

The results reported here are based on modeling conducted using a constant infiltration rate of 1 mm/yr (0.039 in./yr). Modeling conducted using different infiltrations rates will rely on the retention curve data evaluated in this analysis. As a result, although changes in infiltration rate will cause breakthrough times to shift, the relative behavior discussed above is expected to be preserved.

As discussed in Section VIII.3.1, the subsets of retention curves used in the modeling were developed by sorting the 1,000 curves for each unit on the basis of capillary pressure at a saturation of 0.5; the sorted curves were subsequently divided into groups of 5, 10, 25, and 40 retention curves. Sorting the curves using a different saturation level will alter the order of the curves and, as a result, affect the results provided above. To determine the importance of this effect, breakthrough curves were estimated using retention curves that were sorted using a saturation level of 0.25; the median and variance of the breakthrough curves were compared to the median and variance of the breakthrough curves based on retention curves sorted at a saturation level of 0.5. As shown in Figure VIII-5, these statistics compare favorably between the two sets of simulations, indicating that the saturation level used to sort the retention curves is relatively unimportant.

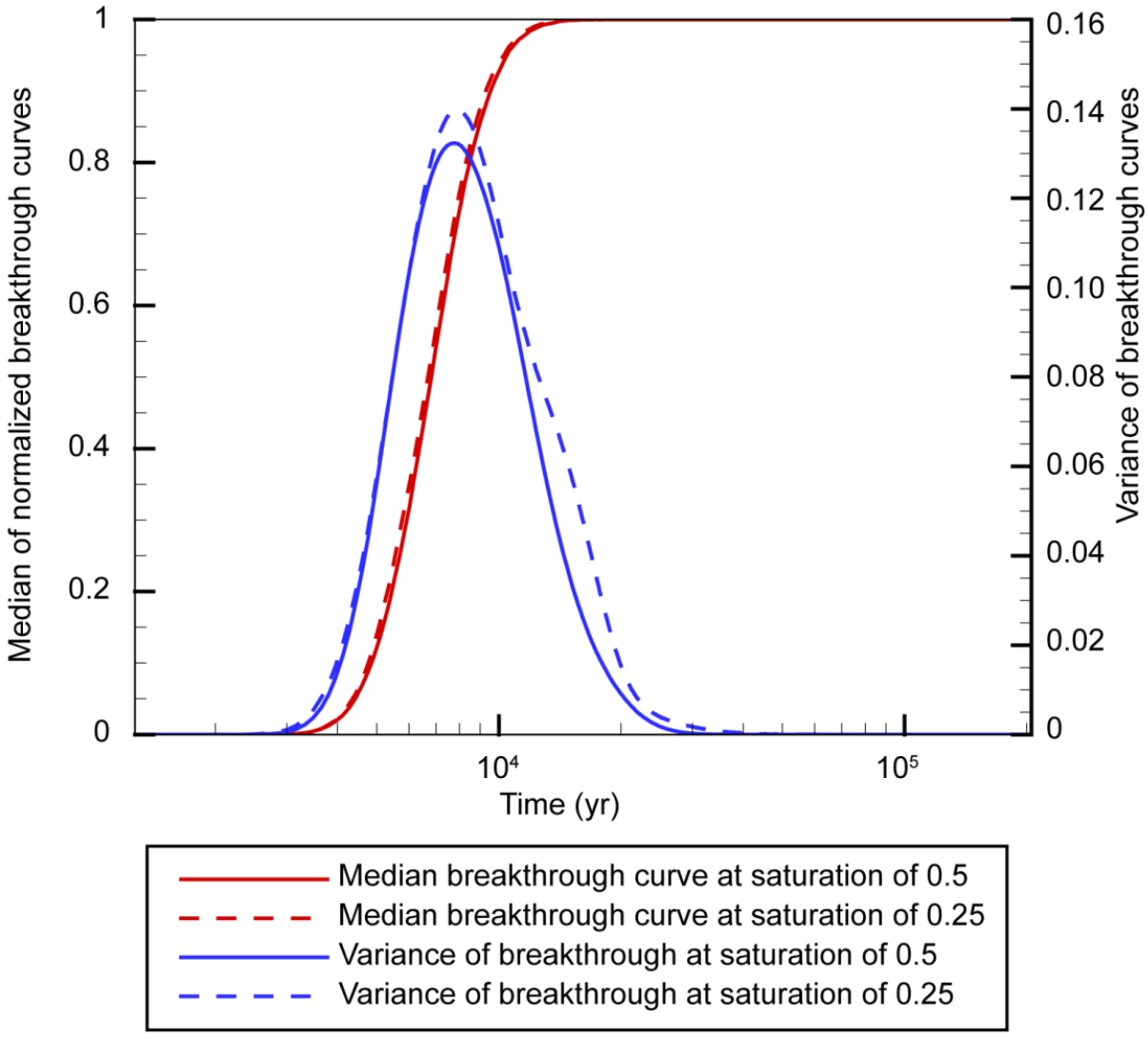

Figure VIII-5
Projected Breakthrough Curves and Variance of Breakthrough Using Retention Curves Sorted at Saturations of 25 and 50 Percent

VIII.4 References

Iman, R.L., J. C. Helton, and J. E. Campbell,1981. "An approach to sensitivity analysis of computer models, Part 1. Introduction, input variable selection and preliminary variable assessment." *Journal of Quality Technology* 13(3): 174–183.

Lu, Z., and D. Zhang, 2002. "Stochastic analysis of transient flow in heterogeneous variably saturated porous media: the van Genuchten-Mualem constitutive model," *Vadose Zone Journal*, 1:137–149.

McKay, M. D., R. J. Beckman, and W. J. Conover, 1979. "A comparison of three methods for selecting values of input variables in the analysis of output from a computer code, *Technometrics*," 21 (2): 239–245.

Springer, E. P., 2005. "Statistical exploration of matrix hydrologic properties for the Bandelier Tuff, Los Alamos, New Mexico," *Vadose Zone Journal*, 4:505–521.

Stauffer, P.H. and Z. Lu, In Press, "Quantifying transport uncertainty in unsaturated rock using Monte Carlo sampling of retention curves," *Vadose Zone J* .

van Genuchten, M. Th., 1980. "A closed-form equation for predicting the hydraulic conductivity of unsaturated soils," *Soil Sci. Soc. Am. J.,* 44: 892–898.